

REPORT DOCUMENTATION PAGE

Form Approved OMB No. 0704-0188

Public reporting burden for this collection of information is estimated to average 1 hour per response, including the time for reviewing instructions, searching existing data sources, gathering and maintaining the data needed, and completing and reviewing the collection of information. Send comments regarding this burden estimate or any other aspect of this collection of information, including suggestions for reducing the burden, to Department of Defense, Washington Headquarters Services, Directorate for Information Operations and Reports (0704-0188), 1215 Jefferson Davis Highway, Suite 1204, Arlington, VA 22202-4302. Respondents should be aware that notwithstanding any other provision of law, no person shall be subject to any penalty for failing to comply with a collection of information if it does not display a currently valid OMB control number.

PLEASE DO NOT RETURN YOUR FORM TO THE ABOVE ADDRESS.

| | | |
|--|---------------------------------------|--|
| 1. REPORT DATE (DD-MM-YYYY) 17-04-2006 | 2. REPORT TYPE Final Report | 3. DATES COVERED (From – To) 01-Apr-02 - 17-Apr-06 |
|--|---------------------------------------|--|

| | |
|--|--|
| 4. TITLE AND SUBTITLE Experimental and Numerical Study of Spacecraft Contamination Problems associated with Gas and Gas-Droplet Thruster Plume Flows | 5a. CONTRACT NUMBER ISTC Registration No: 2298 |
| | 5b. GRANT NUMBER |
| | 5c. PROGRAM ELEMENT NUMBER |

| | |
|---|-----------------------------|
| 6. AUTHOR(S) Professor Mikhail Samuilovich Ivanov | 5d. PROJECT NUMBER |
| | 5d. TASK NUMBER |
| | 5e. WORK UNIT NUMBER |

| | |
|---|--|
| 7. PERFORMING ORGANIZATION NAME(S) AND ADDRESS(ES) Institute of Theoretical and Applied Mechanics 4/1 Institutskaya St Novosibirsk 630090 Russia | 8. PERFORMING ORGANIZATION REPORT NUMBER N/A |
|---|--|

| | |
|---|---|
| 9. SPONSORING/MONITORING AGENCY NAME(S) AND ADDRESS(ES) EOARD PSC 821 BOX 14 FPO 09421-0014 | 10. SPONSOR/MONITOR'S ACRONYM(S) |
| | 11. SPONSOR/MONITOR'S REPORT NUMBER(S) ISTC 01-7002 |

12. DISTRIBUTION/AVAILABILITY STATEMENT
Approved for public release; distribution is unlimited.

13. SUPPLEMENTARY NOTES

14. ABSTRACT

The project consists of two large parts. The first part is the study of plume flows escaping into vacuum, and the second part deals with gas-droplet flows. These two parts are united by a common area of research, namely, contamination problems of space station surfaces due to thruster firing.

The objective of the first part is accurate prediction of force and heat loads and contamination due to interaction of thruster plumes with the spacecraft surface. This requires a detailed knowledge of the plume structure. For this purpose, a software system SMILE (Statistical Modeling In Low-density Environment) is developed for modeling plume flows. This system is based on the Direct Simulation Monte Carlo (DSMC) method and incorporates economical numerical schemes of the DSMC method – majorant frequency scheme, advanced models that describe energy transfer in the case of collisions of diatomic and polyatomic molecules, possibilities of parallelization, and models for chemically reacting flows of polyatomic gases. An important aspect associated with this activity is the use of advanced object-oriented approaches for the development of the SMILE system.

The objective of the second part is an experimental and numerical study of a two-phase gas-droplet flow arising in the case of simultaneous exhaustion of liquid and gas into vacuum. This problem is closely related to the processes of backflow contamination of spacecraft surfaces by thruster plumes with a fuel film used for cooling the inner surface of the nozzle. The main attention is paid to studying the behavior of droplets into which the liquid is decomposed at the initial stage of droplet motion and to the interaction of droplets with a freely expanding gas plume.

15. SUBJECT TERMS
Thruster, plume, gas dynamics, experimental, numerical, spacecraft contamination, EOARD

| | | | | | |
|--|------------------------------|-------------------------------|---|-----------------------------------|---|
| 16. SECURITY CLASSIFICATION OF: | | | 17. LIMITATION OF ABSTRACT UL | 18. NUMBER OF PAGES 218 | 19a. NAME OF RESPONSIBLE PERSON BARRETT A. FLAKE |
| a. REPORT UNCLAS | b. ABSTRACT UNCLAS | c. THIS PAGE UNCLAS | | | 19b. TELEPHONE NUMBER (Include area code) +44 (0)20 7514 4285 |

ISTC 2298

**Final
Project Technical Report
of ISTC 2298**

**Experimental and Numerical Study of Spacecraft
Contamination associated with Gas and
Gas-Droplet Thruster Plume Flows
(From 1 April 2002 to 30 November 2005 for 44 months)**

**Mikhail Samuilovich Ivanov
(Project Manager)
RUSSIAN ACADEMY OF SCIENCES
SIBERIAN BRANCH
Institute of Theoretical and Applied Mechanics (ITAM),
Institute of Thermophysics (IT)
630090, Novosibirsk, Russia**

January 2006

This work was supported financially by EOARD and performed under the contract to the International Science and Technology Center (ISTC), Moscow.

List of contents

| | |
|---|------------|
| 1. INTRODUCTION | 3 |
| 1.1. Brief information on the project | 3 |
| 1.2. Brief description of the work plan: objective, expected results, technical approach | 3 |
| 2. METHODS, EXPERIMENTS, THEORY | 5 |
| 2.1. Task 1 | 5 |
| 2.2. Task 2 | 6 |
| 3. RESULTS | 9 |
| 3.1. Task 1. Investigation of plume flows without drops. | 9 |
| 3.2. Task 2. Investigation of gas-droplet flows | 67 |
| 4. SUMMARY | 209 |
| 5. PAPERS AND REPORTS PUBLISHED | 211 |
| 6. List of presentations at conferences and meetings with abstracts | 216 |

1. INTRODUCTION

1.1. Brief information on the project

Contracting Institute: Institute of Theoretical and Applied Mechanics, Siberian Branch, Russian Academy of Sciences, 4/1 Ul. Institutskaya, 630090, Novosibirsk, Russia

Participating Institutes: Institute of Thermophysics, Siberian Branch, Russian Academy of Sciences, 1 Prospekt Lavret'eva, 630090, Novosibirsk, Russia

Project Manager: Mikhail Samuilovich Ivanov, Head of Laboratory of the Institute of Theoretical and Applied Mechanics, Siberian Branch, Russian Academy of Sciences, Professor. Phone: 7-(383-2)-34-31-63, Fax: 7-(383-2)-34-22-68, e-mail: ivanov@itam.nsc.ru

Commencement Date, Duration: April 1, 2002, 44 months.

1.2. Brief description of the work plan: objective, expected results, technical approach.

The project consists of two large parts. The first part is the study of plume flows escaping into vacuum, and the second part deals with gas-droplet flows. These two parts are united by a common area of research, namely, contamination problems of space station surfaces due to thruster firing.

1. The objective of the first part is accurate prediction of force and heat loads and contamination due to interaction of thruster plumes with the spacecraft surface. This requires a detailed knowledge of the plume structure. For this purpose, a software system SMILE (Statistical Modeling In Low-density Environment) is developed for modeling plume flows. This system is based on the Direct Simulation Monte Carlo (DSMC) method and incorporates economical numerical schemes of the DSMC method – majorant frequency scheme, advanced models that describe energy transfer in the case of collisions of diatomic and polyatomic molecules, possibilities of parallelization, and models for chemically reacting flows of polyatomic gases. An important aspect associated with this activity is the use of advanced object-oriented approaches for the development of the SMILE system.

The milestones of this part are as follows.

- Development and implementation of advanced models of internal energy relaxation and chemical reactions for diatomic and polyatomic molecules.
- Verification and validation of developed models via comparisons with available experimental data
- Creation of an object-oriented version of the SMILE software system in the C++ language.

2. The objective of the second part is an experimental and numerical study of a two-phase gas-droplet flow arising in the case of simultaneous exhaustion of liquid and gas into vacuum. This problem is closely related to the processes of backflow contamination of spacecraft surfaces by thruster plumes with a fuel film used for cooling the inner surface of the nozzle. The main attention is paid to studying the behavior of droplets into which the liquid is decomposed at the initial stage of droplet motion and to the interaction of droplets with a freely expanding gas plume.

The processes of liquid-film dispersion inside the nozzle and the regions and mechanisms of formation of drops of various size is studied, the role of the initial parameters of the gas and liquid parameters and channel geometry are determined, and the effect of free supersonic expansion of the carrier gas into vacuum on the spatial distribution of fluxes of large and small drops is analyzed. Special attention is paid to determining the conditions of origination of backflows of the liquid phase in the case of expansion of the gas-droplet mixture into vacuum. In the experimental part, this part of the project includes quantitative researches of the influence of the governing parameters – nozzle geometry, physical properties of the liquid, velocity and density of the cocurrent gas flow on characteristics of the gas-droplet backflow. The experimental results of the angular distribution of the droplet phase are then used for validation of theoretical models of the gas-droplet plume flow. Based on experimental and numerical results, the physical mechanism that entrains large low-speed droplets in the plume gas backflow are analyzed. The results obtained allow us to explain and predict the process of contamination of the spacecraft surface by thrusters with fuel film cooling of the nozzle.

The experimental results obtained are used as the reference data in the numerical simulation of a gas-droplet flow exhausted into vacuum. Based on the results of experiments and numerical simulation, the reasons of contamination of surfaces, constructional elements, and equipment of orbital stations by attitude and orbit control thrusters, drainage systems of pipelines for refueling and disposal of spent water and other technological liquids are analyzed.

2. METHODS, EXPERIMENTS, THEORY

2.1. Task 1.

In gas dynamics studies the basic criterion of the flow regime is the Knudsen number $Kn=\lambda/L$, where λ is the mean free path in gas and L is the reference flow scale. The flow regime is continuum when the Knudsen number tends to zero. While studying gas flows in this regime, one can disregard its microscopic structure and consider only the macroparameters such as density, velocity, or temperature, etc. For the Knudsen number tending to infinity, the flow regime can be considered as free-molecular. In this case, particle collisions with the body surface play the determining role. There is a transitional regime between the free-molecular and continuum ones, where not only gas-surface collisions but also intermolecular collisions are important. Free-molecular and transitional regimes are the main subject of the study in Problem 1 in the present project. In addition to considerable viscous effects including, apart from viscosity, heat conduction, relaxation, diffusion, and irreversible chemical reactions, an important feature of rarefied hypersonic flows is strong thermal nonequilibrium of the flow, i.e., the velocity distribution function is substantially non-Maxwellian. Thermal and chemical relaxation lengths in such flows become comparable to or larger than the reference flow scale, and the difference in temperatures of translational, rotational, and vibrational molecular modes becomes determining.

For a near-continuum flow ($Kn \ll 1$) it is usually sufficient to take into account the effects of rarefaction through the boundary conditions of slip velocity and temperature jump on the surface for the Navier-Stokes equations. These equations, however, fail when studying rarefied flows with finite Knudsen numbers where the flow becomes considerably nonequilibrium. In this case, the kinetic approach is required, i.e., solving the Boltzmann equation -- the basic equation of the kinetic theory of gases. Recently, the DSMC method has become de facto the main tool for the study of complex multidimensional flows of rarefied hypersonic aerothermodynamics. There are two different approaches to derivation and substantiation of the DSMC method. The first approach [1] (the physical one), is based on stochastic imitation of rarefied gas models by hundreds of thousands of simulated particles. The second approach (the mathematical one) is based on the derivation of numerical schemes of the DSMC method directly from the master kinetic equation using the general theory of Monte Carlo methods [2]. The DSMC method may, therefore, be considered as a statistical method for solving the Boltzmann equation. In the present project, Problem 1 involves the DSMC method as well.

Prof. Ivanov' team from the Institute of Theoretical and Applied Mechanics (ITAM, Russia) has long-term experience in the field of high-altitude aerothermodynamics. The recent years have seen a very successful application of the DSMC tools developed by this team for many complicated aerospace problems, for example, aerodynamics of various models of spacecraft and their elements with real gas effects, rarefied flows with separation, plume and plume impingement problems, viscous flows inside micronozzles, etc [4-9].

References used:

1. Bird, G., Molecular Gas Dynamics and the Direct Simulation of Gas Flows, Oxford, 1994.
2. Ivanov, M.S., Gimelshein, S.F., Computational hypersonic rarefied flows, Annu. Rev. Fluid Mech. 1998. 30:469-505.
3. Gimelshein S.F., Ivanov M.S., Markelov G.N., Gorbachev Yu.E. Statistical Simulation of Nonequilibrium Rarefied Flows with Quasiclassical VVT Transition Models. Journal of Thermophysics and Heat Transfer, Vol.12, No. 4, 1998, pp. 489-495.

4. Ivanov M.S., Kashkovsky A.V., Gimelshein S.F., Markelov G.N. Statistical simulation of hypersonic flows from free-molecular to near-continuum regimes. *Thermophysics and Aeromechanics*. Vol. 4, No. 3, 1997, pp. 251-268.

5. Gimelshein S.F., Boyd I.D., Ivanov M.S. DSMC Modeling of Vibration-Translation Energy Transfer in Hypersonic Rarefied Flows. AIAA Paper 99-3451. Norfolk, VA, June 1999.

6. Gimelshein S.F., Boyd I.D., Ivanov M.S. Modeling of internal energy transfer in plume flows of polyatomic molecules by the DSMC method. AIAA Paper 99-0738. Reno, NV, January 1999.

7. Ivanov M.S., Markelov G.N., Kashkovsky A.V., Gimelshein S.F. Statistical simulation of high-altitude aerodynamic problems. Proc. II European Symposium on Aerothermodynamics for Space Vehicles. ESTEC, Noordwijk, The Netherlands, 24-26 November 1998.

8. Markelov G.N., Kashkovsky A.V., Ivanov M.S. Space station MIR aerodynamics along the descent trajectory, accepted for publication in *Journal of Spacecraft and Rockets*.

9. Markelov G.N., Ivanov M.S. A comparative analysis of 2D/3D micronozzle flows by the DSMC method. AIAA Paper 2001-1009, Jan. 2001.

2.2. Task 2.

The study of the problem of contamination of spacecraft surfaces by thrusters was initiated in [1-3]. The main objective of Task 2 of the project is to develop consistent physical and mathematical models describing properly the back and side portions of the gas-droplet flows exhausted into vacuum. The existent models of the gas-droplet flows are mainly concerned with the prediction of the plume core flow.

The analysis of the plume backflow is impossible without consideration of the nozzle boundary layer even for a mono-phase plume flow. Additional difficulties arise due to rapid expansion of the plume exhaust flow. In this case, the entire range of flow regimes covers regions from the continuum flow within the nozzle, through the transitional flow regime in the near vicinity of the nozzle lip, to the free-molecular flow at a large distance from the nozzle exit plane. Only a combination of the Navier-Stokes (NS) numerical approach with the DSMC method is capable of simulating such flows.

To avoid limitations inherent in the traditional models of two-phase flows, the present project employs the Euler-Lagrangian algorithm of numerical investigation of multiphase media [4]. In this approach, the carrier phase dynamics is described by a combined NS-DSMC method, and the dispersed phase behavior is simulated by the discrete model of probe particles. Phase interaction (processes of interphase transfer of mass, momentum, and energy) is included into consideration by means of an iterative procedure with space-time averaging of trajectory parameters of the test particles inside each computational cell. One of the essential advantages of this algorithm is its flexibility, which allows one to consider comparatively easily various models of the carrier and dispersed phases (Euler and Navier-Stokes models, rarefied gas models, solid particles, liquid droplets, etc.) and also various physicomachanical processes that occur inside each phase and at interfaces (for instance, origination of dispersed inclusions, their coagulation and splitting, etc.). This allows one, in particular, to consider multiphase flows taking into account the condensation of the carrier phase. A semi-empirical model for formation of droplets and their interactions is used [5].

For accurate consideration of the two-phase flow it is also necessary to take into account the dynamics of droplet phase forming inside the nozzle as a result of the interaction of the liquid wall film with gas flow. Another process to be considered is the formation of the droplets near the nozzle lip. Entering vacuum, most liquids become overheated even at room temperature, which leads to explosive boiling of the liquid with its subsequent decomposition into droplets of different size. The process of outflow and decomposition of a liquid jet exhausted into vacuum was considered in [6-9].

For numerical modeling of a gas-liquid mixture exhausting into vacuum, the initial and boundary conditions for the liquid phase should be imposed. One of the goals of Task 2 is to determine experimentally the distribution of the number density of droplets at the nozzle exit plane, and measure their sizes and velocities. These data are used as the initial conditions in numerical simulations.

In solving Task 2, detailed experiments within the Project are performed at the Institute of Thermophysics (IT, Novosibirsk) on the unique facility VIKING (vacuum simulation chamber for investigating nonequilibrium gas-dynamics) [10]. This is a large-scale cryogenic-vacuum gas-dynamic facility (4 m in diameter, 12 m long, chamber volume of 150 m³), which is equipped by advanced electron-beam diagnostics and methods for flow visualization. This facility allows one to study the outflow of gases, liquids, and gas-liquid mixtures into vacuum in steady and pulsed operation modes. Various instrumental techniques: electron-beam method, mass spectrometry, and laser-beam scattering, are used in experiments. Water vapor jets exhausted into vacuum were investigated [11, 12] in the past, and the study of near-wall liquid films exhausting simultaneously with a gas from axisymmetric channels into vacuum has recently been started [13, 14]. The outflow of an ethanol film at room temperature from a cylindrical channel and supersonic nozzle into vacuum was investigated [15]. For the first time, these studies revealed the effect of origination of a liquid backflow.

Numerical activities relevant to the Project are carried out at the Institute of Theoretical and Applied Mechanics (ITAM, Novosibirsk), which has long-term experience in the field of computational rarefied fluid dynamics [16]. The recent years have seen very successful applications of the combined continuum and kinetic approaches developed at ITAM to many complicated aerospace problems [17] including those associated with the plume-plume interaction and plume contamination [18]. For the analysis of the dynamics of liquid droplets, the approach developed in [4, 19] is used. This approach has no constraints inherent in the traditional continuum models of multiphase flows and is based on the effective Euler-Lagrangian algorithm of numerical investigation of multiphase media. Within the framework of this algorithm, the dynamics of the carrier phase is described by different models of gas flow (Euler equations, NS, DSMC), and the behavior of the dispersed phase is described by the discrete model of probe particles.

The algorithms and codes for modeling gas-droplet plume flows are described in the previous reports submitted to ISTC and to the partner.

References used:

1. Trinks, H., Hoffman, R.J. Experimental Investigation of Bipropellant Exhaust Plume Flowfield, Heating and Contamination, and Comparison with the CONTAM Computer Model Predictions. AIAA Paper-83-1447.
2. Trinks, H., Kaelsch, I. Exhaust Plume Effects of Small Thrusters on Spacecraft Surfaces. AIAA Paper-87-1603.
3. Trinks, H. Experimental Investigation of the Exhaust Plume Flow Fields of Various Small Bipropellant and Monopropellant Thrusters. AIAA Paper-87-1607.
4. Kurakin, Yu.A., Schmidt, A.A. Eulerian-lagrangian description of two-phase reactive flows with discontinuities. *Lett. J. Tech. Phys.*, 1997, 23, (3), 26-32.
5. Sallam, R.F., Dai, Z., Faeth, G.M. Drop formation at the surface of plane turbulent liquid jets in still gases, *Int. J. Multiphase Flows*, 25, (1999), 1161-1180
6. Zuev, N.D., et al. Experimental Investigation of Spraying Liquids into Vacuum. In: "Flow of a Rarefied Gas with Nonequilibrium Physicochemical Processes". Proc. VIII All-Union Conf. on Rarefied Gas Dynamics. Moscow, 1987, pp. 145-148.
7. Fuchs, H., Legge, H. Flow of water jet into vacuum. *Acta Astronautica*. 1979, v. 6, N 9, pp. 1213-1226.

8. Mikatarian, R.R., Anderson, R.G. An Experimental Investigation of a Liquid Jet Expelled into a Vacuum. *J. Spacecraft Rockets*. -1966, v. 3, N 2, p. 267.
9. Alred, J.W., et al. Modeling of Water Injection into a Vacuum. NASA, Eight Annual Thermal and Fluid Analysis Workshop. *Spacecraft Analysis and Design*, Sept. 8-11, 1997, University of Houston-Clear Lake. Houston, Texas.
10. Prikhodko, V.G., Khramov, G.A., Yarygin, V.N. A Large-Scale Cryogenic Vacuum Plant for Gas-Dynamics Research. *Instruments and Experimental Techniques*, Vol. 39, No 2, 1996, pp. 162-164.
11. Prikhod'ko, V.G., Gall, L.N., et al. Electrohydrodynamic Injection of Liquid Substances into a Mass Spectrometer. *Zhurn. Tekhn. Fiziki*, 1984, V. 54, N 8, pp. 1559-1571.
12. Yarygin, V.N., et al. The effect of homogeneous condensation on gasdynamics and IR radiation of carbon dioxide and water vapor free jets. *Proc. 14th Int. Symp. RGD. Univ. of Tokyo Press*, 1984, vol. II, pp. 951-958.
13. Yarygin, V.N., Gerasimov, Yu.I., Prikhodko, V.G., Kuznetsov, L.I. Gasdynamic Aspects of Contamination Problem on a Space Station. *Proc. of the Third Int. Symp. KORUS'99, Novosibirsk*, v. 1, pp. 74-77.
14. Yarygin, V.N., Prikhodko, V.G., Gerasimov, Yu.I. Wall liquid film outflow from a supersonic nozzle into vacuum. *Proc. X Int. Conf. On the Methods of Aerophysical Research (ICMAR' 2000)*, Novosibirsk, Russia, 9-16 July 2000, Part III.
15. Prikhodko, V.G., Yarygin, V.N. Arising of the return flow in a wall liquid film expelled into vacuum from a cylindrical channel. *Thermophysics and Aeromechanics*, 2000, Vol. 7, No 3, pp. 443-445.
16. Ivanov M.S., Markelov G.N., Gimelshein S.F. Statistical Simulation of Reactive Rarefied Flows: Numerical Approach and Applications. *AIAA Paper 98-2669*, Albuquerque, June 1998.
17. Ivanov, M.S., Gimelshein, S.F., Computational hypersonic rarefied flows, *Annu. Rev. Fluid Mech.* 1998. 30:469-505.
18. Ivanov M.S., Markelov G.N., Gerasimov Yu.I., Krylov A.N., Mishina L.V., and Sokolov E.I. Free-flight experiment and numerical simulation for cold thruster plume. *J. Propulsion and Power*, Vol. 15, No.3, 1999, pp. 417-423.

3. RESULTS

3.1 Task 1. Investigation of plume flows without drops.

Task 1.1 Implementation and verification of models of internal energy relaxation for the DSMC method.

A model of internal degrees of freedom with discrete and continuous spectra of energy for rotational and vibrational modes based on the modified Larsen-Borgnakke model was developed. Numerous tests were performed for verification of the model of internal degrees of freedom; one of them is described below.

There is a tube with adiabatic mirror walls located along the X axis. The tube length is 80 m. At the coordinate $X=0$, a mixture of gases (water, atomic nitrogen, and molecular oxygen) with identical concentrations enters the tube. The flow velocity is 5000 m/s, and the number density (number of molecules per cubic meter) is $6.e+19$. Temperature nonequilibrium of the flow is artificially generated: the internal temperature is $T_{rot}=T_{vib}=500$ K and the translational temperature is $T_{trans}=5000$ K. The use of the tube allows us to obtain a “one-dimensional” test case.

When particles collide, a redistribution of internal and translational energies occurs, which results in temperature equalization. Obviously, temperature equalization occurs gradually rather than instantaneously.

Since the gas moves along the tube, temperature convergence is observed in the case of steady motion along the X coordinate. This is shown in Fig. 1.1.

Such tests are usually performed only for the collisional stage of the DSMC method, whereas either the molecular displacements are artificially canceled or a mirror box is used (i.e., zero-dimensional tests). In this case, time relaxation of temperatures occurs. If particle displacements have to be verified as well, the above-indicated “one-dimensional” test case should be used. This example is suitable for testing plume flows.

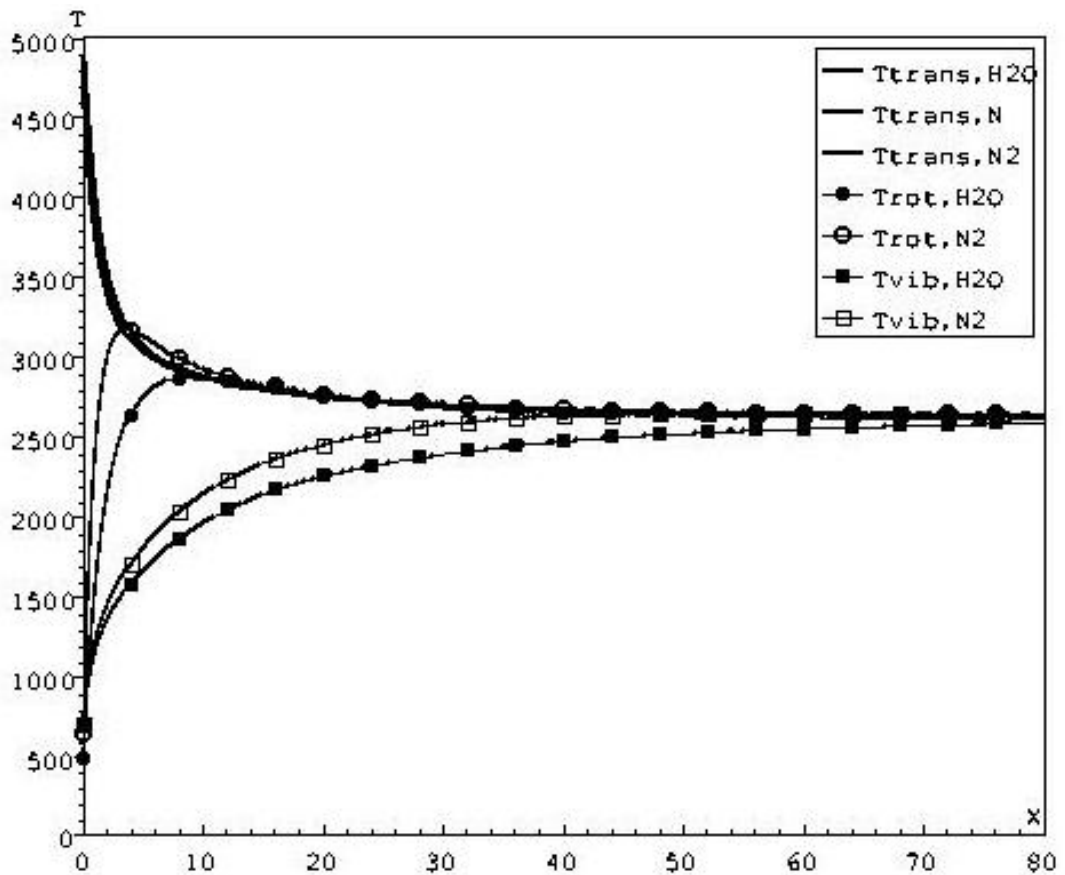


Fig. 1.1. Temperature convergence

Task 1.2. Implementation and verification of models of chemical reactions.

The model of chemical reactions on the basis of the hybrid model of total collisional energy and vibrational dissociation was developed.

1. The model of total collision energy (TCE) for chemical reactions was implemented into the DSMC method for continuous spectra of internal energies of molecules.
2. An approach of extending conventional chemical reaction models to the case of discrete energy distributions of rotational and vibrational modes is proposed. The problems inherent in continuous internal energy models lead to the conclusion that the use of discrete models in the DSMC method is preferable. One problem related to the use of discrete energy levels is that the existing chemical reaction models derived for continuous internal energies generally cannot be used with discrete internal energy modes. The approach allows modification of conventional models used with discrete rotational and vibrational levels of diatomic and polyatomic molecules.
3. The TCE model was adapted to the discrete case using the proposed approach. The conventional TCE model is constructed in such a manner that it reproduces the rate constant in the Arrhenius equation: $k(T) = AT^B \exp(-E_a/kT)$ for equilibrium continuous distribution of reactant energies. When the continuous distribution is replaced with the discrete one, the reaction rate produced by this model can differ from the Arrhenius rate. It can be easily seen in Fig. 1.2, where a comparison of the temperature dependence of the $N_2 + O \rightarrow NO + N$ reaction rate with the Arrhenius equation is given. The conventional TCE model being used with discrete internal energies, curve (3), overestimates the original Arrhenius values by about 20 percent in the range of temperatures from 10000 to 20000 K. The modification of the TCE model enables

obtaining reaction rate coefficients that are in very good agreement with the Arrhenius data.

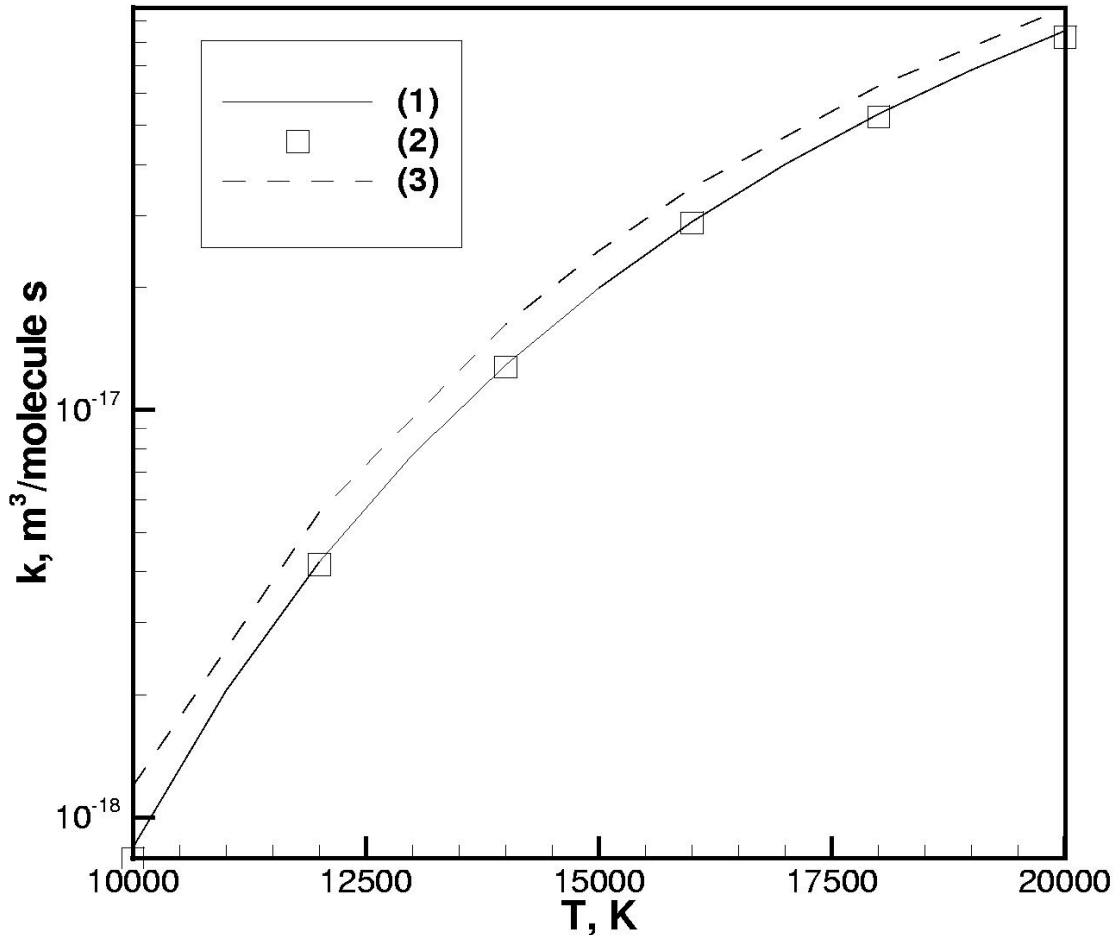


Fig. 1.2. Temperature dependence of the $N_2+O \rightarrow NO+N$ reaction rate. (1) Original Arrhenius equation, (2) adapted TCE model with discrete distributions, (3) conventional TCE model with discrete distributions

Task 1.3. Design of the general structure of the software system Smile++ in terms of the C++ program language and development of a pilot version.

A pilot version of the SMILE++ software system for two-dimensional rarefied gas flows was developed and tested.

The SMILE++ (Statistical Modelling In Low-density Environment) software system written in the C++ computer language was developed to compute planar and axisymmetric plume flows by the DSMC method. This system incorporates the following elements.

- Economical numerical schemes of the DSMC method with the use of effective collision models for the description of real gas effects, parallel algorithms of the DSMC method, and special techniques for decreasing the computational cost.
- Pre- and post-processing codes, which simplify the entire cycle of aerodynamic research from definition of the geometric model to visualization of results.
- Database of gas properties, which contains all physicochemical properties of gases necessary for DSMC computations.

Initial data necessary for the DSMC method

Obviously, the DSMC method requires a large amount of initial data:

- Gas properties. These are both real physical properties (molecular weight, number of atoms, etc.) and specific parameters of the DSMC method (collisional cross section, collisional model, etc.).
- Grid. In the simplest case, this is a uniform rectangular grid. Still, this can also be a multilevel grid, where some part of the cells is not used in computations.
- Free-stream parameters. These include direction, velocity, density, temperature, composition of the gas, etc.
- Plume parameters. These are the geometric shape of the starting surface, gas composition, velocity, direction, etc.
- Geometric model of the spacecraft. This is a set of arcs or segments in the 2D or axisymmetric cases. In addition, gas-surface interaction properties should be prescribed.
- Parameters of the method. These include the time step, stabilization criteria, the number of steps for accumulation of results, etc.

The specific feature of initial data is their multiple-choice alternatives. For instance, instead of density, it is possible to set the mean free path or the Knudsen number. Velocity can be prescribed in meters per second or in Mach numbers. The interval for saving dump files can be defined by the number of model steps or by a real period of time.

The system allows the user not only to read out these data but also to verify correctness of their values and bring to the form used in the DSMC method.

Separation of DSMC computations into stages

DSMC computations usually require considerable computer resources (memory and performance). Depending on the problem, the computational process can take from several hours to several days. To save resources and monitor the computations, the computational process is divided into three stages:

- **Pre-processing** At this stage, the initial data are prepared (definition of geometry, calculation grid, etc.).
The pre-processing stage is interactive and has a developed system of windows for interaction with the user. Separation of the pre-processing stage guarantees to a certain extent (because of the different names of files invoked) that, if the task is restarted, the computation will begin from the last saved point rather than from the very beginning.
- **Processing** This is the stage of computations. This is the longest stage, which should be optimized to the largest possible extent.

Since the computation time is large, all the necessary information is saved in special **dump** files. This allows the user to continue computations in the case of hardware malfunction or another reason that requires temporal termination of computations and to monitor the current state of computations.

- **Post-processing** This stage includes the processing of the results obtained, visualization, and, possibly, conversion of the data to initial data for another calculation.

The information for obtaining results is extracted from **dump** files.

Task 1.4. Development of pre- and post-processing subsystems.

An important feature of the SMILE++ system under development is that all computations related to DSMC simulations of rarefied gas flows are performed by means of only one executable file. This executable file includes all possible numerical algorithms and molecular models, whereas a particular set of models and algorithms is determined by the initial data. This approach requires not only the development of a powerful pre-processing system but also the development of a universal structure of initial data files, which would be flexible enough to tune the code for a particular problem to be considered but, at the same time, could be readily analyzed by both the program code and pre-processing system. In the SMILE++ system, we tried to use the idea of universal readout algorithm capable of reading initial data from the file for an arbitrary variation of initial conditions.

All initial information is divided into groups in accordance to some generic features. For instance, one group contains all data concerning the grid, the second group contains all parameters of the geometric model, the third group contains information on the gas used, etc. Depending on the problem to be solved, different methods can be used for certain actions (e.g., transfer of particles in 2D and axisymmetric cases) and, hence, different initial data; therefore, each method has its own group of data.

Each group has a unique name. It is this name that is a description of the further initial data and methods that will be used for data interpretation and flow simulation. Reading the group name, the universal readout program informs the executable program which method will be used and is adapted to reading data required for this method. Each datum within the group has a reserved word. Each method informs the readout program where the data corresponding to this or that reserved word should be placed. It is this procedure that allows generation of a unified universal program for data input.

The interactive pre-processing system is written in the C++ programming language with the use of the wxWindow window system and the Postgres database management system. The pre-processing system allows the user not only to prepare all initial data rapidly but also to analyze the previously prepared initial data using the above-described universal program for data input.

Testing of the program demonstrated significant advantages of such data input as compared to traditional procedures. The initial data are readily modified and flexibly tuned to the problem to be solved. In testing and choosing the optimal algorithms, the cost of preparation and input of the required initial information significantly decreased.

The format of files with computation results is also standardized. All data are marked by reserved words and the number indicating the length of data in bytes. If the program for processing results does not know how to interpret data corresponding to some reserved word, it “skips” these data and reads the next reserved word. This allows the user not only to use different programs for processing the same results but also to use an analyzer program that simply browses the result files and informs the user about the content of these files. In addition, this allows the user to be easily guided in large amount of results stored for a long time.

The files with computation results contain all the necessary information for reconstructing the values of physical parameters, both integral and distributed over the surface and volume. To reduce the file size, parameters that can be unambiguously calculated from other parameters are not stored and binary recording is used.

The objective of the post-processor system is conversion of data from result files to a format that can be viewed, analyzed, or visualized by conventional tools the user is accustomed to. For instance, the flow fields can be prepared in the format of the *TecPlot* or *kaptic* system; the surface characteristics can be prepared in the ASCII format in the tabular or graphical form or, again, in the *TecPlot* or *kaptic* format. As the range of tools for visualization or analysis is extended, it is

implied that the post-processing system should also be extended to prepare data in the format of new programs.

Thus, the post-processing system is an extendible set of utilities written both in the high-level languages (C, C++) and in command interpreters (bash, TCl/Tk). The necessary parameters can be defined both in the window interface of the Smile++ manager and in the windows of utilities.

References used:

1. Bird, G.A., *Molecular Gas Dynamics and the Direct Simulation of gas Flows*, Clarendon Press, Oxford, England, 1994.
2. Borgnakke, C., and Larsen, P.S., *Statistical collision model for Monte Carlo simulation of polyatomic gas mixture*, J.Comp.Phys., Vol. 18, No. 4, 1975, pp.405-420.
3. Haas, B.L., Hash, D., Bird, G.A., Lumpkin, F.E., Hassan, H. *Rates of thermal relaxation in direct simulation Monte Carlo methods*, Phys. Fluids A Vol. 6, No.6, 1994, pp.2191-2201.
4. Millikan, R.C., Whilte, D.R. *Systematics of Vibrational Relaxation*, J.Chem.Phys., Vol. 39, No.12, 1996, pp. 3209-3213.
5. Ivanov M.S., Gimelshein S.F. Current Status and Prospects of the *DSMC Modeling of Near-Continuum Flows of a Non-Reacting and Reacting Gases* (Invited Plenary Talk). To be published in Proc. Of 23-rd International Symposium on Rarefied gas Dynamics, Whistler, BC, Canada, July 2002.
6. Gimelshein N.F., Gimelshein S.F., Ivanov M.S., Levin D.A., Wysong I. *Reconsideration of DSMC Models for Internal Energy Transfer and Chemical Reactions*. To be published in Proc. Of 23-rd International Symposium on Rarefied gas Dynamics, Whistler, BC, Canada, July 2002.
7. Ivanov M.S., Bondar Ye.A., Markelov G.N., Gimelshein S.F., Taran J.-P., Study of the Shock Wave Structure about a Body Entering the Martian Atmosphere. To be published in Proc. Of 23-rd International Symposium on Rarefied gas Dynamics, Whistler, BC, Canada, July 2002.
8. Gimelshein S.F., Gimelshein N.E., Levin D.A., Ivanov M.S., Markelov G.N. Modeling of rarefied hypersonic flows over spacecraft in Martian atmosphere using the DSMC method. AIAA Paper 2002-2759, June 2002.

Task 1.5. Development of the axisymmetric version of SMILE++ and testing the code by comparison with experimental results from University of South California (USC).

Nomenclature

A -- orifice area
D -- orifice diameter
d -- distance between orifices
 γ -- specific heat ratio
 \dot{m} -- mass flux
F -- force
 μ -- viscosity coefficient
p -- pressure
 ρ -- density
T -- temperature
U -- axial velocity

subscripts

0 -- stagnation, plenum reservoir

Introduction

Development of nozzles of advanced spacecraft thrusters and vacuum devices, one has often to solve the problem of gas exhaustion from an orifice in a thin wall into vacuum. For gas expansion through the orifice, an analytical solution is known for the limiting case of the Knudsen number $Kn=\infty$, i.e. a collisionless flow. The first-order correction for the mass flux of a thin orifice were obtained by Liepmann for near zero and large Kn . Numerical results for the mass flux in the near free-molecular regime were obtained using a first-iterate solution of the Boltzmann equation and were found to agree with experimental data [Liepmann, 1961]. It is also known that the mass flux through the orifice of negligible lip thickness in the continuum limit $Kn = 0$ is always smaller than that of comparable smooth nozzle [Liepmann, 1961]. The discharge coefficient, i.e., the ratio of the orifice mass flux to that of an isentropic inviscid nozzle flow with the same throat area, was measured by different workers for various gases and aperture shapes at high Re , the specific values may be found in Ref. [Barashkin, et al., 1977] and Ref. [Livesey, 1998].

The advantage of experimental investigations of aerodynamics problems is the rapid obtaining of reliable results. However, it is not always possible to perform a physical experiment. One of experiments difficult for implementation is the problem of exhaustion of a rarefied gas from an orifice into vacuum.

Gas exhaustion from microthrusters in the transitional regime between free-molecular and continuum modes produces a thrust of the order of milli- and micronewtons. The experimental study of such small values requires the use of highly accurate equipment. In addition, the experiment itself becomes difficult to perform because the smallest vibrations or oscillations of the measurement equipment yield significant errors in the measurement results.

A numerical experiment deals with the mathematical model rather than with the real medium itself; however, using a good mathematical model that correctly describes real gas parameters essential for a particular problem, one can obtain results that fairly reliably reproduce the flow behavior. In addition, numerical experiments do not require expensive equipment and are rather cheap as compared to full-scale experiments. The results of numerical simulation of gas exhaustion from a single orifice in a thin wall were published, e.g., in Ref. [Alexeenko et. al., 2001] and Ref. [Sharipov, 2001]. Shakhov solved axisymmetric problems of rarefied gas dynamics by the finite-difference method [Shakhov, 1074].

In the present work, numerical simulation of gas exhaustion from a single orifice and a pair of closely located orifices into vacuum is performed. The objective of the work is to analyze the effect of interaction of two plumes.

Geometry and initial parameters

In the present work, we simulate gas exhaustion from a single orifice and from a pair of orifices with different distances between them (see Fig. 1.3). The letters A and B in the figure denote the points at the orifice edges, which are most remote and close to the second orifice, respectively. The orifice diameter in all variants was 1mm. The wall thickness in three-dimensional computations was 0.015 mm. In axisymmetric computations, the wall was assumed to be infinitely thin. The initial parameters of the gas inside the reservoir and the variants of reservoir geometry are listed in Table 1. The letters 'X' and 'Y' refer to three-dimensional and axisymmetric computations, respectively. The only geometric parameter changed was the distance between the orifices. The computations were performed for a diatomic gas. The gas temperature in the reservoir was 300K for all computations. Reflection of particles from the reservoir walls was simulated in accordance with the diffuse law with full accommodation of energy.

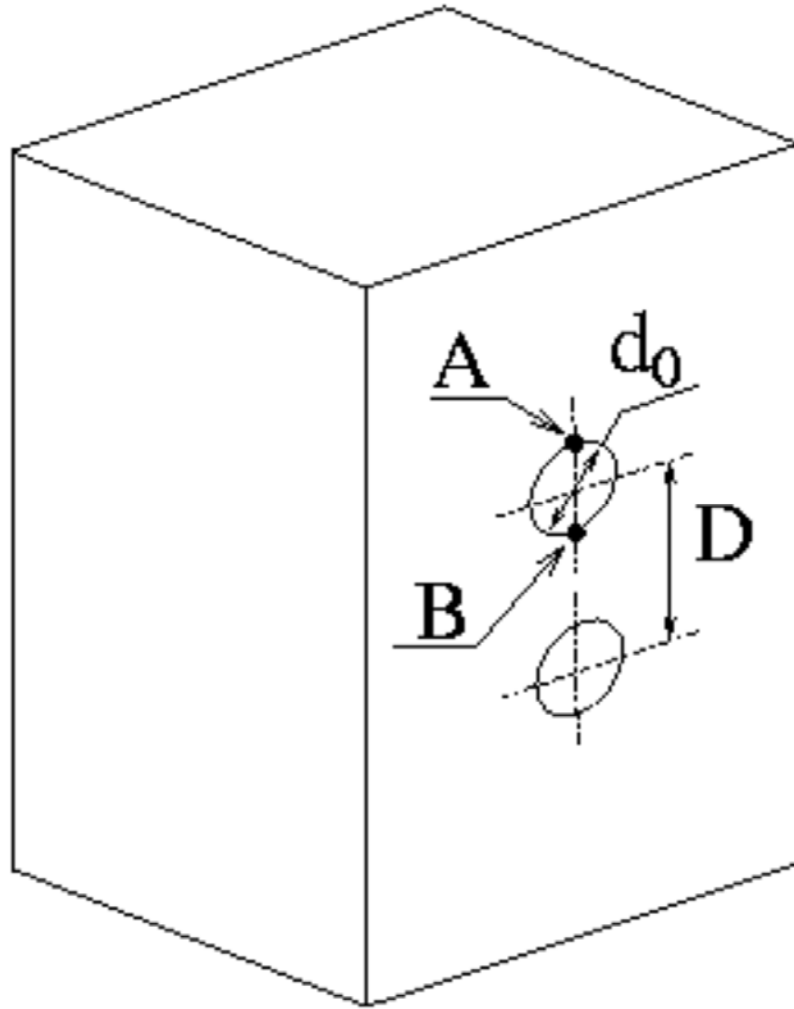


Fig. 1.3. Scheme of reservoir geometry

| P_0 , torr | Kn | D = 0mm | D = 2mm | D = 4mm | D = 16 mm |
|--------------|-------|---------|---------|---------|-----------|
| 0.01 | 4.11 | Y,X | X | X | X |
| 0.05 | 0.82 | Y | X | X | X |
| 0.1 | 0.41 | Y | X | X | X |
| 0.5 | 0.082 | Y | X | X | X |
| 1 | 0.041 | Y | X | X | X |
| 4 | 0.010 | Y,X | X | X | X |

Table 1. Parameters of the gas in the reservoir.

Numerical method

Gas exhaustion was numerically simulated by the Direct Statistical Monte Carlo (DSMC) method. Today, this method is the most widespread numerical tool for simulating gas flows in the transitional regime. Intermolecular collisions were calculated by the Variable Hard Sphere model. The number of collisions was calculated by the majorant frequency scheme [Ivanov, Rogasinsky, 1991]. A diatomic gas was used. The intermolecular potential was assumed to be a variable hard sphere model. Energy redistribution between the rotational and translational modes was performed in accordance with the Larsen-Borgnakke model with a constant rotational collision number. Diffuse reflection of molecules from the nozzle wall was implied.

To solve this problem, the computations were performed in two stages. At the first stage, the computational domain was rather large to determine the region of disturbance decay. These computations revealed the regions where flow disturbances near the orifice were significant. In subsequent computations, it was the flow near the orifice that was carefully simulated to determine thrust produced by the gas exhausting from the reservoir.

The computations were performed on a computational cluster of the Joint Supercomputer Center (Moscow, Russia). Depending on the gas pressure in the reservoir and on the fact whether axisymmetric or three-dimensional flow was simulated, 16 to 128 processors were used.

Results of computations

For a single orifice, axisymmetric computations were performed for all values of pressure from Table 1. Figure 1.4 shows the distributions of density and longitudinal velocity in the plane of the orifice for a gas with a stagnation pressure of 0.01 torr and 4 torr. The density is normalized to the density in the reservoir, and the distance from the center is normalized to the orifice diameter. If the flow is close to free-molecular, the gas-exhaustion parameters in the plane of the orifice change insignificantly. Only near the orifice wall is a drastic change in density and velocity observed. For gas exhaustion with a stagnation pressure of 4 torr, the flow parameters change almost over the entire section from the orifice axis to the wall.

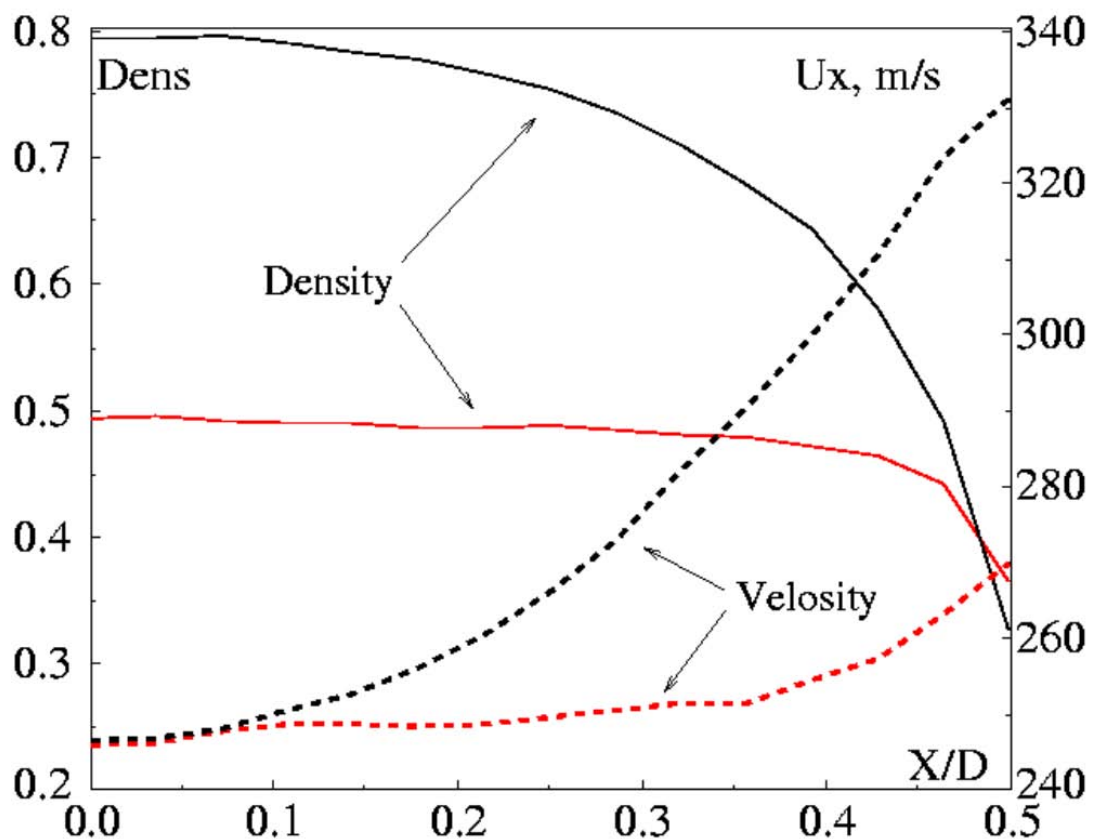


Fig. 1.4. Distributions of normalized density and longitudinal velocity at the orifice axis. The red and black curves refer to $P_0=0.01$ torr and $P_0=4$ torr. $X/D=0$ is the orifice axis.

The density flowfields are shown in Figs. 1.5 and 1.6. The change in flow parameters caused by the influence of the orifice is observed in a small upstream region, about one diameter of the orifice for the gas pressure in the reservoir equal to 0.01 torr. For denser flows, the upstream influence zone of the orifice decreases and reaches approximately 0.5D.

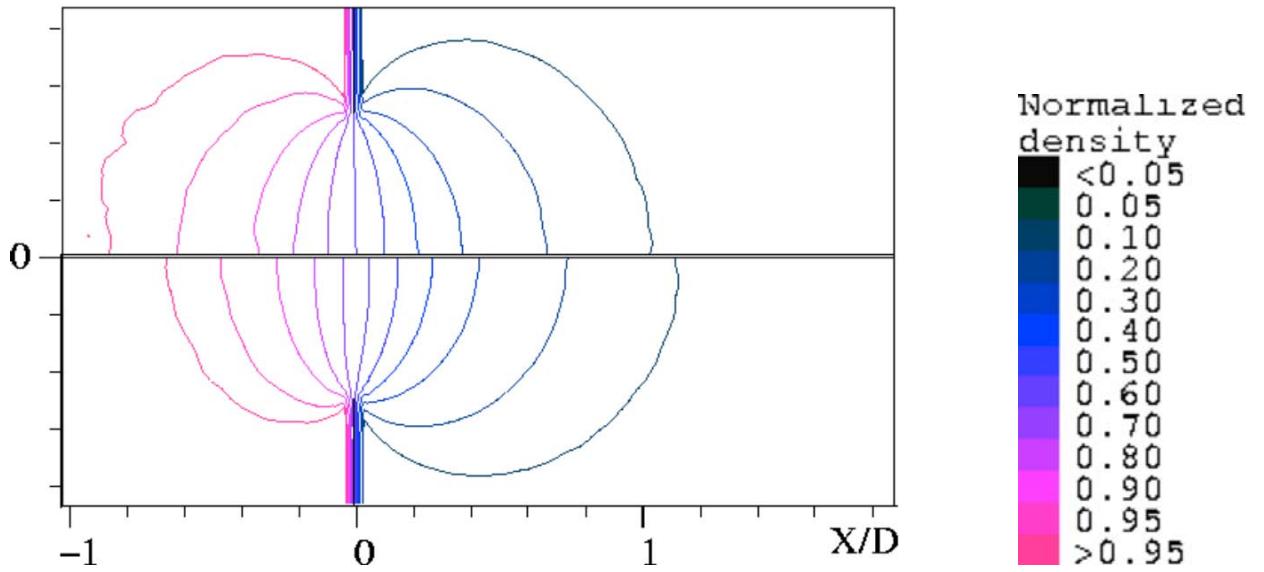


Fig. 1.5. Density flowfields. The upper and lower pictures refer to $P_0=0.01$ torr and $P_0=0.1$ torr, respectively

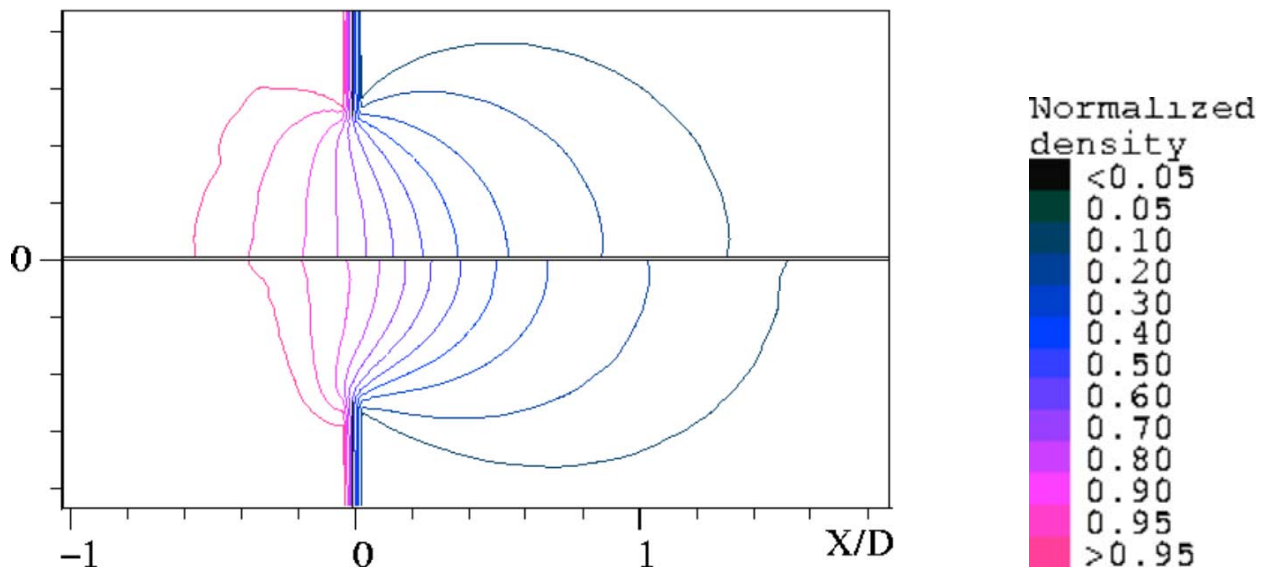


Fig. 1.6. Density flowfields. The upper and lower pictures refer to $P_0=0.5$ torr and $P_0=4$ torr, respectively

Axisymmetric computations provided the values of thrust and gas flow rate through the orifice for different gas pressures in the reservoir. Figure 1.7 shows the distribution of the flow rate coefficient

$$W = \frac{\dot{m}}{\dot{m}_0}$$

as a function of the rarefaction parameter

$$\delta = \frac{\sqrt{\pi d}}{2\lambda}$$

where λ is the mean free path. The solid curve in this figure is interpolation of experimental data of [Fujimoto and Usami, 1984]. As is seen from the figure, the dependence of the flow rate coefficient is in good agreement with the experimental results on the entire sector considered in terms of the rarefaction parameter.

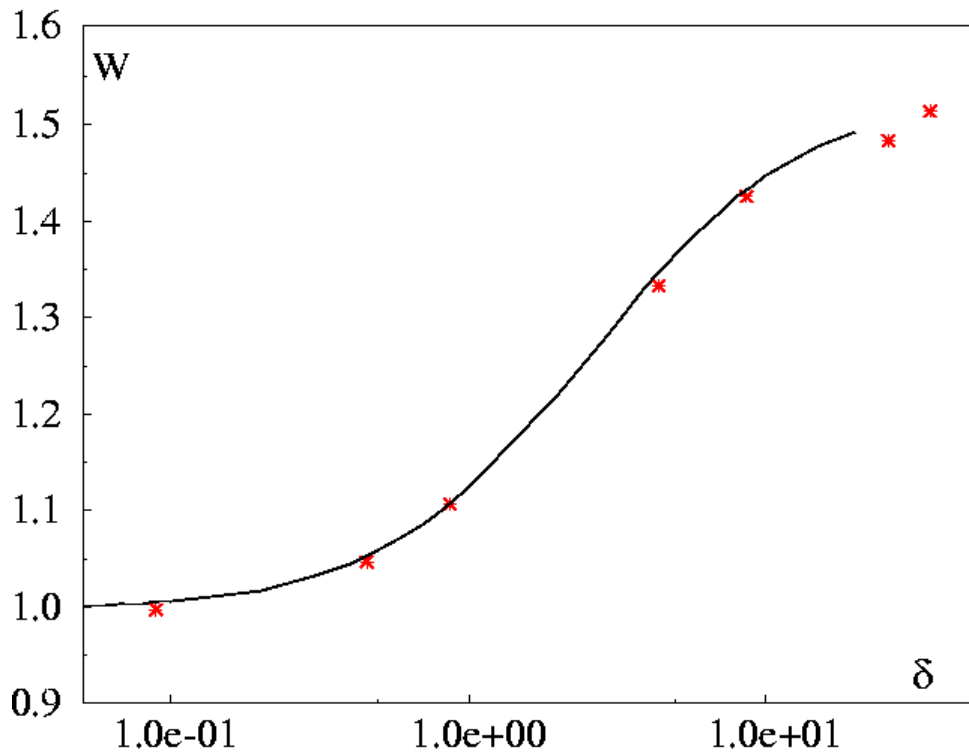


Fig. 1.7. Mass flow rate vs. rarefaction parameter. The asterisks indicate the computed results; the solid curve refers to the empirical formula

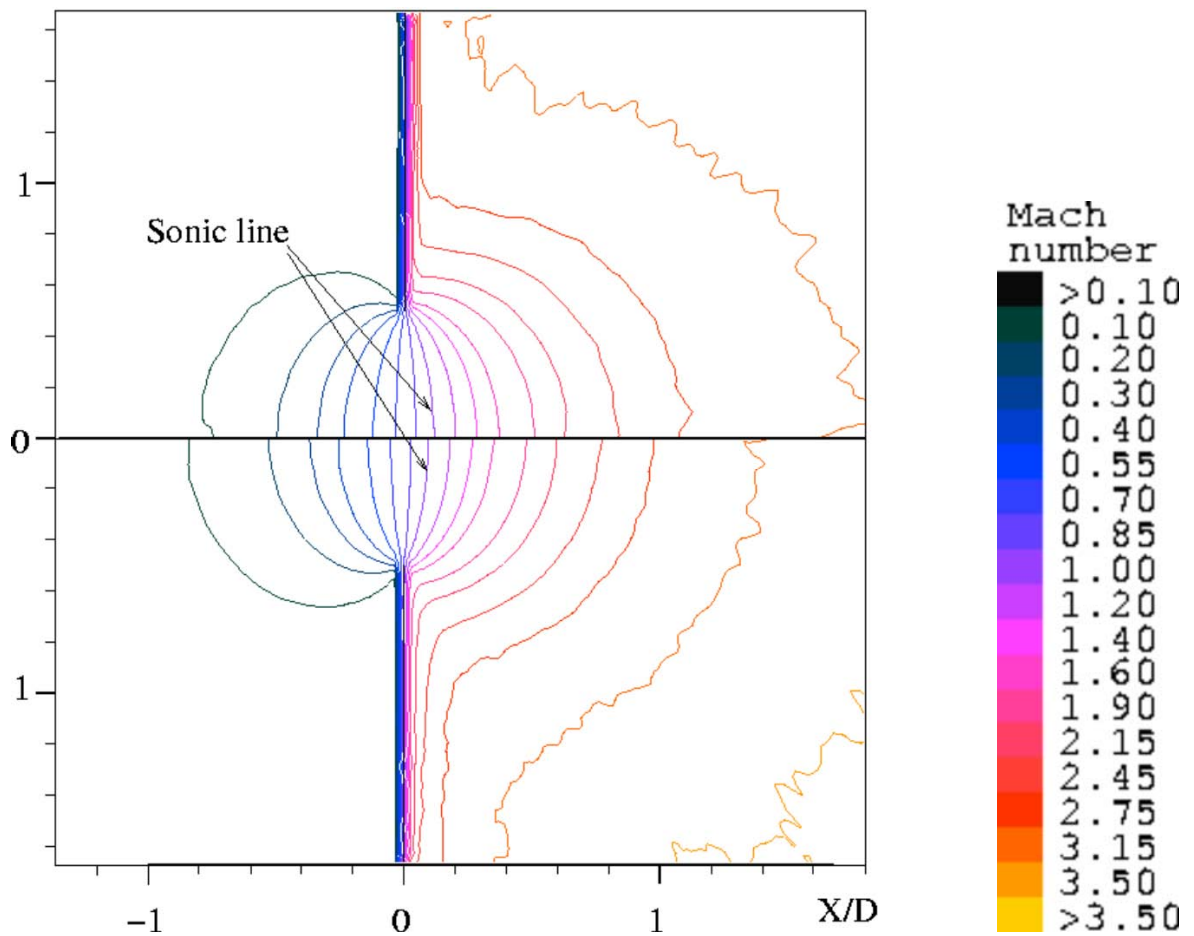


Fig. 1.8. Mach number flowfields. The upper and lower pictures refer to $P_0=0.01$ torr and $P_0=0.1$ torr

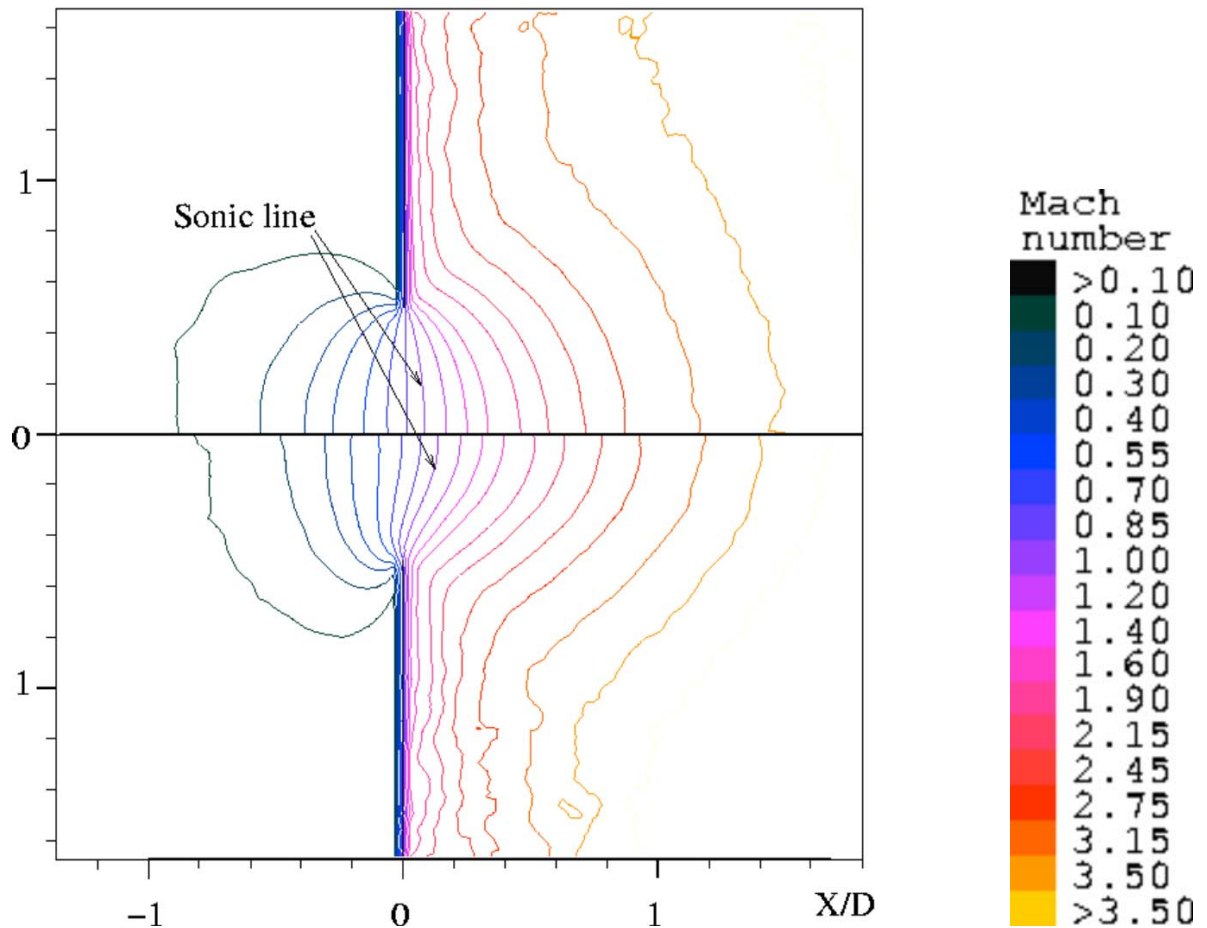


Fig. 1.9. Mach number flowfields. The upper and lower pictures refer to $P_0=0.5$ torr and $P_0=4$ torr

3D-results

Three-dimensional computations were performed for a pair of orifices with a distance between the centers equal to $2D$. Obviously, for the almost free-molecular flow regime, there should be no effect of one orifice on the other, since the particles reflected from the wall near the orifice do not collide with other particles and cannot transfer disturbances upstream.

In the other extreme case ($P_0=4$ torr), for an almost continuum regime, one can see in Fig. 1.6 that disturbances moving upstream and along the inner side of the wall propagate at a rather small distance not exceeding $0.2D$. This means that the region where disturbances from one orifice propagate does not reach the second orifice. Thus, one should not expect mutual influence of two orifices in almost free-molecular and near-continuum regimes of exhaustion.

Figures 1.9-1.10 show the curves that describe the mass-flux distribution from the center of the orifice toward the edges for a reservoir pressure of 0.05, 0.1, 0.5, and 1 torr. The solid curve shows the distribution of the mass flux from the center to the point A, and the dashed curve shows the distribution from the center to the point B (see Fig. 1.3). One can see in these graphs that gas exhaustion is symmetric over the entire plane of the orifice. Thus, we can conclude that the influence of one orifice on exhaustion parameters from the other orifice is not observed in the case of gas exhaustion from a pair of orifices spaced by a distance of $2D$.

Figure 1.13 shows the mass flow rate as a function of the gas pressure in the reservoir. The plot contains the data of the experiment whose details are given in Ref. [Ketsdever et. al., 2001], the results of an axisymmetric computation with one orifice (marked by asterisks), and the

results of three dimensional simulation of gas exhaustion from a pair of orifices with a distance of $2D$ between their centers. For the three-dimensional simulation, the mass flow rate through one orifice is plotted in the figure. The computed results are in good agreement with the experimental data. The thrust as a function of stagnation pressure is shown in Fig. 1.14. The numerical results are again in good agreement with the experimental data. Based on Figs. 1.13 and 1.14, we can conclude that, in the case of gas exhaustion into vacuum from a pair of orifices with a distance between the centers greater than $2D$, the flow in each orifice can be considered independent of each other.

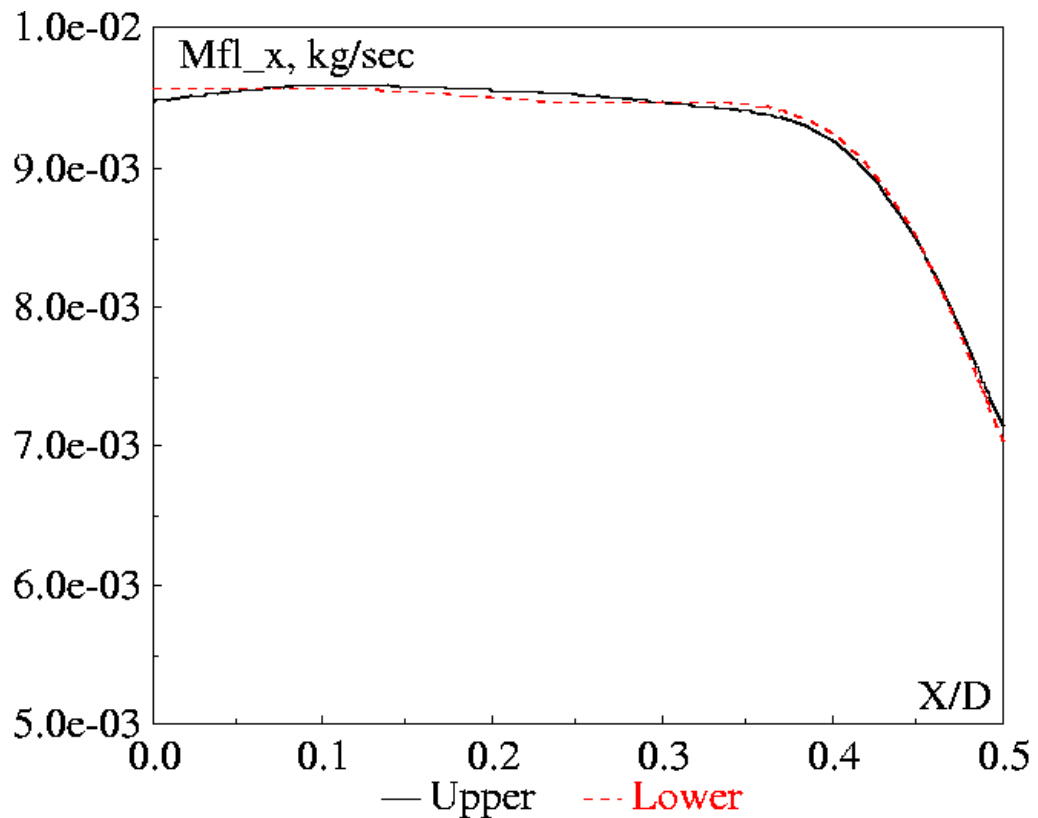


Fig. 1.10. Mass flux distribution in the plane of the orifice for exhaustion with $P_0=0.05$ torr. $X/D=0$ is the center of the orifice and $X/D=0.5$ is the boundary of the orifice.

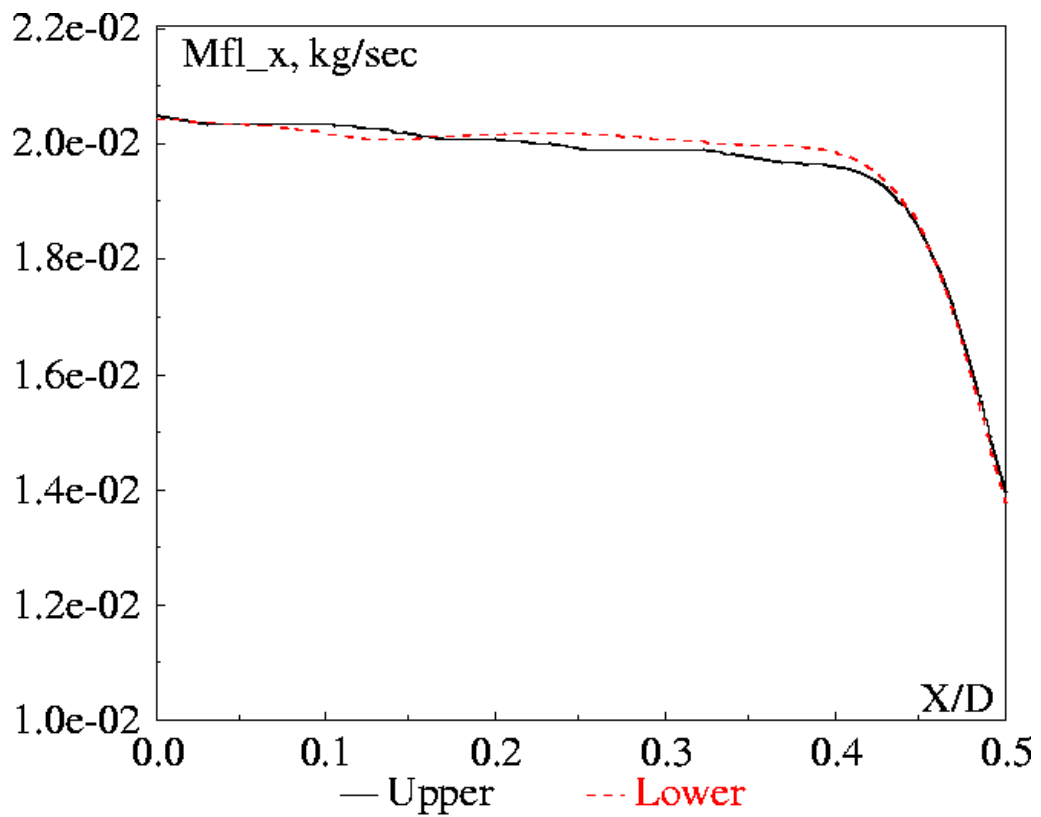


Fig. 1.11. Mass flux distribution in the plane of the orifice for exhaustion with $P_0=0.1$ torr. $X/D=0$ is the center of the orifice and $X/D=0.5$ is the boundary of the orifice.

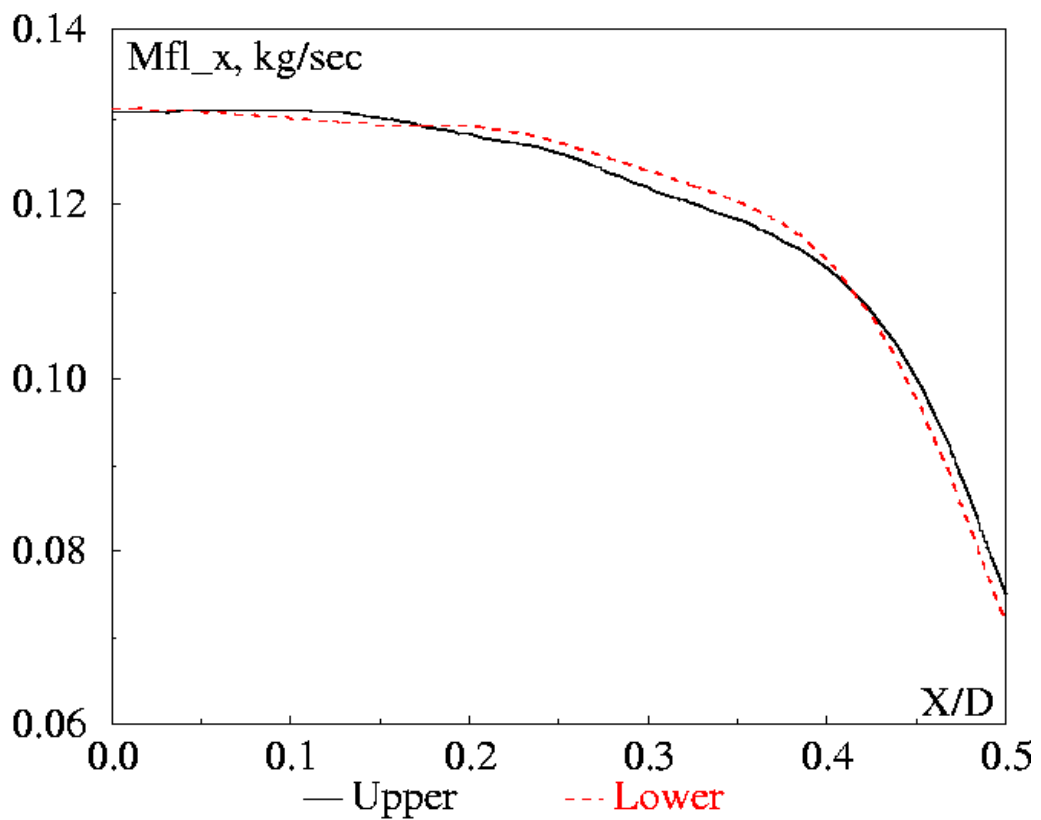


Fig. 1.12. Mass flux distribution in the plane of the orifice for exhaustion with $P_0=0.5$ torr. $X/D=0$ is the center of the orifice and $X/D=0.5$ is the boundary of the orifice.

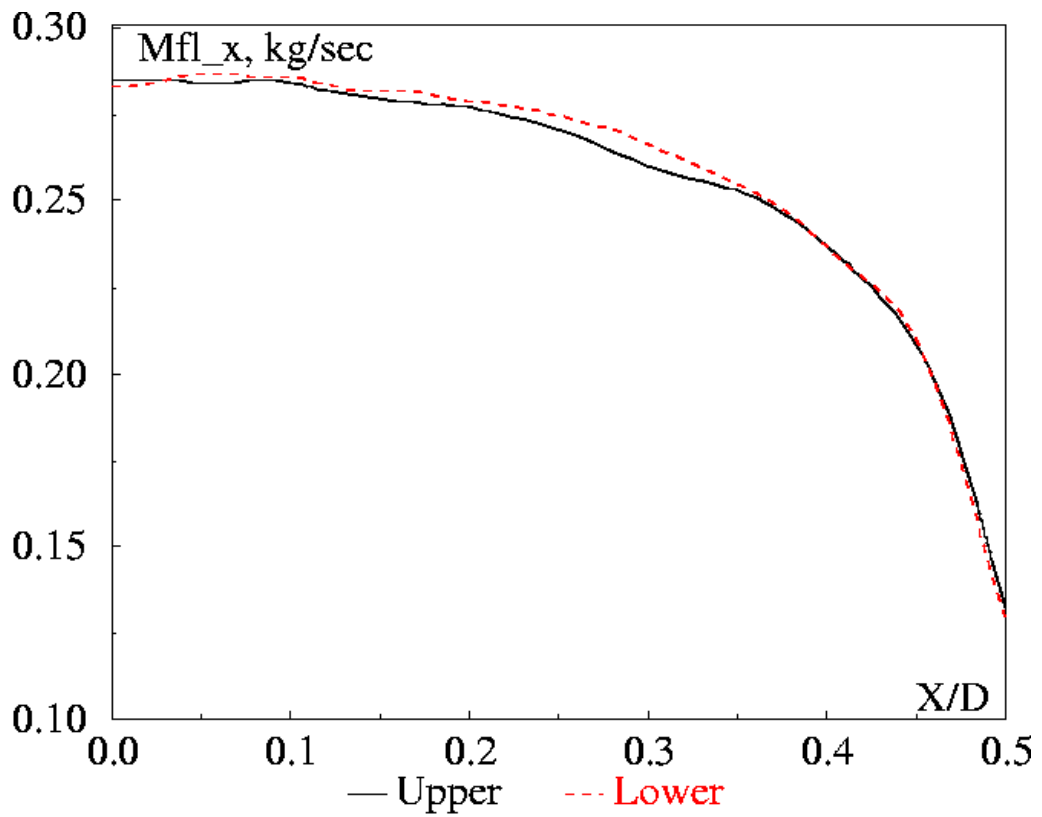


Fig. 1.13. Mass flux distribution in the plane of the orifice for exhaustion with $P_0=1$ torr. $X/D=0$ is the center of the orifice and $X/D=0.5$ is the boundary of the orifice.

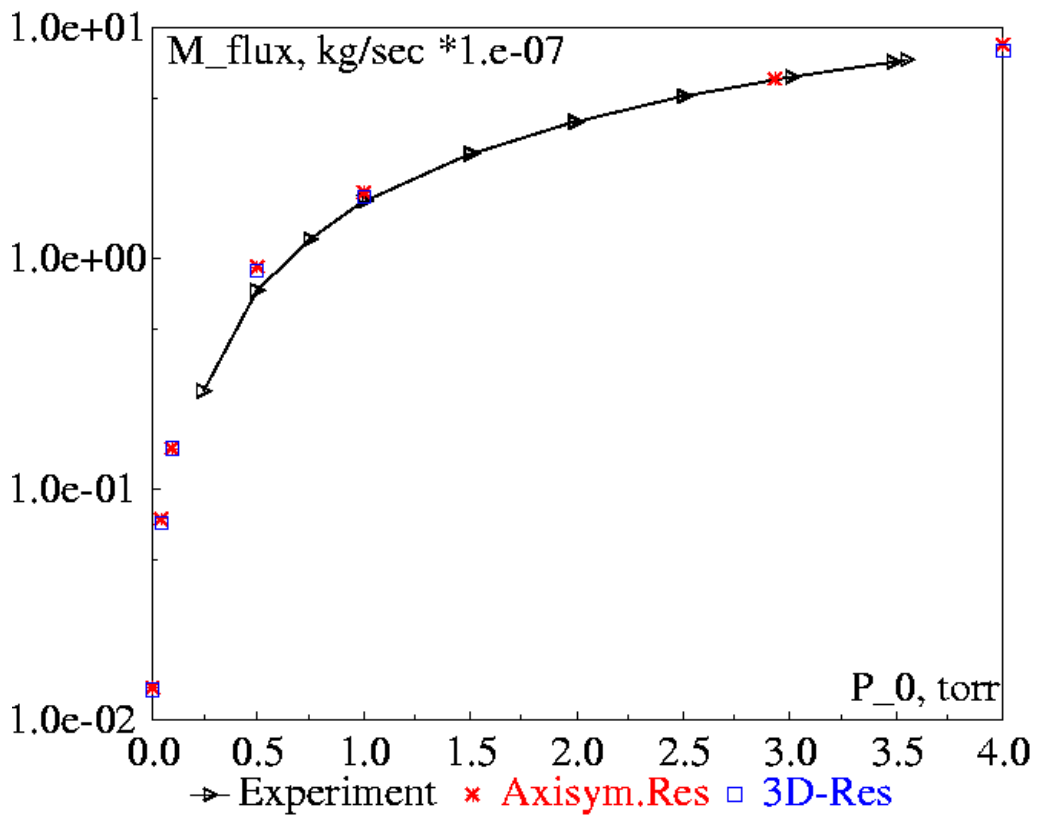


Fig. 1.14. Mass flux through the orifice versus the pressure in the receiver.

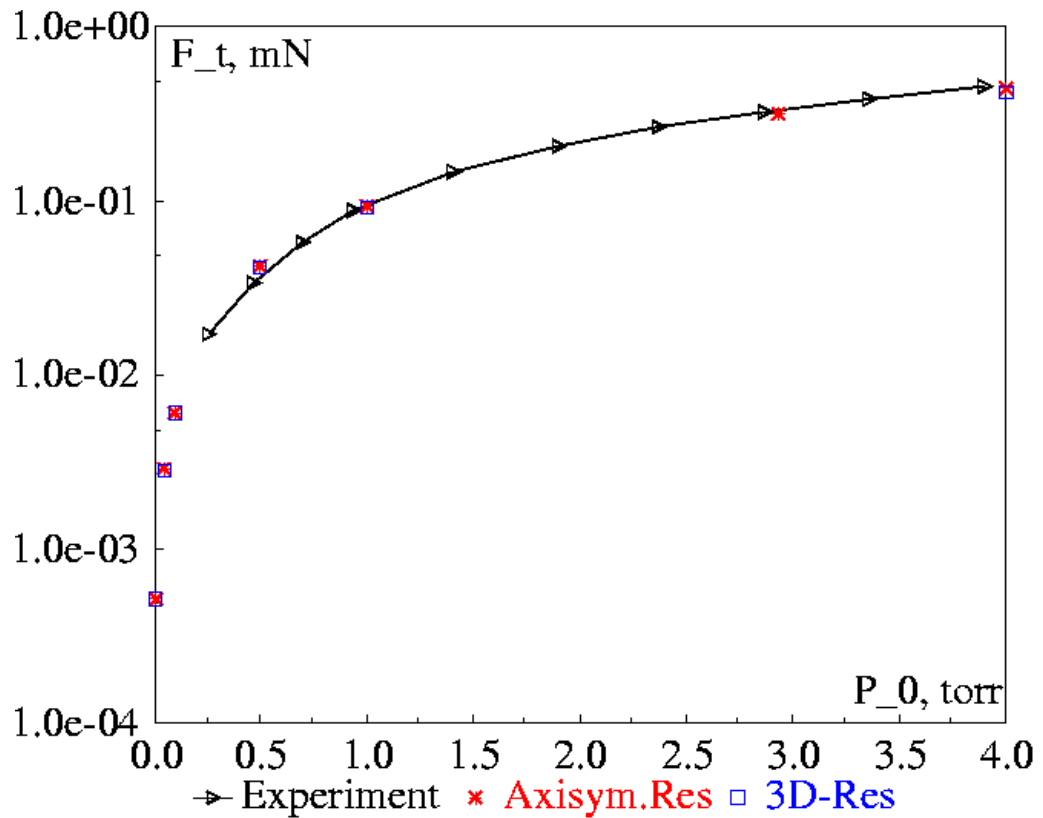


Fig. 1.15. Thrust versus the pressure in the receiver.

As is seen from Figs. 1.13 and 1.14, the difference between three-dimensional and axisymmetric results for all considered cases is less than 4 %. This small difference in results for a single orifice and a pair of orifices does not allow us to conclude that there is some mutual effect of two orifices. Most probably, this difference can be explained by the higher level of statistical scatter inherent in three-dimensional computations.

Conclusions

In computing the flow exhausting from an orifice, the DSMC simulation of the subsonic part of the flow is a labor-consuming problem that imposes high requirements to computer power. For this reason, three-dimensional computations were performed only for exhaustion from a reservoir through a pair of orifices with a distance between their centers equal to $2D$ and for some cases for a pair with a distance $4D$. The results obtained, however, allow us to state that exhaustion from each orifice already for these distances between the centers can be considered as independent. Therefore, it was decided that there is no mutual influence of the orifices for the remaining cases presented in Table 1.

Task 1.6. Application of SMILE++.

Presently, one of the most challenging problems in terms of the DSMC method development and improvement is related to the need to effectively and reliably simulate processes of energy transfer between internal and translational modes and chemical reactions. Whereas the energy dependent cross sections of these processes may not be known from experiment or theoretical analysis, their temperature dependence is often known with an acceptable accuracy. It is therefore critical for the DSMC models to reproduce the known temperature dependence. For the internal energy transfer, it is probably sufficient to match the rotational and vibrational relaxation governed by the Jeans and Landau-Teller equations with the

temperature-dependent rotational and vibrational relaxation numbers Z_r and Z_v , respectively. For chemical reactions, it is necessary to match the Arrhenius reaction rates at equilibrium. Thus, verification of models of the DSMC method is performed by comparing the results of DSMC simulations with appropriate temperature dependences.

1.6.1. The study of rotational and vibrational processes in homogeneous adiabatic bath for diatomic and triatomic molecules for continuous and discrete models of internal degrees of freedom. Comparison with Jeans and Landau-Teller equations.

Rotational relaxation.

At the macroscopic level, rotational relaxation is described by the Jeans equation, which has the following form for a single-species gas:

$$\frac{dT_r(t)}{dt} = \frac{T_t(t) - T_r(t)}{\tau_c Z_r}$$

Here, t is the time, τ_c is the mean time between collisions, T_t and T_r are the translational and rotational temperatures, respectively. In the adiabatic case, translational temperature changes during relaxation and is related to rotational temperature by the equation of conservation of energy

$$\xi_r T_r(t) + 3T_t(t) = \xi_r T_r^0 + 3T_t^0,$$

where T_t^0 and T_r^0 are the initial values of translational and rotational temperatures, respectively, and ξ_r is the number of rotational degrees of freedom of the gas molecule.

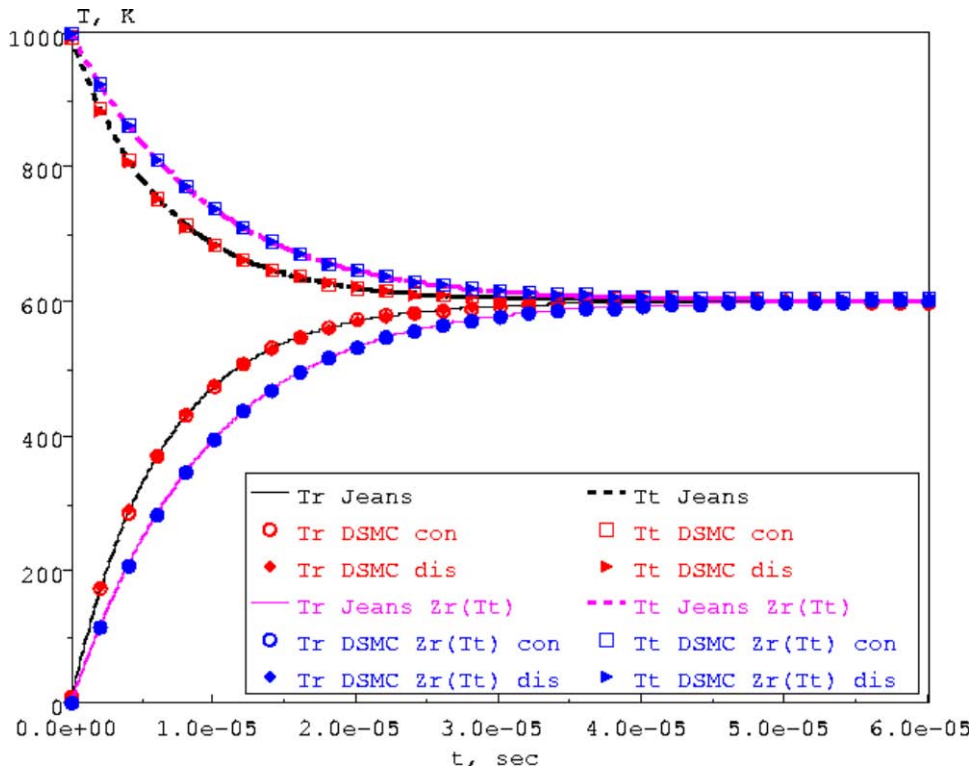


Fig. 1.16. Rotational relaxation of N2

Numerical integration of the Jeans equation in the present study was performed by the fourth-order explicit Runge-Kutta method. The initial values of translational and rotational temperatures were assumed to be 1000° K and 0, respectively, in all cases. Note, for such values

of temperature, vibrational excitation of molecules can be ignored. The present study included gases with different types of molecules: diatomic (N_2), linear polyatomic (CO_2), and spherical polyatomic (CH_4). Both constant and temperature-dependent relaxation numbers were used (Parker's relation). The DSMC computations of rotational relaxation in an adiabatic reservoir were performed with the use of a two-dimensional version of the SMILE++ software system. About 100,000 modeling particles were used in computations. The computational domain was a square, and specular reflection of molecules was used at the domain boundaries. The domain was not divided into collisional cells, and all molecule could collide with one another (actually, the domain consisted of one collisional cell). The values of translational and rotational temperatures at different times were calculated over all modeling molecules.

Figure 1.16 shows the time evolution of translational and rotational temperatures for rotational relaxation of molecular nitrogen. The curves show the solutions of the Jeans equation for constant and temperature-dependent relaxation numbers. The DSMC results are plotted by symbols. It is clearly seen that the DSMC method, with both continuous and discrete models, adequately predicts the behavior of temperatures, which is in excellent agreement with the solution of the Jeans equation both for constant and for temperature-dependent relaxation numbers.

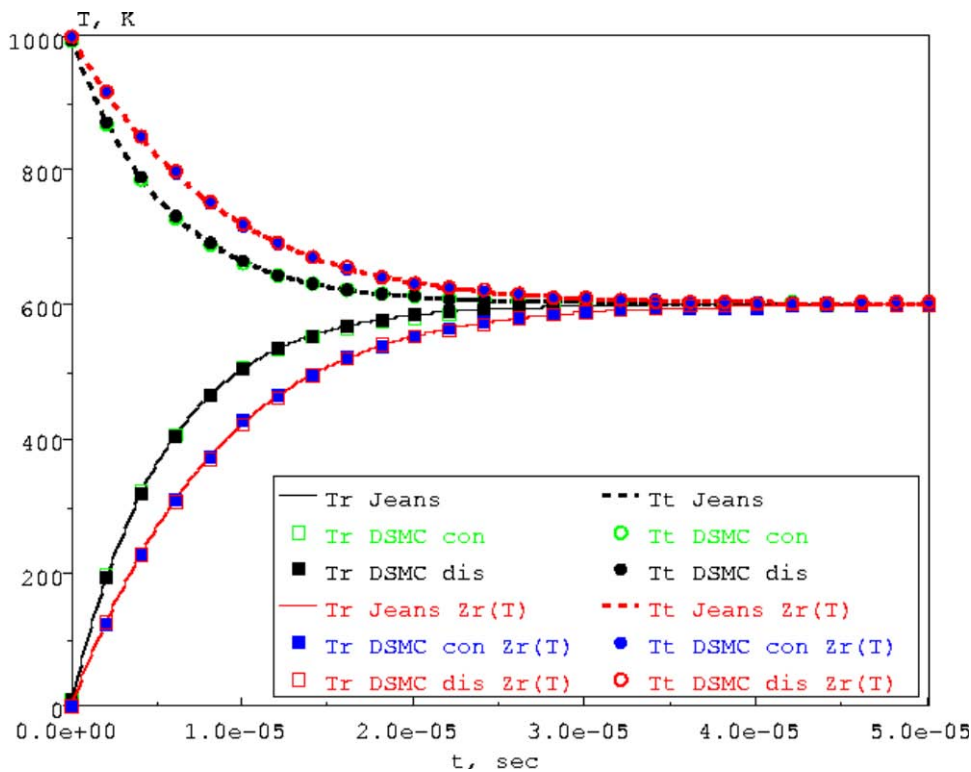


Fig. 1.17. Rotational relaxation of CO_2

The time evolution of translational and rotational temperatures for CO_2 and CH_4 in Figs. 1.17 and 1.18 shows that rotational relaxation in gases consisting of linear and spherical molecules is also described by DSMC computations in complete agreement with the solution of the Jeans equation for the continuous and discrete models. The result demonstrate that both DSMC models implemented into the SMILE++ system allow adequate reproduction of theoretical rates of rotational relaxation for molecules of various types.

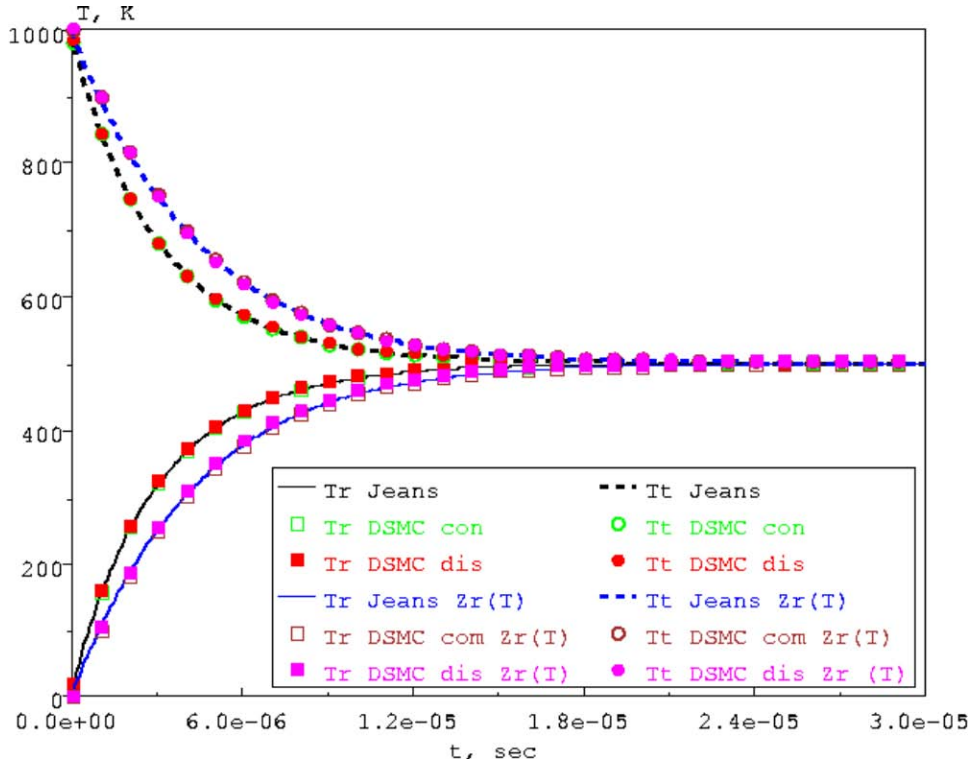


Fig. 1.18. Rotational relaxation of CH4.

Vibrational relaxation.

At the macroscopic level, vibrational relaxation is described by the Landau-Teller equation, which has the following form for a single-species diatomic gas:

$$\frac{d\xi_v(T_v(t)) \cdot T_v(t)}{dt} = \frac{\xi_v(T_t(t)) \cdot T_t(t) - \xi_v(T_v(t)) \cdot T_v(t)}{\tau_c Z_v}$$

Here, ξ_v is the effective number of vibrational degrees of freedom and T_v is the vibrational temperature. As in the case of rotational relaxation, both constant and temperature-dependent relaxation numbers (Millikan-White) are used to describe vibrational relaxation. In the present study of vibrational relaxation in an adiabatic bath, we confined ourselves to a more complicated case of temperature-dependent vibrational relaxation numbers. Note, in studying vibrational relaxation, one cannot ignore excitation of rotational energy modes and, sometimes, the translational and rotational temperatures cannot be assumed to be identical. Therefore, the Landau-Teller equation was numerically integrated together with the Jeans equation in order to describe vibrational relaxation. Under adiabatic conditions, this system is closed by the equation of conservation of energy

$$\xi_v(T_v(t))T_v(t) + \xi_r T_r(t) + 3T_t(t) = \xi_v(T_v^0)T_v^0 + \xi_r T_r^0 + 3T_t^0,$$

where T_v^0 , T_r^0 , and T_t^0 are the initial values of vibrational, rotational, and translational temperatures.

The system was numerically integrated by the further-order explicit Runge-Kutta method. The initial value of vibrational temperature was chosen to equal 0. The initial values of translational temperature and rotational temperature were assumed to be identical: $T_t^0 = T_r^0 = T^0$. Since the rate of vibrational relaxation strongly depends on temperature, several values of T^0 were used in the study (5000°K, 10000°K, and 20000°K).

The computational domain and the boundary conditions in DSMC computations were the same as in the rotational relaxation study. About 100,000 modeling molecules were used in computations.

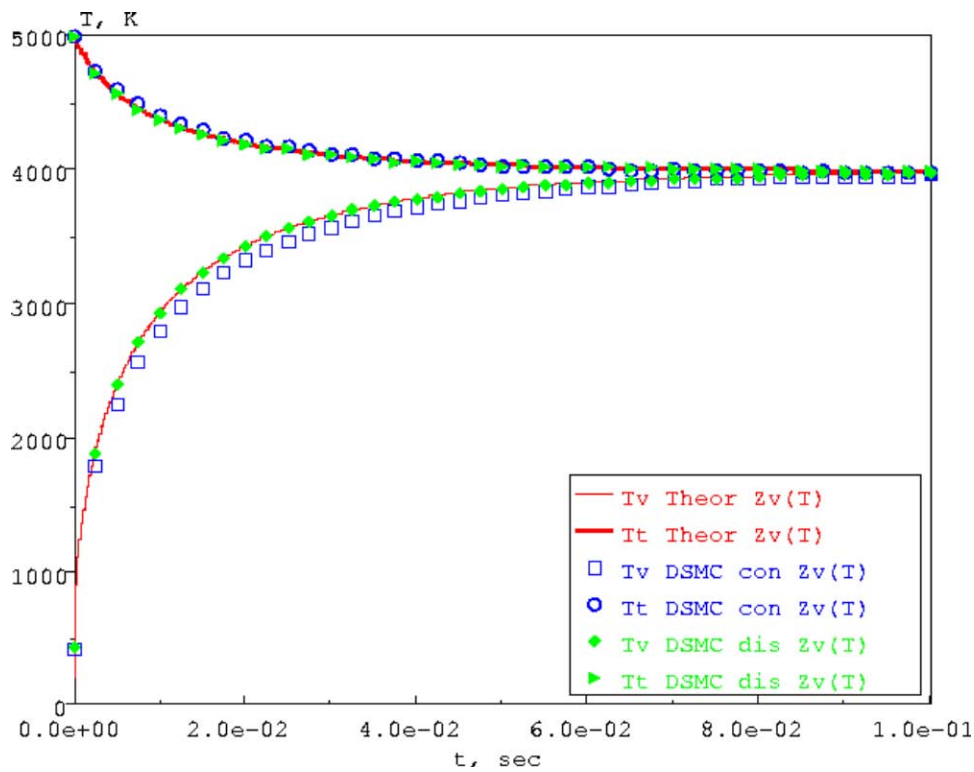


Fig. 1.19. Vibrational relaxation of N2. $T^0=5000^\circ\text{K}$

Figure 1.19 shows the time evolution of translational and vibrational temperatures for vibrational relaxation of molecular nitrogen N2 for $T^0=5000^\circ\text{K}$. The DSMC computations with the continuous model predict the vibrational relaxation rate slightly lower than the theoretical value. At the same time, the results of DSMC computations with the discrete model are in excellent agreement with the solution of the Landau-Teller equation.

With increasing initial values of translational and rotational temperatures to $T^0=10000^\circ\text{K}$ (see Fig. 1.20), vibrational relaxation is significantly accelerated: equalization of temperatures of all three modes requires about 0.1 s for $T^0=5000^\circ\text{K}$ and about 0.005 s for $T^0=10000^\circ\text{K}$. The results of DSMC simulations with the use of the discrete model are in excellent agreement with the solution of the Landau-Teller equation. In turn, the results of DSMC computations with the continuous model are also in good agreement with the theoretical result.

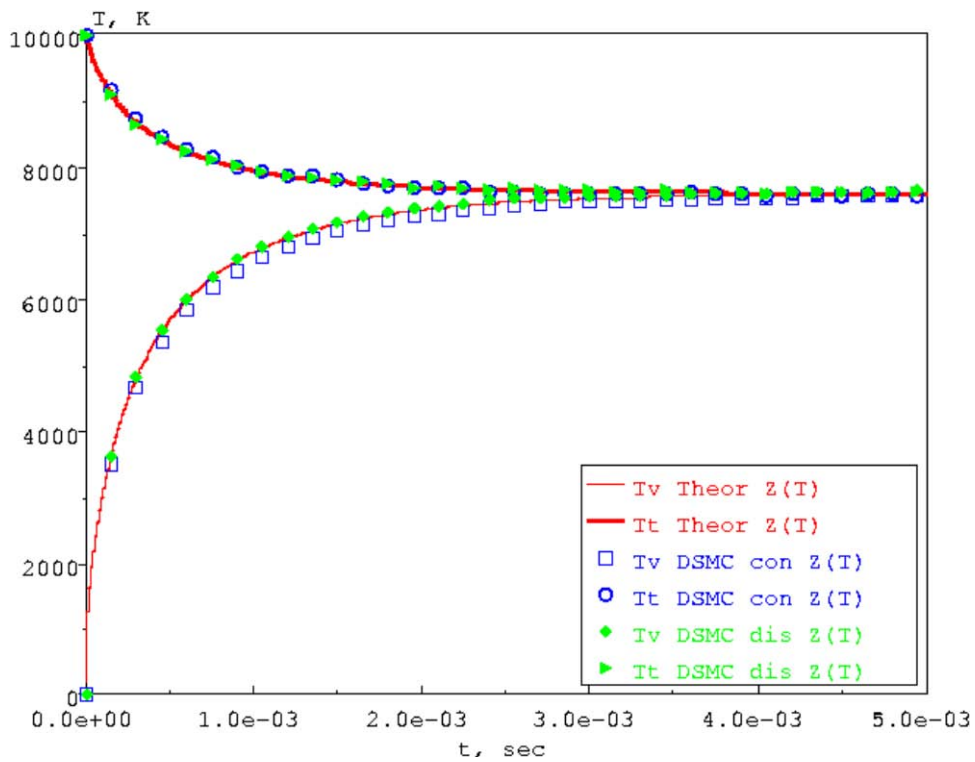


Fig. 1.20. Vibrational relaxation of N2. $T^0=10000^\circ\text{K}$

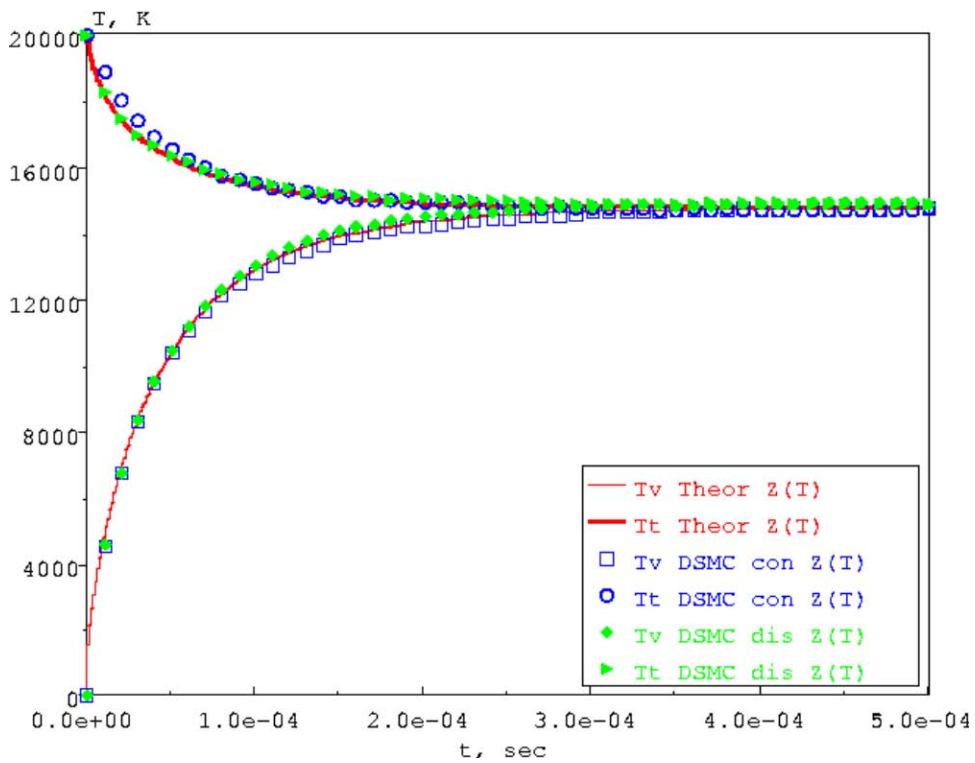


Fig. 1.21. Vibrational relaxation of N2. $T^0=20000^\circ\text{K}$

With a further increase in the initial values of translational and rotational temperatures to $T^0=20000^\circ\text{K}$, a further increase in relaxation rate is observed, and the temperatures of all modes become identical in less than 0.0005 s. As for different values of T^0 , the DSMC results with the

discrete model exactly reproduce the solution of the Landau-Teller equation, and the results obtained with the use of the continuous model are also rather close to this solution. Thus, we can conclude that both models (continuous and discrete ones) provide a correct description of the process of vibrational relaxation in a wide range of temperatures for diatomic molecules.

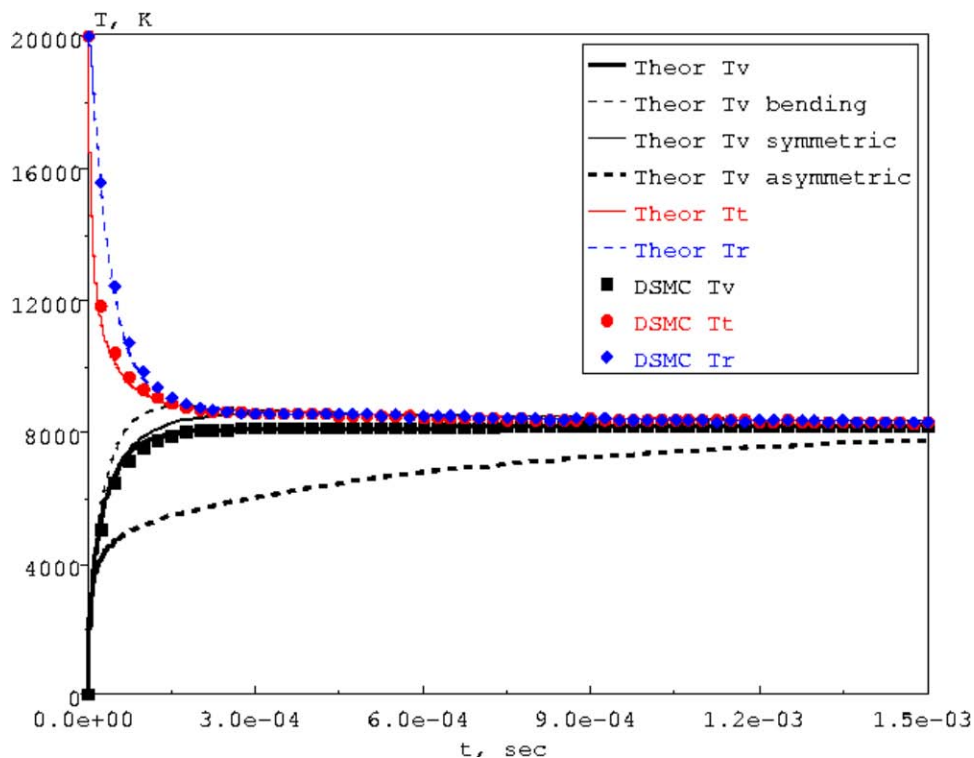


Fig. 1.22. Vibrational relaxation of CO₂. $T^0 = 20000^\circ\text{K}$

In contrast to diatomic molecules, which have one vibrational mode, polyatomic molecules have several vibrational modes with different characteristic temperatures. In the description of polyatomic molecules within the framework of the continuous model, a certain value of the characteristic vibrational temperature is usually chosen, and it is assumed that vibrational energy is not divided over different vibrational modes. Thus, the description of translational-vibrational energy transfer for polyatomic molecules within the framework of the continuous model actually coincides with the case of diatomic molecules and is not considered below. The discrete model takes into account the distribution of vibrational energy over different vibrational modes with different characteristic temperatures. Each mode of the molecule has its own set of vibrational levels and relaxes independently; each vibrational mode has its own value of the relaxation number, i.e., each mode relaxes with its own rate.

To describe vibrational relaxation of a polyatomic gas at the macroscopic level, one has to solve a system of the Landau-Teller equations (each vibrational mode has its own equation) together with the Jeans equation for the rotational mode. Under adiabatic conditions, this system is supplemented by the corresponding equation of conservation of energy.

In the present study, we considered vibrational relaxation of a polyatomic gas by an example of carbon dioxide. The CO₂ molecule is linear and has three vibrational modes; one of them (vibrational bending mode) is degenerate. Figure 1.22 shows the time evolution of temperatures of different energy modes in the process of vibrational relaxation of CO₂ for $T^0 = 20000^\circ\text{K}$. Note, the relaxation rates of vibrational modes of CO₂ are significantly different. Equalization of translational temperature, rotational temperature, and temperatures of vibrational bending and symmetric modes requires about 0.0003 s; on the other hand, equalization of temperatures of the asymmetric mode and other modes requires more than 0.0015 s.

The time evolution of translational, rotational, and vibrational temperatures, which were obtained by DSMC computations of vibrational relaxation of CO₂ with the use of the discrete model, are in good agreement with the solution of the system of the Landau-Teller equations, which was discussed above. Hence, we can argue that the discrete model of translational-vibrational energy transfer provides correct vibrational relaxation rates for polyatomic gases.

1.6.2. The study of chemical relaxation in homogeneous bath and comparison with Arrhenius chemical reaction rates in equilibrium. The study of the 2D nitrogen-dissociating flow around a wedge and comparison with Hornung's experimental data

Verification of the models of chemical reactions

The present section deals with verification of two chemical reaction models implemented in the SMILE++ system.

- conventional Total Collision Energy (TCE) model derived for continuous internal energies,
- modification of TCE model for discrete internal energies.

The first model is used together with the model of translational-internal energy transfer for continuous internal energies and is hereinafter called the continuous model. The second model is used with the model for discrete internal energies and will be called the discrete model.

The basic requirement to the DSMC model of chemical reactions is that the temperature dependence of the reaction rate constant predicted by this model should coincide under conditions of thermal equilibrium with that given by the Arrhenius equation

$$k_r = AT^B \exp\left(\frac{-E_a}{kT}\right),$$

where A and B are the Arrhenius constants and E_a is the reaction activation energy. The rate constant of the bimolecular dissociation or exchange reaction k_r relates the rate of decomposition of molecules of one reacting component i to the number densities of reacting components n_i and n_j :

$$\frac{dn_i}{dt} = -n_i n_j k_r \tag{1.1}$$

Equation (1.1) used in DSMC computations to calculate the reaction rates constants. The computational domain in DSMC simulations was of the same type as that in the case of rotational and vibrational relaxation, and about 100,000 simulated particles were used. At the initial time, the domain was populated by molecules in accordance with prescribed initial number densities of the components and temperature. At each time step during the collision process, the number of chemical reaction acts was sampled. Then, the domain was again populated by molecules in accordance with initial values, and the sampling was continued. Thus, a steady state for averaging over a large time interval was sustained.

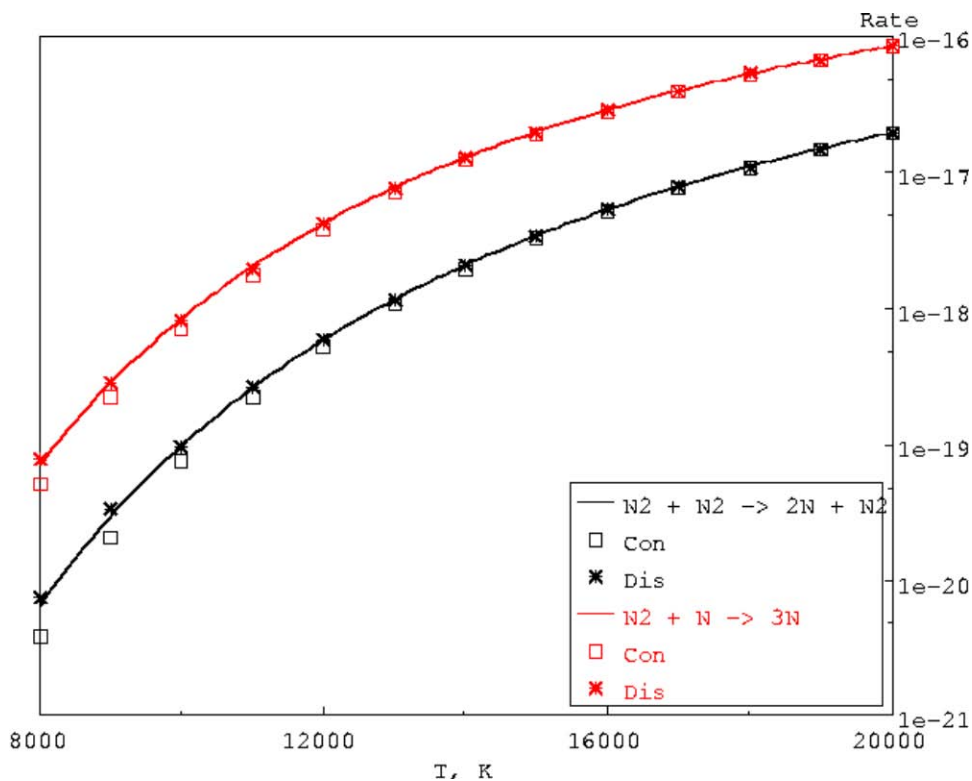


Fig. 1.23. Reaction rate, $s^{-1}m^{-3}$.

Figure 1.23 shows the temperature dependences of reaction rate constants for dissociation of molecular nitrogen:

- $N_2 + N_2 \rightarrow 2N + N_2$
- $N_2 + N \rightarrow 3N$.

The curves show the Arrhenius fits, and the DSMC results are indicated by symbols. Note, results of DSMC computations with the discrete model are in excellent agreement with the theory. The DSMC with the continuous model adequately reproduces the Arrhenius rate at high temperatures but significantly underpredicts the theoretical rate at low temperatures (about two times lower for the second reaction at a temperature of 8000 K). This underprediction of reaction rates by the continuous model can be attributed to the incorrect representation of the distribution function used in the continuous model for an effective number of vibrational degrees of freedom smaller than two. For diatomic molecules (such as N_2), this number varies from 0 to 2 as the temperature varies from 0 to ∞ . The lower the temperature, the greater the difference of the actual distribution of vibrational energy from the correct Boltzmann distribution, and hence, the greater the reaction-rate error.

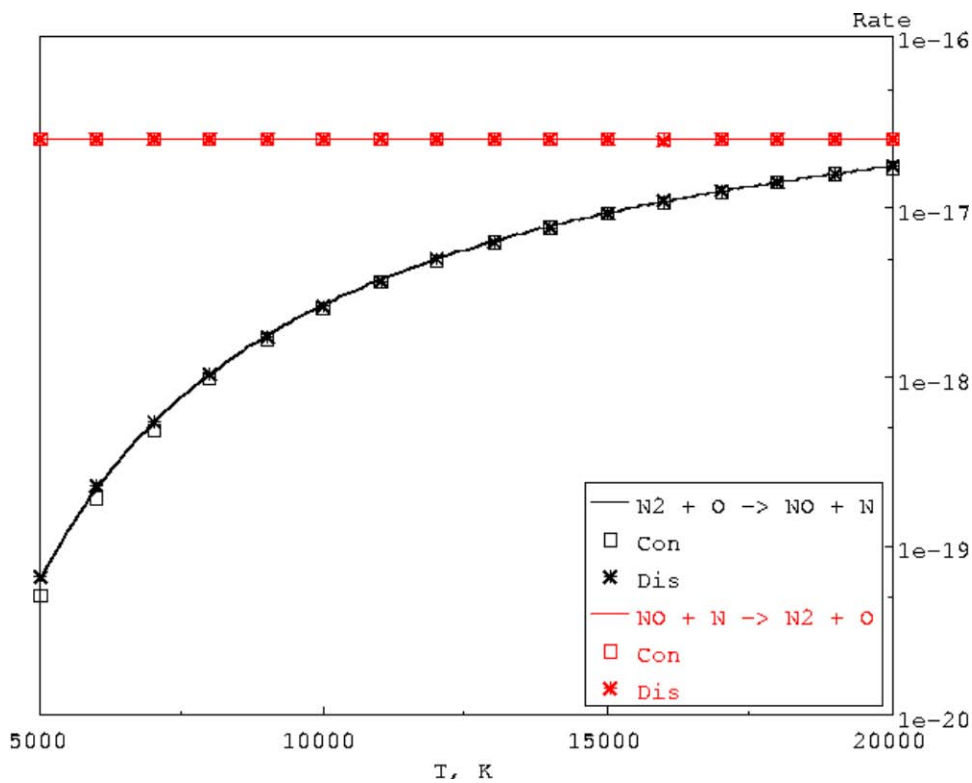
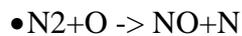
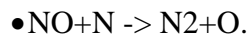


Fig. 1.24. Reaction rate, $s^{-1}m^{-3}$.

Figure 1.24 shows the temperature dependences of the reaction rate constant for the exchange reaction



and the reverse reaction



The discrete model ensures excellent agreement of the rates of both exchange reactions with the Arrhenius rates. As for dissociation reactions, the continuous model slightly underpredicts the rate of the direct reaction as compared to the theoretical value. At the same time, for the reverse reaction, the continuous model provides excellent agreement with the Arrhenius rate. The reason is that the probability of the reverse thresholdless reaction ($E_a = 0$) depends weakly on the energy of colliding molecules; hence, the inaccuracy in the representation of the distribution function of vibrational energy exerts no significant effect on the reaction rate.

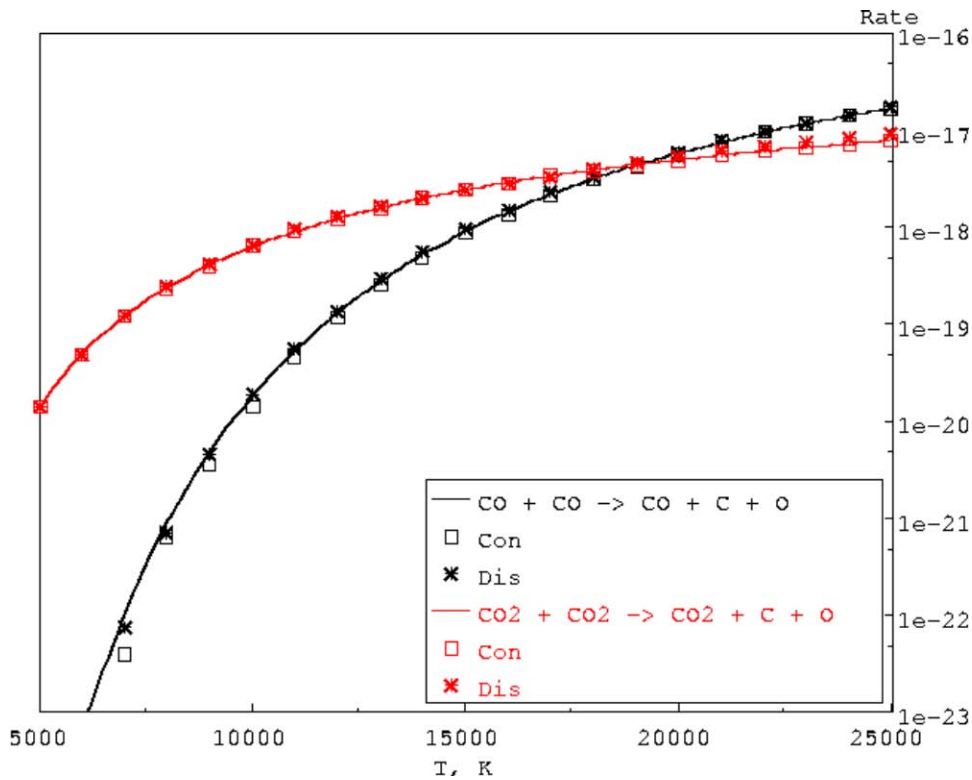


Fig. 1.25. Reaction rate, $s^{-1}m^{-3}$.

In what follows, we consider the dissociation and exchange reactions proceeding in the carbon dioxide flow. Figure 1.25 shows the temperature dependences of reaction rate constants for the dissociation reactions:

- $CO+CO \rightarrow CO+C+O$
- $CO_2+CO_2 \rightarrow CO_2+C+O$.

For the first reaction, the DSMC method with the discrete model is again in excellent agreement with the theory, whereas the continuous model at comparatively low temperatures significantly underpredicts the reaction rates (up to 50%). The rate of the second reaction is adequately predicted by DSMC computations with the use of both models in the entire temperature range. The good accuracy of the continuous model for the second reaction at comparatively low temperatures can be explained by the fact that the number of effective degrees of freedom of CO_2 in the continuous model is greater than seven at 5000 K and only increases with temperature. With such a great number of effective vibrational degrees of freedom, the continuous model describes the Boltzmann distribution function rather accurately, which is responsible for the good agreement with the Arrhenius rate.

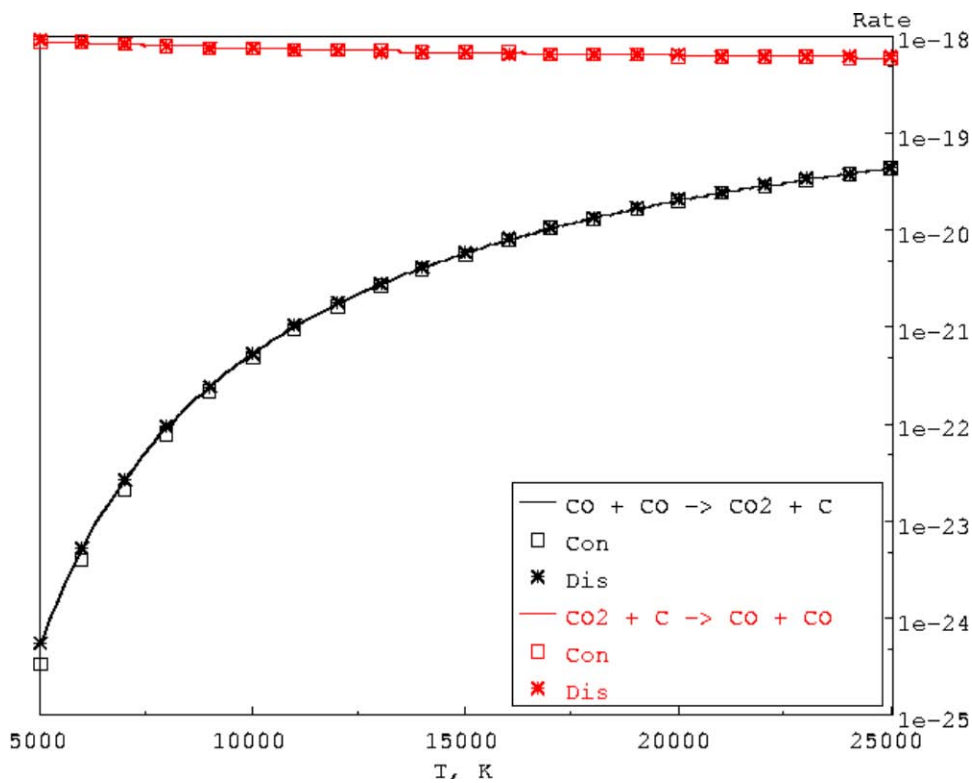
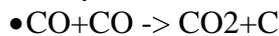
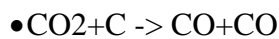


Fig. 1.26. Reaction rate, $s^{-1}m^{-3}$.

The temperature dependences of the rate constants of the exchange reactions proceeding in a CO₂ flow, namely, the reaction



and the reverse reaction



are shown in Fig. 1.26. As in the case of the nitrogen oxidation reaction (see Fig. 1.24), DSMC computations with the discrete model accurately predict the Arrhenius rate both for the direct and for the reverse reaction, and DSMC results with the continuous model are in excellent agreement with the Arrhenius rate for the reverse reaction and slightly underpredicts the reaction rate of the direct reaction at low temperatures. This fact is explained in a manner similar to that for the dissociation reaction of CO₂.

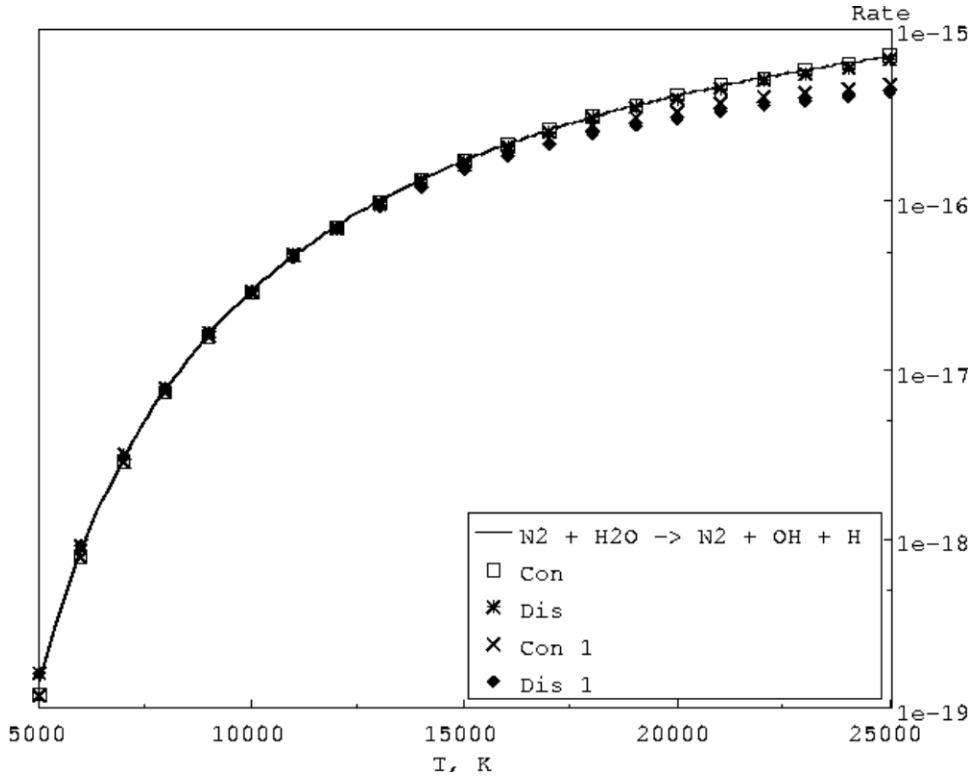
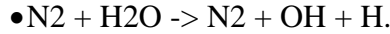


Fig. 1.27. Reaction rate, $s^{-1}m^{-3}$.

Let us also consider dissociation and exchange reactions with participation of H₂O molecules. These reactions are characterized by a high reaction rate. Figure 1.27 shows the reaction rate constant versus temperature for the dissociation reaction



The Arrhenius dependence is plotted by the solid curve, and the DSMC computations with the continuous and discrete models are shown by symbols designated as *Con 1* and *Dis 1*, respectively. The behavior of the temperature dependences obtained previously by DSMC computations in the temperature range from 5000K to 15000K is in qualitative agreement with the results obtained for dissociation reactions for N₂, CO, and CO₂. For temperatures above 15000K, DSMC computations underpredict the theoretical reaction rate.

This fact can be explained as follows. The TCE model is constructed under the assumption of a special form of reaction probability as a function of the total energy of colliding particles. It is known that the reaction probability can be greater than unity if the total energy of colliding particles is high enough. For fast reactions, this can lead to significant underprediction of reaction rates in DSMC computations even for rather low temperatures.

Figure 1.27 also shows the results of DSMC computations where the reaction rate was not calculated by sampling the number of elementary chemical acts, it was found by averaging the reaction probability P_r by the distribution function of the total collision energy of colliding particles f_B :

$$\bar{P}_r = \int P_r(E) f_B \left(\frac{E}{kT} \right) d \frac{E}{kT} \quad (1.2)$$

With the use of Eq.(1.2) and the relation

$$\frac{dn_i}{dt} = -N_{col}^{ij} \bar{P}_r,$$

where N_{col}^{ij} is the frequency of collisions of the components i and j , we can express the reaction rate constant via the mean reaction probability \bar{P}_r .

This method of calculating the reaction rate does not correspond to the real reaction rate obtained in DSMC computations but makes it possible to estimate the influence of the effect of the reaction rate exceeding unity. Indeed, the time dependences of the reaction rate constant calculated in this manner (denoted in Fig.1.27 by symbols with the subscripts *Con* and *Dis* for the continuous and discrete models, respectively) are in excellent agreement with the Arrhenius rates at temperatures above 15000 K.

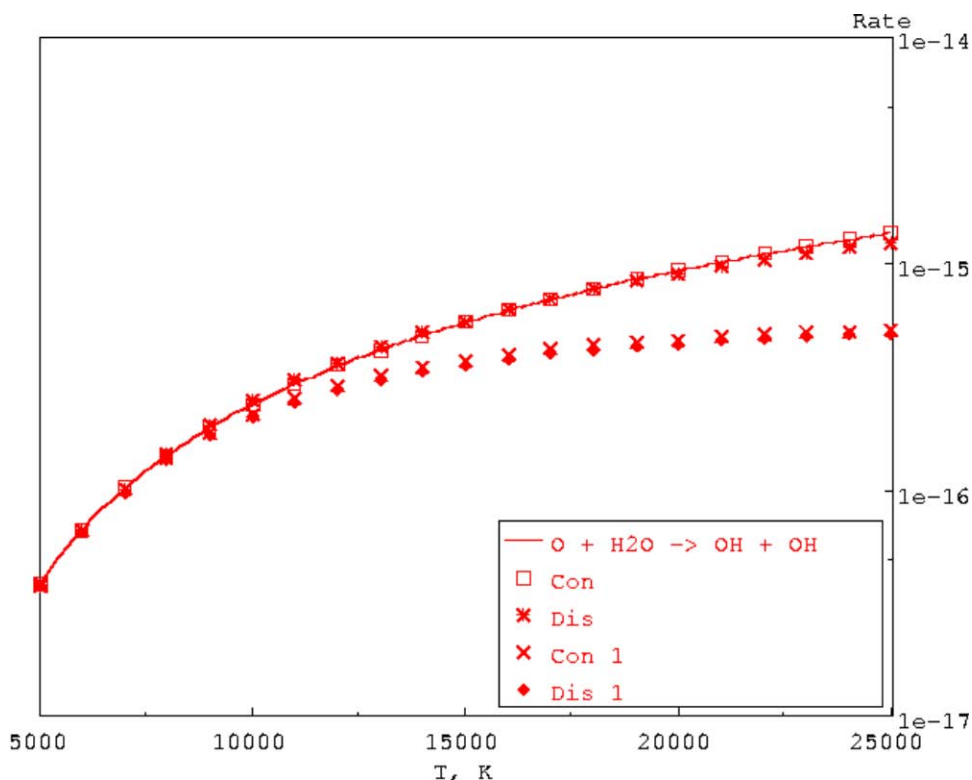
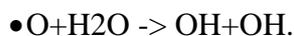


Fig. 1.28. Reaction rate, $s^{-1}m^{-3}$.

Figure 1.28 shows the temperature dependences of the reaction rate constant for the exchange reaction



For this reaction, good agreement of the reaction rates predicted by DSMC (with both continuous and discrete models: *Con 1* and *Dis 1*, respectively) with the Arrhenius rate is observed only for temperatures below 10000K. For temperatures higher than 10000K, DSMC computations significantly underpredict the theoretical rate (by more than a factor of 2 at 25000K). At the same time, as in the case of the dissociation reaction of H₂O, the reaction rates calculated by reaction probability averaging are in very good agreement with the Arrhenius rate in the entire range of temperatures under consideration, both with the continuous and with the discrete model.

We can conclude that both models of chemical reactions implemented in the SMILE++ software system provides reaction rates that are in good agreement with the Arrhenius rates in thermal equilibrium in a wide range of temperatures. For many reactions, the continuous model underpredicts the Arrhenius rate (up to 50%) at comparatively low temperatures (about 5000 K). For certain fast reactions, where the TCE probability of reactions can exceed unity (e.g., reactions with H₂O molecules), both models can also underpredict the Arrhenius reaction rate at high temperatures (up to 50%).

FLOW ABOUT A WEDGE

The validation of DSMC models of translational-internal energy transfer and chemical reactions (hereinafter, they will be called models of real gas effects) is difficult due to the lack of experimental data on rarefied hypersonic reacting flows. The lack of data is principally related to the complexity of experimental studies of high-enthalpy rarefied flows in ground-based facilities. As a result, most of currently available experimental conditions pertain to high-density, continuum flows, with the Knudsen number, Kn , ranging typically from 0.00001 to 0.000001.

An example of the scarce data suitable for validation of real gas effect models for the DSMC method is the experimental results presented in Ref. [Hornung, Smith, 1979]. Principal attention was paid to the effects of thermal relaxation and dissociation on the shock-wave stand-off distance for a flow about a wedge placed symmetrically in a uniform hypersonic flow. Near-continuum flows of argon, dissociating nitrogen, and dissociating carbon dioxide over a wedge with $Kn \sim 0.0005$ were examined there, providing therefore good grounds for the DSMC model validation.

The principal goal of this study is the validation of the DSMC models of real gas effects by an example of a hypersonic flow over a wedge by the DSMC method in the near-continuum flow regime. For this purpose, DSMC computations of an argon flow and also nonreacting and reacting nitrogen flows were performed with the use of the continuous model and discrete model of real gas effects, and the results on the shock-wave stand-off distance were compared with the experimental data of [Hornung, Smith, 1979]. In addition, Navier-Stocks (NS) computations were performed for these flows, and the results were compared to DSMC data on flowfields.

Flow Conditions

Ref. [Hornung, Smith, 1979] used a wedge of length $w=0.051\text{m}$. Since the wedge spanwise dimension was $L=0.152\text{m}$, the flow in the symmetry plane could be considered as two-dimensional. A 2D statement was used, therefore, in the present study.

The free stream conditions are listed in Table 2. The values of the main parameters (velocity V_∞ , temperature T_∞ , density ρ_∞ , and flow composition) were taken from Ref. [Hornung, Smith, 1979]. Based on these four parameters, all the remaining parameters listed in Table 2. were calculated, namely, the pressure p_∞ , Mach number M_∞ , Knudsen number, Kn_∞ , and Reynolds number Re_∞ (the Knudsen and Reynolds numbers were based on the wedge length).

| | Argon | Nitrogen |
|--------------------------------|----------------------|------------------------------|
| $V_\infty, m/s$ | 2200 | 5500 |
| T_∞, K | 57 | 1100 |
| p_∞, Pa | 26.11 | 940.3 |
| $\rho_\infty, kg/m^3$ | 0.022 | 0.026 |
| M_∞ | 15.64 | 7.7 |
| Kn_∞ | 4.7×10^{-4} | 6.52×10^{-4} |
| Re_∞ | 41500 | 14485 |
| Composition, <i>mole/kg</i> | Ar 25 | N ₂ 31.9 N 7.7 |

Table 2. Free-stream conditions

The following dissociation reactions were taken into account in studying the chemically reacting nitrogen flow both in DSMC and NS computations:

- $N_2 + N_2 \rightarrow N + N + N_2$
- $N_2 + N \rightarrow N + N + N$

The recombination reactions were not modeled in the present study. Under given conditions, recombination is essential in the boundary layer only, which will be demonstrated below.

Computational Methods

DSMC Method. The DSMC computations were performed using the SMILE software system based on the majorant frequency scheme. SMILE employs two independent grids adapted in the course of computation: the first one for organizing particle collisions, and the second one for sampling of macroparameters. Both grids are based on uniform rectangular background cells, which are split into smaller cells, if necessary.

The following models were employed in the computations:

- Variable Hard Sphere and Variable Soft Sphere molecular collision models
- diffuse reflection model with complete accommodation of translational and internal energies at the wedge surface
- two models of real gas effects: continuous and discrete
- temperature-dependent rotational and vibrational collision numbers in both models of real gas effects for modeling translational-rotational and translational-vibrational energy transfer

Most of the DSMC computations were performed on a multiprocessor computer MVS1000M at the Interdepartmental Supercomputer Center (Moscow, Russia).

NS computations were performed with commercial software, CFD-FASTRAN, which is a compressible finite-volume flow solver. The software provides advanced features including 6-DOF modeling for simulating the unsteady, dynamic motion of multi-body configurations and thermochemistry for reacting flows.

The following features of CFD-FASTRAN are used in the present study.

- structured grid solver
- Roe's approximate Riemann solver as a flux difference scheme with the minmod limiter to allow up to second order accuracy
- implicit scheme with local time stepping
- Sutherland law for the viscosity and kinetic theory for viscosity and diffusion for one- and multi-species flows, respectively
- two-temperature model for nitrogen flow
- no-slip isothermal wall conditions

The computational grid was multi-block structured, and the cells were stretched to the wedge surface to enhance spatial resolution of the boundary layer.

Argon Flow

The first set of computations was performed for an argon flow. From the viewpoint of real gas effects, this is the simplest case, which can serve as a reference point for subsequent study of a more complicated nitrogen flow.

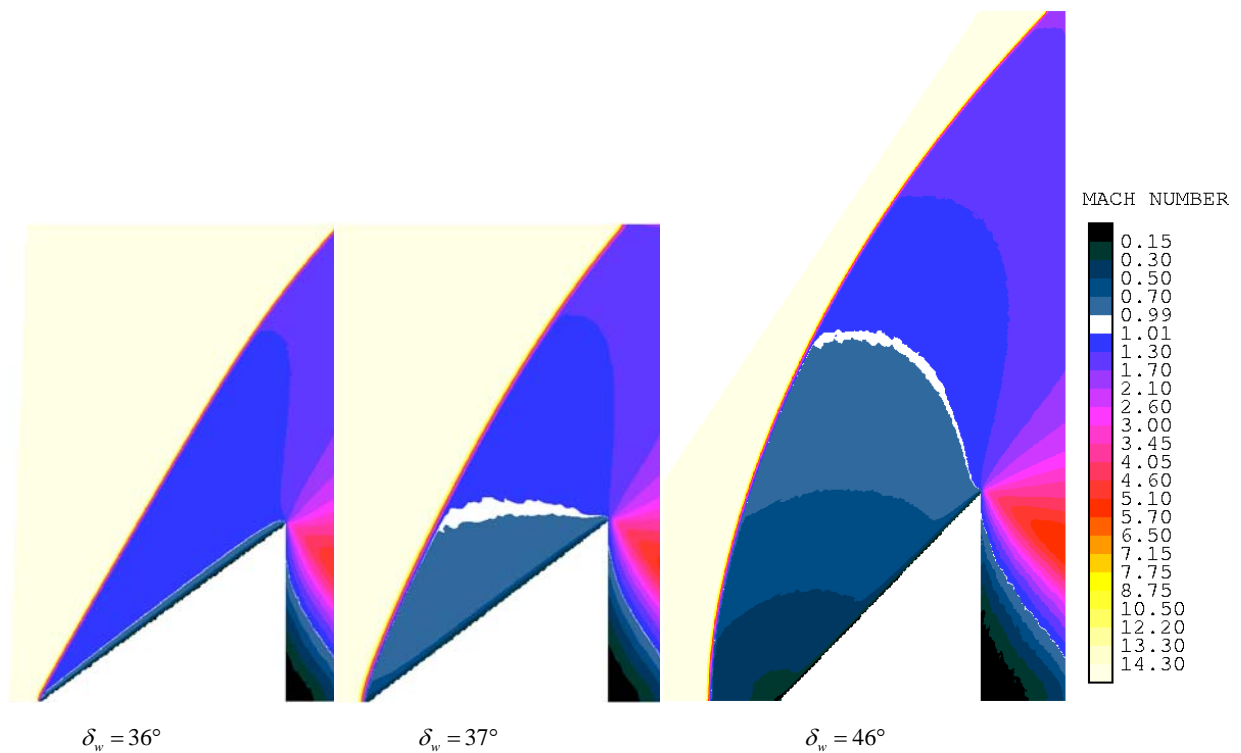


Fig. 1.29. Mach number flowfields for different wedge angles (argon flow)

Typical patterns of an argon flow about a wedge are presented in Fig. 1.29, where the Mach number fields obtained by DSMC computations are plotted for different values of the wedge angle. Parts of the flow where the Mach number is within $0.99 < M < 1.01$ have the white color: this allows one to see the position of the sonic line. For a wedge angle of 36° , the oblique shock wave is attached to the wedge, and the flow is supersonic everywhere behind the wave front. The shock wave is straight until it is affected by the expansion fan at the trailing edge of the wedge. As the wedge angle is increased to 37° , the flow pattern becomes completely different: a subsonic region is formed behind the wave, and the wave itself is noticeably curved. In fact, the wave is already detached, though its front cannot be rigorously distinguished from the boundary layer in the plane of symmetry (lower boundary of the domain). For a wedge angle of 46° , a flow with a bow shock wave and a large subsonic region behind the wave is formed. The stand-off distance is more than 20 % of the wedge length. The accuracy of the DSMC results is discussed in the next Section; special emphasis is laid on the accuracy of stand-off distance determination.

Accuracy of DSMC Results. The following conditions should be satisfied for accurate DSMC simulation of the gas flow:

- the time step should be smaller than the local mean time between collisions and residence time;
- the linear size of the collisional cell should be smaller than the local mean free path;
- the elementary volume whose side is equal to the local mean free path should contain more than one modeling particle.

These conditions guarantee that the error associated with time and space discretization and the error related to the finite number of particles in the system are small.

According to these requirements, more than 70 million of modeling particles should be used for accurate DSMC modeling of an argon flow around a wedge (for a wedge angle 46°). Even with the use of supercomputers, manipulation with this number of particles is rather difficult from the computational point of view. Therefore, the sensitivity of DSMC modeling results to the number of modeling particles was considered.

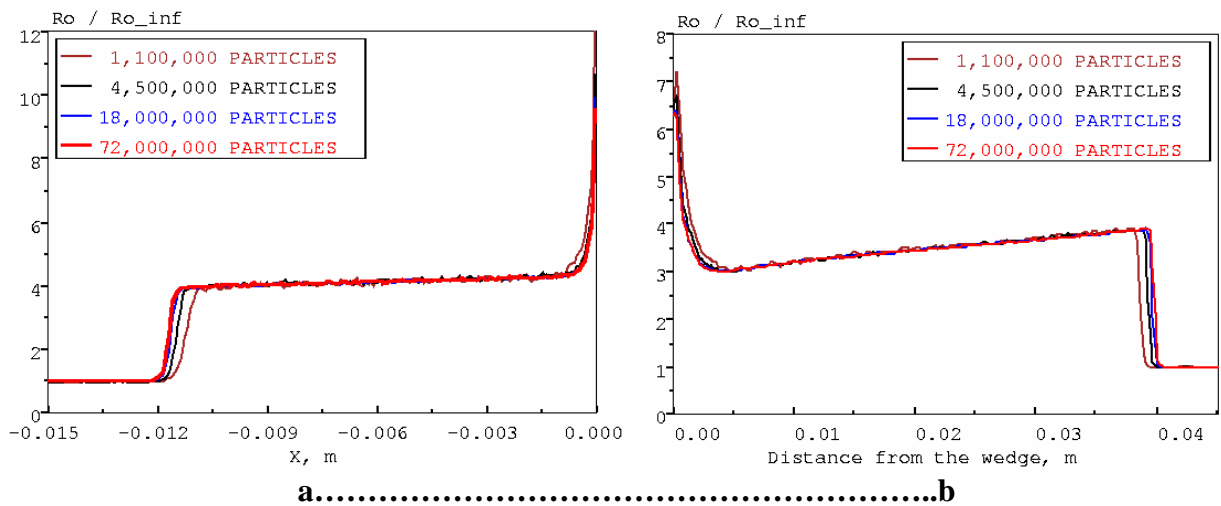


Fig. 1.30. Density along the stagnation streamline (a) and in the cross section perpendicular to the wedge surface and passing through the trailing edge of the wedge (b). DSMC computations with different numbers of modeling particles. Argon flow, wedge angle of 46°

Figure 1.30a shows the density distributions along the stagnation streamline for a wedge angle 46° in the series of computations with increasing number of modeling particles and collisional cells. The number of particles was approximately 1,100,000 in the first computation of this series and was increased fourfold in each next computation. The number of collisional cells in all computations was approximately four times smaller than the number of particles. In the last computation of the series, 72,000,000 particles were used. Obtaining of this result required more than two days of computer time with the use of 200 processors. As the number of modeling particles increases from 1,100,000 to 18,000,000 (see Figure 1.30a), the shock-wave stand-off distance increases, and the boundary-layer thickness decreases. With further increase in the number of particles up to 72,000,000, however, the density profile remains unchanged.

Figure 1.30b shows the density for the same series of computations in a cross-section perpendicular to the wedge plane and passing through the trailing edge of the wedge. The distance from the shock-wave front to the wedge plane in this cross section increases with increasing number of particles, as in the case along the stagnation streamline. There is practically no noticeable difference between the density distributions for 18,000,000 and 72,000,000 particles.

Thus, all the DSMC results for the argon flow described below were obtained with the use of approximately 20,000,000 particles in the system, which is sufficient for obtaining accurate results (in particular, precise determination of the stand-off distance).

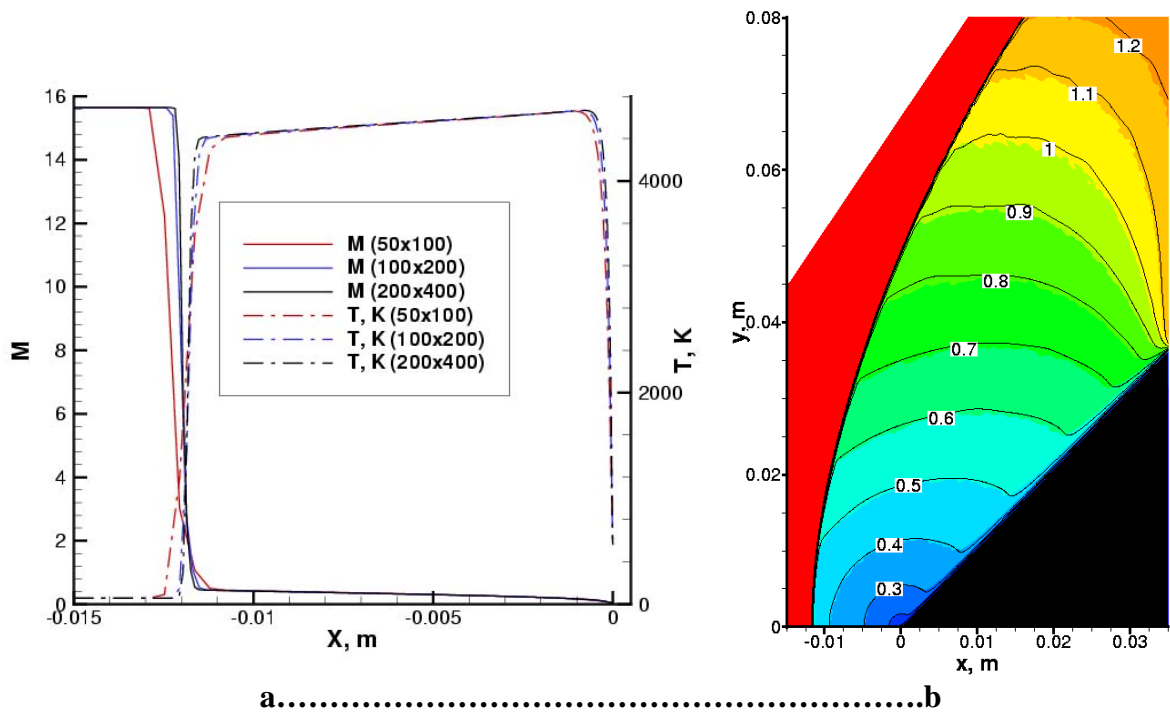


Fig. 1.31. Flow parameters along the stagnation streamline in NS computations with different grids (a). Mach number flowfields (b), DSMC - flood, NS - lines.
 Argon flow, wedge angle of 46°

Accuracy of NS Results. NS computations with different numbers of cells show that the main result of the increase in the number of cells is the change in the bow-shock thickness. The boundary-layer thickness also becomes different, which is clearly seen in the distribution of parameters along the stagnation streamline for 50×100, 100×200 and 200×400 grids shown in Fig. 1.31a. A further increase in the number of cells (400×800) has no effect on the boundary-layer parameters and bow-shock position. The bow-shock thickness becomes different in magnitude but remains unchanged in terms of the number of cells (~5 cells). Therefore, the NS results described below were obtained for the 200×400 grid.

Comparison of NS and DSMC Results. The Mach number fields obtained by DSMC (flood) and NS (curves) computations for a wedge angle of 46° are compared in Fig. 1.31b. The kinetic and continuum approaches predict a similar flow pattern, in particular, the bow-shock position is identical in both cases. An insignificant difference in Mach numbers is observed far from the plane of symmetry. Flowfields of other macroparameters (density, temperature, pressure, velocity, etc.) for both methods also coincide. For a more detailed comparison of DSMC and NS results, the distributions of macroparameters in different cross sections for a wedge angle of 46° are presented below.

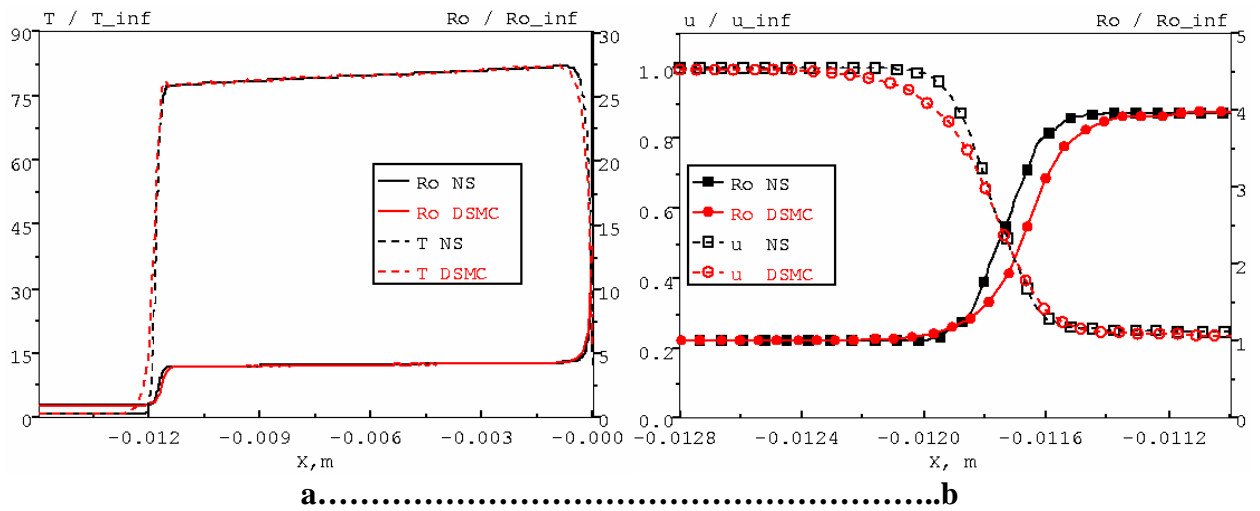


Fig. 1.32. Flow parameters along the stagnation streamline. Argon flow, wedge angle of 46°

Figure 1.32a shows the density and temperature profiles along the stagnation streamline. The NS and DSMC density profiles are in good agreement. A minor difference in density is observed only in the vicinity of the shock-wave front ($x \sim -0.011m$) and near the stagnation point (inside the boundary layer). The same refers to temperature distributions, except for the fact that the difference between the NS and DSMC temperature profiles in the vicinity of the shock-wave front is more pronounced: the NS profile is steeper than the DSMC profile.

Figures 1.32b and 1.33a show the NS and DSMC macroparameters along the stagnation streamline in the near vicinity of the shock-wave front. The density and velocity profiles are plotted in Fig. 1.32b. One can clearly see that the DSMC density and velocity profiles inside the shock-wave front are less steep than the NS profiles. This result could be expected and explained by the commonly known fact that the Navier-Stokes equations cannot correctly describe the internal structure of front of strong shock waves for Mach numbers $M > 2$. The DSMC method offers a detailed description of the internal structure of the front at the kinetic level with allowance for strong nonequilibrium of the velocity distribution function of molecules.

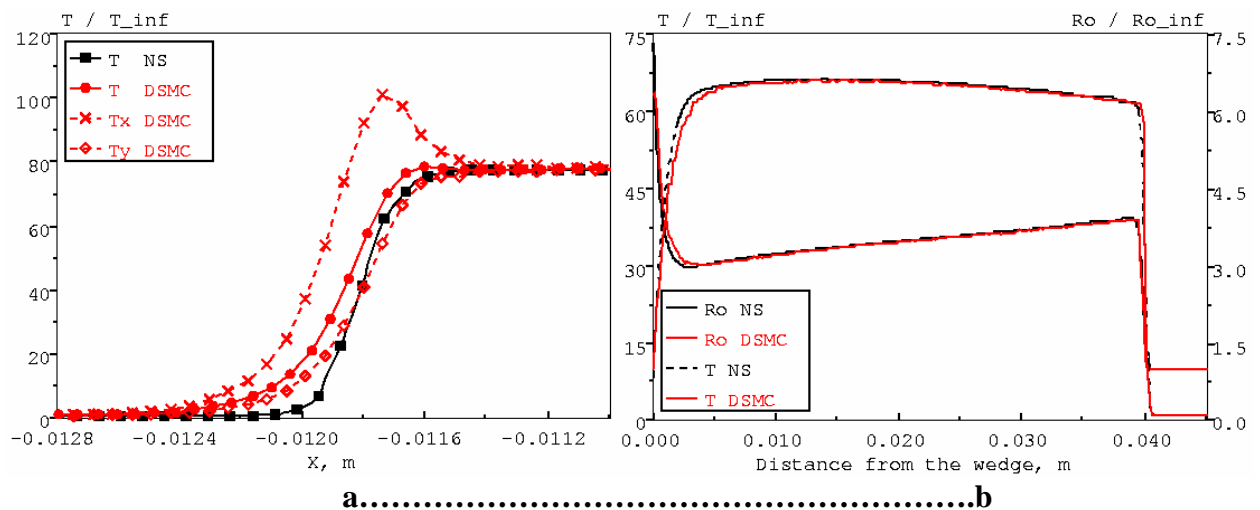


Fig. 1.33. Flow parameters along the stagnation streamline (a) and in the cross section perpendicular to the wedge surface and passing through the trailing edge of the wedge (b). Argon flow, wedge angle of 46°

The nonequilibrium of the distribution function is characterized, in particular, by the strong difference in the values of parallel T_x and perpendicular T_y temperatures whose profiles are

plotted in Fig.1.33a together with DSMC and NS temperature curves. The parallel temperature has a clearly expressed maximum inside the front. As a whole, the temperature profile obtained by DSMC simulations is less steep than the NS temperature profile and has a moderate maximum (about 1% of the temperature value behind the wave). The presence of this maximum in strong shock waves in monatomic gases is a well-known fact (see, e.g., Ref. [Bird, 1994]).

Figure 1.33b shows the density and temperature profiles in a cross section perpendicular to the wedge plane and passing through the trailing edge of the wedge. The DSMC and NS values are in very good agreement, except for a small difference in the vicinity of the trailing edge. Both methods also predict an identical distance from the wedge to the shock-wave front in this cross section.

As a whole, we can conclude that the results of DSMC simulations are in excellent agreement with the solution of the Navier-Stokes equations outside the shock-wave front and boundary layer. Note, the differences observed inside the shock-wave front are not important in the problem considered and, because of the small thickness of the shock-wave front, have not any significant effect on the accuracy of stand-off distance determination.

Comparison of Numerical Results and Experimental Data. As was mentioned above, Hornung and Smith measured the stand-off distance of the shock wave for a hypersonic argon flow with different wedge angles. The results of these measurements and the values of the stand-off distance obtained by NS and DSMC computations are plotted in Fig. 1.34. Note the good agreement between the NS and DSMC values of the stand-off distance in the entire range of wedge angles for which the computations were performed. Some minor differences are observed for wedge angles of 40° and 42.5° only.

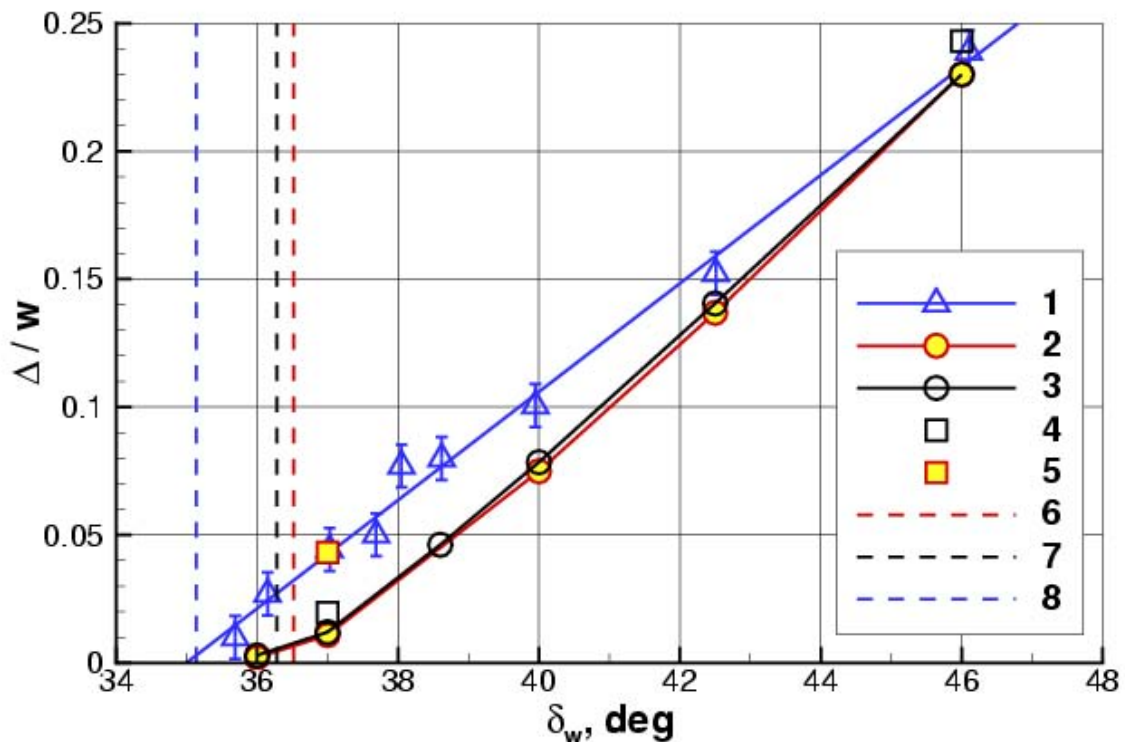


Fig. 1.34. Stand-off distance for different wedge angles for the argon flow.

Line 1 - experiment of Ref. [Hornung, Smith, 1979], Line 2 - DSMC, Line 3 - NS, Line 4 - NS for M=12, Line 5 - DSMC for M=7, Lines 6, 7, and 8 - detachment angles for Mach numbers M=15.64, M=12, and M=7, respectively

A comparison with experimental data shows that the computations significantly underpredict the stand-off distance, especially for small wedge angles (more than three percent of the wedge length). For all wedge angles except for 46°, the computation results are outside the

measurement error of the stand-off distance in the experiment (see Ref. [Hornung, Smith, 1979]). Apparently, the reason for this difference is caused by the lack of knowledge of the exact Mach number value at the nozzle exit: "...the displacement thickness of the nozzle wall boundary is quite large at this condition, so that the exit Mach number may be significantly reduced."

To evaluate the Mach number effect on the stand-off distance, additional NS computations for $M=12$ (for the wedge angles of 46° and 37°) and DSMC computations for $M=7$ (wedge angle of 37°) were performed. The free-stream parameters (velocity, temperature, and density) for these computations with a reduced Mach number were recalculated from the conditions of conservation of mass flow rate and total enthalpy.

It is clearly seen (see Figure 1.35) that a decrease in the Mach number increases the stand-off distance. In particular, the NS results for $M=12$ are in somewhat better agreement with experimental data than the results of the basic series of computations. The DSMC computation for $M=7$ and the wedge angle of 37° predicts the stand-off distance completely coincident with the experimental value for this angle.

The dashed vertical lines in Fig. 1.34 show the theoretical values of the detachment angle (i.e., the maximum angle of flow deflection) for different Mach numbers. One can clearly see that the results of the basic series of NS and DSMC computations are in excellent agreement with the theoretical value of the detachment angle for $M=15.64$. On the other hand, wave detachment in the experiment occurs at lower wedge angles than those expected for the Mach number $M=15.64$.

Thus, further research is necessary to clarify the reasons for the difference between the experimental and numerical data. It is also desirable to obtain more detailed information about the experimental facility used in Ref. [Hornung, Smith, 1979].

Nitrogen Flow

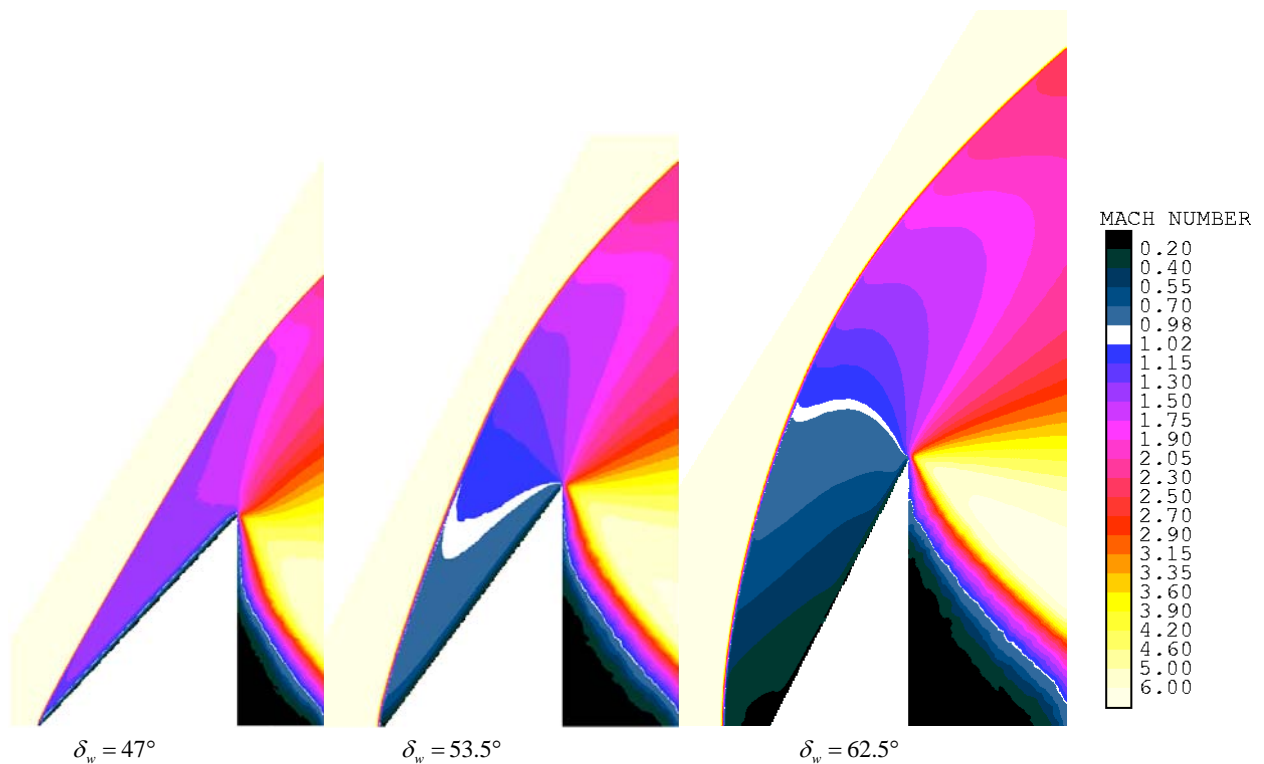


Fig. 1.35. Mach number flowfields for different wedge angles (reacting nitrogen flow)

The next stage was to study the influence of relaxation of the internal energy of the gas and chemical reactions on the flow structure around the wedge. The dissociating nitrogen flow

pattern for different wedge angles is demonstrated by the Mach number flowfields plotted in Fig. 1.35. For an angle of attack of 47° , the flow pattern with an attached wave is formed. For a wedge angle of 53.5° , one can observe the flow pattern with a slightly detached shock wave. The stand-off distance of the wave for a wedge angle of 62.5° is about 15 % of the wedge length. The main qualitative difference of the flowfields of dissociating nitrogen from those of argon is the shape of isolines immediately behind the shock-wave front (cf. Fig. 1.29 and Fig.1.35). The Mach number behind the shock-wave front in the monatomic gas decreases monotonically with increasing distance from the front. In dissociating nitrogen, the Mach number behind the shock wave first slightly increases and then gradually decreases. The growth of the Mach number behind the shock-wave front is associated with relaxation processes (relaxation of internal energy and dissociative relaxation) behind the front (see Ref. [Hornung, Smith, 1979]).

Two cases were considered to obtain an independent effect of relaxation of internal energy of molecules and dissociation on the flow:

- nonreacting flow with allowance for excitation of vibrational degrees of freedom of molecules;
- reacting flow with allowance for excitation of vibrational degrees of freedom of molecules.

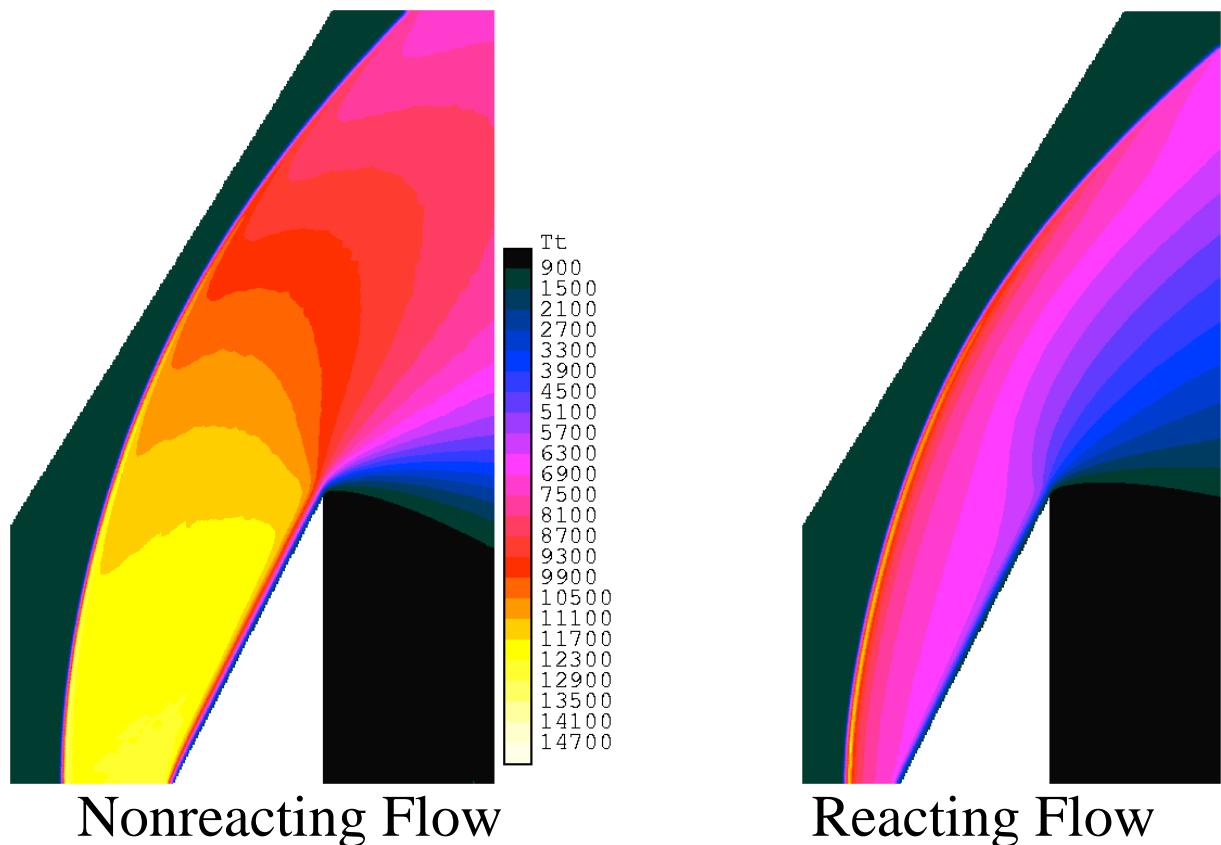


Fig. 1.36. Translational temperature flowfields for the nitrogen flow, wedge angle of 62.5°

Figure 1.36 shows the fields of translational temperature for the flow with a strongly detached shock wave (wedge angle of 62.5°) for these two cases. Allowance for chemical reactions significantly decreases the temperature behind the shock-wave front. The most important fact for this study is that the chemical reactions lead to an approximately twofold decrease in the stand-off distance. In the next two subsections, DSMC results with continuous and discrete internal energy models and NS results are compared separately for these two cases.

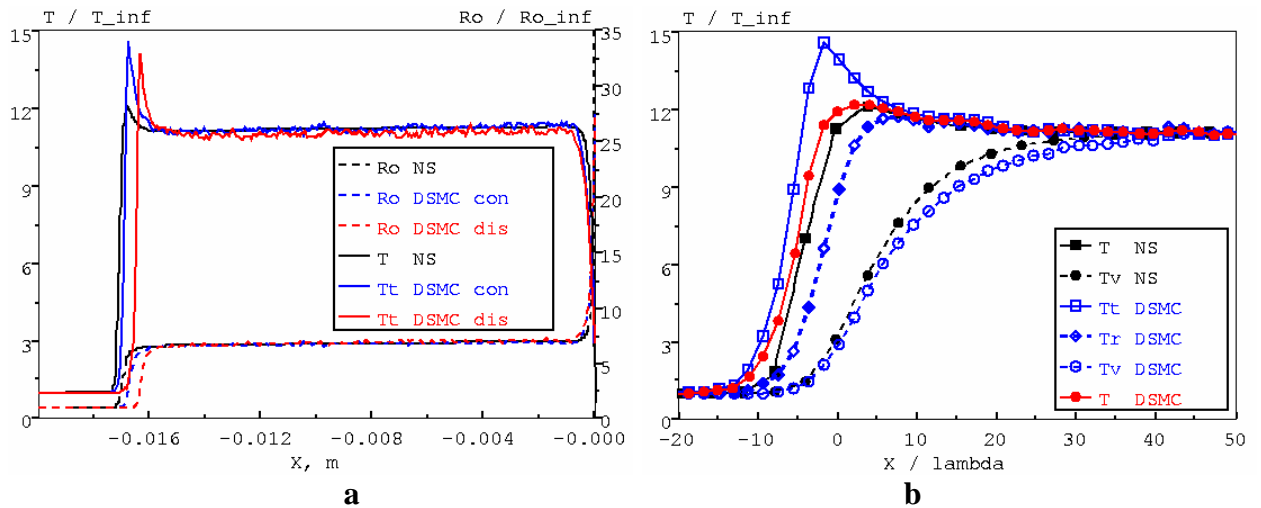


Fig. 1.37. Flow parameters along the stagnation streamline. Nonreacting nitrogen flow, wedge angle of 62.5°

Nonreacting Flow. A comparison of density and translational temperature along the stagnation streamline for a wedge angle of 62.5° is shown in Fig.1.37a. All three density profiles (DSMC profiles for both models and NS profile) coincide fairly well almost on the entire stagnation streamline except for two regions. The first one is the vicinity of the stagnation point, where the NS computation predicts a slightly smaller boundary-layer thickness than the DSMC method. The second region is the vicinity of the shock-wave front where the difference primarily refers to the position of the front itself. The NS computation predicts the greatest stand-off distance. The stand-off distance for DSMC results with the continuous model is slightly smaller than in NS results. The smallest stand-off distance is predicted by the DSMC computation with the discrete model. Note, all differences in the stand-off distance between three profiles are within 5 %.

All three profiles of translational temperature are also in good agreement almost along the entire stagnation streamline. As in the case of density, there are little differences in the vicinity of the stagnation point. The value of translational temperature behind the shock-wave front in the DSMC computation with the discrete model is slightly lower on the average than that in NS and DSMC with the continuous model. The DSMC temperature distributions with the continuous and discrete models also differ in the wave-front position (different stand-off distance). The differences between the DSMC results for the nonreacting flow with the use of different models can be explained using the contours of the specific heat ratio along the stagnation streamline shown in Fig. 1.37b. Indeed, the specific heat ratios behind the shock-wave front are somewhat different. This is quite natural: in contrast to the continuous model derived for a simple harmonic oscillator (SHO), the discrete model takes into account anharmonicity of molecular vibrations (anharmonicity parameter of 0.82 was used for N_2 molecules), and the number of effective vibrational degrees of freedom (and hence, the specific heat ratio) is different in these two models for an identical temperature. Thus, the coincidence of the stand-off distance between DSMC computations with the use of the continuous and discrete models can hardly be expected. On the other hand, NS computations employ the SHO model, as the continuous DSMC model, which is responsible for their good agreement in terms of the stand-off distance value.

The greatest difference in the translational temperature distribution (see again Fig. 1.37a) between the NS and DSMC results is observed in the vicinity of the shock-wave front. The main difference of the NS temperature distributions from that of the DSMC results with the continuous model is a significantly lower value of the temperature maximum inside the shock-wave front.

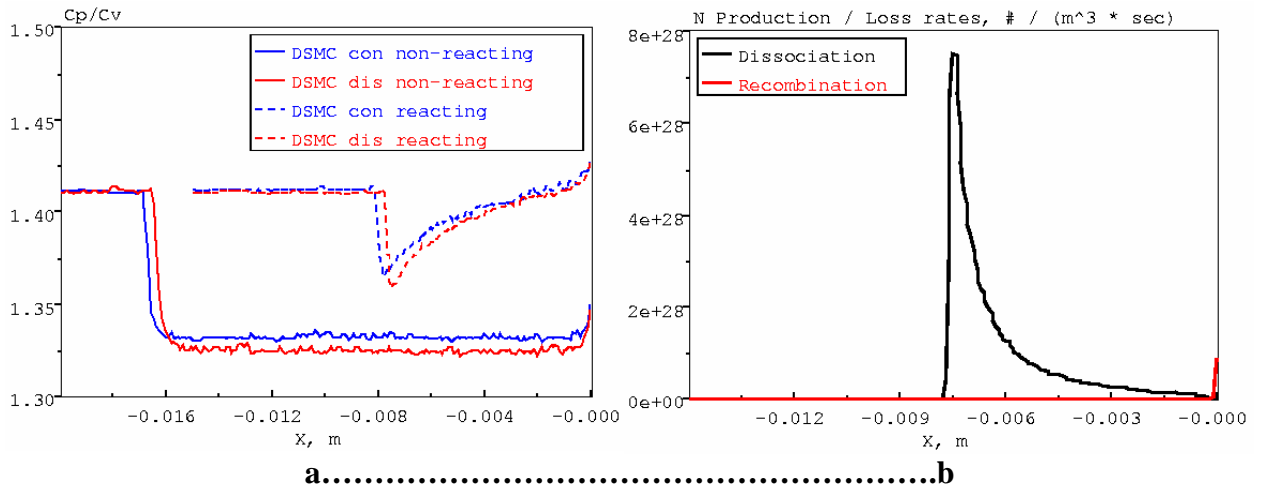


Fig. 1.38. Flow parameters along the stagnation streamline for wedge angle of 62.5°
 Temperatures along the stagnation streamline for the nonreacting flow (a). Atomic nitrogen production/loss rate due to dissociation/recombination (b).

Let us consider the shock-wave front structure in more detail. Figure 1.38a shows the distributions of various temperatures for NS computations and DSMC computations with the continuous model in the coordinate system fitted to the center of the shock-wave front. By definition, the center of the shock-wave front is the point where the density equals the halved sum of densities upstream of the front and immediately behind the front. The x coordinate in Fig. 1.38a is normalized to the free-stream mean free path. The reason for the difference in the maximum value of translational temperature for NS and DSMC computations (denoted in the figure as T for NS and T_t for DSMC results, respectively) occurs owing to the fact that, in contrast to the DSMC internal energy models, the two-temperature model used in NS computations ignores the difference in temperature of translational and rotational modes. Hence, the value of translational temperature in NS computations should be treated as the mean value of temperature of translational and rotational molecular modes (the mean value is taken with weights equal to the number of degrees of freedom of the corresponding mode). It is clearly seen that the DSMC values of rotational temperature (T_r , DSMC) inside the shock-wave front are significantly lower than those of translational temperature. Therefore, the mean temperature of translational and rotational modes (T , DSMC) is significantly lower than translational temperature and is in good agreement with T , NS in terms of the maximum value.

It should also be noted that the DSMC and NS curves for vibrational temperature (T_v , DSMC and T_v , NS, respectively) are fairly close (the DSMC profile is slightly less steep). Thus, we can conclude that NS computations and DSMC computations with the continuous model predict a similar vibrational relaxation length. This is explained by the use of similar models for vibrational energy and vibrational relaxation in DSMC (continuous model) and NS computations: SHO model for molecular vibrations, temperature-dependent vibrational collision numbers (Millikan-White), and Landau-Teller relaxation equation (this equation is not used explicitly in DSMC computations, but the DSMC models of translational-vibrational energy transfer is constructed in such a way that the relaxation rates satisfy the Landau-Teller equation in equilibrium).

Reacting Flow. Recall that only dissociation reactions were taken into account in the present study. Indeed, under conditions considered, dissociation makes the main contribution. Figure 1.38b shows the estimate of the rates of production and loss of atomic nitrogen due to dissociation and recombination, respectively, along the stagnation streamline. This estimate is

based on flow parameters obtained by DSMC simulation of the dissociating nitrogen flow. The chemical reactions in the estimate were assumed to follow the Arrhenius law

$$k_r = AT^B \exp\left(\frac{-E_a}{kT}\right)$$

where the overall kinetic temperature of the flow is used as T . It is clearly seen that this estimate shows that recombination can be substantial inside the boundary layer only.

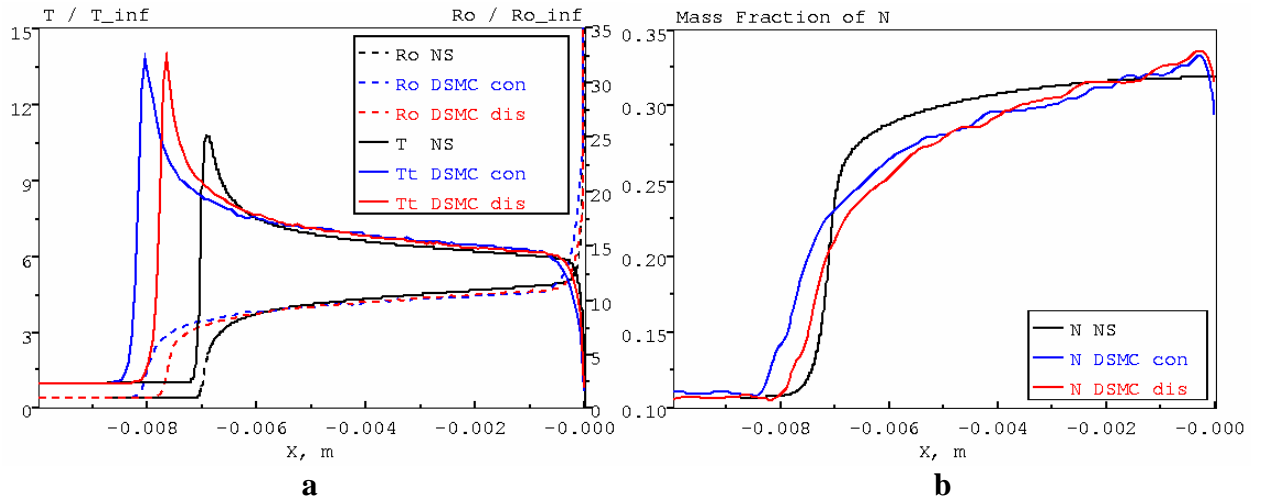


Fig. 1.39. Flow parameters along the stagnation streamline. Reacting nitrogen flow, wedge angle of 62.5°

Figure 1.39a shows the distributions of density and translational temperature for a chemically reacting flow for a wedge angle of 62.5°, obtained by NS and DSMC computations with both models. As for a nonreacting flow, the use of the discrete model yields a smaller shock-wave stand-off distance. DSMC results with different models of real gas effects differ significantly in the vicinity of the shock-wave front and in a certain region immediately behind the front. Both the density and translational temperature distributions show that the differences in NS and DSMC results are more substantial, as compared to the nonreacting flow. In addition to the difference in the maximum value of translational temperature (which can be explained by the same reason as for the nonreacting flow) and differences inside the boundary layer, there are also differences along the entire stagnation streamline, namely, NS computations yield a faster decrease in temperature and increase in density behind the shock-wave front and also a significantly smaller stand-off distance (by more than 10 %) than in DSMC computations.

A comparison of the distributions of the atomic nitrogen mass fraction for the same computations is shown in Fig. 1.39b. DSMC computations with different models of real gas effects yield a qualitatively identical result, and the main differences are related to the different value of the stand-off distance (mass fraction of N starts to grow earlier in DSMC computations with the continuous model). NS computations predict a significantly sharper increase in the mass fraction of N inside the shock-wave front than DSMC computations. Immediately behind the front, vice versa, the increase in the mass fraction of N is less steep in NS computations than in DSMC computations. Thus, we can conclude that the difference between the chemical reaction models used in DSMC and NS computations is substantial.

There is also a qualitative difference in the neighborhood of the stagnation point: NS computations predict a constant value of the mass fraction of N , whereas the latter decreases near the wall in DSMC computations. Apparently, this difference can be attributed to the different description of diffusion processes in two approaches. A more detailed analysis of the reasons for these differences is planned for the future.

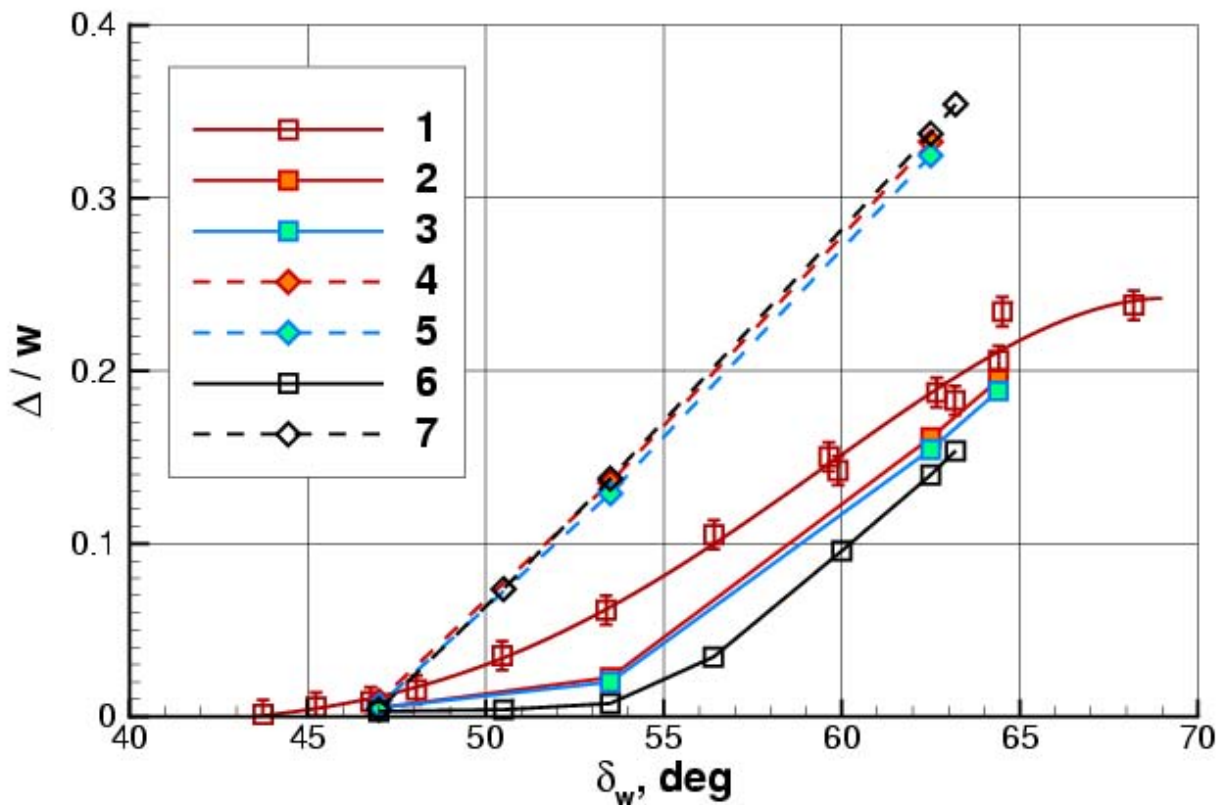


Fig. 1.40. Stand-off distance for different wedge angles for the nitrogen flow.

Line 1 - experiment of Ref. [Hornung, Smith, 1979].

Line 2 - DSMC for reacting flow with the continuous model,

Line 3 - DSMC for reacting flow with the discrete model,

Line 4 - DSMC for nonreacting flow with the continuous model,

Line 5 - DSMC for nonreacting flow with the discrete model,

Line 6 - NS for reacting flow,

Line 7 - NS for nonreacting flow

Comparison of Numerical Results and Experimental Data. The experimental and numerical curves for the stand-off distance versus the wedge angle for a nitrogen flow are plotted in Fig. 1.40. First, note that the computations predict an almost linear dependence of the stand-off distance on the wedge angle for the nonreacting gas. DSMC simulation results for the nonreacting gas with the use of the continuous model are in very good agreement with NS results for several values of the wedge angle. Application of the discrete model in DSMC simulations slightly reduces the stand-off distance.

Allowance for chemical reactions in numerical simulation (NS and DSMC) leads to a slower and nonlinear increase in the stand-off distance with increasing wedge angle. NS results predict an interval of the nonlinear increase in the stand-off distance from 47° to 56.5° . For wedge angles greater than 56.5° , the stand-off distance increases almost linearly in NS computations. DSMC computations for the reacting flow predict a dependence of the stand-off distance on the wedge angle, which coincides qualitatively with NS results, though the DSMC method yields a noticeably greater stand-off distance than NS computations in the entire range of wedge angles. As in the nonreacting case, the stand-off distance is slightly smaller if the discrete model of real gas effects is used in DSMC computations than for the continuous model.

A comparison of numerical simulation results for the reacting gas with the stand-off distance measured in the experiment shows that numerical simulations offer a qualitatively

correct description of the non-linear dependence of the stand-off distance on the wedge angle, which is in agreement with the conclusions of Ref. [Hornung, Smith, 1979]. Note, nevertheless, a significant quantitative difference between the computational results and experimental data. First, the computations (both DSMC and NS) predict detachment at a higher wedge angle ($> 47^\circ$) than the experiment ($\sim 45^\circ$). Second, the computations underpredict the stand-off distance. Almost for all values of the wedge angle, the computation results are outside the measurement error for the stand-off distance.

Since the computation results for the dissociating nitrogen flow, as for the argon flow, underpredict experimental data, some uncertainty in free-stream conditions is also possible for the nitrogen flow. Another possible reason for the difference between experimental and numerical data is the fact that reaction constants used in computations do not provide an adequate description of real reaction rates. Note that the chemical reaction DSMC models used in the present study do not take into account vibration-dissociation coupling, which may affect the shock-wave stand-off distance. A more profound study of the chemically reacting nitrogen flow around the wedge and a more detailed analysis of the reasons for the difference in computational and experimental results are necessary.

Conclusions

A steady hypersonic 2D flow around a wedge with a Knudsen number $Kn \sim 0.0005$ was numerically studied by the kinetic (DSMC method) and continuum (Navier--Stokes equations) approaches both for a monatomic gas (argon) and a diatomic reacting and nonreacting gas (nitrogen). Two models of real gas effects were used in DSMC computations of the nitrogen flow: with continuous and discrete representations of internal energy of molecules. DSMC computations were performed on a multiprocessor computer with the use of up to 200 processors and up to 70 million of modeling particles.

Very good agreement was obtained between DSMC results for the argon flow and the numerical solution of the Navier--Stokes equations in a wide range of wedge angles. The differences are observed inside the shock-wave front only. Numerical results underpredict the experimentally measured stand-off distance of the shock wave. The most probable reason for this distinction can be the difference between actual free-stream conditions in the experiment of [Hornung, Smith, 1979] and the values cited in Ref. [Hornung, Smith, 1979].

For the nitrogen flow around the wedge, the difference in the stand-off distance between the DSMC results obtained with the continuous and discrete models of real gas effects is within several percent both for the reacting and nonreacting nitrogen flow.

A comparison of the numerical solution of the Navier--Stokes equations (with the two-temperature model) for the nonreacting nitrogen flow with the results of DSMC simulations (with the use of both models of real gas effects) reveals their good agreement. DSMC computations for reacting nitrogen predict a greater stand-off distance than NS computations. A detailed comparison of results shows that the chemical reactions in NS modeling proceed much faster than in the DSMC approach. Therefore, a detailed analysis of the models of chemical reactions used in the CFD-FASTRAN NS solver is needed.

Numerical results for the nonreacting nitrogen flow predict a linear increase of the stand-off distance with increasing wedge angle. Allowance for chemical reactions in numerical modeling yields a nonlinear dependence of the stand-off distance on the wedge angle, which is in qualitative agreement with experimental data. Quantitatively, the numerical simulation results overpredict the detachment angle and underpredict the stand-off distance obtained in experiments. To analyze this discrepancy, as for the argon flow, refinement of the free-stream conditions and further numerical studies are necessary. Also a study of vibration-dissociation coupling effect on the shock stand-off distance is planned.

Task 7.

User manual for SMILE++ with detailed description of models and basic variables.

The use of the SMILE++ software system implies the use of the xSMILE windows interface, which ensures preparation of initial data, program running, and analysis of results. Yet, to modify the SMILE++ code or to run some special capabilities, which are not included into the xSMILE system, the user needs a detailed manual, which would give a comprehensive idea about the program structure, its capabilities, and ways for upgrading.

The manual includes the following sections.

- Description of input and output files.

Being started, the program reads out the initial data file indicated in command arguments. Depending on their purpose, the input data are divided into groups. For instance, there are groups that describe properties of gases, parameters of chemical reactions, grid, geometry, or manner or particle storage; there is also a group of control commands. The use of groups allows one to focus data readout exactly in the class where they are used and easily change the flux of input information when one class is replaced by another. The data begin from a keyword that alerts the readout program and defines which data follow.

Apart from the division into groups, the data can be divided into separate files attached to the basic file of initial data. This allows the user to separate data preparation into several modules, each module preparing its own data. For example, the structure for the description of gas properties and chemical data is presented below.

The text from the symbol “!” to the end of the string is a comment. Empty strings are ignored.

1) Group that enumerates the gases used.

```
#group Gases
```

```
#group Gas
```

```
.....
```

```
#end
```

```
#group Gas
```

```
.....
```

```
#end
```

```
#end
```

2) Group that describes chemical reactions (if any)

```
#group Chemistry
```

```
....
```

```
#end
```

3) General parameters (without #group)

```
VariableZrZv 0      ! Temperature-dependent ZrZv
```

```
Discret 0  ! use of discrete or
```

```
! continuous spectrum
```

```
! 1 - yes, 0 - no
```

Structure of each gas:

```
#group Gas
```

```
..
```

```

..
..
#end
Between them, there are properties of a gas (one),
Keywords, and values:
Name N2 ! Name of the gas
Type DIATOMIC ! Type of gas molecules:
! ATOM, DIATOMIC, LINEAR,
! SPHERICAL, GENERAL
! General parameters
Atoms 2 ! number of atoms
Diametr 4.11e-10 ! cross-sectional diameter
! collisions
Mass 4.649e-26 ! molecular weight
Alpha 0.24 ! viscosity index
Tref 273. ! reference temperature

! collisional parameters

ZR 10 ! constant Zr
ZV 100 ! constant Zv
ZRoo 18.1 ! Zr for VariableZrZv=1
Tstar 91.5 ! T* for VariableZrZv=1

EDiss 1.561e-18 ! dissociation energy

TetaVc 3371. ! characteristic vibrational temperature
TetaR 2.88 0 ! characteristic rotational temperature [2 values]

```

The chemical reactions can be of three types:

1) Exchange:

```

#group Exchange
R1 N2 ! name of reagent 1
R2 O2 ! --" 2
P1 NO ! name of product 1
P2 NO ! --" 2
Ea 0. ! activation energy
A 2.49e-17
B 0
Heat 0
VDC 0. ! 0. - TCE, >0 VDC
#end

```

2) Dissociation

```

#group Dissociation
R1 N ! name of reagent 1
R2 N2 ! --" 2
P1 N ! name of product 1
P2 N ! --" 2
P3 N ! --" 3
Ea 1.561e-18

```

```

A 6.9e-8
B -1.5
Heat -1.561e-18
VDC 0. ! 0. - TCE, >0 VDC
#end

```

To reduce the amount of stored results and increase the recording speed, the computation results are recorded in a binary form. To convert these files into convenient text files, there are special utilities; some of them are included into the xSMILE system. Upgrading of SMILE++ will most probably require additional information, and the knowledge of the structure of binary files and the interface of conversion utilities will be helpful.

Structure of Dump files.

The file is binary, i.e., all numbers are written in a binary form. It contains keywords (four bytes each, including blank spaces), which comment on the meaning of information following this word. After each keyword, there is a four-byte number, which can denote the amount of something, e.g., the number, version, etc. This allows the use of macros, which immediately read the keyword and the number after the keyword.

The file begins from the heading:

```
TYPExxxx
```

TYPE –file type, which allows one to determine what this file contains

xxxx – number of the version

Then, there follow simple data and blocks.

The file ends by

```
ENDFxxxx
```

The file can contain both simple data (numbers of arrays) and data blocks. In each block, similar data are read out (i.e., data containing identical keywords). The number of blocks can be arbitrary. Each block starts from the key BLOKxxxx and ends by the key ENDBxxxx. Simple data are located between these keywords. All blocks should follow one another, and the first block should be preceded by the keyword BLKSxxxx. The program should respond to this key by running a cycle for block read out.

If there are several types of block data, the program should either know the sequence of block information or contain simple data indicating the type of the current block information ahead of the keyword BLKSxxxx.

The simple data are represented in the following form:

```
wordxxxxxyyyy...
```

.

word – keyword indicating the direction or name of data

xxxx – number of data bytes that refer to a given keyword (e.g., 4 for a single integer, 8 for a single double element, 40 for an array of 5 double elements)

yyy...- data themselves.

It is convenient if the number of data bytes is multiple to 8 or, at least, 4. This significantly simplifies viewing of the file by standard tools, e.g., "od" code.

```
od -c file - text interpretation
```

```
od -t d4 file - int/long "-"
```

```
od -t f4 file - float "-"
```

```
od -t f8 file - double "-"
```

The keywords are specified by the user, and the response to these keywords should also be prepared by the user. If the readout code does not contain responses to keywords, the data are skipped by a length xxxx, i.e., the position in the file is set to the next keyword.

The following keywords cannot be used because they are reserved for special purposes:

BLKSxxxx – number of blocks. xxxx – number of blocks.
 BLOKxxxx – beginning of the block. xxxx – number of the block.
 ENDBxxxx – end of the block. xxxx – number (or type) of the block.
 ENDFxxxx – end of file. It serves to verify that the file is recorded completely. xxxx – is an arbitrary number, which does not mean anything and is employed to prevent the use of macros that read out the keyword and the number behind it.

A response to the reserved keywords is obligatory, since the information that follows them does not define the shift, and readout control will be lost.

Structure of Dump files of the fields.

File type: FILD

The file type should be followed by

Dim - field dimension

yyyy - 2-2D, 3-3D, 4-axisymmetric.

Simple data (in an arbitrary order):

| Keyword | Size | Comment |
|---------|------|---|
| "Step" | f,8 | Time step |
| "Time" | f,8 | Current time |
| "Xmin" | f,8 | Xmin of the domain |
| "Xmax" | f,8 | Xmax "-" |
| "Ymin" | f,8 | Ymin "-" |
| "Ymax" | f,8 | Ymax "-" |
| "Nx " | i,4 | Number of cells along X |
| "Ny " | i,4 | Number of cells along Y |
| "Cels" | i,4 | Total number of cells |
| "Num " | i,4 | Number of accumulated events |
| "Fnum" | f,8 | Ratio of the number of real molecules to modeling molecules |
| "RefN" | f,8 | reference number density |
| "RefD" | f,8 | reference density |
| "RefT" | f,8 | reference temperature T [K] |
| "RefV" | f,8 | reference velocity [m/s] |

Blocks in terms of the number of components

| Keyword | Size | Comment |
|---------|---------|---------------------------------|
| "Name" | c,16 | name of the gas |
| "Mass" | f,8 | molecular weight |
| "R " | f,8 | gas constant |
| "Nptc" | i,4*NC | number of particles in the cell |
| "Vel " | v,24*NC | adder of velocities |
| "Vel2" | v,24*NC | adder of velocities squared |

Size: c - text, i - integer, f - real, v – vector of three real numbers.

Structure of Dump files of 2D aerodynamic characteristics.

File type: ADCH

The file type should be followed by

Dim - field dimension

yyyy - 2-2D, 3-3D, 4-axisymmetric.

Simple data (in an arbitrary order):

| Keyword | Size | Comment |
|---------|------|---|
| "Name" | c,32 | name of the geometric model |
| "Step" | f,8 | time step |
| "Time" | f,8 | current time |
| "SamF" | i,4 | beginning of data acquisition |
| "SamT" | f,8 | time of data acquisition |
| "Fnum" | f,8 | ratio of the number of real particles to modeling particles |
| "RefS" | f,8 | reference area |
| "RefL" | f,8 | reference size |
| "RefD" | f,8 | reference density |
| "RefV" | f,8 | reference velocity |
| "RefC" | v,24 | center of mass |
| "NGas" | i,4 | number of gases in the mixture (NG) |

There are four ADC blocks, each of length equal to NG: ADC (incident/reflected) error (incident/reflected)

Each ADC contains (block length L)

| Keyword | Size | Comment |
|---------|-------|----------------------|
| "Nptc" | i,4*L | numbers of particles |
| "Cx " | f,8*L | counter for Cx |
| "Cy " | f,8*L | counter for Cy |
| "Mz " | f,8*L | counter for Mz |
| "E " | f,8*L | counter for energy |

Blocks in terms of the number of elements:

| Keyword | Size | Comment |
|---------|------|---------------------|
| "Type" | c,8 | type of the element |
| "Name" | c,32 | name of the element |
| "Npan" | i,4 | number of panels |

Each element contains two ADC blocks of length NG*NP*2: ADC (incident/reflected, for each gas, for each panel)

- Options of code initiation

These options determine the specific features of a particular run of SMILE++.

-new – command for running a new computation. If this command is not used, the data from dump files of the previous state of the problem are reconstructed, and the computation is continued.

-fill – initial filling of the domain by particles. This option operates only with the option “new”.

-nogen – cancels generation of new particles at each step. This option is used in some tests with uniform relaxation, where the particles are used only inside a “box” with mirror walls. This option operates only with the option “fill”.

-inp – name of the initial data file. The default name is dsmc.inp

- Description of possibilities of controlling the executed program.

The SMILE++ software system can accept and execute some user’s commands directly during its operation. By means of commands of the UNIX operational system, the user can send a signal (SIGUSR1); after receiving this signal and finalizing execution of the next step, the code reads out a specified file and executes commands from this file. These commands can control the display of current information, forced saving of the current state, termination of the running code, etc.

- Description of the code structure.

Any upgrading of the code requires detailed knowledge of the code structure and interaction between its individual components. Therefore, careful, detailed, and clear documenting of the code is necessary.

Unified Modeling Language (UML) is a graphical language for visual representation, preparing specifications, design, and documenting of systems.

One of the most important components of the documenting process is the diagram of classes illustrating the relations between the classes of the project (inheritance and nesting of some classes in others).

For instance, Fig. 1.41 shows the structure of particle storage. The basic class for storage is the class cgMol. This class determined the interface for generation and deleting of particles and for obtaining information about particles (coordinates, velocity, internal energy, etc.).

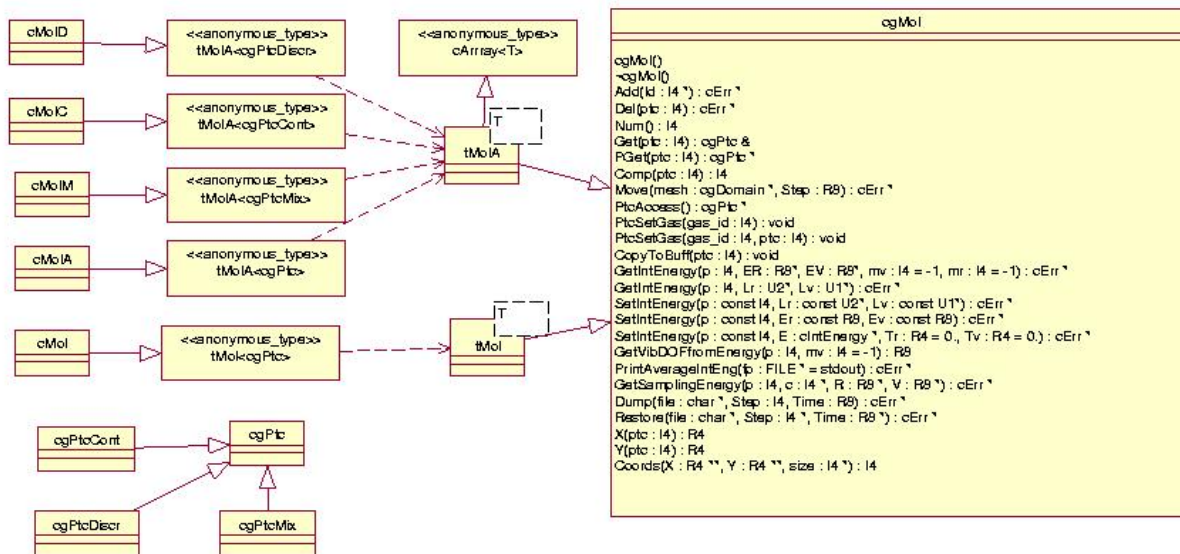


Fig. 1.41. Diagram of classes

The derived classes of this class are parameterized classes (templates) with different methods of particle storage. Both templates involve a dynamic change in memory with increasing or decreasing number of particles. The class `tMol` employs one array, which is copied to the newly allocated memory of needed size if it is necessary to change the array length. The class `tMolA` employs a set of blocks of fixed length; the number of these blocks changes depending on the required memory.

As a parameter of both templates, we use the class `cgPtc` (or one of classes derived from this one) responsible for storage of properties of each individual particle. The class `cgPtc` stores the general properties of particles (coordinates and velocities), and each derived class adds its own specific properties (sort of the gas, various models of internal energy).

Thus, combinations of a template and a particle correspond to different methods of storage of various properties of particles:

- - classes `cMol` and `cMolA` – storage of monatomic, single-species particles.
- - class `cMolM` – storage of monatomic, multiple-species particles.
- - class `cMolD` – polyatomic particles with the discrete representation of internal energy.
- - class `cMolC` – polyatomic particles with the continuous representation of internal energy.

Another diagram, which is not less important, is the diagram of sequences. For example, Fig. 1.44 shows the sequence of events in the operation "particle collisions" for a single-species monatomic gas. The diagram shows which classes participate in this operation, in which sequence they are involved, and which methods are used.

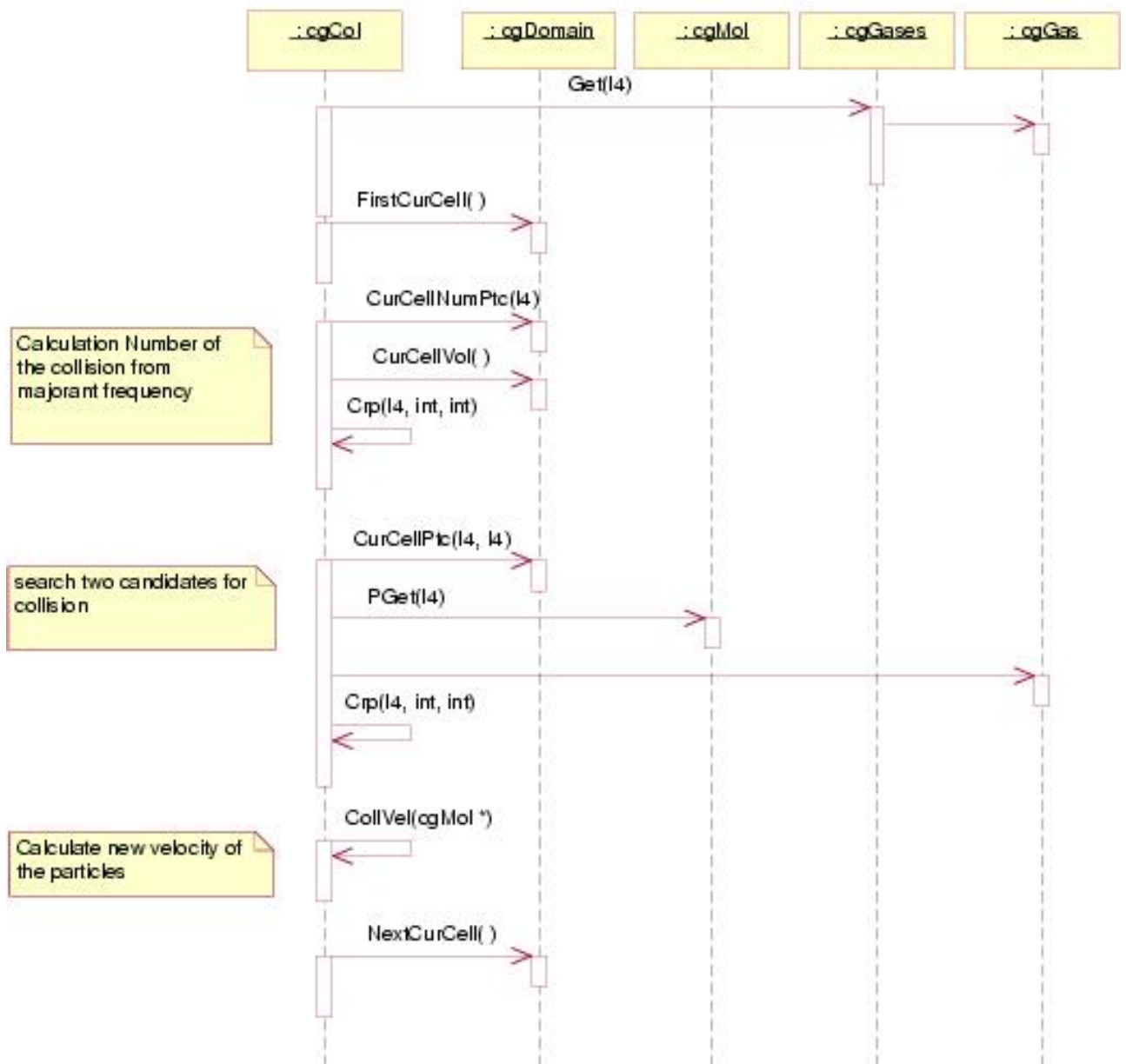


Fig. 1.42. Diagram of sequences

Some objects are not attributed of any class. These objects are global, and the manual has a complete list of such objects.

References used:

9. Liepmann, H.W. "Gas kinetics and dynamics of orifice flow," J. of Fluid Mech., Vol. 10, 1961, pp.65-79
10. Barashkin S.T., Porodnov B.T., Suetin P.E. "Gas exhaustion through the orifice," Zhurnal Tekhnicheskoy Fiziki, 47, 1977, p.199. [in Russian]
11. Livesey, R., "Flow of gases through tubes and orifices", In *Foundation of Vacuum Science and Technology*, edited by J.M.Lafferty, Willey-Interscience, 1998, pp. 81-140
12. A.A.Alexeenko, D.A.Levin, S.G.Gimelshein, M.S.Ivanov, A.D.Ketsdever "Numerical and experimental study of orifice flow in the transitional regime", AIAA 2001-3072
13. Shakhov E.M. "Solution of axisymmetric problems of the rarefied gas theory by the finite-difference method," Zh. Vychislitel'noj Matematiki i Matematicheskoy Fiziki, 14, 1974, p. 970. [in Russian]

14. Sharipov F. "Rarefied gas flow through a thin orifice," Proc. 22-nd Int. Symp. on Rarefied Gas Dynamics. 2001, pp. 4094-501.
15. Ivanon M.S., Rogasinsky S.V., Theoretical analysis of traditional and modern schemes of the DSMC method. Proc. XVII Int. Symp. on Rarefied Gas Dynamics. Aachen, Germany, 1991, pp.629-642.
16. T.Fujimoto and M. Usami, J. Fluids Eng. 106, 367(1984)
17. Ketsdever, A.D., Green, A. and Muntz, E.P., "Momentum flux measurements from underexpanded orifices: application for micropropulsion systems," AIAA Paper 2001-0502, Jan. 2001.
18. J.H. Jeans. The dynamical theory of gases. Cambridge University Press, London, 1916.R.C. Millikan, D.R. White. Systematics of vibrational relaxation. J. Chem. Phys., 1963, Vol. 39, pp. 3209-3213.
19. C. Park. Nonequilibrium hypersonic aerothermodynamics. Wiley, New York, 1990.
20. Gimelshein N.E., Gimelshein S.F., Levin D.A., Ivanov M.S., Wysong I.J. Reconsideration of DSMC models for internal energy transfer and chemical reactions. Rarefied Gas Dynamics. 23rd International Symposium (20-25 July 2002 : Whistler, BC, Canada). AIP Conference Proceedings, No. 663, 2003, pp. 349-357.
21. Gimelshein S.F., Gimelshein N.E., Levin D.A., Ivanov M.S., Wysong I.J.
22. On the use of chemical reaction rates with discrete internal energies in the direct simulation Monte Carlo method. Submitted to the Physics of Fluids, November 2003.
23. Bird, G.A., "Simulation of Multi-Dimensional and Chemically Reacting Flows," Rarefied Gas Dynamics, Vol. 1, edited by R. Campargue, COMMISSARIAT A LENERGIE ATOMIQUE-Paris 1979, pp. 365-388.
24. Hornung, H.G., Smith, G.H, "The influence of relaxation on shock detachment", J. Fluid Mech., **93**(2), pp. 225-239 (1979).
25. Moss J.N., Bird G.A., Dogra V.K. "Nonequilibrium thermal radiation for an aeroassist flight experiment vehicle." AIAA Paper 88-0081.
26. M.S. Ivanov, G.N. Markelov, and S.F. Gimelshein. "Statistical simulation of reactive rarefied flows: numerical approach and applications." AIAA Paper 98-2669.
27. Bird, G.A., Molecular Gas Dynamics and the Direct Simulation of Gas Flows, Clarendon Press, Oxford, 1994.
28. CFD-FASTRAN: User manual, Version 2003, CFD Research Corporation (Huntsville, AL), 2003.
29. Ivanov M.S. and Gimelshein S.F. Current Status and Prospects of the DSMC Modeling of Near-Continuum Flows of Non-Reacting and Reacting Gases, Proc. 23th Intern. Symp. on RGD, AIP Conference proceedings, Vol. 663, 2003, pp. 339-348.
30. Ye.A. Bondar, G.N. Markelov, S.F. Gimelshein, and M.S. Ivanov "DSMC Modeling of Near-Continuum Flow Over a Wedge with Real Gas Effects" AIAA Paper 2004-1183

ADDENDUM. *Development of a model of a chemically reacting gas for the DSMC method, which would describe chemical reactions (exchange reaction and dissociation) in strongly nonequilibrium flows at high temperatures. Implementation of this model into the DSMC code and its numerical verification and validation.*

Introduction

The classical description of chemical reactions in the gas phase employs the Arrhenius presentation of the rate constants of these reactions, which depend on only one variable: gas temperature T . This means that all internal degrees of freedom of reacting gas components, first of all, vibrational and rotational degrees of freedom of molecules, are in equilibrium with the translational temperature of the gas T . In this case, the vibrational levels of molecules have the Boltzmann distribution of populations; hence, their populations are described by a common

vibrational temperature T_v equal, as was noted above, to the translational temperature T . A similar situation is observed for rotational levels.

With rare exceptions (such as hydrogen halide molecules), rotational quanta of molecules are rather small; if there are some changes in gas temperature, its rotational temperature equalizes with the translational temperature within several (~5-20) collisions. Therefore, the rotational and translational temperatures of the gas are assumed to be identical in what follows.

The situation with the populations of vibrational levels of molecules in a high-temperature gas flow is different, because it depends both on gas temperature and on its gradient. In particular, it is well known that temperature, density, and hence, collision frequency in supersonic cooling nozzle flows decrease so rapidly that vibrations excited ahead of the nozzle entrance do not have enough time for deactivation; the so-called "freezing" of vibrations occurs, i.e., a "cold" gas with "hot" vibrations passes through the nozzle. Publications offer several theoretical models of "two-temperature" rate constants of chemical reactions, which take into account the situation with $T_v > T$ [1a,1b]; in many cases, however, the drastic decrease in density and translational temperature of the gas in the nozzle "cancels" chemical reactions, and the difference between T_v and T affects only the heat balance in the system.

In the case of sudden heating of the gas, e.g., behind the shock-wave front, the distribution of temperatures is different. If the shock wave is not too strong (see below), vibrations are not excited before chemical reactions begin, and the latter proceed with a common translational-vibrational temperature T . Behind the front of a strong shock wave, however, chemical reactions in the gas can start and proceed simultaneously with excitation of molecular vibrations, i.e., molecules with insufficiently excited vibrations can participate in reactions, which naturally affects the rate constants of these reactions. The distribution of populations of vibrational levels of reacting molecules can differ from the Boltzmann distribution; in this case, one has to use the so-called "level-by-level" kinetics of chemical reactions, where molecules populating each vibrational level are considered as an independent component of the reacting mixture [2]. Despite a certain number of models that describe such a "level-to-level" kinetics of chemical reactions, however, the necessary set of parameters for such a description of the kinetics is missing at the moment. In what follows, therefore, we will consider only the "two-temperature" kinetics, i.e., a description of reaction rate constants under the assumption of the Boltzmann distribution of populations of vibrational levels of reacting molecules. This approach is justified both by available experimental data and by a significant number of theoretical models that offer an adequate description of these experimental data. Results available in this aspect are briefly described below.

Dissociation of molecules behind the shock-wave front

Experimental data suggest that vibrations behind the shock-wave front at comparatively moderate temperatures within a doubled characteristic vibrational temperature of the molecule Θ (2240 K for oxygen, 3350 for nitrogen, etc), which means for temperatures within 5000-6000 K, are completely excited before the beginning of dissociation, and dissociation is described by the conventional rate constant of the Arrhenius type $K_0(T) = A T^B \exp(-E/T)$ with the translational temperature T only, because the vibrational temperature T_v has enough time to reach the translational temperature, $T_v = T$.

If processes at significantly higher temperatures (10,000-20,000 K) are considered, however, the molecule starts decomposing with vibrations not excited to a sufficient extent: $T_v < T$. The upper vibrational levels of the molecule, where dissociation predominantly occurs, are underpopulated; as a result, the dissociation rate constant, first, is smaller than the constant K_0 extrapolated from lower temperatures and, second, becomes dependent not only on translational temperature but also on the degree of vibrational excitation, i.e., on vibrational temperature, $K=K(T,T_v)$. It is obvious that the deviation from the extrapolated Arrhenius dependence K_0 is not very large if the difference between T_v and T is small, first of all, because the gas temperature is

not very high. At temperatures of 15,000-20,000 K, however, the difference of the real rate constant from extrapolated low-temperature data can reach an order of magnitude or more, which reduces the dissociation rate accordingly. Everything is determined by efficiency of partners in excitation of vibrations and dissociation processes. A similar situation is observed for exchange reactions.

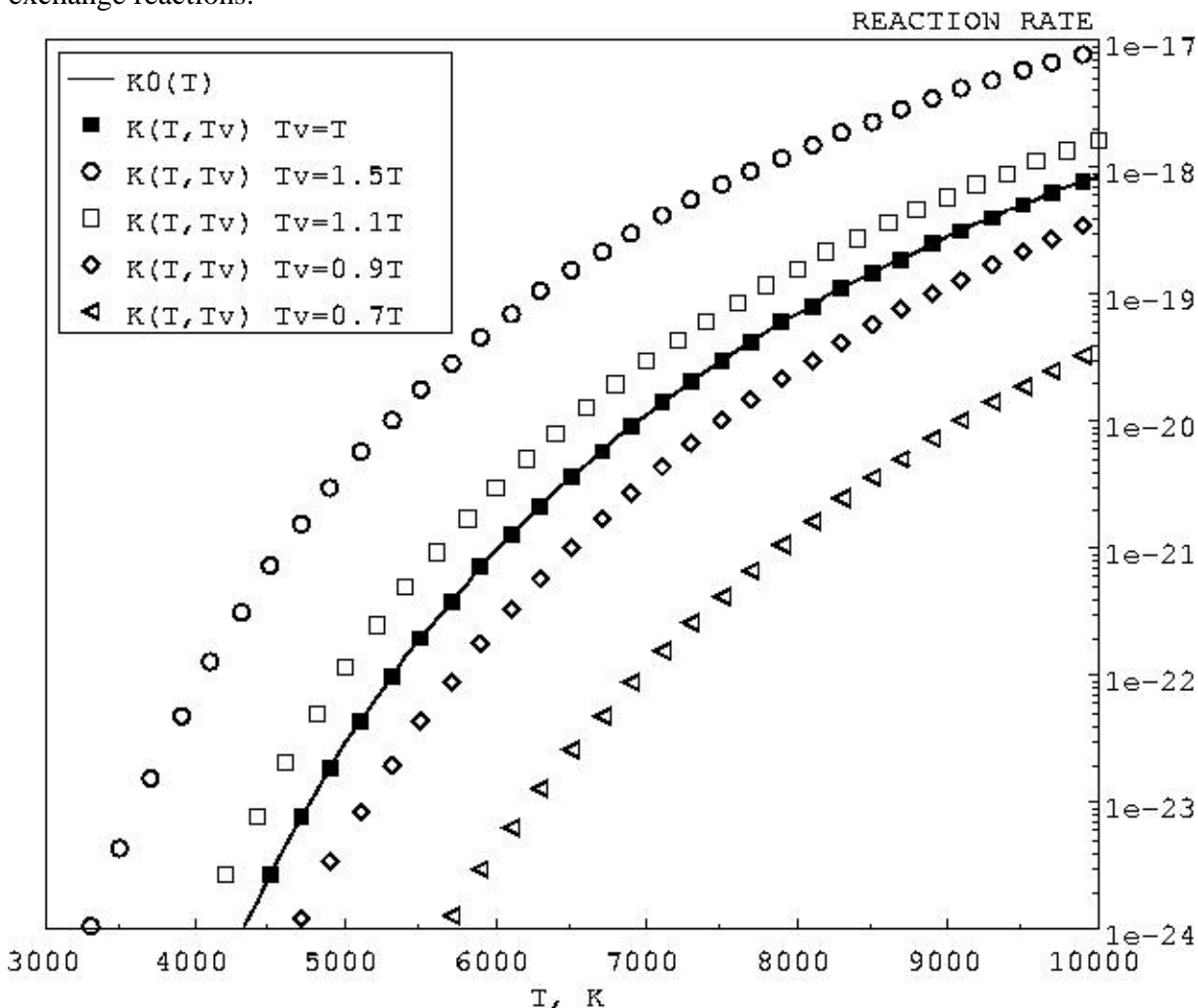


Fig.1.43. Temperature dependence of the $N_2+N \rightarrow 3N$ reaction rate, for the one-temperature model and for Kuznetsov's two-temperature model for different ratios of translational and vibrational temperatures.

The above-described behavior of the constant was first predicted theoretically by Hammerling (Hammerling, 1959) and Marrone and Treanor (Marrone, Treanor, 1963). These papers were analyzed in detail in [2]. Currently there are several dozens of models for rate constants of chemical reactions in gases, which take into account thermal nonequilibrium of this process [1b].

The thermally nonequilibrium dissociation rate constant is usually written in the form $K=K_0(T)Z(T,T_v)$, where $K_0(T)$ is the equilibrium rate constant extrapolated from “low” temperatures (where $T_v = T$) and Z is a coupling factor, which takes into account the deviation from the Arrhenius dependence due to retardation of vibrational temperature. The coupling factor behind the wave front is smaller than unity. Numerous existing models of the coupling factor were obtained on the basis of various assumptions on the kinetics of population and decay of vibrational states of reacting molecules.

Park's two-temperature model of rate constants of chemical reactions is very popular in the literature (see, e.g., [4]). In this model, the reaction rate constants have a simple Arrhenius

form and depend on a certain effective temperature, which is the mean geometric value between T_v and T . Nevertheless, this model has not sufficient theoretical grounds, and the calculations based on this model sometimes disagree with experimental data.

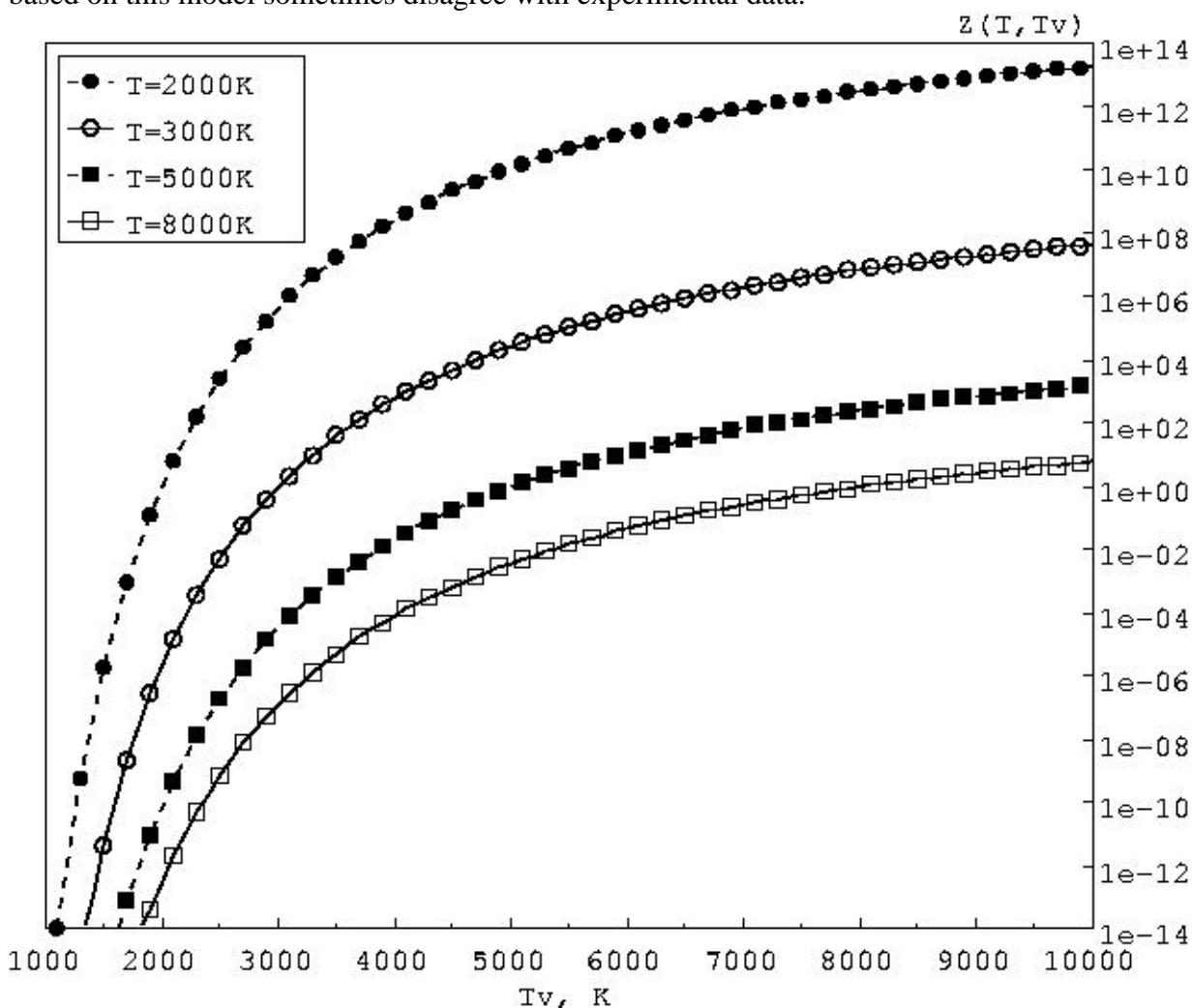


Fig.1.44. Vibrational temperature dependence of the coupling factor in Kuznetsov's two-temperature model for the $N_2+N \rightarrow 3N$ reaction for different values of translational temperature.

The analysis performed within the present study shows that Kuznetsov's model described in his paper in 1971 and in the monograph in 1982 can be reasonably used [1a, 3]. This model is fairly well justified and, simultaneously, simple and convenient for calculations:

$$Z(T, T_v) = [Q(T)/Q(T_v)] \exp[-E^*_v \{1/T_v - 1/T\}]. \quad (1.3)$$

Here Q are vibrational partition functions, $Q(T) = 1/(1 - \exp(-\Theta/T))$, and E^*_v equal approximately 0.7 of dissociation energy. It should be noted that this model is also effective for $T_v > T$ [1b].

The dependence of Kuznetsov's two-temperature constant $K(T, T_v)$ on translational temperature for different values of the ratio of translational and vibrational temperatures is plotted in Fig. 1.43. Under thermal equilibrium ($T = T_v$), the value of $K(T, T_v)$ exactly coincides with the one-temperature Arrhenius constant $K_0(T)$. A small deviation of vibrational temperature from translational temperature changes the value of the reaction rate by orders of magnitude. This fact is also supported by the shape of the dependence of the coupling factor $Z(T, T_v)$ on T_v for different particular values of T plotted in Fig.1.44.

It should be simultaneously noted that 90 % of time of molecular dissociation behind the shock-wave front are spent under quasi-steady (in terms of vibrations) conditions (except for the initial moment and the last period of time before reaching the equilibrium state). The analysis

performed in [5] showed that the numerical values of the dissociation-rate constants obtained from different models under these conditions are little different from each other (within a factor of 2 to 3).

Presentation of the reaction rate constants in the form $K=K_0(T)Z(T,T_v)$ arouses a question about correct extrapolation of the value of $K_0(T)$ to high temperatures. Based on some theoretical approaches and low-temperature experimental data, Krivonosova and Shatalov [5] suggested the values for $K_0(T)$ at high temperatures for a number of diatomic molecules and the CO_2 molecule.

The rate constants of exchange reactions under conditions of thermal nonequilibrium have been studied to a smaller extent. The reference book [1b] offers two models of these reactions, which have the same form as the models of the rate constants of thermally nonequilibrium dissociation, $K=K_0(T)Z(T,T_v)$, but the particular form of nonequilibrium factors in these models is rather cumbersome, and their parameters are given for some particular cases or require additional extensive calculations.

Construction of the model of high-temperature dissociation for the DSMC method

The major challenge of the present activities was to develop a model for the DSMC method, which would describe nonequilibrium dissociation and could be applicable for high temperatures. In contrast to numerical methods of continuum gas dynamics, information on the dependence of the reaction rate on the values of translational and vibrational temperatures is insufficient for the DSMC method. DSMC simulations of chemical reactions require the knowledge of the total reaction cross section as a function of energies of different modes of the colliding molecules and also the law of energy distribution between different modes of molecules that are produced in the reaction.

In constructing the dissociation model for the DSMC method, we decided to use an approach based on seeking for the dissociation cross section as a function of the total energy of the colliding pair and vibrational energy of the dissociating molecule under the following condition: the dissociation rate under conditions of equilibrium population of vibrational levels of molecules (corresponding to the temperature T_v) and equilibrium velocity distribution function and population of rotational levels of molecules (corresponding to the temperature T) should coincide with the dissociation rate determined by the two-temperature nonequilibrium constant $K(T,T_v)$ in a wide range of values of T and T_v .

An important feature of the proposed model is the possibility of its use in hybrid continuum/DSMC codes. In this case, chemical reactions in the continuum module are modeled by the two-temperature (T, T_v) model with the rate constant $K(T,T_v)$, which is a procedure typical for continuum approaches, whereas the model suggested here is used in DSMC computations. Such an approach allows taking into account the processes of high-temperature dissociation in hybrid codes. Thus, the two-temperature chemical model of the DSMC method can bridge the gap in creating a hybrid CFD/DSMC code.

As a nonequilibrium constant $K(T,T_v)$, we decided to use the constant from Kuznetsov's model. In addition to its advantages mentioned, this model possesses some important mathematical properties, which allow constructing models of the DSMC method on the basis of Kuznetsov's model.

An approach that allows constructing a model of the DSMC method for modeling high-temperature dissociation was suggested in the present study. This model has the following specific features.

- The model is used for dissociation reactions of a molecule colliding with an atom.
- Under conditions of complete thermal equilibrium, this model yields a reaction rate corresponding to the equilibrium Arrhenius constant.
- In the gas with translational-rotational temperature T and vibrational temperature T_v , with equilibrium distributions in terms of velocities, rotations, and vibrations, the model yields a

- dissociation rate corresponding to the two-temperature constant, where the coupling factor is determined by Kuznetsov's model .
- The model is also applicable in the case of nonequilibrium distributions in terms of velocities, rotations, and vibrations of molecules.
- The dissociation cross section is a function of the vibrational level from which the molecule dissociates and of the total translational-rotational energy.

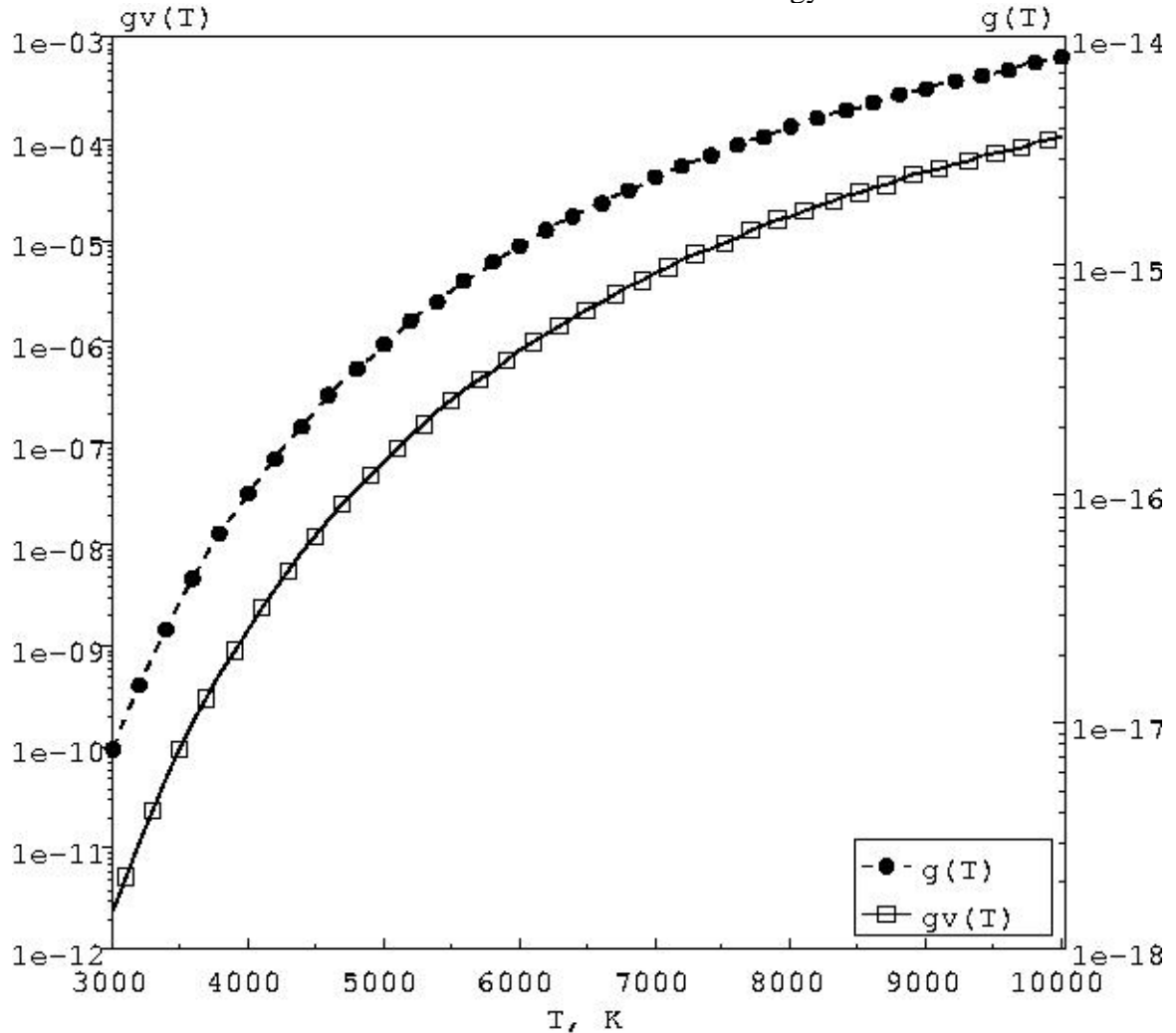


Figure 1.45. Functions $g(T)$ and $g_v(T_v)$ for $N_2+N \rightarrow 3N$ reaction.

The a set of level dissociation cross sections σ_n is found by solving a rather complicated integral equation

$$\sum_{n=0}^{N_{\max}} f_v(n, T_v) \int_0^{\infty} \int_0^{\infty} \sigma_n(E_r + E_t) \sqrt{\frac{2E_t}{m_r}} f_r(E_r, T) f_t(E_t, T) dE_r dE_t = K(T, T_v) \quad (1.4)$$

Such a set of level cross sections in the case of equilibrium distribution functions of all energy modes provides the macroscopic dissociation rate that agrees with the two-temperature constant $K(T, T_v)$. From the mathematical viewpoint, finding a solution this equation is a complicated problem because of the following factors:

- complicated form of the operator acting on σ_n (including operations of integration and summation);
- high dimensionality of the problem (both the solution and the right-hand side $K(T, T_v)$ are functions of two variables);

- ill-posedness and nonuniqueness of the solution (this issue will be discussed in detail later).

To overcome the first two difficulties, the problem will be subjected to transformations, and the solution will be sought in a special form. The two-temperature constant of Kuznetsov's model can be presented as the product

$$K(T; T_v) = g(T) g_v(T_v)$$

The functions g and g_v for the nitrogen dissociation reaction are plotted in Figure 1.45. We seek the solution in the form

$$\sigma_n(E_r + E_t) = \gamma(n) \sigma_n'(E_r + E_t)$$

for each vibrational level n , where $\gamma(n)$ and $\sigma_n'(E_r + E_t)$ are the solutions of the equations

$$\int_0^\infty \int_0^\infty \sigma_n'(E_r + E_t) \sqrt{\frac{2E_t}{m_r}} f_r(E_r, T) f_t(E_t, T) dE_r dE_t = g(T) \quad (1.5)$$

and

$$\sum_{n=0}^{N_{\max}} \gamma(n) f_v(n, T_v) = g_v(T_v). \quad (1.6)$$

Thus, the initial problem is reduced to solving two equations of a simpler form. It should also be noted that we can integrate the left-hand side of Eq. (1.5) in terms of rotational energy. After substitution of the variable this equation acquires a form similar to the Fredholm equation of the first kind. The problem of seeking for its solution belongs to the class of ill-posed inverse problems, which can be solved by using regularization algorithms and data based on the physical analysis of the problem [7,8]. The same algorithms can be used to solve Eq.(1.6).

References used:

- 1a. Kuznetsov N.M. Teoreticheskaja i Eksperimental'naja Himija. 1971. V.7. No 1. P.22. (In Russian).
- 1b. Physical and Chemical Processes in Gas Dynamics: Cross Sections and Rate Constants for Physical and Chemical Processes. Vol.1. Ed. by G.G.Chernyi et al. //Progress in Astronautics and Aeronautics. 2002. Vol.196.
2. Stupochenko E.V., Losev S.A., Osipov A.I. Relaxation Processes in Shock Waves. Springer-Verlag, Berlin. 1967.
3. Kuznetsov N.M. Kinetics of Unimolecular Reactions. Nauka. Moscow. 1982. (In Russian).
4. Josyula, Bailey. J. of Thermophysics and Heat Transfer. 2001. V.15. No.2. P. 157-167.
5. Krivonosova O.E., Shatalov O.P. Chem. Phys. Reports. 2000. V.18. No. 9. P. 1621-1630.
6. Ibraguimova L.B., Smekhov G.D., Shatalov O.P. Fluid Dynamics. 1999. V. 34. No. 1. P. 153-157.
7. Groetsch C.W, The Theory of Tikhonov Regularization for Fredholm Equations of the First Kind, Research Notes in Mathematics 105, Pitman, Boston, 1984.
8. Tikhonov A.N. and Arsenin V.A., Solution of Ill-posed Problems. Winston & Sons, Washington, 1977.

3.2. Task 2. Investigation of gas-droplet flows.

Task 2. Investigation of gas-droplet flows 1st year

In terms of task 2 of the project, investigations within the framework of tasks 2.1, 2.2, 2.3, and 2.4 of the work plan were performed during the first year.

Task 2.1.1. Comparative analysis of methods for obtaining a gas-droplet flow. Designing of the test section.

Real (joint flight of Shuttle-MIR) and model [1,2] experiments show that the basic sources of contamination of the surface of space vehicles are jets of their control thrusters, containing products of poor combustion (droplets) propellants. Thus, the maximal angles of dispersion of droplets significantly exceed 90° from the jet axis, i.e., back flows occur.

The elements of the space vehicle surfaces exposed to the exhaust plume of the control thrusters experience mechanical, physical and chemical impacts, which are a definitely negative factor for them. The existence of cold surfaces (even those beyond the flow field) may cause secondary processes of condensation and makes the contamination zone even larger.

Drainage devices and propellant refueling systems are also supplementary sources of contamination of space vehicles.

Despite a certain interest in this problem, the number of papers concerning the outflow of fluids and gas-liquid mixtures into vacuum is extremely limited [3-6]. For the most part, they deal with water exhaust into vacuum. It was found that injection of water and other fluids possessing rather high pressure of saturated vapors at room temperature into vacuum leads to jet bursting accompanied by the formation of a disperse plume of droplets of different sizes and vapor fractions. Therefore, an increase in the initial water temperature, nozzle diameter, and initial gas fraction results in earlier destruction of the jet (at a closer distance from the nozzle) [4].

As for the papers [1,2] they deal with the study of real thrusters with small thrust (from 5 N up to 66 N) in a vacuum chamber. Extensive information on the jet flow structure including the droplet phase behind this thruster was obtained. Small droplets ($\varnothing = 2.5 \mu\text{m}$), large droplets ($\varnothing = 10\text{-}20 \mu\text{m}$), and very large droplets ($\varnothing = 100\text{-}500 \mu\text{m}$) shed from the exit edge of the nozzle were observed in experiments.

The principal aim of the work executed at the Institute of Thermophysics in Quarter I consisted in elaborating the concept of gas-droplet flow organization in vacuum as applied to objectives of the Project and developing a test section for obtaining a gas-liquid flow with a required range of operation conditions based on this concept.

This concept was justified, and design documentation based on the conception was developed for two variants of the test section. A brief description of these test sections is given below.

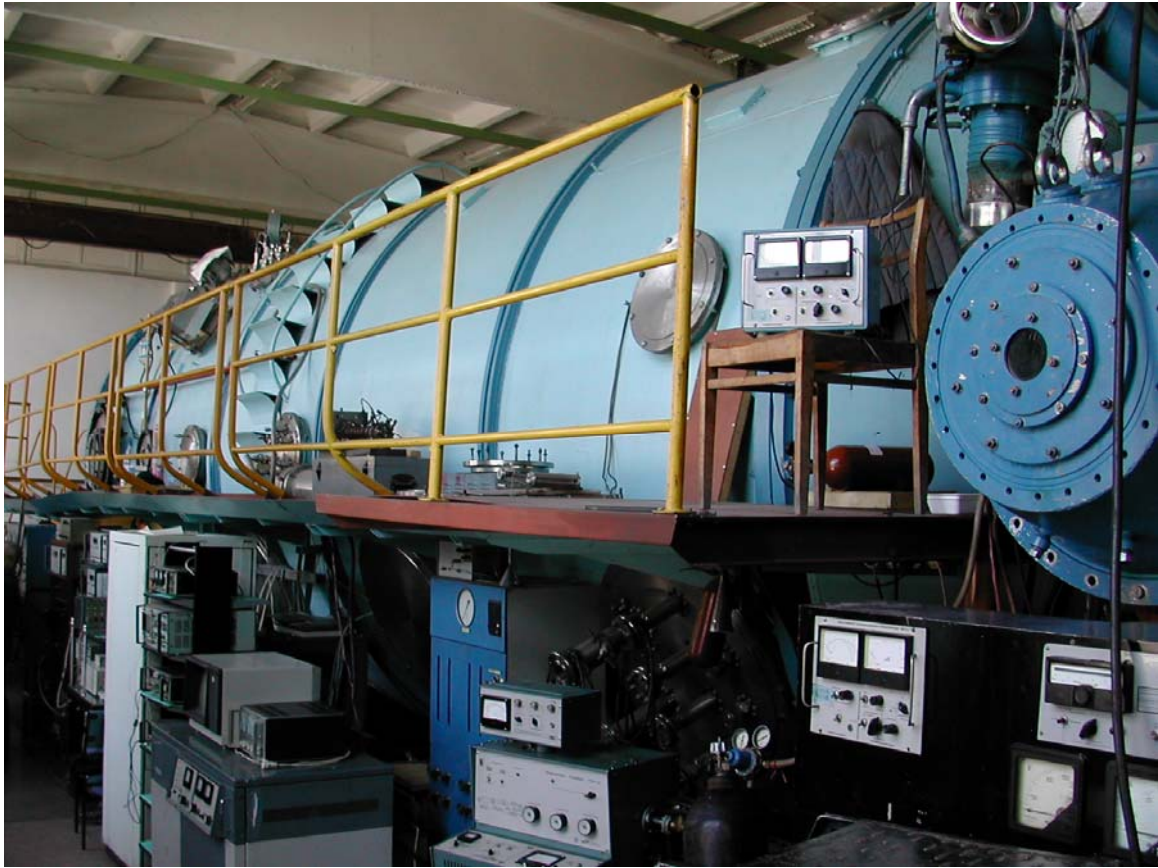


Fig. 2.1. General view of the VIKING facility of the Institute of Thermophysics SB RAS

Comparative analysis of methods for obtaining a gas-droplet flow in vacuum

There are two main methods of obtaining a gas-droplet flow in vacuum. In the first method, let us call it volumetric, the gas-droplet flow is obtained by spraying the liquid, for example, using an injector, in the plenum chamber of the nozzle and further mixing of drops with the carrier gas flow. In this case, the major part of the liquid enters the gas flow and only a small part hits the wall of the nozzle or device.

In the second method, let us call it the film method, the gas-droplet flow is formed by interaction of a cocurrent gas flow with the near-wall liquid film, partly in the nozzle, but mainly due to the decay of the liquid film at the nozzle exit.

Although dispersion of fuel components is used in real control thrusters of space vehicles, this method of obtaining the gas-droplet flow is not attractive for objectives of the present project. The question is, that, as is shown in [2, 7], the main contribution to the formation of a contaminating backflow is made by relatively large droplets, whose formation is caused by near-wall liquid film decay at the nozzle exit. The central part (core) of the jet does not participate in backflow formation, although it introduces independent scientific concern. Based on the above reasoning, at the given stage of studies, the choice was made in favor of the film method of obtaining the gas-droplet flow in vacuum.

Now, there are a lot of papers that study, primarily, the so-called gravitation films, i.e., films flowing under the action of gravitation forces. The results of these works can be found, for example, in [8].

A considerably smaller number of articles deal with fluid films with a co-current gas flow, and rather low, obviously subsonic speeds of the co-current gas flow are considered there. Moreover, there are practically no works on fluid films in the presence of a supersonic co-current

gas flow. Nevertheless, available publications, both on gravitation films and on films with a co-current gas flow, contain information beneficial for designing a test section for obtaining a gas-droplet flow in vacuum. Thus, it was shown that for thin films ($\delta_{\text{film}} \leq 100 \mu\text{m}$), the flow in the film becomes unstable from a certain moment, which results in its breaking down with the formation of rivulets. As a result, at the nozzle exit, we have a system of rivulets instead of a film homogeneous over its circumference. According to estimations, this regime is possible if the near-wall liquid film is supplied into the subsonic part of the nozzle (into the stagnation chamber). Therefore, simultaneously with the development of the test section with feeding of the liquid film into the stagnation chamber, which looks quite natural, another concept of generating the film with adjustable parameters (first of all, thickness and homogeneity) in the output section of the nozzle was developed. In the second variant, it was decided to obtain the near-wall film by feeding the fluid into the supersonic part of the nozzle, comparatively close to the nozzle-exit section.

A specification statement for both variants of designed constructions of the test section is given below.

Test section with the supply of the near-wall liquid film into the subsonic part of the nozzle (variant 1)

A sketch of this variant of the test section is shown in Fig. 2.2. The basis of the test section with a circular supply of the fluid into the stagnation chamber is body 15. A slot approximately 0.1 mm wide is formed by the wall of body 15 and bush 13, the fluid being fed onto the stagnation-chamber wall through this slot. The slot is closed up by a special circular valve opened by means of an electromagnet. The valve is sealed by packing rubbers 16, 17 and a membrane. At the top, the body of the test section is joined to the body of electromagnet 23 through adapter 21. Spring 18, which closes the valve when there is no voltage on the coil of the electromagnet, is located in the adapter. The adapter and the body of the test section together with elements of the valve and bush 13 form the stagnation chamber. Through the pipe of the adapter, the stagnation chamber is attached to a pneumatic valve that opens feeding of the compressed gas. Measuring washer 19 between the pneumatic valve and stagnation chamber serves for sustaining the required stagnation pressure of the gas.

To prevent electric breakdowns during operation of the electromagnet at low pressure, the cavity where the coil of the electromagnet is located is sealed and connected to the atmosphere through tube 6 in cover 2. Spacer 7 limits electromagnet armature motion. Bush 13 helps in obtaining a uniform distribution of the liquid on the stagnation-chamber wall. Removable tips (nozzles, cylindrical tubes) can be screwed into the body of the test section from below or inserted in and fastened by a coupling nut. Unions 12 are welded at the side of the body to connect the source to the fluid feeding line and remove air occurring in the line. Plates 9 are designed for fastening the diagnostic sensors.

Test section with feeding of the liquid into the supersonic part of the nozzle (variant 2)

A drawing of this variant of the test section is shown in Fig. 2.3. A thin channel (about 1 mm in diameter) parallel to the nozzle axis is drilled in the supersonic part of nozzle 5. The liquid is supplied into the channel from the side through union 6, which is joined to an electromagnetic opening valve in the hydraulic feeding line. The nozzle is connected to the pneumatic valve of the pressure gas line by means of spacer tube 2 and coupling nut 1.

Systems of feeding and measuring of liquid and gas consumption

The principal draft of the test section together with systems of feeding and measuring of liquid and gas consumption is shown in Fig. 2.4. Test section 1 is mounted inside vacuum chamber 15 of the VIKING facility.

Electromagnetic valve 5 opens the feeding of the gas from the pressure pipeline through measuring washer 4 into the stagnation chamber of the nozzle.

The liquid is fed into the source after opening of the circular valve or the valve of the hydraulic feeding line with the help of plunger 13 displacing the liquid from the cylinder. The flow rate is regulated by changing the velocity of plunger motion. The velocity of plunger motion is controlled by varying the spacing interval D on a circular table, which is set into motion by electric motor 14. When the plunger returns to the original position, the cylinder is filled by the liquid through an inlet orifice being opened, and the volume of the discharged liquid is determined by the change in the liquid level in measuring tube 9. Drain valve 10 is intended for pressure release in the line. Faucet 2 is intended for air removal during priming the mainline of liquid feeding.

To measure the liquid pressure and gas pressure in the stagnation chamber, transducers 6 and 12 are mounted. Their power supply is performed from a low-voltage source of direct current 8. The readings of the transducers are registered with the help of X-Y-plotter 7.

The opening and closing of the pneumatic valve and circular valve, plunger motion, and pressure release in the liquid feeding line are controlled by control unit 11, which defines the sequence of their switching on and turn-off times.

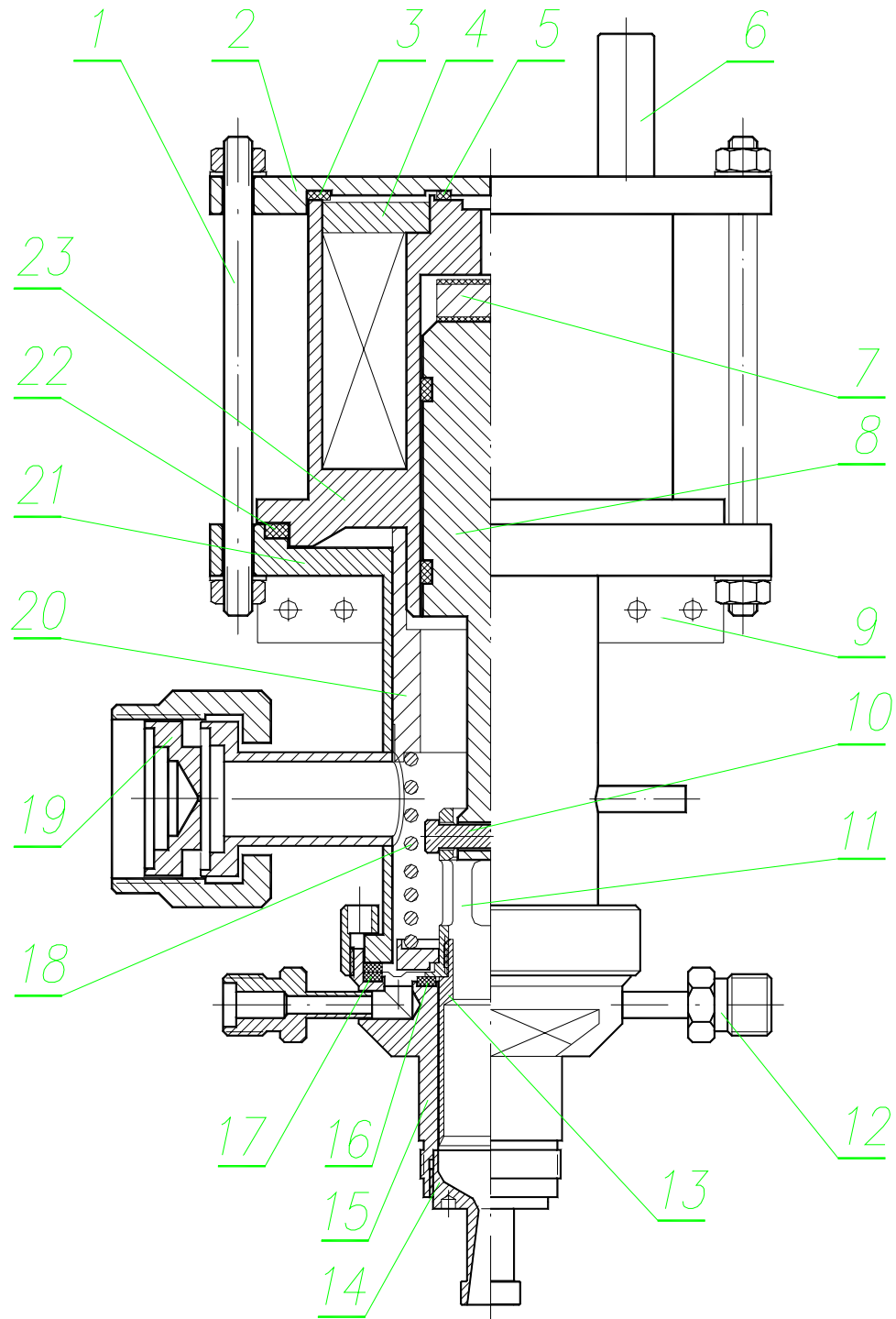


Fig. 2.2. Layout of the test section (variant 1).

1 – stud, 2 – cover, 3 – gasket, 4 – flange, 5 – gasket, 6 – tube, 7 – spacer,
 8 – electromagnet armature, 9 – plate, 10 – pin, 11 – coupling, 12 – union,
 13 – bush, 14 – nozzle, 15 – body, 16 – gasket, 17 – gasket, 18 – spring,
 19 – diaphragm, 20 – sleeve, 21 – adapter, 22 – gasket, 23 – electromagnet body.

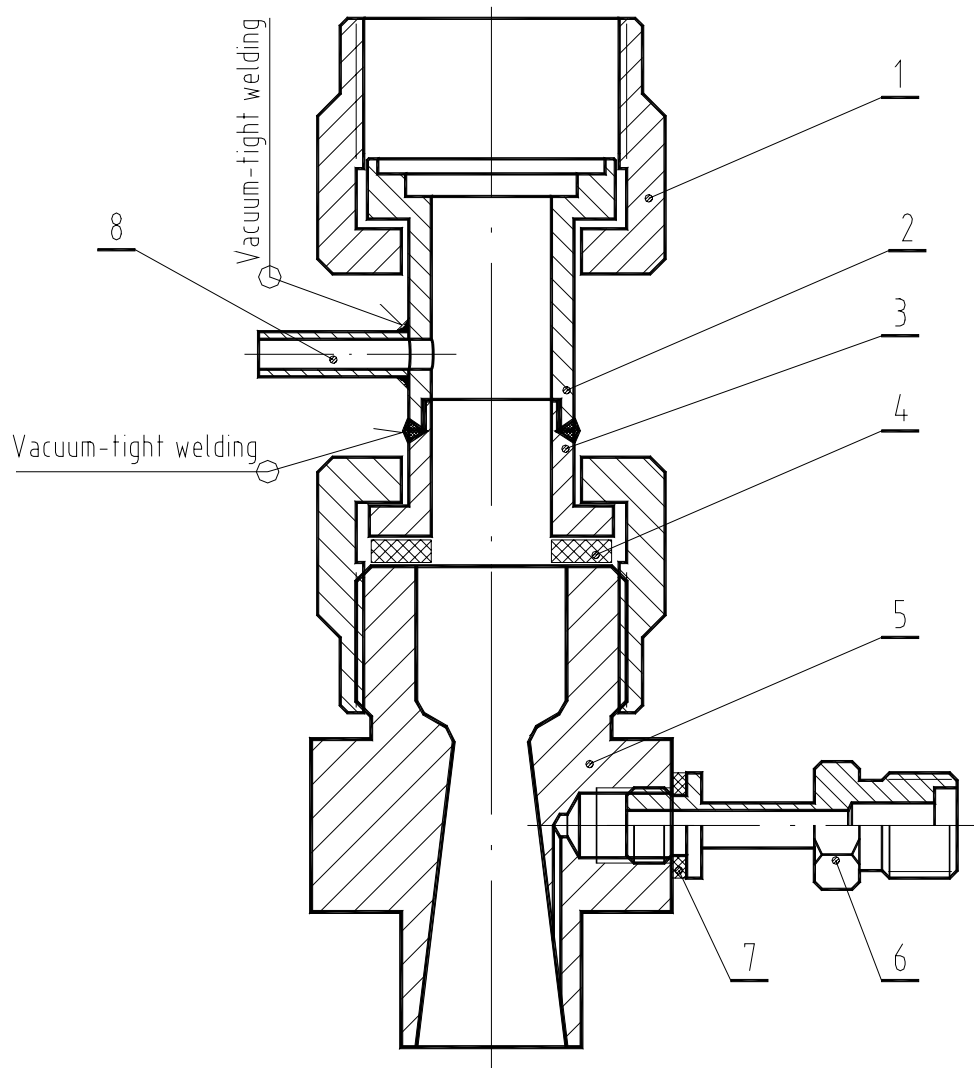


Fig. 2.3. Test section (variant 2).

1 – coupling nut, 2 – tube, 3 – tube, 4 – gasket, 5 – nozzle,
6 – connecting tube, 7 – gasket, 8 – tube.

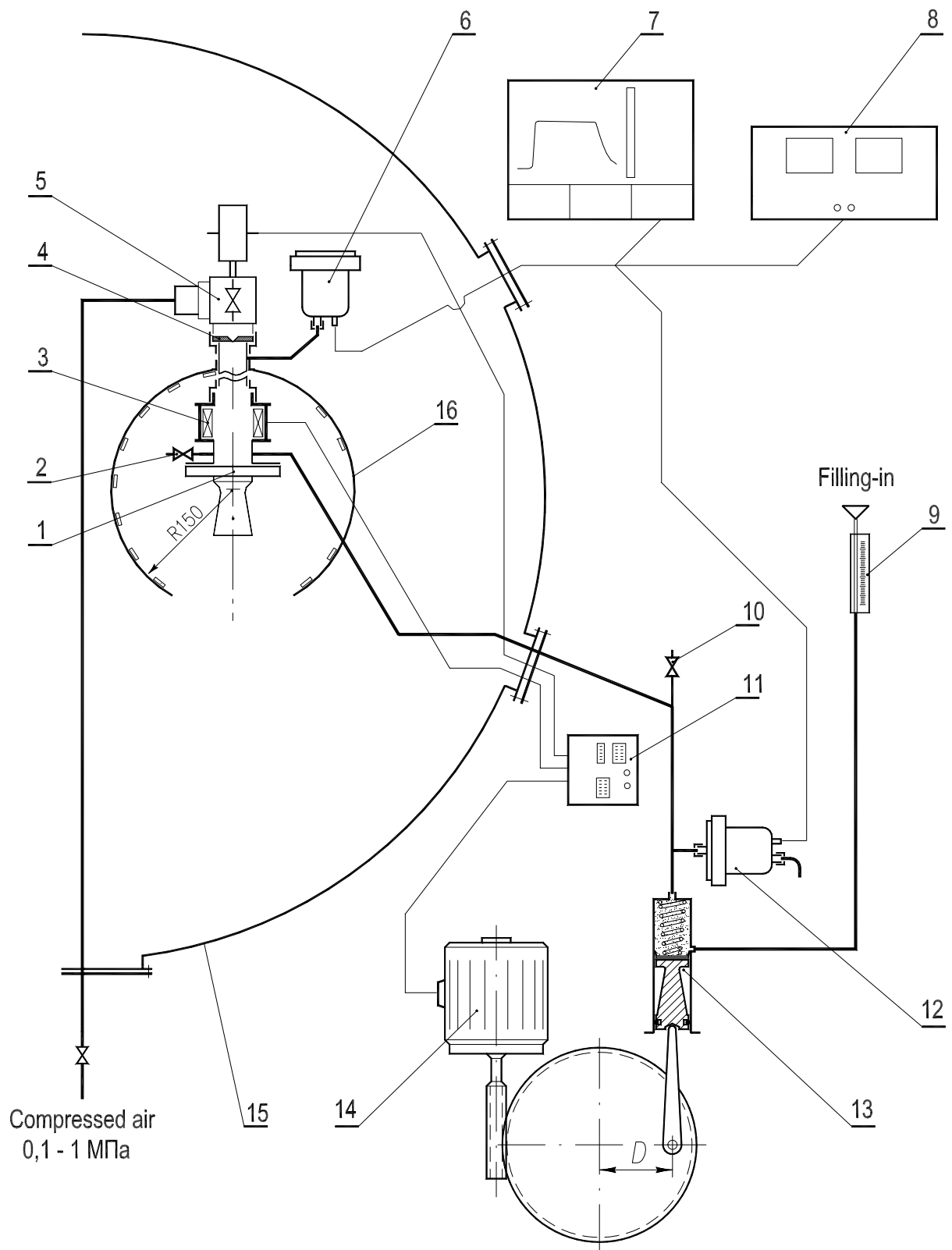


Fig. 2.4. Scheme of gas and liquid supply into the tests section.

- 1 – test section, 2 – valve, 3 – electromagnet, 4 – diaphragm, 5 – pneumatic valve, 6 – pressure transducer, 7 – X-Y-plotter, 8 – power supply, 9 – measuring tube, 10 – drain valve, 11 – control unit, 12 – pressure transducer, 13 – plunger, 14 – electric motor, 15 – vacuum chamber, 16 – QMB transducers.

Task 2.1.2. Manufacturing and calibrating of the test section

Photos of the manufactured test sections and exchangeable exit channels (supersonic nozzles and tubes) are shown in Figs. 2.5-2.7.

Before calibration, the test sections were alternatively mounted into the VIKING vacuum chamber. During calibration, the following parameters were measured:

- gas pressure P_0 in the stagnation chamber (stagnation pressure) – using an IKD sensor;
- pressure in the pipeline of liquid supply – using an IKD sensor;
- pressure in the VIKING vacuum chamber – using the BARATRON appliance;
- quantity of the liquid in one start Δh ;
- delay of appearance of the liquid at the inner surface of the channel – by means of videoshooting of the outflow process using a Canon XM1 video camera.

The measurements were carried out in a pulsed mode. The pulse duration was approximately several seconds. The ranges of regime parameters were chosen in accordance with the objectives of the project and possibilities of the VIKING facility. Air was used as a test gas, and ethanol was used as a test liquid. Consumptions of the gas G_g and liquid G_l could be chosen independent of each other. Typical records of the pressure sensors for one of the calibration regimes of the test section with circular supply of the liquid film (experiment dated 25.09.2002) are given in Figs. 2.8-2.10. Readings of all sensors were fed into a computer. The computer, through the control unit, also controlled the time of switching on and switching off the valves of gas and liquid feeding and the time of their operation. The usual times of liquid and gas feeding were 4 and 5 s, respectively. The readings of sensors, shown in Figs. 2.8-2.10, give a clear idea about the time-dependent behavior of the main parameters of the test section and the pressure in the vacuum chamber during the pulse. It is seen in Fig. 2.10, for example, that the pressure in the VIKING chamber increases approximately by two orders of magnitude during one pulse (about 5 s) for gas consumption of about 30 g/s (close to maximum).

The delay time (time of appearance of the liquid film at the exit edge of the channel) was registered using the video camera. Synchronization between videoshooting and the moment of switching on the test section was provided by means of an LED.

Results of calibration of the test sections are presented in the test protocol. In the protocol, it is possible to see that gas consumption may vary from 0 to 33 g/s, and liquid consumption from 0 to 0.7 g/s. These ranges of variation of regime parameters ensure fairly wide possibilities for experimental investigation of gas-droplet flows into vacuum.

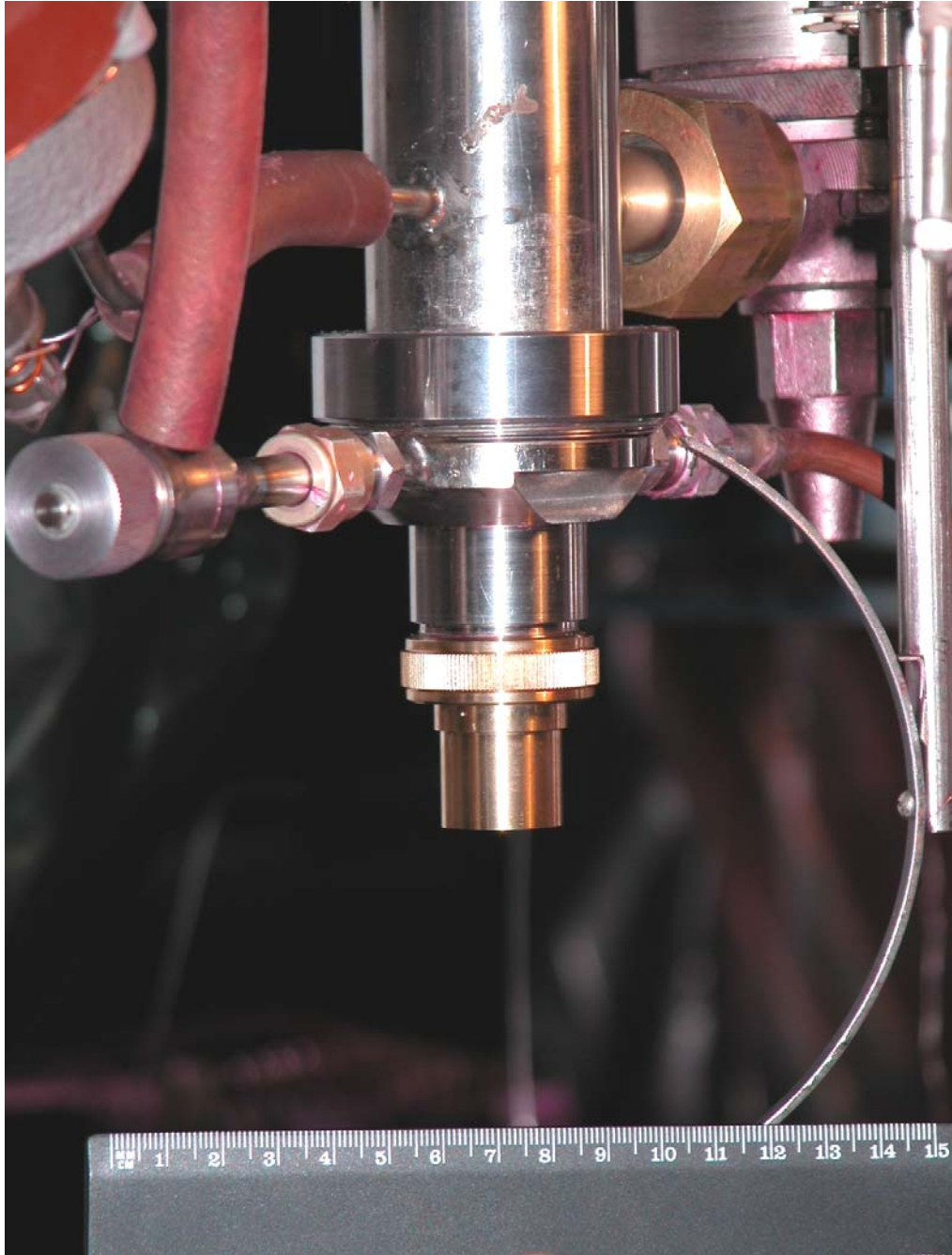


Fig. 2.5. Test section (variant 1)



Fig. 2.6. Exchangeable exit channels



Fig.2.7. Nozzle with pointwise feeding of the liquid (test section, variant 2)

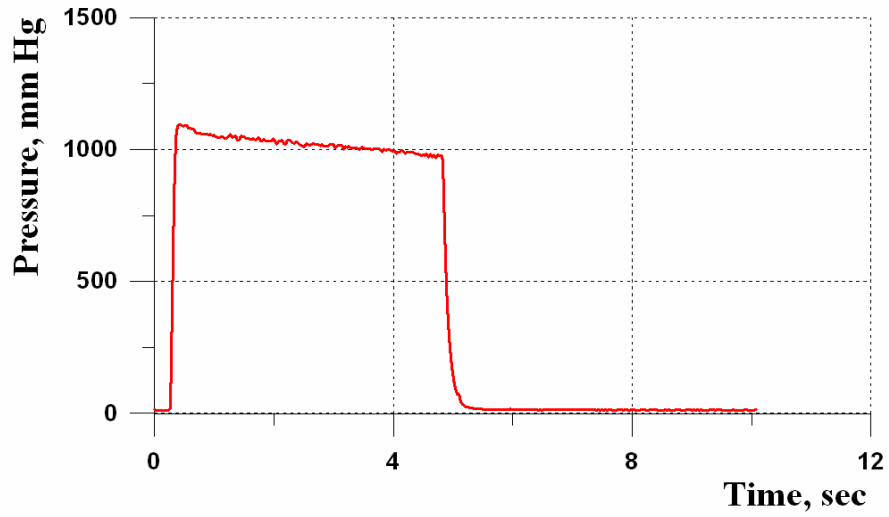


Fig. 2.8. Record of gas pressure in the stagnation chamber

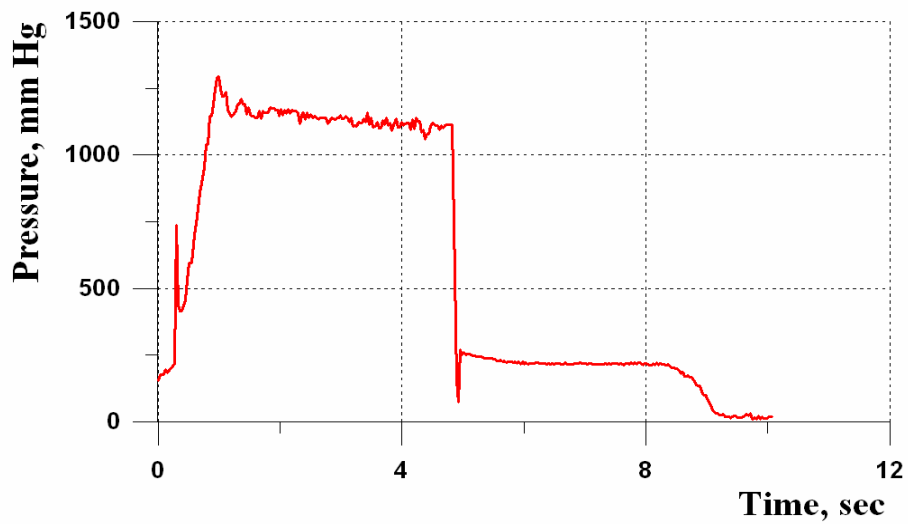


Fig.2.9. Record of pressure in the pipeline of feeding the liquid

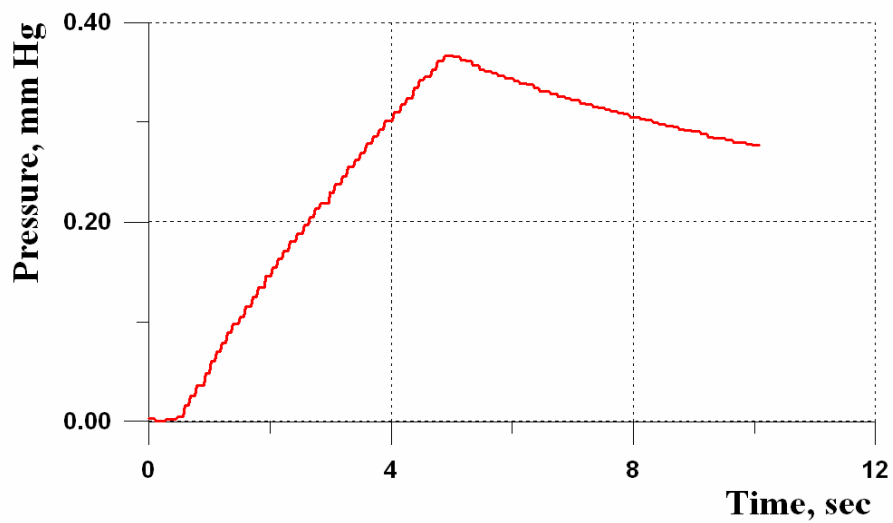


Fig. 2.10. Record of pressure in the vacuum chamber

PROTOCOL
of calibration of the test sections for obtaining
the gas-droplet flow in the VIKING facility

Test section (variant 1)

| № | Date | P ₀ , Pa | G _g , g/s | Δh, mm | G _l , g/s | Exit channel |
|----|----------|----------------------|----------------------|--------|----------------------|--------------------------|
| 1 | 02.09.02 | 3.66·10 ⁴ | 7.05 | 40 | 0.51 | Tube, Ø 10 mm |
| 2 | 03.09.02 | 3.32·10 ⁴ | 6.43 | 39 | 0.49 | Tube, Ø 10 mm |
| 3 | 05.09.02 | 2.93·10 ⁴ | 5.66 | 41 | 0.50 | Tube, Ø 10 mm |
| 4 | 09.09.02 | 1.33·10 ⁴ | 2.57 | 42 | 0.54 | Tube, Ø 10 mm |
| 5 | 10.09.02 | 3.99·10 ³ | 0.77 | 44 | 0.57 | Tube, Ø 10 mm |
| 6 | 13.09.02 | 0 | 0 | 45 | 0.58 | Tube, Ø 10 mm |
| 7 | 16.09.02 | 3.65·10 ⁴ | 7.02 | 38 | 0.39 | Supers. nozzle, d* 10 mm |
| 8 | 16.09.02 | 1.22·10 ⁵ | 7.03 | 33 | 0.34 | Tube, Ø 5 mm |
| 9 | 17.09.02 | 1.23·10 ⁵ | 7.08 | 32 | 0.33 | Tube, Ø 5 mm |
| 10 | 18.09.02 | 3.05·10 ⁴ | 1.77 | 35 | 0.36 | Tube, Ø 5 mm |
| 11 | 19.02.02 | 1.52·10 ⁴ | 0.89 | 34 | 0.35 | Tube, Ø 5 mm |
| 12 | 20.09.02 | 1.13·10 ⁵ | 25.60 | 29 | 0.37 | Supers. nozzle, d* 10 mm |
| 13 | 23.09.02 | 1.55·10 ⁵ | 32.58 | 26 | 0.33 | Supers. nozzle, d* 10 mm |
| 14 | 24.09.02 | 1.58·10 ⁵ | 33.23 | 52 | 0.67 | Supers. nozzle, d* 10 mm |
| 15 | 25.09.02 | 1.42·10 ⁵ | 29.86 | 55 | 0.71 | Supers. nozzle, d* 10 mm |
| 16 | 25.09.02 | 1.42·10 ⁵ | 29.86 | 0 | 0 | Supers. nozzle, d* 10 mm |

Test section (variant 2)

| № | Date | P ₀ , Pa | G _g , g/s | Δh, mm | G _l , g/s | Exit channel |
|---|----------|----------------------|----------------------|--------|----------------------|--------------------------|
| 1 | 26.09.02 | 1.22·10 ⁵ | 23.61 | 15 | 0.12 | Supers. nozzle, d* 10 mm |
| 2 | 26.09.02 | 1.22·10 ⁵ | 23.61 | 0 | 0 | Supers. nozzle, d* 10 mm |
| 3 | 27.09.02 | 2.72·10 ⁴ | 5.24 | 10 | 0.08 | Supers. nozzle, d* 10 mm |
| 4 | 30.09.02 | 1.36·10 ⁴ | 2.62 | 8 | 0.06 | Supers. nozzle, d* 10 mm |
| 5 | 30.09.02 | 0 | 0 | 18 | 0.14 | Supers. nozzle, d* 10 mm |

Task 2.2. Developing of the combined Navier-Stokes/DSMC approach for simulation of gas flow inside the nozzle and in near vicinity of the nozzle exit plane.

To simulate weakly rarefied gas flows, the existing programs for solving the Navier-Stokes equations were modified (task 2.2.1). The initial set of programs is based on the use of advanced TVD (total variation diminishing) schemes. The inviscid fluxes at the boundaries of the computational cells are calculated with the third-order accuracy from the approximate solution of the Riemann problem, and second-order central differences are used to approximate viscous fluxes. Integration in time is performed with the help of explicit Runge-Kutta schemes. The codes were modified to include the boundary conditions of velocity slip and temperature jump, which have to be used in simulating flows with rarefaction effects. For verification of the computational programs developed, test computations were performed, and comparisons were made with the data obtained without allowance for slip conditions and with the results of the DSMC computations. The results obtained were also compared to experimental data available in the literature for several problems including significant rarefaction effects: 1) flow past a flat plate with a free-stream Mach number $M = 21$; 2) laminar separated flow above a hollow cylinder-flare configuration ($M=9.91$), and 3) low-density flow inside a supersonic nozzle. In all cases, the numerical and experimental results were in good agreement.

A combined approach to numerical simulation of gas flows inside the nozzle and in the vicinity of its exit cross section was developed (task 2.2.2). The approach is based on dividing the flowfield into domains, where, respectively, the Navier-Stokes equations with velocity slip boundary conditions and the DSMC method are used. The flowfields obtained by the numerical solution of Navier-Stokes equations are used as the initial data for the program of modeling rarefied gas flows by the DSMC method. To implement this zonal approach, an interface was developed, which allows the user to prepare distributions of gas-dynamic quantities in a certain cross section (usually, at a small distance upstream of the nozzle-exit cross section) to be further used in the Smile++ software system.

Task 2.3.1. Analysis of the possibility of using electron-beam diagnostics for density measurements in a gas-droplet flow. Calibration experiments

Analysis of the possibility of using electron-beam diagnostics for density measurements in a gas-droplet flow

The electron-beam method is now one of the basic methods in rarefied gas flow research. The main idea of this method consists in the analysis of processes accompanying the passage of the beam of fast electrons through the medium under study. Excitation of energy levels of molecules and atoms, dissociation, ionization, scattering of electrons on nuclei of atoms, and their deceleration in the Coulomb field of the nucleus results in occurrence of radiation in a wide spectral range, from infra-red up to X-ray. The method has a good spatial resolution (about 1 mm^3), allows determination of such parameters as density, partial concentration of components, translational temperature, temperature of internal degrees of freedom etc., and provides flow visualization in cross-sections considered.

Concerning the history of the question, it is necessary to note that the first practical steps in using an electron beam for diagnostics of gas flows were made in the early 60s of the last century.

Great attention to the development of this method was given at the Institute of Thermophysics SB RAS [9]. A comprehensive bibliography on electron beam diagnostics (455 titles) can be found in the review [10]; references to the appropriate works performed at the Institute of Thermophysics SB RAS are also given there.

Providing broad opportunities for examining gas streams, the electron-beam method has some particular restrictions. These restrictions have a physical nature and are caused by the

influence of collisional processes in the gas on excitation and radiation processes. The opportunities and restrictions of the electron-beam method are surveyed in more detail in [11].

It should be noted that practically all available publications concerning the use of the electron beam deal with investigations of low-density gas and gas-mixture flows.

In the present work, the attempt to analyze the possibilities of the electron-beam method for diagnostics of gas-droplet flows is undertaken for the first time. The presence of a condensed phase in the flow, in our case, a liquid-droplet phase, can essentially, depending on particular conditions, complicate the analysis of radiation-excitation processes caused by the passage of the electron beam through a gas-droplet medium.

The basic idea of the approach developed in the present work consists in a combined usage of optical and X-ray ranges of the spectrum excited by the electron beam in the examined flow.

As was mentioned in our previous reports, proceeding from the objectives and tasks of the Project and capabilities of experimental facilities, a mixture of air and ethanol was chosen as a model of a gas-droplet flow.

Let us consider interaction of an electron beam having an energy of about 20 keV with a rarefied flow of air containing drops of ethanol. When the electron beam of such energy passes through such a flow, radiation appears both in the optical and in X-ray (the short-wave boundary is near 0.5 Å) ranges of the spectrum.

The use of radiation excited by an electron beam in the optical area of the spectrum for diagnostic purposes implies a number of requirements to the choice of the spectral range. The optical transition chosen for measurements should ensure:

- sufficient intensity for maintaining a necessary accuracy;
- high probability of spontaneous radiation, i.e., small lifetime of the excited state; in this case, radiation processes are not disturbed by quenching collisions and the drift of luminescence is insignificant;
- no effect of secondary electrons on the population of the chosen energy level.

If these conditions are satisfied, the intensity of radiation for the chosen electron transition $j \rightarrow k$ is linearly related to the gas concentration n and the beam current i :

$$I_{jk} = A n \cdot i \quad (1.7)$$

where A is a constant determined from the calibration measurements.

Electron-beam excitation of the optical spectra of N_2 and O_2 molecules that are the basic components of air have been fairly well investigated. Optical transitions (spectral regions) recommended for density measurements can be found, e.g., in [10, 11]. For N_2 molecules, the 1st negative system of bands in the wavelength range near 3914 Å is usually used.

Thus, we can assume that the local density of air for the gas-droplet flow considered can be determined from the radiation intensity of N_2 molecules in the spectral range of 3914 Å. As to the contribution of other molecules (in our case, C_2H_5OH) in this spectral range, it is negligible, which is verified by the literary data and special methodical electron-beam experiments with ethanol vapor. It should be noted that, in accordance with the data of [12], the spectral range of 4861 Å (line H_β) can be recommended for density measurements of C_2H_5OH molecules in the vapor state.

Let us now analyze the opportunities of using the X-ray spectral region excited by an electron beam. Under interaction of fast electrons with atoms, there are two kinds of X-ray radiation: bremsstrahlung and characteristic ones.

Bremsstrahlung arises upon interaction of fast electrons with the Coulomb field of the atom nucleus. The energy spectrum of such radiation is continuous.

Characteristic x-ray radiation arises owing to shock ionization of internal electron shells of atom by fast electrons, for example, the K -shell, with subsequent emission of an X-ray quantum as an electron from an external level passes to a vacant place in this internal shell. Such radiation has a line spectrum.

Though both kinds of X-ray radiation can be used for diagnostic purposes, the use of characteristic radiation is not attractive for the task considered, since the energy levels of *K*-shells of H, C, N, and O atoms, which the molecules of air and ethanol consist of, are small. Thus, the energy of the *K*-level is 595 eV for the oxygen atom and even lower for other atoms. The low value of energy incurs difficulties for registration of characteristic X-ray spectra of the above-mentioned elements, which are usually called "light".

It is of interest for the purposes of the present work to use bremsstrahlung excited by the electron beam. The integral intensity of bremsstrahlung is

$$I = C \cdot Z^2 \cdot n \cdot i, \quad (1.8)$$

where Z is the atomic number of the chemical element of the target and C is a constant determined from calibration measurements.

Let us emphasize some features making, in our opinion, the use of bremsstrahlung attractive for rarefied gas flow diagnostics:

- the time of emission of the γ -quantum is smaller than 10^{-10} s; therefore, the upper limit of density measured by this method is an order and more higher than the corresponding limit with using the optical range of the spectrum excited by the electron beam;
- the measurement results in the X-ray range of the spectrum are free from the influence of temperature and degree of dissociation and ionization of the medium considered; therefore, the measurements of density in high-temperature (including plasma) flows are possible;
- the universal character of the dependence of bremsstrahlung intensity on the governing parameters (1.8) allows one to calculate calibration dependences for all gas media, including mixtures, if their atomic structure is known. Indeed, if for some gas, for example, nitrogen or air, the calibration dependence is experimentally obtained, i.e., the instrumental constant C is determined, this dependence can be recalculated for any other molecules or atoms in the same measurement geometry, using the value of Z^2 . This circumstance is the basic one, since it offers an opportunity to apply the electron X-ray method to study jets of liquid vapors and vapors of metals, for which it is practically impossible to obtain the calibration dependence of intensity of electron-beam excited radiation on density in a traditional manner under static conditions;
- dependence (1.8) is in good agreement with the data of experiments performed with thin metal foils [13], where the loss of energy of the beam of electrons is small. It can be assumed that, under certain conditions, dependence (1.8) is also valid for liquid drops; however, this certainly requires experimental verification.

The analysis shows that the combined measurements in the optical and X-ray ranges of the spectrum opens some prospects of the electron-beam method for diagnostics of gas-droplet flows.

Electron-beam diagnostic unit

To perform electron-beam measurements in gas and gas-droplet flows, an electron-beam diagnostic unit was assembled. The scheme of this unit is shown in Fig. 2.11 and includes the following basic functional systems:

- system of generation of the electron beam and measurement of its parameters;
- system of measurement of optical radiation;
- system of measurement of X-ray bremsstrahlung.

The systems listed above were mounted on a vacuum module connected through a vacuum gate with the VIKING facility.

The system of generation and measurement of the electron-beam parameters includes an electron gun with a two-stage differential pump system, focusing and deflecting systems, and a collector of electrons for measuring beam current. Typical parameters of the electron beam are the energy of electrons $E \approx 20$ keV and the beam current $i \approx 1$ -5 mA. The beam diameter is approximately equal to 1 mm.

The system of measurements of optical radiation includes a focusing lens, an SPM-2 monochromator, an FEU-39 photomultiplier, an IMT-05 amplifier, and a plotter.

The system of bremsstrahlung measurement includes a BDS-9-04 scintillation X-ray detector with a preamplifier and a BR-1 block of registration. Localization of X-ray measurements was carried out with the help of a plane-parallel slit (Soller's collimator) and was about 1 mm over the beam height.

The electron-beam measurements were performed in continuous and pulsed modes of facility operation. An analog-to-digital converter connected to a computer was used to maintain a desired time resolution.

In pulsed regimes, the radiation-intensity profiles are recorded in the following manner. A measurement point is selected, for example, on the jet axis, the electromagnet valve feeds the gas into the nozzle, and the time dependence of the radiation intensity is measured at a time constant of 0.1 s. The valve and recording instruments are triggered simultaneously. The measurement point is then shifted along the jet axis (for recording the axial density profile) or transversely to it (for recording the transverse density profile), and a new oscillogram is recorded. In order to check the reproducibility of the exhaust regimes, pressure oscillograms for the plenum chamber of the nozzle are recorded. The beam current and the pressure value in the vacuum chamber are monitored in these measurements.

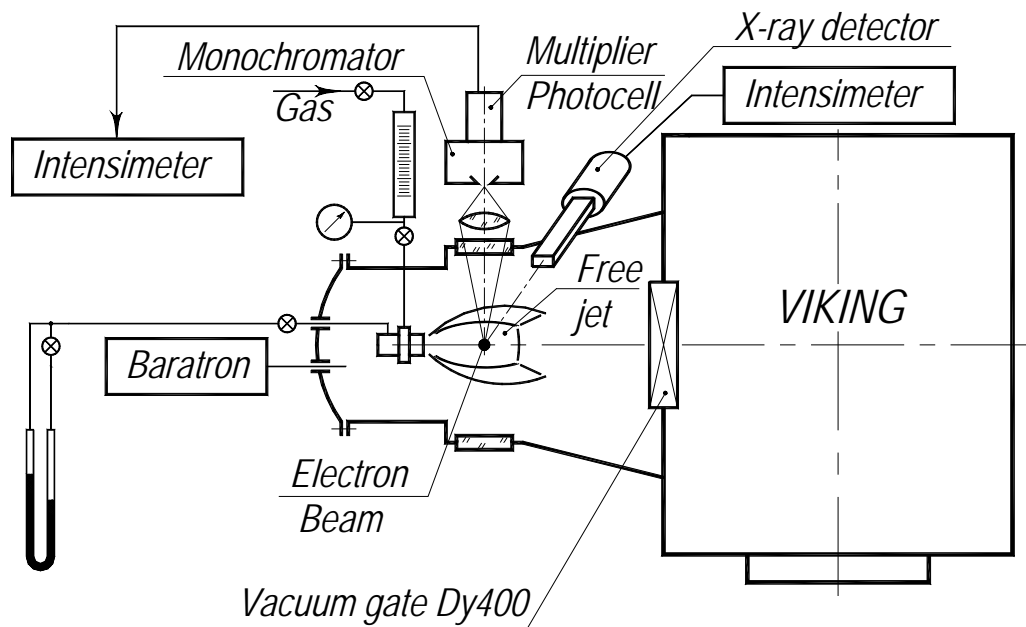


Fig. 2.11. Schematic of the electron-beam diagnostic unit

Source for methodical and calibration experiments

As the experiments on application of an electron beam for gas-droplet flow diagnostic have a research character, various variants and schemes of sources for creating liquid-droplet flows in vacuum were analyzed. Finally, it was decided at the given stage to use the variant with ethanol outflow into vacuum from a convergent conic nozzle (the total cone angle was 15°) with an exit diameter of 0.2 mm. Such a source provided a rather stable thin liquid jet during a time sufficient to register density profiles across the jet with the help of an electron beam. The source was placed on a three-component traversing gear located inside the vacuum chamber and could be moved with a given speed relative to the motionless electron beam. Ethanol was fed with a flow rate of about 0.37 g/s to the nozzle from a vessel under excess pressure. The following quantities were measured in the experiments:

- current of the electron beam;
- pressure in the vacuum chamber (using the BARATRON device);
- intensity of bremsstrahlung;
- intensity of optical radiation.
-

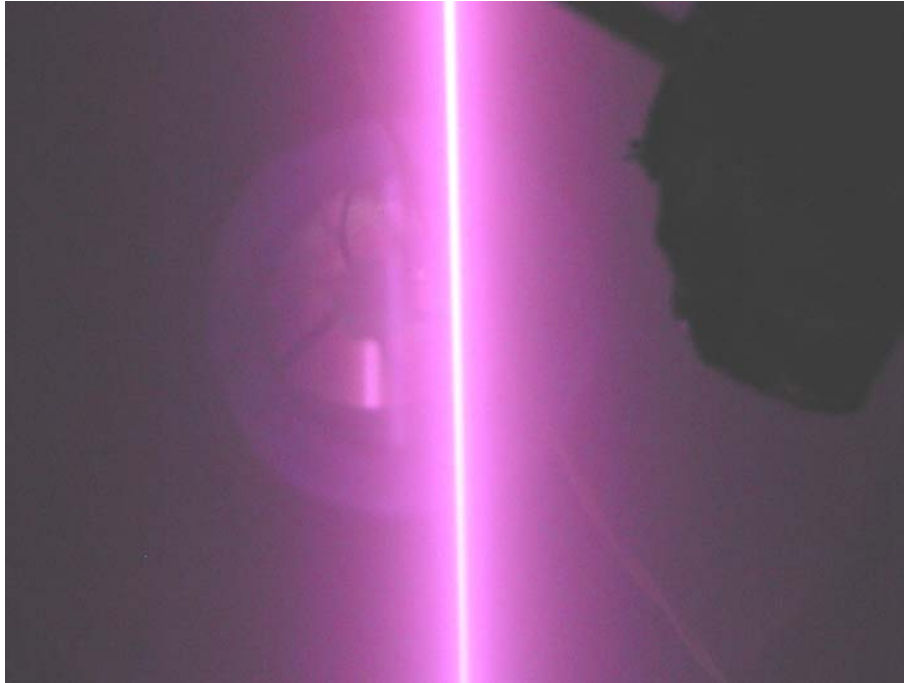


Fig. 2.12. Electron beam in stagnant air

Videoshooting and photographing of the electron beam and the process of its interaction with the liquid jet were also carried out in the experiments. For example, Figs. 2.12 and 2.13 show the photo of the electron beam in stagnant air and the photo of interaction of the electron beam with the ethanol jet, respectively.

The transition from the measured values of radiation intensity (in optical and X-ray ranges of the spectrum) to real values of density was performed with the help of calibration dependences obtained under static conditions. The calibration procedure consists in the following. The vacuum chamber VIKING was pumped out down to an extremely low pressure, further it was disconnected from the vacuum-pump system by closing the vacuum gates, and the given amount of ethanol was injected into the chamber. After evaporation, ethanol created a required pressure of its vapor in the chamber. The ethanol-vapor temperature was assumed to be room temperature. Further, after the pressure in the chamber became constant, the intensity of radiation of ethanol vapor in the chamber, excited by an electron beam in optical and X-ray ranges of the spectrum, were recorded.

Results of experiments and their analysis

First, we analyze the calibration dependences. The calibration dependence for air in the X-ray spectral range is shown in Fig. 2.14. It is seen that the bremsstrahlung intensity normalized to the beam current is linear within the measured range of concentrations. The result obtained could be expected and does not require additional comments.

The calibration dependence for ethanol vapors in the X-ray range was obtained experimentally, according to the technique described above, and theoretically, by recalculation of the calibration dependence for air (Fig. 2.14) to ethanol with the use of expression (1.8):

$$\frac{I_{C_2H_5OH}}{I_{air}} = \frac{2 \cdot z_C^2 + 5 \cdot z_H^2 + z_O^2 + z_H^2}{0.78 \cdot 2 \cdot z_N^2 + 0.22 \cdot 2 \cdot z_O^2} = \frac{2 \cdot 6^2 + 5 \cdot 1^2 + 8^2 + 1^2}{0.78 \cdot 2 \cdot 7^2 + 0.22 \cdot 8^2} \approx 1.36 \quad (1.9)$$

From (1.9), it follows that, for identical concentrations, beam currents, and measurement geometry, the intensity of bremsstrahlung of ethanol molecules is 1.36 times that of air molecules. A comparison of experimental and theoretical calibration dependences, which are given in Fig. 2.15, shows their good correlation.

The calibration dependence of radiation intensity for ethanol vapors in the optical range is plotted in Fig. 2.16. With increasing concentration, the intensity becomes more and more different from the linear dependence, which corresponds to the existing concepts. According to [11], the transition lifetime for H_β (4861 Å) is $2 \cdot 10^{-7}$ s. The corresponding theoretical limit of concentration when the time between molecular collisions becomes equal to the lifetime of the excited state is about $5 \cdot 10^{15} \text{ cm}^{-3}$. In other words, the calibration dependence should be nonlinear for $n > 10^{15} \text{ cm}^{-3}$ and can be approximated by a straight line for $n < 10^{15} \text{ cm}^{-3}$.

Now let us consider the measurement results of transverse density distributions in the ethanol jet. These distributions are shown in Figs. 2.17 and 2.18, based on the measurement results in the optical range of the spectrum for $x = 15$ mm (x is the distance from the nozzle exit) and in the X-ray range for $x = 12, 15, 30,$ and 50 mm.

The main difference, which follows from a comparison of these figures, consists in the maximum value of density. For X-ray measurements, the density is more than two orders higher than the density of optical measurements. Since only molecules in the vapor or gaseous state radiate in the optical range and molecules in any state radiate in the X-ray range, it is possible to assume that the increase in the signal in the X-ray range is caused by the influence of the droplet phase. At the same time, it is known that the value of n for liquid ethanol at room temperature is approximately 10^{22} cm^{-3} . The maximum value of n obtained by measurements (Fig. 2.18) is lower approximately by 3.5 orders of magnitude. Such a strong difference can be caused by several reasons.

First, it was mentioned above that the electron-beam method has a physical limit in terms of the density value. The time of emission of γ -quanta (life time) is about 10^{-10} s. The corresponding theoretical limit in density is approximately 10^{18} cm^{-3} . To use the electron-beam method for $n > 10^{18} \text{ cm}^{-3}$, we should take into account the influence of collisional processes on the processes of excitation and radiation in the x-ray spectral range. This can be done theoretically and experimentally in principle, but it is a serious physical problem. An additional difficulty is the necessity of considering the interaction of high-energy electrons with the medium in the liquid state.

Second, the data in Fig. 2.18 were obtained using the calibration dependence for ethanol (Fig. 2.15) under the assumption of the linear dependence at values of n higher than those shown in Fig. 2.15.

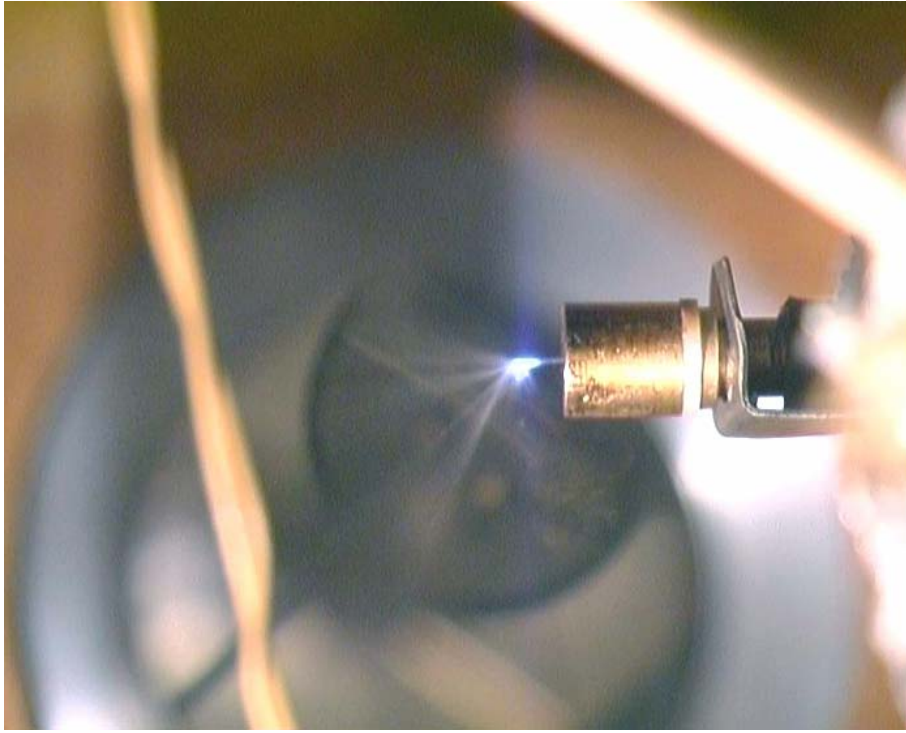


Fig. 2.13. Interaction of the electron beam with the ethanol jet.

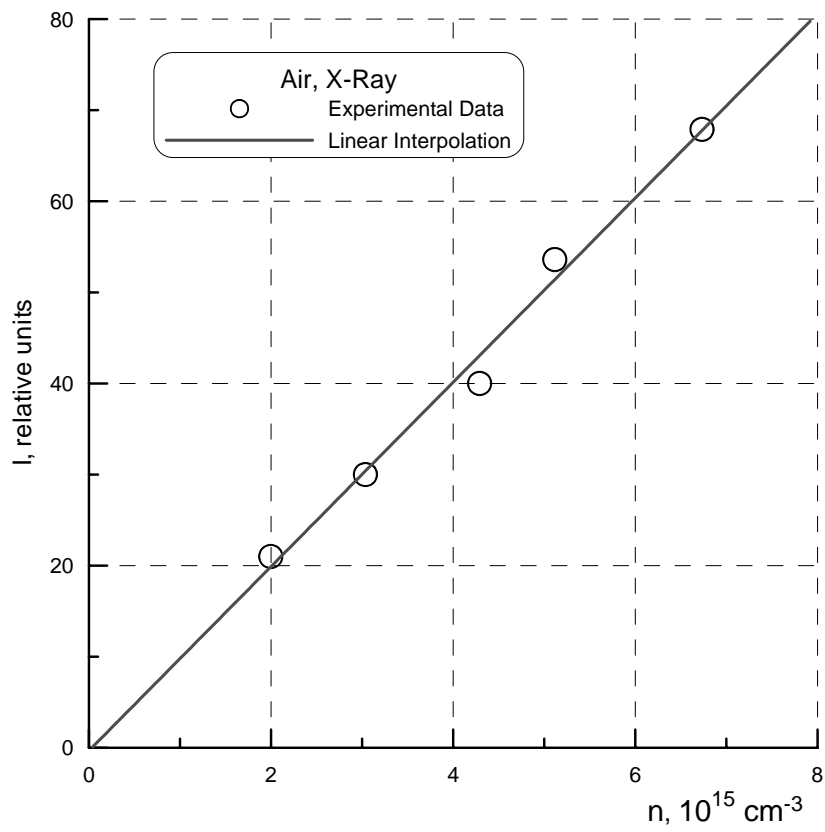


Fig. 2.14. Calibration dependence of bremsstrahlung intensity on air density

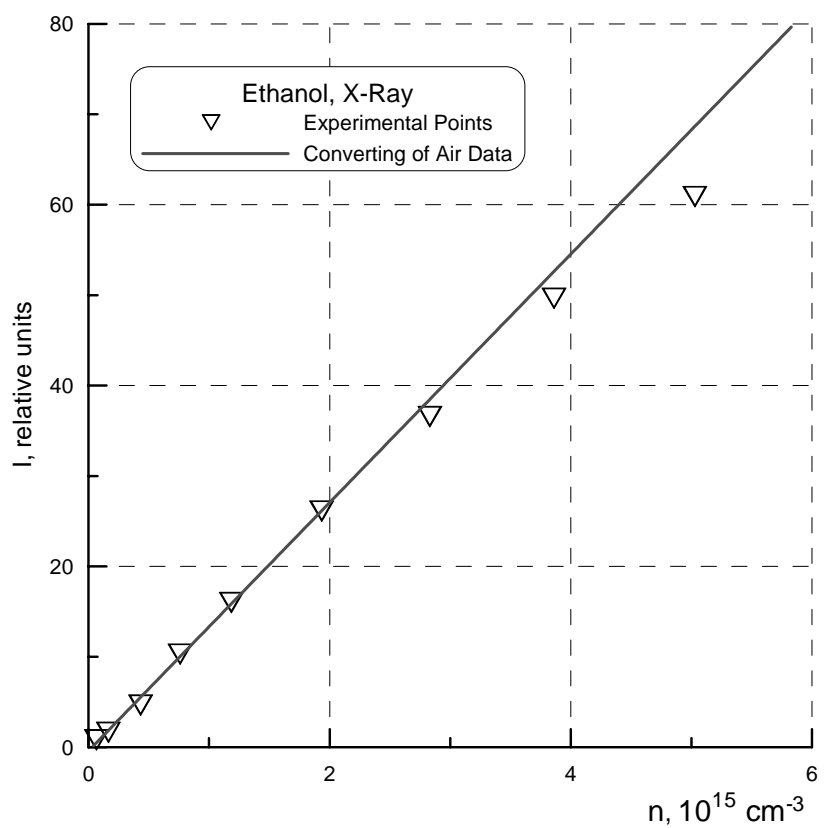


Fig. 2.15. Calibration dependence of bremsstrahlung intensity on ethanol vapor density

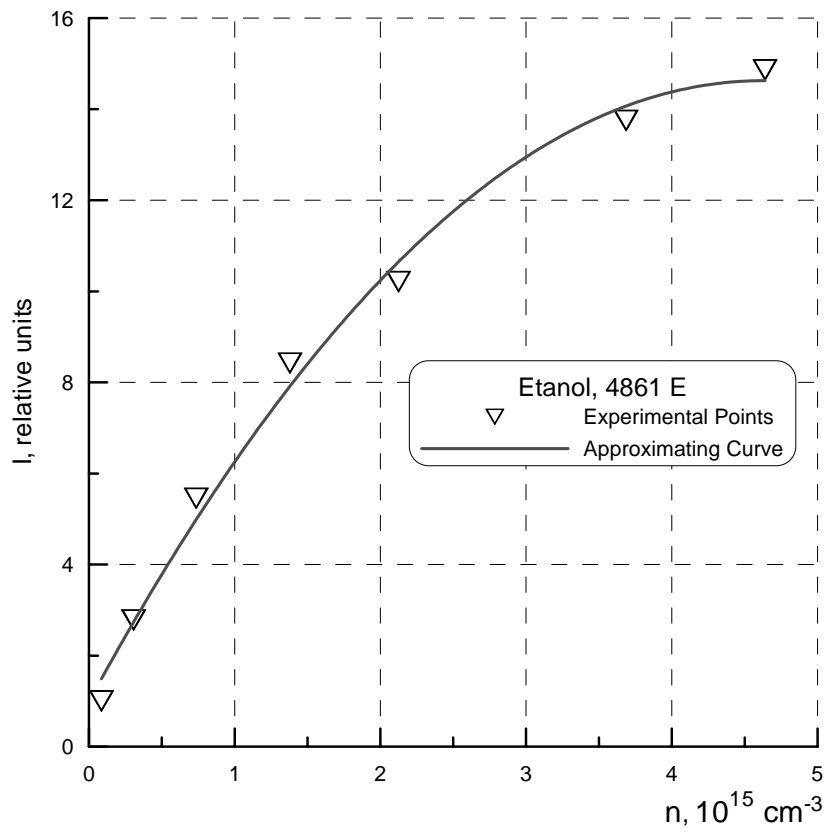


Fig. 2.16. Calibration dependence of optical radiation intensity for ethanol vapors

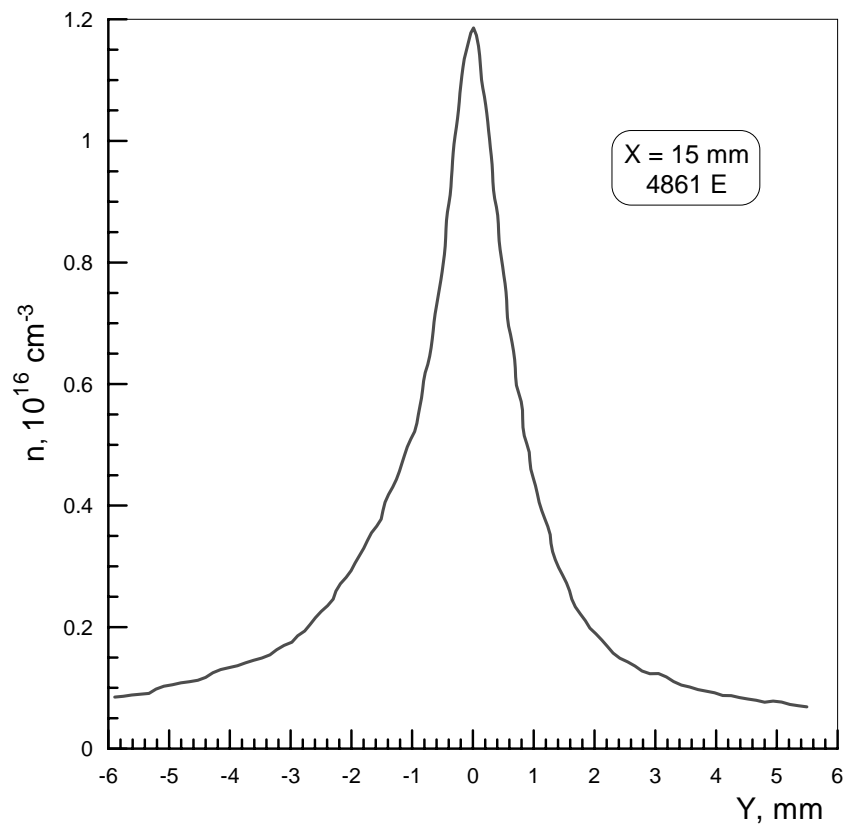


Fig. 2.17. Transverse density profile of the ethanol jet in the optical spectral range

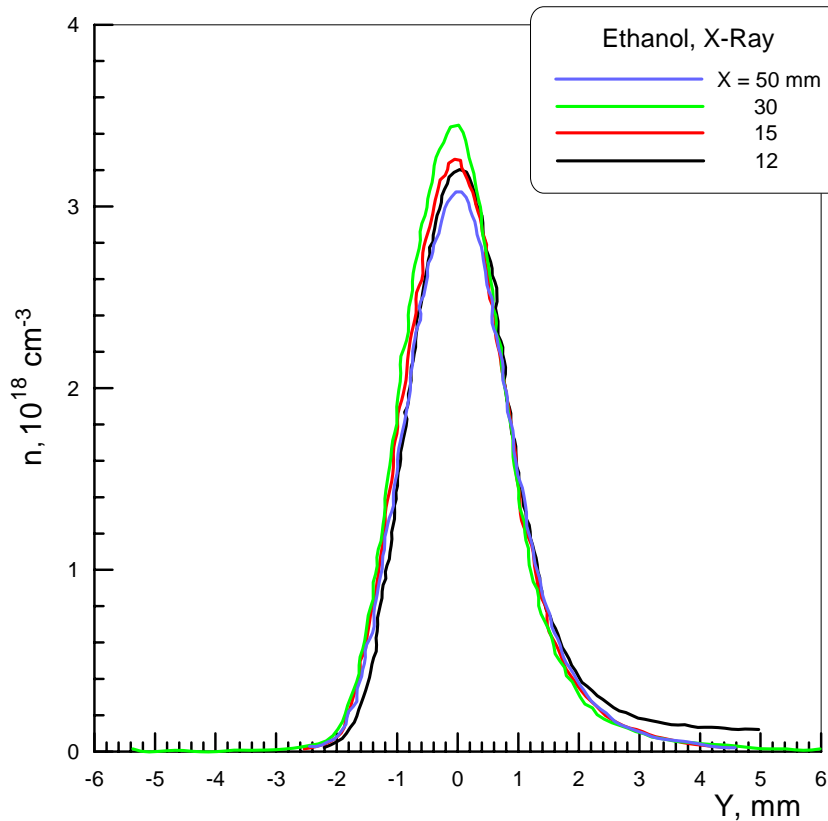


Fig. 2.18. Transverse density profile of the ethanol jet in the X-ray spectral range

Third, as we can see in Fig. 2.13, the electron beam exerts a rather strong effect on the liquid jet, which results in jet disintegration into drops. As a result «the mean density» of the vapor-liquid medium is lower than the density of the liquid. Probably, there is a lower limit of the droplet size, when the drops of small size are not destroyed by the electron beam. It could be verified experimentally, but in this case, it is necessary to generate homogeneous flows with monodrops, which involves technical difficulties.

Although the discourse given above makes the situation clearer, it does not give the ultimate answer to the questions posed. It does not follow from the results obtained and discussions, however, that the electron-beam method cannot be used for gas-droplet flow diagnostics. Obviously, everything depends to a large extent on the mean sizes of drops and their concentration in the gas flow. It could be confidently stated that the electron-beam method will allow us to estimate experimentally the possible influence of the droplet phase on gas-dynamic parameters (density) of the carrier gas flow. For this purpose, it is necessary to measure the local density of air (by the intensity of optical radiation at $\lambda=3914 \text{ \AA}$) in the absence and presence of drops in the flow.

Task 2.3.2. Measurement of density fields in a flow with and without droplets. Comparison of the data obtained for the flowfield without droplets with numerical computations

Measurement of density fields in a flow without droplets. Comparison with numerical computations for the flowfield without droplets

Jet outflow of gases from sonic and supersonic nozzles into vacuum was the object of many experimental and theoretical researches. By now, for this class of flows, which are usually called strongly underexpanded or nonisobaric, the determining parameters have been obtained

and the influence of viscosity and nonequilibrium effects (first of all, nonequilibrium condensation and oscillatory relaxation) both on the region of free supersonic expansion and on the structure of the initial region of the jet as a whole has been found. In particular, it was shown that the character of the core flow in an underexpanded jet and in the compressed layer at the jet boundary is determined by the Reynolds number

$$\text{Re}_L = \text{Re}_* / \sqrt{N},$$

where Re_* is the Reynolds number based on parameters in the nozzle throat and $N = P_0/P_\infty$ is the ratio of the pressure in the plenum chamber of the nozzle to the pressure of the background gas (nozzle-pressure ratio).

For $\text{Re}_L \geq 100$, the distribution of parameters in the jet region bounded by the central and lateral compression shocks is self-similar in terms of N , corresponds to gas exhaustion into vacuum, and is not complicated by diffusion of molecules from the ambient space. These were the flow conditions in the underexpanded jet that were provided in the present work during electron-beam density measurement.

The linear size of the self-similarity region realized in experimental investigations is determined by the vacuum-facility performance in continuous or pulsed modes of operation.

Other issues taken into account in formulating and performing experiments of the present work on local-density measurement in the flow behind the nozzle included the choice of the basic parameters of the supersonic nozzle - geometry, Mach number, sort of the gas, its temperature, consumption, and stagnation pressure. On one hand, it was possible to choose an arbitrary nozzle satisfying the capabilities of the VIKING facility in terms of consumption characteristics. On the other hand, the present project is focused on the study of gas and gas-droplet flows applied to the problem of spacecraft contamination by jets of control thrusters. Therefore, it is expedient to coordinate parameters of the model nozzle and the jet behind it with jets of a real thruster. In the present work, the nozzle parameters were chosen from the concept of papers [14, 15] on modeling jets of spacecraft thrusters.

One of the control thrusters of the International Space Station was chosen as the object of modeling. The corresponding parameters of the model nozzle are the Mach number $M_a = 2.84$, air as a test gas; and the nozzle-throat diameter $d_* = 10$ mm was chosen from the capabilities of the VIKING facility in terms of consumption. The supersonic part of the nozzle was made as a cone with an apex half-angle equal to 7° . The nozzle was mounted inside the vacuum chamber of the VIKING facility (see Fig. 2.4) on a 3-component coordinate gear, and the electron-beam measurements of axial and transverse distributions of density in the jet behind the nozzle were performed.

The measurements were performed both in continuous (with stagnation pressure in the plenum chamber of the nozzle $P_0 < 40$ torr) and in pulsed modes (with $P_0 > 40$ torr) of the VIKING facility operation. The minimum value of P_0 was 10 torr and maximal value was 450 torr.

The results of experiments were compared with the results of numerical simulation based on the Navier-Stokes equations.

Before proceeding to discussion of the results obtained, we briefly stop on the analysis of physical processes accompanying the gas flow inside the nozzle and in the jet behind the nozzle under expansion into vacuum. If the initial temperature of the gas is close to room temperature, only gas viscosity and homogeneous condensation can potentially influence the gas flow inside the nozzle and in the jet behind it. Condensation effects depend on the sort of the gas, size and geometry of the nozzle, and stagnation parameters. For a number of gases, like Ar, Kr, CO_2 , and vapors of H_2O , condensation effects can exert a very strong influence on the gas flow inside the supersonic nozzle and in the jet behind it. For example, for Ar, condensation can severalfold reduce the Mach number at the nozzle exit as compared to its geometric value. Because of condensation, the relative density in the jet behind the supersonic nozzle can also be much lower than the corresponding isentropic values.

At the same time, according to the available data, we can state that the influence of condensation on the flow inside the nozzle and in the jet behind it is negligible in our case (test gas - air, stagnation temperature equal to room temperature, stagnation pressure below 450 torr).

Thus, the gas viscosity is the only factor that can affect the gas flow inside the nozzle and, consequently, in the jet behind it. Quantitatively, the influence of viscosity is determined by the Reynolds number based on nozzle parameters, in our case, $Re \approx (P_0 \cdot d_*) \cdot (L/d_*)$, where L is the length of the generatrix of the supersonic part of the nozzle. As d_* and L are given, we have $Re \approx P_0$.

In experiments and computations, the range of P_0 was chosen such that it ensured both “viscous” and “inviscid” regimes of the gas flow in the nozzle.

Most experiments were performed in the pulsed modes of VIKING operation. Therefore, we first present pressure oscillograms in the electron-beam module and in the vacuum chamber of the VIKING facility, which served as a receiver. They are plotted for the modes with stagnation pressures $P_0 = 450$ torr (Fig. 2.19) and for 102.5 torr (Fig. 2.20). When the electromagnetic valve of air supply into the plenum chamber of the nozzle is switched on, the pressure in the module increases almost instantaneously to ≈ 0.1 Topp (point 1 in Fig. 2.19) and remains constant for ≈ 2 s. After that, up to the moment of closing the valve (point 2 in Fig. 2.19), a small increase in pressure in the module is observed. At the moment the valve is closed ($t = 5$ s), there is a jumplike increase in pressure in the module up to ≈ 0.22 torr (point 3 in Fig. 2.19), and then the pressure monotonically decreases (point 4 in Fig. 2.19). The reason for this pressure increase can be explained with the help of the pressure oscillogram in the VIKING facility. As we may see on this oscillogram (dashed curve in Fig. 2.19), the pressure in the VIKING chamber monotonously increases during the time of nozzle operation and, starting from approximately 2 s, becomes higher than the pressure in the module. This means that the aperture (slide gate Du 400) connecting the module to the vacuum chamber of the VIKING facility is, in a certain sense, an ejector (the jet axis is directed to the aperture). When the nozzle is switched off, the gas from the receiver returns to the module, which is responsible for the pressure jump observed. Then, the pressure decreases because of the pumping out of the VIKING facility. Thus, we can assume that a quasisteady flow regime is maintained in the module during the nozzle-operation time.

The pulsed mode of nozzle operation with $P_0 = 102.5$ torr (Fig. 2.20) differs from the mode with $P_0 = 450$ torr mainly in lower final pressure of the gas in the module.

Now we consider typical results of density measurements in the jet behind the supersonic nozzle.

Figure 2.21 illustrates the influence of the stagnation pressure P_0 (or, which is that same, Reynolds number) on the relative density n/n_0 at a point on the jet axis for $x/r_a = 5.2$. Both experiments and computations show that the role of viscosity on the flow inside the nozzle for $P_0 > 60$ torr is negligible and the relative density in the jet behind the nozzle is close to isentropic values. As the pressure P_0 decreases, the influence of viscosity on the flow inside the nozzle becomes stronger: the effective diameter of the nozzle exit decreases, the Mach number of the nozzle decreases, and consequently, the relative density at the chosen point on the jet axis decreases. For $P_0 = 10$ torr, the decrease in n/n_0 in comparison with the isentropic value is already about 30%. Satisfactory agreement of the experimental and numerical data should also be noted.

Axial and transversal distributions of density in the jet behind the nozzle at fixed values of P_0 were further measured.

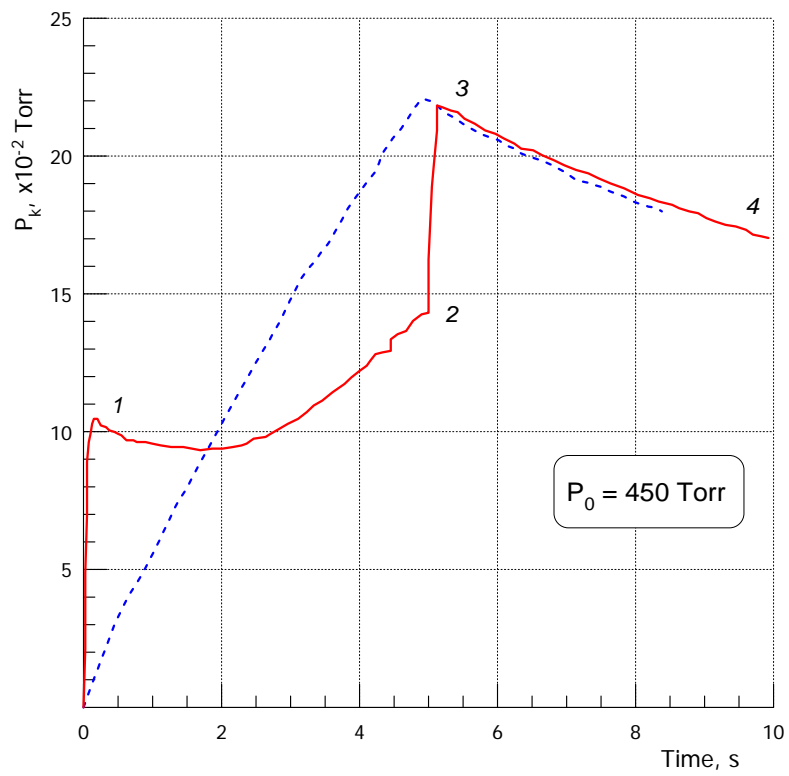


Fig. 2.19. Oscillograms of pressure in the module (solid curve) and in the vacuum chamber of the VIKING facility (dashed curve)

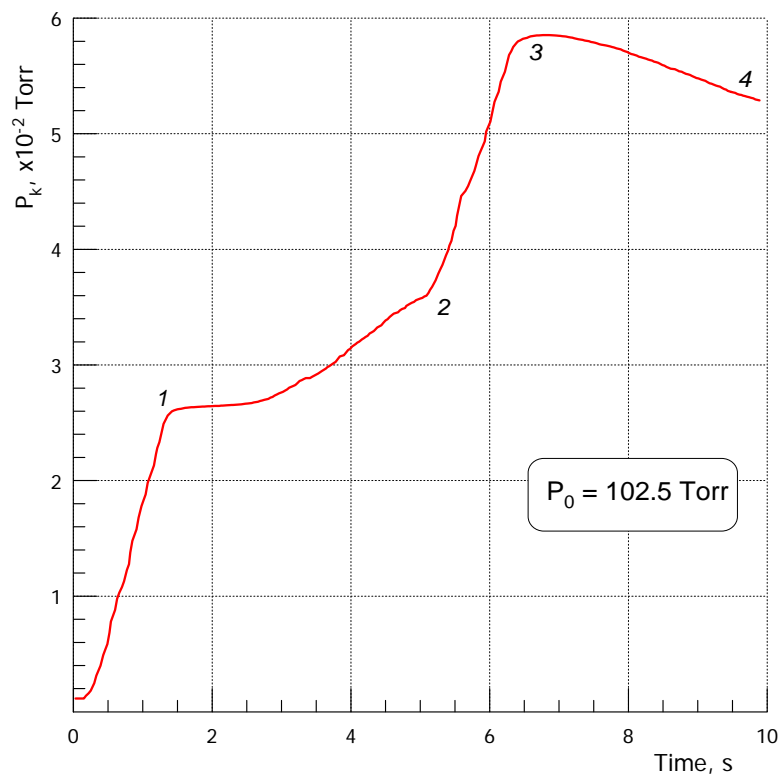


Fig. 2.20. Oscillograms of pressure in the module

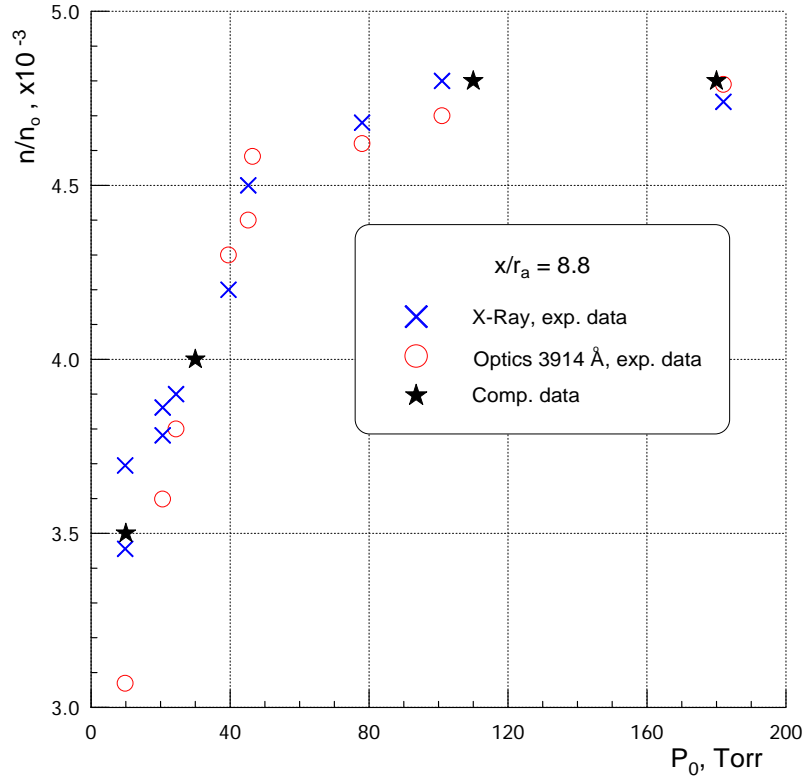


Fig. 2.21. Influence of the stagnation pressure P_0 on the relative density n/n_0 on the jet axis

Figure 2.22 shows the change in n/n_0 along the air jet axis for $P_0 = 450$ torr, based on the results of electron-beam measurements in the x-ray spectral range. The measurements were performed in a rather large area - from 100 to 500 mm from the nozzle exit ($x/r_a = 10-50$). Rather good agreement of the measured values of n/n_0 and computed isentropic values of n/n_0 for the given nozzle can be noted. It is also seen that the central shock wave starts to form in the free jet approximately at $x/r_a = 40-45$. It is in complete correspondence to the existing notions about exhaustion of jets into the ambient space and test conditions.

The results of measurements of transverse distributions of density are given in Fig. 2.23. The measurements were performed in the continuous mode of VIKING operation. The results presented do not require detailed comments. We only note that lateral shock waves are formed at some distance from the axis, and the measured values of n/n_0 on the jet axis correspond to the numerical values of n/n_0 within the measurement error.

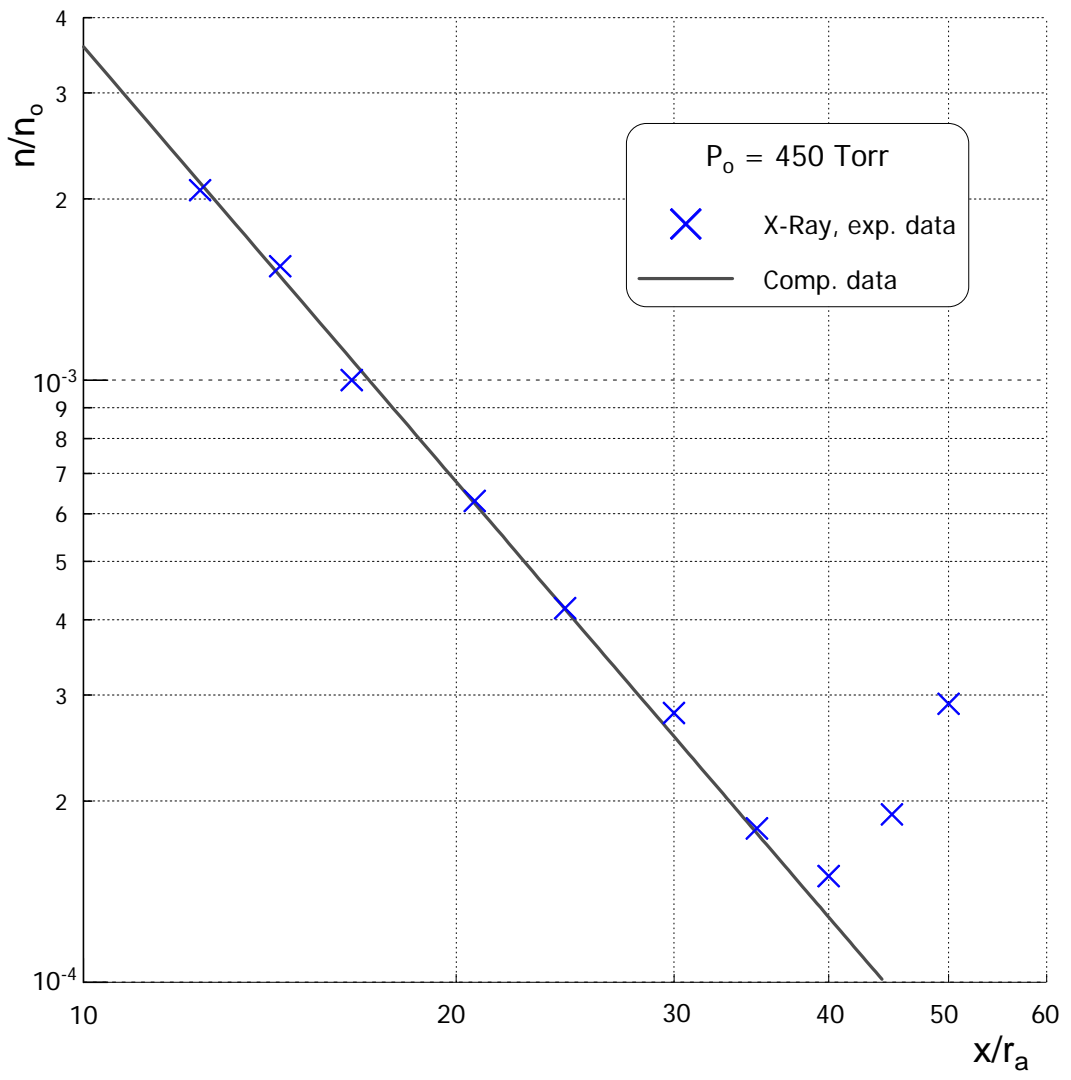


Fig. 2.22. Axial distribution of relative density

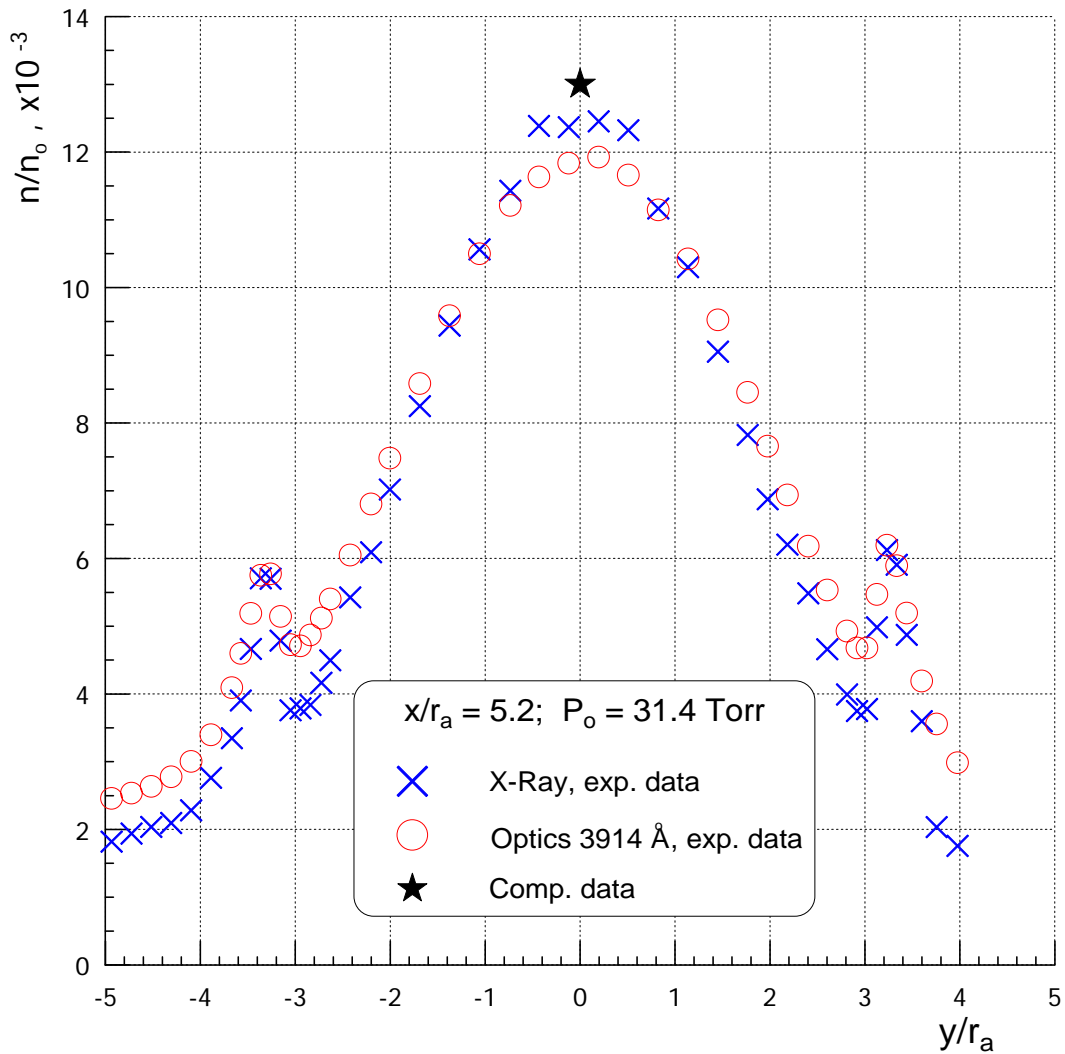


Fig. 2.23. Transverse distribution of relative density

Measurement of density fields in a flow with droplets

We now proceed to the description and analysis of electron-beam measurements of density in a supersonic flow with drops. Generally speaking, these measurements were planned and carried out in order to answer two questions. The first question: Is it possible to detect the liquid droplets in a supersonic flow by means of an electron beam? The second question: Do the drops affect the gas dynamics of the supersonic flow under the present test conditions? Running forward, we can tell a negative answer was obtained for both questions. First, with the help of an electron beam, it was not possible to unambiguously register the droplet phase and to measure its concentration in the flow. Second, for the chosen regime parameters of the experiments, the droplet phase, within the measurement error, does not exert any influence on the density distribution in the carrier gas flow.

We comment the results obtained in more detail. As our early researches have shown [7], in the case of exhaustion of the near-wall liquid film with a cocurrent gas flow from a supersonic nozzle into vacuum, there are two maximums in the angular distributions of the droplet phase in the jet behind the nozzle. One maximum is located on the jet axis; it is related to droplet shedding from the film surface in the nozzle-throat region. The other maximum is located in the peripheral part of the jet; it is related to decomposition of the near-wall liquid film on the exit edge of the nozzle.

Electron-beam measurements were conducted in the regions of the most probable occurrence of the droplet phase: near the jet axis and at the periphery. Air at room temperature was used as a test gas, and ethanol was used as a test liquid. The mass consumption of ethanol did not exceed 10% of the air consumption. The maximal consumption of air was 11 g/s.

The transverse distributions of density in the flow with and without droplets were measured in the experiments. The measurements in the axial and peripheral regions of the jet were performed at various distances from the nozzle exit x/r_a to provide approximately identical values of density.

The measured results are plotted in Figs. 2.24 and 2.25 for the axial part of the jet and in Fig. 2.26 for the jet periphery. Within the measurement error (10-15%), the droplet phase has no effect on the results of electron-beam measurements both in optical and in x-ray spectral ranges.

Though the methodical investigations performed previously within the project have shown rather high sensitivity of the electron-beam method for studying liquid jets of ethanol, the concentration of the droplet phase of ethanol in the gas-droplet flow under the present test conditions is, apparently, insufficient for its registration by the electron-beam method. On the other hand, higher initial mass fractions of liquid in the gas flow ($> 10\%$) are outside the scope of the present project.

The main conclusion that follows from this part of the work is that the “gas-dynamic” and “droplet” parts of the problem can be divided, namely, the gas-dynamic structure of the flow can be considered (experimentally and theoretically) irrespective of the droplet phase; the motion of drops in the supersonic flow can be considered as a separate problem with given distributions of gas-dynamic parameters both inside the nozzle, and in the plume behind it.

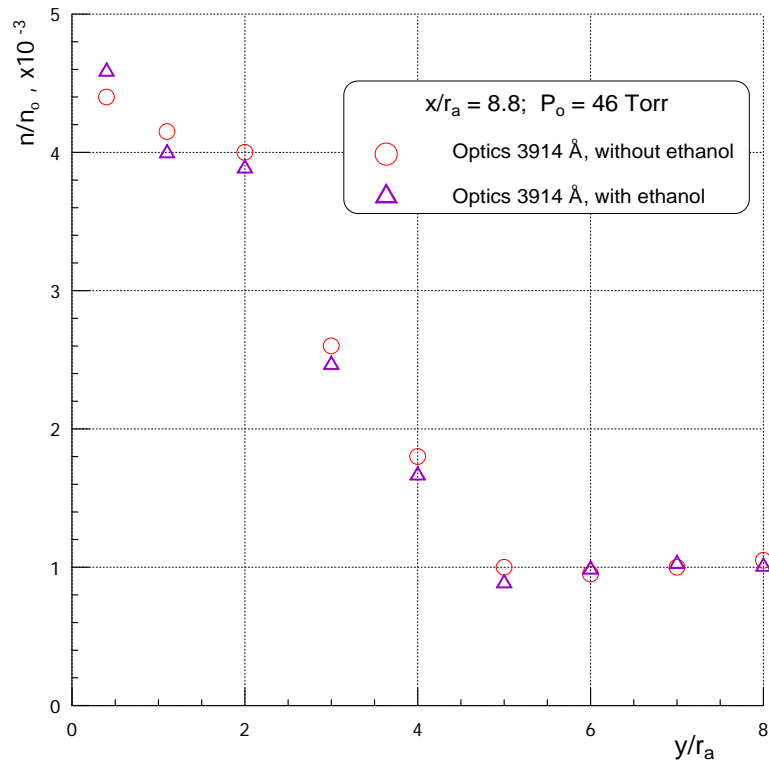


Fig. 2.24. Transverse distributions without droplets and with droplets in the axial region of the jet, based on the results of optical measurements

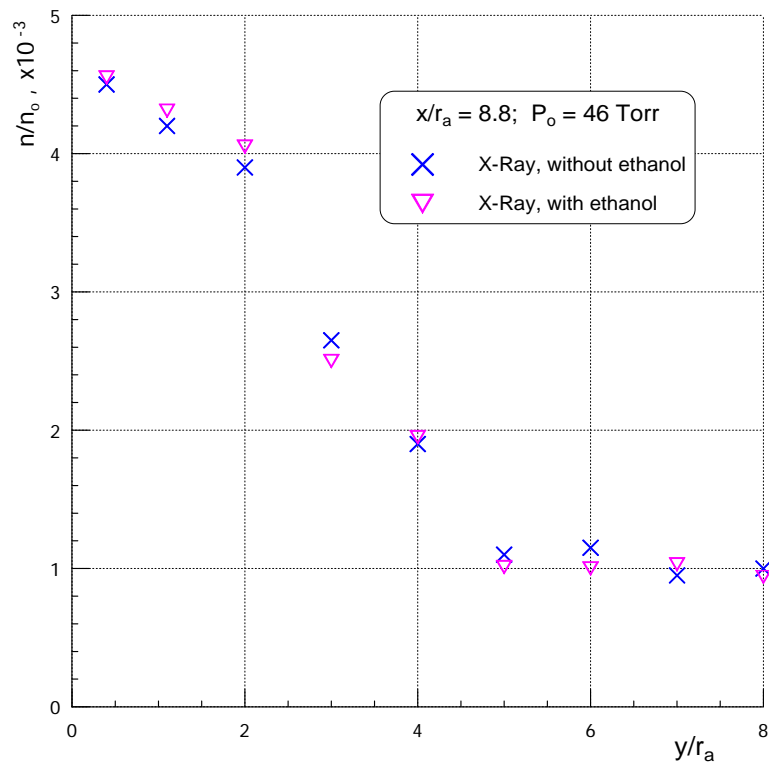


Fig. 2.25. Transverse distributions without droplets and with droplets in the axial region of the jet, based on the results of x-ray measurements

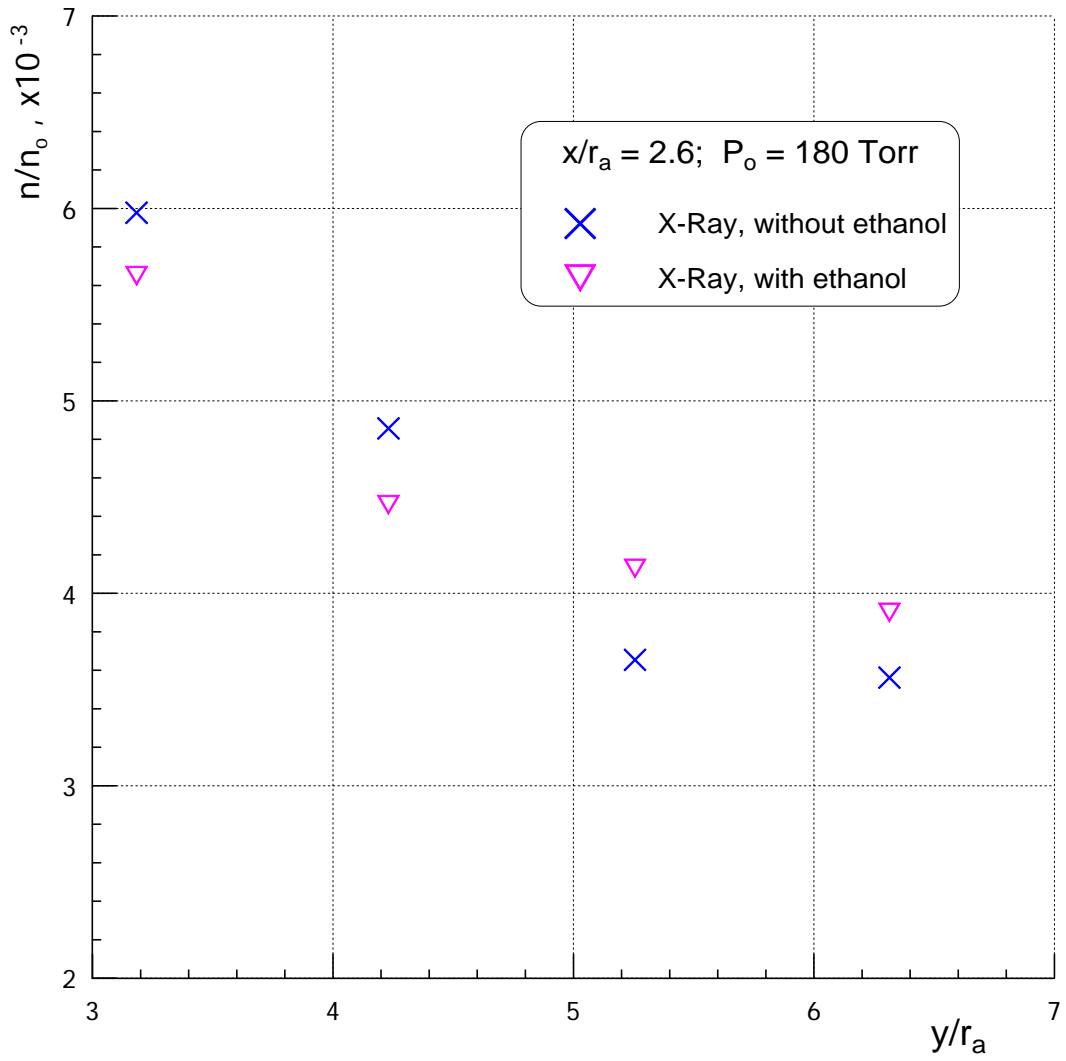


Fig. 2.26. Transverse distributions without droplets and with droplets in the peripheral region of the jet

Task 2.4. Numerical simulations of carrier gas flow at experimental conditions inside the nozzle and in near vicinity of the nozzle exit plane. Comparison with the experimental results for the carrier gas.

The gas flow inside a supersonic nozzle was calculated on the basis of Navier-Stokes equations with different boundary conditions at the nozzle exit (task 2.4.1). In particular, extrapolation of primitive variables inside the computational domain was used, which corresponds to the so-called “soft” boundary conditions (vanishing of the first or second derivative in the streamwise direction). It was shown that these conditions are valid for rather high Reynolds numbers, when the boundary layer is thin. With increasing flow rarefaction, the upstream influence via the subsonic part of the boundary layer becomes more and more significant. To take this influence into account, boundary conditions with extrapolation of Riemann invariants and a prescribed external pressure were used. Computations were also performed for an extended domain including a certain vicinity of the nozzle lip. Several types of output conditions were tested.

Gas flows inside a supersonic nozzle and in the near field of a plume escaping into vacuum were calculated using the earlier developed hybrid approach (task 2.4.2). The flow field in the upstream zone calculated by Navier-Stokes equations was used as the initial flow field for downstream computations by the DSMC method. The position of the boundary between the zones varied from a cross section close to the nozzle throat to a cross section located almost in the nozzle-exit plane. The parameters for which the computations were performed corresponded to Rothe’s experiments available in the literature. It was shown that the interface procedure developed previously is rather effective. Results obtained by the hybrid approach are in excellent agreement with results obtained by the purely continuum approach (with slip conditions) within almost the entire flow field. Some difference is observed near the wall only, where nonequilibrium effects are significant (noticeable difference between translational and rotational temperatures).

Special attention was paid to the formation of a reverse flow with flow turning by more than 90° . It was found that gas particles that enter the reverse flow arrive from the near-wall part of the boundary layer whose thickness is vanishingly small. The total flow rate of the gas in the reverse flow is very small, and the density here rapidly decreases by several orders of magnitude; therefore, the continuum description becomes inapplicable almost immediately behind the nozzle lip.

The flow of the carrier gas inside the nozzle and in the exhausting supersonic plume was numerically simulated on the basis of the Navier-Stokes equations under conditions corresponding to experimental ones (task 2.4.). The computations were performed for a conical nozzle with an apex half-angle $\alpha = 7^\circ$ and design Mach number $M_d = 2.85$. The pressure in the plenum chamber p_0 varied from 10 to 30 mmHg; for comparison, an inviscid computation was also performed. The region outside the nozzle extended downstream to a distance equal to $25R_a$, where R_a is the radius of the nozzle-exit cross section. The ambient pressure was sufficiently low for the plume to be considered to escape into vacuum. The resultant fields of gas-dynamic quantities were used for comparison with the experimental results obtained at the Institute of Thermophysics (IT) of the Siberian Branch of the Russian Academy of Sciences. Numerical and experimental data for density distributions $\rho(x)$ along the plume centerline were directly compared. The data are in satisfactory agreement. It was found that the limiting velocity of gas exhaustion is reached already within the computational domain used; thus, the density along the centerline at distances greater than $15R_a$ from the nozzle exit varies in accordance with the known theoretical dependence $\rho(x) \propto 1/x^2$. The effect of the boundary-layer thickness on the nozzle walls on the plume flow was considered by comparing data obtained for different values of p_0 .

The effect of the procedure of setting the boundary conditions at the output boundary on the computation results was analyzed. It was shown that extrapolation of numerical data outward from the domain yields good results if the plume pressure remains appreciably higher than the ambient pressure p_a (exhaustion into vacuum). If the pressure within the computational domain decreases to values lower than p_a , then the exhaustion occurs into the ambient space, and the influence of counterpressure should be taken into account for adequate simulation of the plume flow. For this purpose, we used the boundary conditions with external pressure applied and extrapolation of those Riemann variants that correspond to characteristics leaving the computational domain. The influence of the output-boundary position on the accuracy of the plume-flow description was also considered.

Thus, during the first year of project fulfillment

1. The test section for obtaining and investigating gas-droplet flows in vacuum was justified, developed, and manufactured.
2. A system of independent feeding and measurements of the consumptions and pressure of the gas and liquid and measurement of pressure in the vacuum facility was created.
3. The test section was calibrated in the ranges of regime parameters in terms of consumptions of the test gas and liquid, pulse duration, and value of pressure in the vacuum chamber required for implementation of the project.
4. The possibility of application of the electron-beam method for diagnostics of gas-droplet flows in terms of radiation intensity in x-ray and optical spectral ranges was analyzed. The electron-beam diagnostic complex was upgraded for research of gas-droplet flows in continuous and pulsed modes of operation of the VIKING facility.
5. The density fields in a supersonic flow with and without droplets were measured with the use of the electron-beam method.
6. It was experimentally demonstrated that the problem posed within the project on the study of gas-droplet flows can be divided into independent “gas-dynamic” and “droplet” parts within the pressure range considered.
7. A set of codes for simulating the carrier gas flow inside the nozzle and in the plume, based on the Navier-Stokes equations, was developed. These codes allow the user to take into account the initial effects of gas rarefaction by using boundary conditions with velocity slip and temperature jump on the solid surface.
8. A hybrid approach for simulating the gas flow inside the nozzle and in the plume was developed, which employs both continuum and kinetic algorithms. The approach is based on dividing the computational domain into zones where the Navier-Stokes equations are solved and the DSMC method is used. An interface for matching the kinetic and continuum algorithms at internal boundaries between the zones was developed.
9. The flow inside the nozzle and in the near vicinity of the nozzle exit was computed on the basis of the hybrid approach. It was found that gas particles entering the backflow (turning by more than 90°) arrive from the near-wall part of the boundary layer whose thickness is very small.
10. Based on the Navier-Stokes equations, the flow inside the nozzle and in the plume was computed under conditions corresponding to experimental ones. Good agreement of numerical and experimental data was obtained. It was shown that the flow reaches the limiting exhaust velocity within the chosen computational domain.

References used:

1. H. Trinks, I. Kaelsch. Exhaust Plume Effects of Small Thrusters on Spacecraft. AIAA Paper No 87-1603, AIAA 22nd Thermophysics Conference, June 8-10, 1987 / Honolulu, Hawaii.

2. H. Trinks. Experimental Investigation on the Exhaust Plume Flow Fields of Various Small Bipropellant and Monopropellant Thrusters. AIAA Paper No 97-1607.
3. Mikatarian R.R., Anderson R.G. An Experimental Investigation of a Liquid Jet Expelled into Vacuum. J. of Spacecraft and Rockets, 1966, Vol. 3, No. 2, p.267.
4. Fuchs H., Legge H. Flow of Water into Vacuum. Acta Astronautica, 1979, Vol. 6, pp. 1213-1226.
5. Zuev, N.D. et al. Experimental Investigation of Spraying Liquids into Vacuum. In: "Flow of a Rarefied Gas with Nonequilibrium Physicochemical Processes". Proc. VIII All-Union Conf. on Rarefied Gas Dynamics. Moscow, 1987, pp. 145-148.
6. Alred J.W., Smith L.N., Wang K.C., Lumpkin F.E., Fitzgerald S. M. Modelling of Water Injection into Vacuum. NASA, Eight Annual Thermal and Fluid Analysis Workshop. Spacecraft Analysis and Design, Sept. 8-11, 1997, University of Houston-Clear Lake. Houston, Texas.
7. Yarygin, V.N., Prikhodko, V.G., Gerasimov, Yu.I. Wall liquid film outflow from supersonic nozzle into vacuum. Proc. X Int. Conf. On the Methods of Aerophysical Research (ICMAR' 2000), Novosibirsk, Russia, 9-16 July 2000, Part III, pp. 189-194.
8. Alekseenko S.V., Nakoryakov V.E., Pokusaev B.G. Wave Flow of Liquid Films. 1994 by Begell House Inc., 313 p.
9. A.K. Rebrov and V.N. Yarygin. Molecular gasdynamics and nonequilibrium processes, Thermophysics and Aeromechanics, 1997, Vol. 4, No. 2, P. 143-150.
10. L.A. Gochberg. The electron beam fluorescence technique in hypersonic aerothermodynamics, Proc. 18th AIAA Aerospace Ground Testing Conf., 1994, AIAA Paper 94-2635, 42 p.
11. Experimental Methods for Rarefied Gas Dynamics, Inst. Thermophysics, Sib. Branch, USSR Acad. Sci., Novosibirsk, 1974, 218 p.
12. Yu.S. Kusner et al. Measurement of Density of Electrohydrodynamical Jets Flowing into Vacuum, JTPH Letters, Vol. 7, No. 5, 1981.
13. I.B. Borovskiy. Physical Bases of Roentgenospectral Researches, Moscow, 1956, 311 p.
14. Gerasimov Y.I. Parameters of similarity of the problem of interaction of a free expanding jet with a plate. Izv. AN SSSR, MZhG, 1981, No. 2, pp.169-173.
15. Gerasimov Y.I., Gorchakova N.G., Palopezhentsev S.A., Yarygin V.N. Modelling of parameters of strongly nonisobaric jet flows in vacuum chambers. Proc. IX USSR Conf. On Dynamics of rarefied gases. Sverdlovsk, UPI, 1988, Vol.3, pp.144-151.

Task 2. Investigation of gas-droplet flows. - 2nd year

During the second year, experimental investigations required by items 2.5 and 2.6 and computational investigations corresponding to items 2.7 and 2.8.

Task 2.5.1. Verification of the method of droplet visualization at the nozzle-exit edge and measurement of the droplet velocity in the flow.

The main objective of the given task of the Project consist in development of a technique of measurement of the sizes and velocities of drops arising during ejection of the near-wall liquid film with a co-current gas flow from a nozzle in vacuum. The difficulties in development of such a technique consist, first of all, in substantiating and choosing both the illumination scheme and registration of images of the droplet phase of the flow.

Systems of illumination for visualization of the droplet phase flow

In the given work, according to the analysis of the expected sizes and velocities of drops, two systems of illumination (with incandescent lamps and with a laser) were chosen and created.

The first system included ordinary and halogen lamps. The results of videoshooting of the liquid ejection process into vacuum with this scheme of illumination allowed obtaining a detailed picture of the general structure of the flow and gives an idea about the process of disintegration of the liquid film into drops. In the shots, it was possible to observe a significant amount of drops scattering in different directions, including the opposite direction. Imperfection of such a method of visual registration of the process consists in impossibility of reliable estimation of velocity of the formed drops because of uncertainty of the distance covered by them and the time of flight. The reason is related to the fact that the plane in which the drop moves and the plane of observation may not coincide. On the shots, we obtained the projection of the drop trajectory onto the plane of observation. Therefore, the real velocity of drops can be higher than the measured one. The time of presence of drops in the frame can differ from the exposure time, for example, because of the limited field of vision of the camera lens, because of asynchronous moments of opening the camera shutter and formation of drops. For these reasons, the errors in estimation of the drop sizes are also possible.

These drawbacks can be avoided with the help of the system of illumination of the gas-droplet flow by the method of «optical sheet» - a flat flow of light with a very narrow cross section. To increase light exposure of the object, a semiconductor laser, which can work both in continuous and pulsed modes, was used as a light source.

The scheme of measurements with the use of «laser sheet» is shown in. 2.27. A thin focused beam of laser 7 with the help of cylindrical lens 6 transformed to a divergent flat beam of light, so that the longitudinal axis of the nozzle 1 and the flow were in the plane of the beam. The height of the light beam near the nozzle was about 50 mm, and the center of the beam coincided with the plane of the nozzle-exit cross section. The width of the beam was about 0.3 mm. Thus, in experiments it was possible to register drops that occur within 25 mm from the nozzle edge. Only the particles that appear in the plane of «laser sheet» at the moment of exposition of the frame are observed. Radiation scattered by particles passes through optical window 3 of vacuum chambers 5 of the VIKING setup and is registered by the Nikon 5700 photo camera or Canon XM1 videocamera 4. To reduce spurious illumination and increase sensitivity, all windows of the vacuum chamber were covered by a light-tight material, and a dark screen was mounted on the background of the nozzle. To reduce intensity of radiation reflected from the nozzle, the external surface of the nozzle was covered with soot.

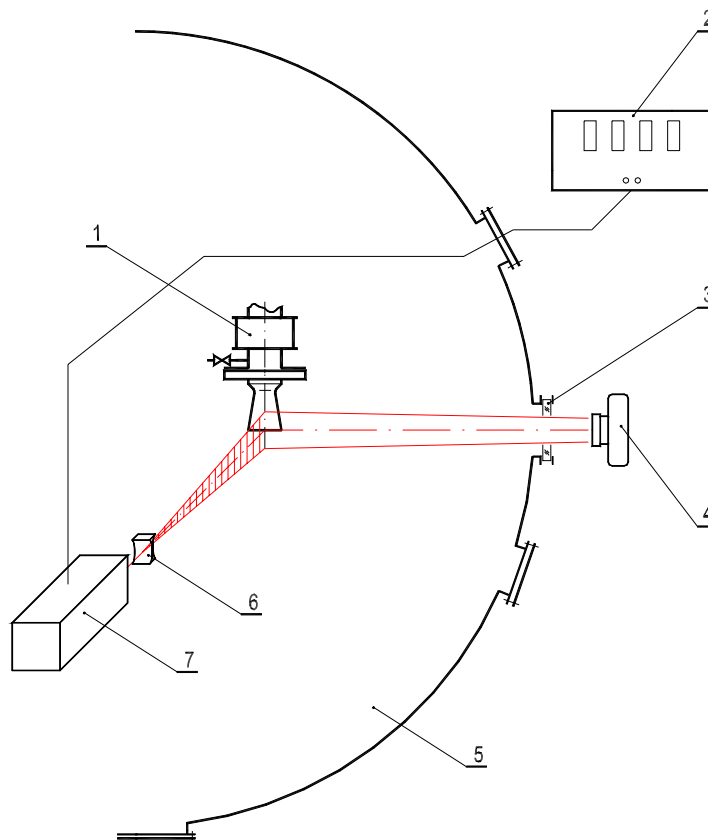


Fig. 2.27. Scheme of visualization with the method of «laser sheet»

To avoid electrical disruptions in the feeding circuit and to control the laser, the latter together with the cylindrical lens was located in a specially designed and made leak-proof casing, in which the atmospheric pressure was supported, and which allowed focusing the laser beam and regulating the light beam being formed relative to the nozzle axis and the plane of its exit cross section. The casing was mounted on a traversing gear inside the VIKING setup. For stroboscopic illumination, the pulsed mode of operation of the laser with external control by the generator of synchronizing pulses 2 was used in experiments. The frequency of flashes could vary from 10 Hz to 5 kHz, and the duration of flashes could be varied from 1 to 255 microseconds.

Processing of the obtained videoimages

The technique of ejection process videoshooting and the technique of processing of the obtained videoimages were verified on the model of near-wall ethanol liquid film ejection with a co-current air flow into vacuum from a cylindrical tube 5 mm in diameter with a rounded exit edge.

As an example, Fig. 2.28 shows the video frames of the droplet phase flow with illumination by incandescent lamps. Two processes are well observed: the rise of the liquid film on the outer surface of the tube and the back flow of droplets.

The results both of video and photo shooting with the help of the «laser sheet» method are given in Figs. 2.29 and 2.30, respectively. These figures show individual typical fragments of the gas-droplet mixture ejection process from the cylindrical channel with a round exit edge into vacuum. The photos show the presence and behavior of drops in the plane that passes through the flow centerline. The flows of finely dispersed particles shed from the tube are clearly visible on the shots. The size of these particles is so small that individual particles cannot be observed in

the shots, but as their number is large, being aggregated, they form luminous zones ("tongues"). There are two characteristic directions of flight of these drops: one is directed at an angle of $\sim 20^\circ$ from the flow axis (high intensity) and the other one at an angle of $\sim 60^\circ$ (weak intensity). For such particles, it is impossible to estimate their velocity by the length of the "tongues", as this length is determined by the density of these particles. With increasing distance from the nozzle, the density of particles decreases owing to flow expansion and, probably, evaporation of the particles; the luminescence of the "tongue" vanishes.

On the best frames, the trajectories of individual drops whose characteristic size reaches fractions of a millimeter are registered. Viewing of individual video frames allows us to conclude that the drops of such a size are formed upon destruction of the liquid film moving on the external surface of the tube in the opposite direction, and this destruction has, basically, an explosive character.

The small cross size (~ 0.3 mm) of the light flow («laser sheet») limits the amount of observable drops. The drops can take off from the surface of the external film at an arbitrary angle to the plane of registration; therefore, most of them are registered only as points in the photos, and the trajectories of only a small portion of drops coincide with this plane and leave the trace on the shots as tracks. It is possible to notice that, in all photos in the radial plane, the primary direction of motion of the drops is the motion in the back sector.

Typical times of drop formation (and processes upon explosive boiling of the external liquid film) are much smaller than the period of shooting; therefore, some frames are empty (without drops) in the experiment, and each subsequent frame cannot be always presented as the evolution of the previous one. For our conditions, the optimum mode of photoregistration of the process of liquid ejection turned out to be videoshooting with an exposure time of $1/50$ s and the frequency of the following light flashes of 5 kHz, i.e., when 100 flashes got into one frame. It allowed obtaining a plenty of "stop-shots" and increased the probability of registration of motion of individual drops in the "laser sheet" plane. After viewing all the shots, those with visible drops and their trajectories were selected, and then processing of the shots was performed: the number of drops, their size by the diameter of the stain on the shot, their velocity by the distance between the stains, and also the direction of motion were determined. The results of such processing are shown in Figs. 2.31-2.32.

Thus, as a result of performance of the given stage of the project, the technique of measurement of the drop sizes, velocities, and trajectories in a gas-droplet flow in vacuum was developed.

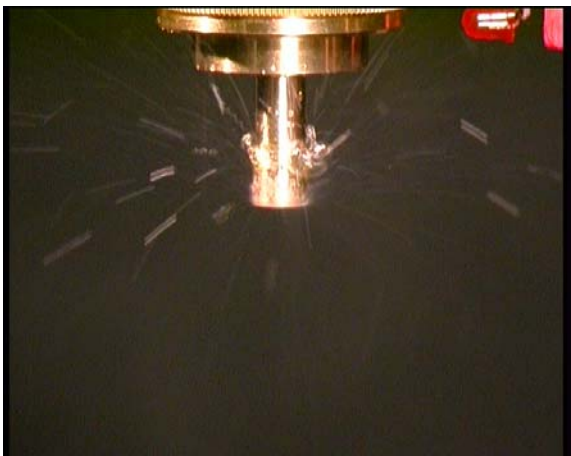
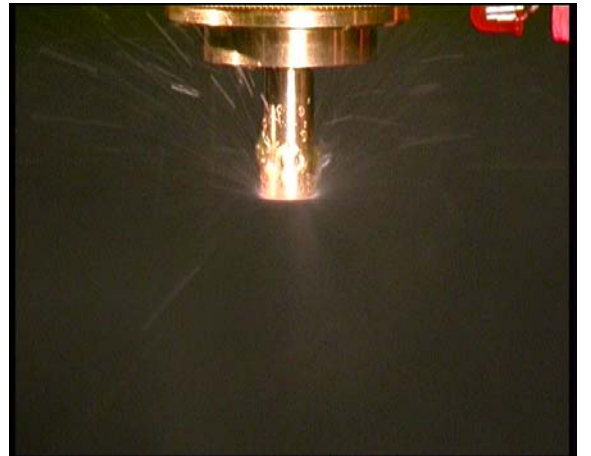
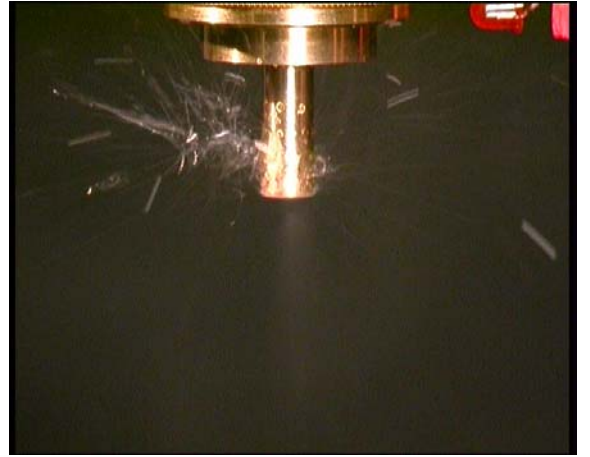
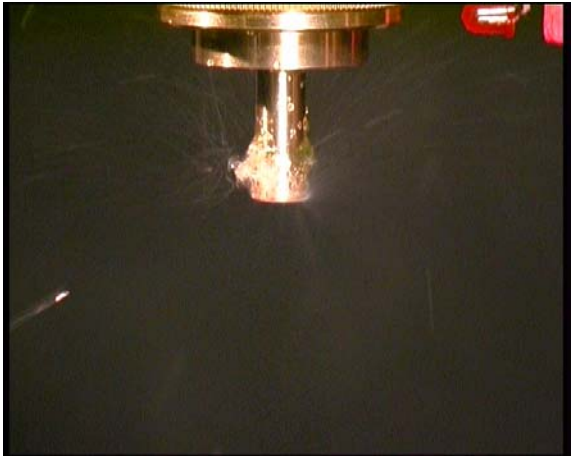


Fig. 2.28. General structure of the droplet phase flow with incandescent lamp illumination

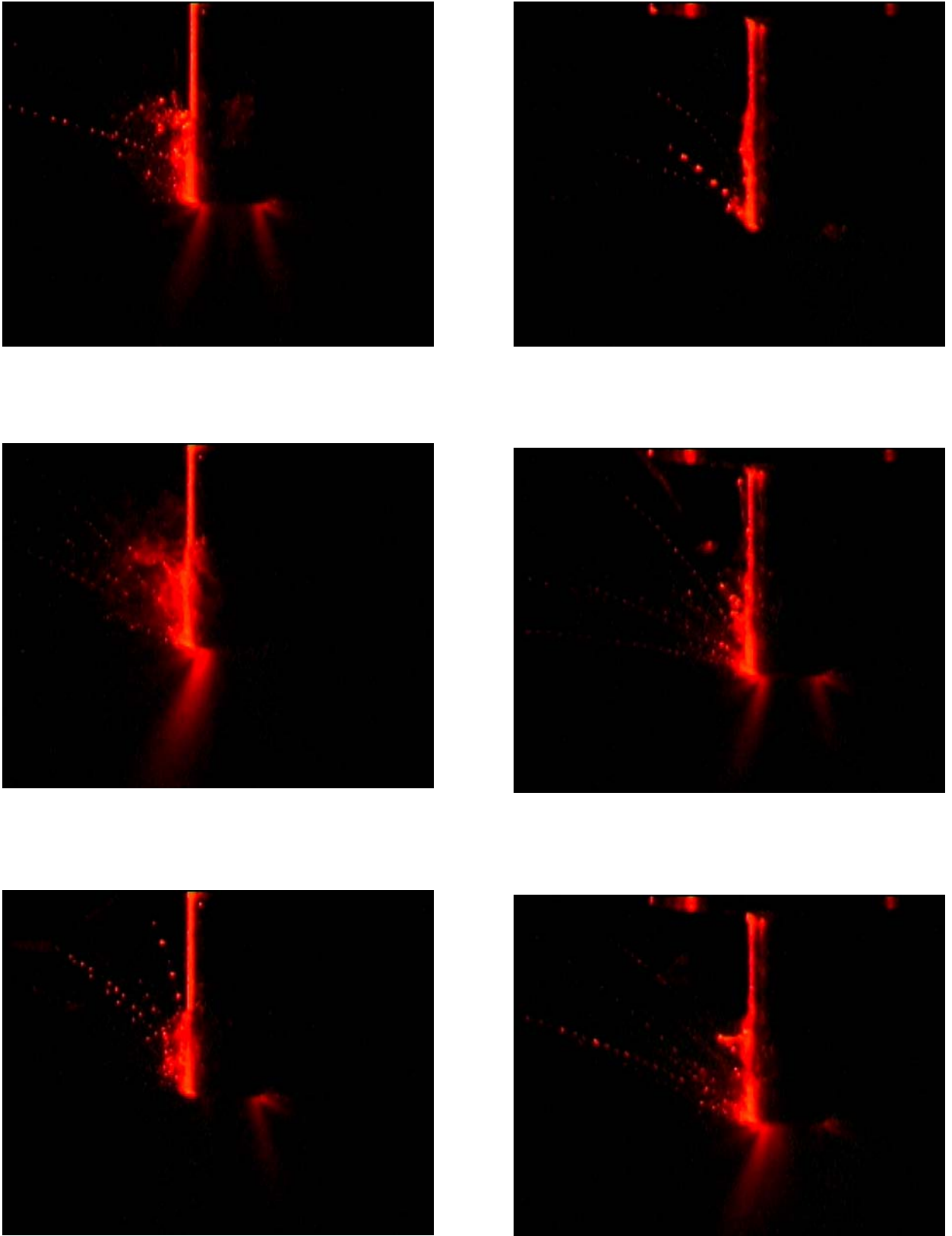


Fig. 2.29. Structure of the droplet phase flow in the plane passing through the tube axis. "Laser sheet" method illumination

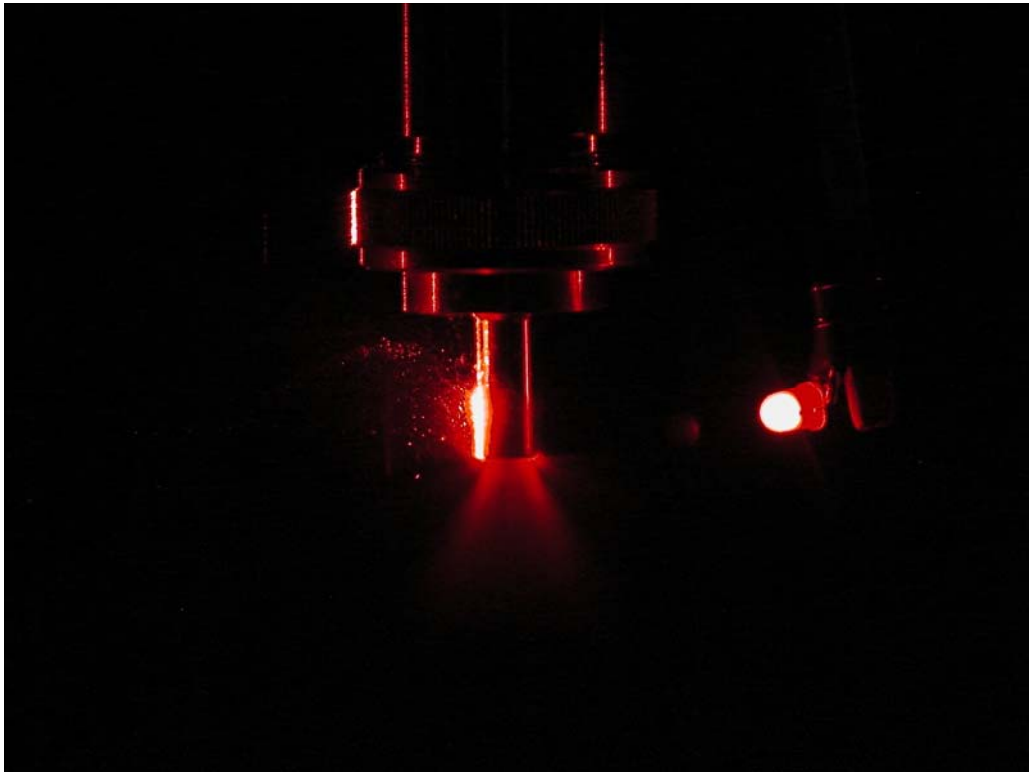
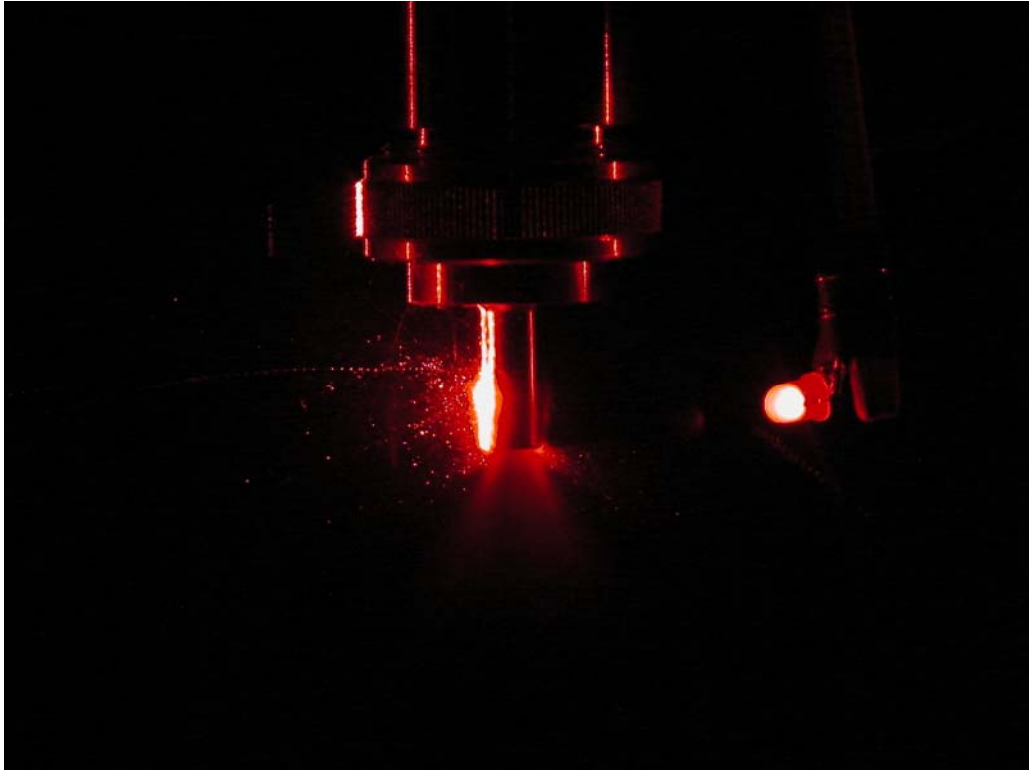


Fig. 2.30. Photos of the droplet phase flow structure.
"Laser sheet" method illumination

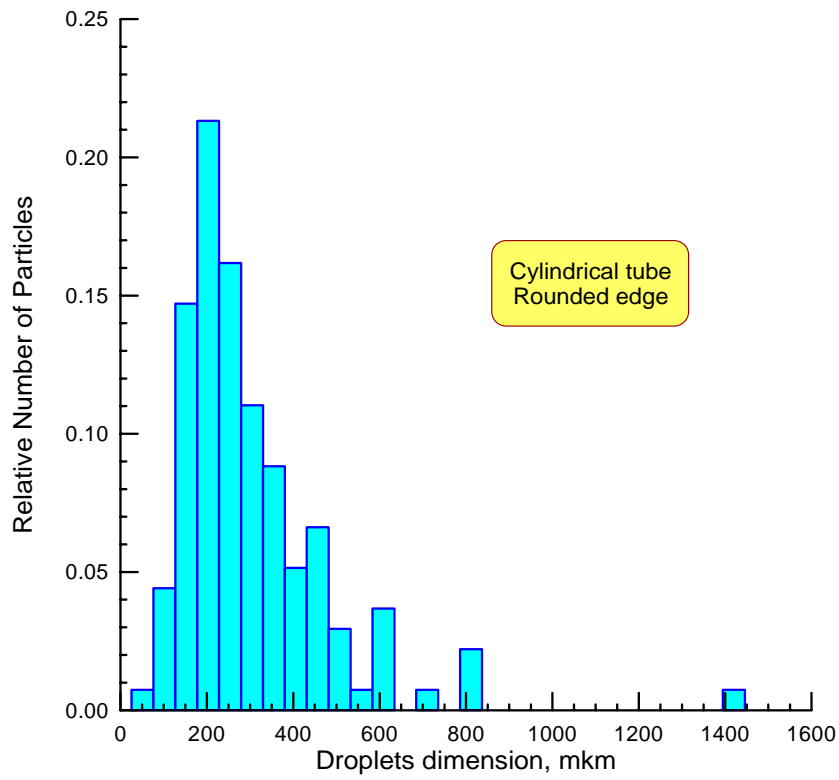


Fig. 2.31. Size distribution of the registered droplets

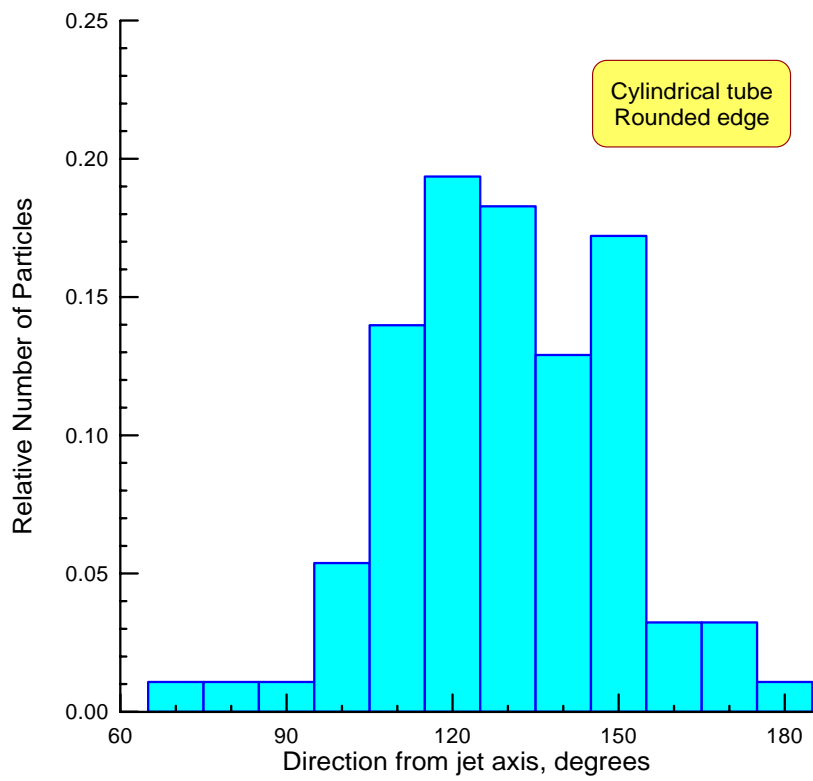


Fig. 2.32. Directional distribution of the registered droplets

Task. 2.5.2. Experiments on the effect of the nozzle geometry, gas-flow parameters, and physical properties of the liquid on the formation and behavior of droplets starting from the nozzle lip

With the help of the measurement techniques developed earlier, the influence of the nozzle geometry, gas-flow parameters, and physical properties of the liquid on formation and behavior of drops arising upon supersonic gas outflow into vacuum with a near-wall liquid film was investigated. In the experiments, we used a cylindrical tube with a diameter of 5 mm and a conical supersonic nozzle with an apex half-angle $\alpha = 7^\circ$, which had throat and exit cross-sectional radii of 5 and 10 mm, respectively, and a cylindrical external surface. In both cases, the thickness of the exit edge was $l = 1$ mm. The nozzles were mounted vertically with the exit cross section directed downward. Ethanol was mainly used as a working liquid; however, to investigate the influence of physical properties of the liquid on the gas-droplet flow structure, butanol was used, which has a pressure of saturated vapors approximately an order of magnitude smaller than ethanol ($6.65 \cdot 10^2$ Pa for butanol and $5.85 \cdot 10^3$ Pa for ethanol at room temperature). Air was used as a working gas. The liquids and air were used at room temperature.

Let us consider the main results of experiments.

Influence of channel geometry

In this series of measurements, the results for a supersonic conical nozzle and a tube were compared. The film Reynolds number $Re_l = \frac{\rho_l \cdot V_l \cdot \delta_l}{\mu_l}$ and the gas-dynamic pressure at the nozzle-exit edge $q_a = \frac{\rho_a \cdot V_a^2}{2}$ were maintained identical in the experiments. The values of Re_l and q_a were 19 and $2.4 \cdot 10^4$ Pa, respectively.

The experimental results are plotted in Figs. 2.33-2.38 as distribution functions of drops in terms of sizes, directions, and velocities.

It is possible to see a significant difference in experimental results for a supersonic nozzle and a tube. For example, it follows from Figs. 2.35 and 2.36 that most drops (preferential direction) fly with an angle of approximately 80° from the jet axis for the supersonic nozzle and with an angle of approximately 150° for the tube. At the same time, in both cases, drops scatter practically into a full sphere. It is also visible that some differences in velocities and sizes of the formed drops are observed.

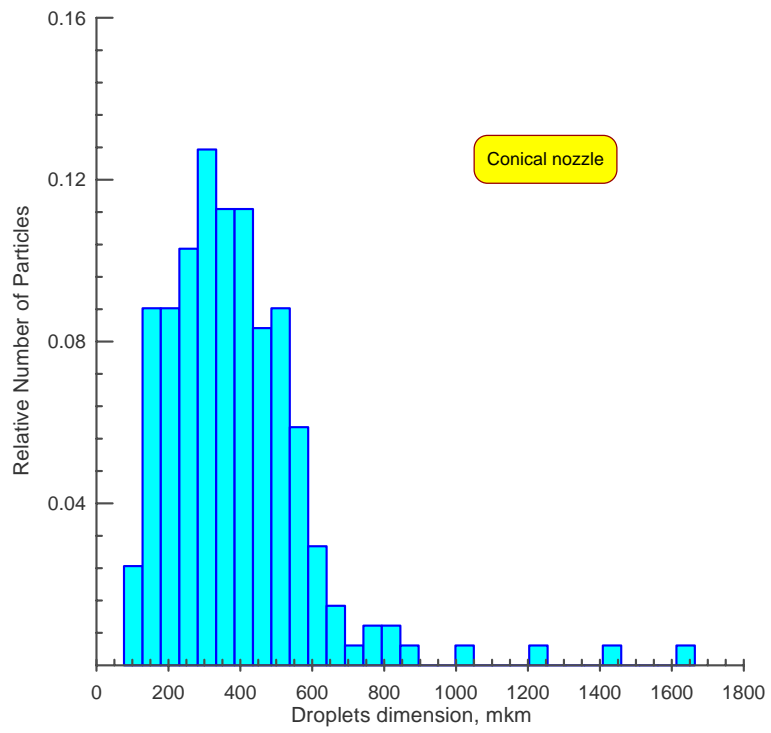


Fig. 2.33. Size distribution of drops for the conical nozzle with ethanol

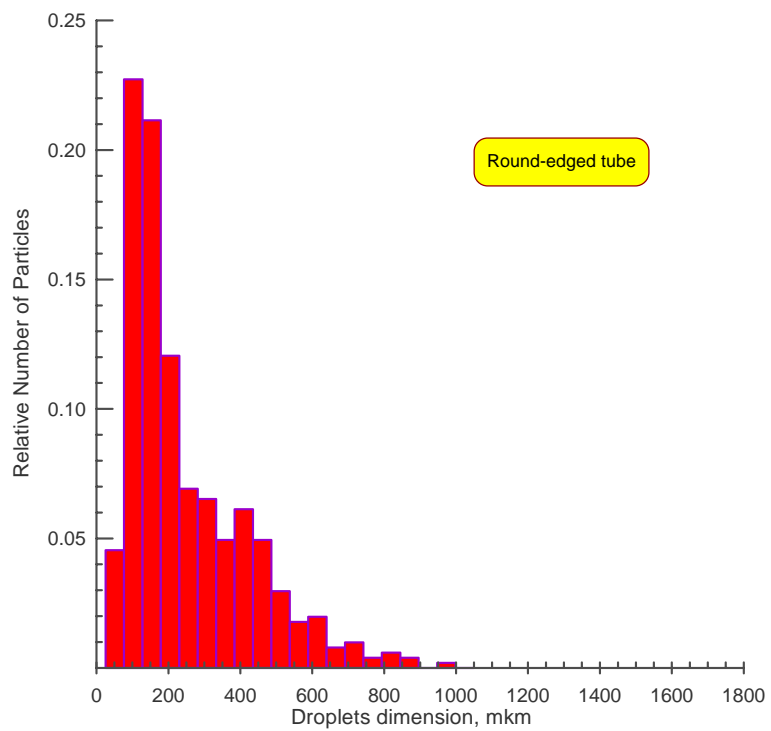


Fig. 2.34. Size distribution of drops for the tube with ethanol

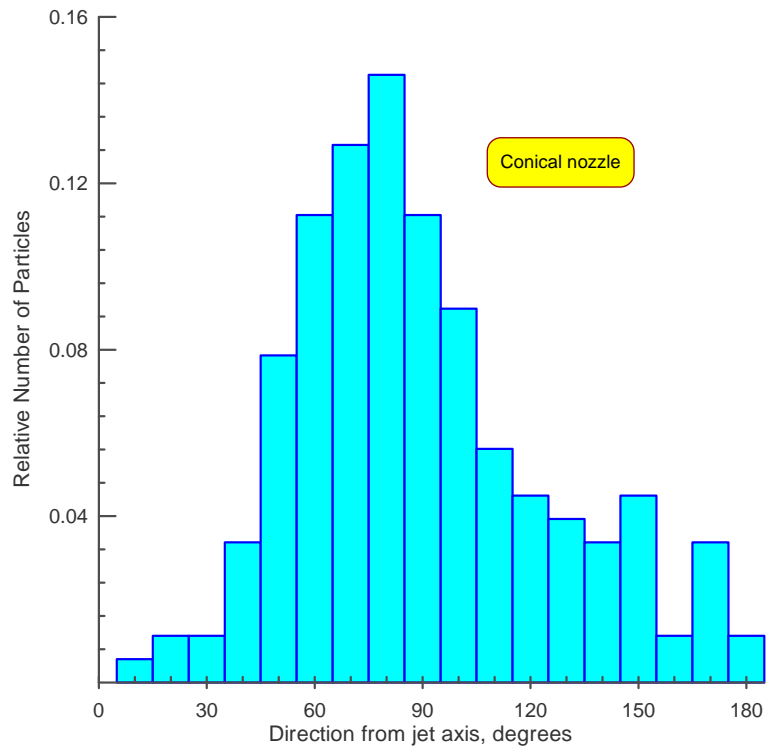


Fig. 2.35. Direction distribution of drops for the conical nozzle with ethanol

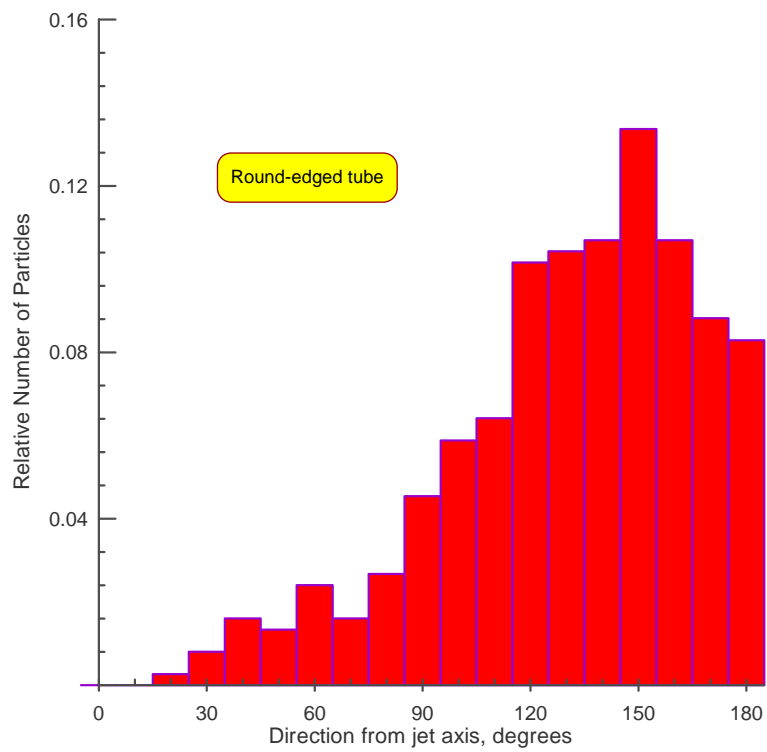


Fig. 2.36. Direction distribution of drops for the tube with ethanol

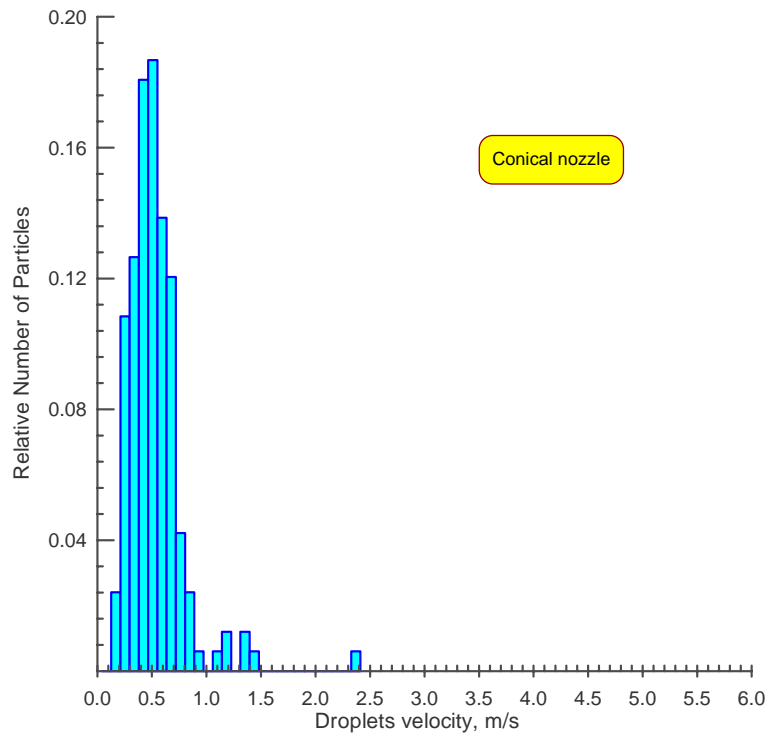


Fig. 2.37. Velocity distribution of drops for the conical nozzle with ethanol

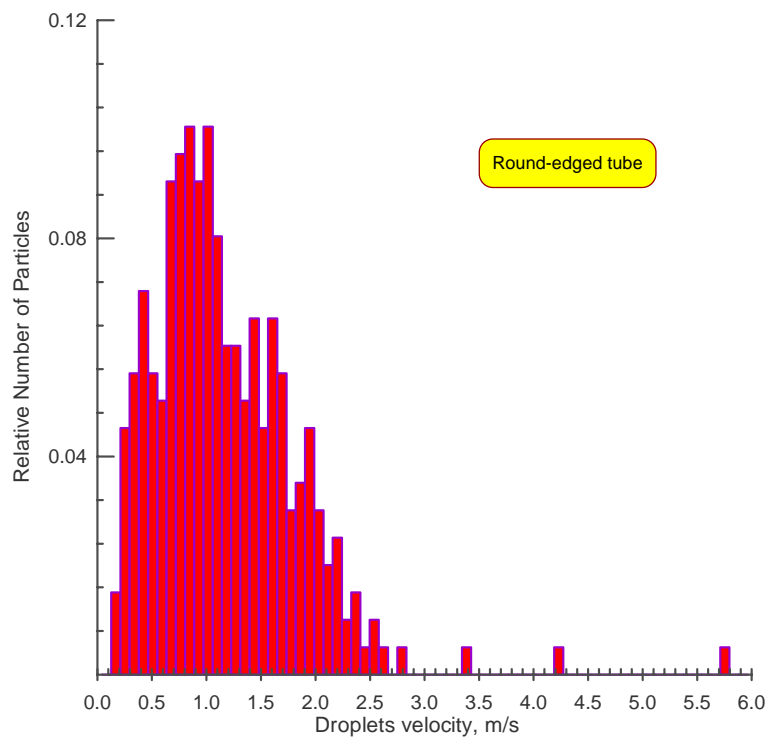


Fig. 2.38. Velocity distribution of drops for the tube with ethanol

Influence of gas-flow parameters

In this series of measurements, the results for the same tube for different flow rates of the co-current air flow (different gas pressures in the plenum chamber) were compared at approximately identical Reynolds numbers of the film $Re_l \approx 19$. The corresponding results for the size distributions of drops are shown in Figs. 2.39 and 2.40 for $p_o = 7.6 \cdot 10^4$ Pa and $p_o = 1.3 \cdot 10^5$ Pa. Figure 2.39, in fact, reproduces Fig. 2.34; however, for convenience of comparison, it is placed together with Fig. 2.40. From the comparison, it is definitely visible that the effect of parameters of the co-current gas flow is observed.

Influence of physical properties of the liquid

In this series of measurements, the results for various liquids (ethanol and butanol) were compared. All other parameters (nozzle geometry and flow rates of the gas and liquids) were identical. As was already mentioned, ethanol and butanol differ in terms of saturated vapor pressure approximately by an order of magnitude. At the same time, other physical properties (density, viscosity, surface tension, etc.) are not much different. The measured results on the size distribution of drops for butanol and ethanol are plotted in Figs. 2.41 and 2.42. One can see that the results are qualitatively similar.

Certainly, to completely eliminate the effect of explosive evaporation of the liquid in vacuum on the measurement results, it is necessary to use liquids with very low pressure of saturated vapors at room temperature, for example, vacuum oils. However, their viscosity is greater than the ethanol viscosity by one or two orders. Other liquids, with more suitable properties than butanol, for example, butylbenzene ($C_{10}H_{14}$), are extremely expensive.

The above-given experimental data on the influence of the number of important parameters on formation and behavior of drops arising upon supersonic gas outflow into vacuum with the near-wall liquid film allowed us to obtain new interesting information on gas-droplet flows in vacuum. Nevertheless, it is difficult to give now unequivocal explanations to the facts observed in the experiments. Further accumulation and analysis of experimental data for constructing models of interaction of the co-current gas flow with the near-wall liquid film inside the nozzle and, especially, of disintegration of the near-wall film on the exit edge and external surface of the nozzle are needed. Such attempts were made, and some of the results obtained are presented below.

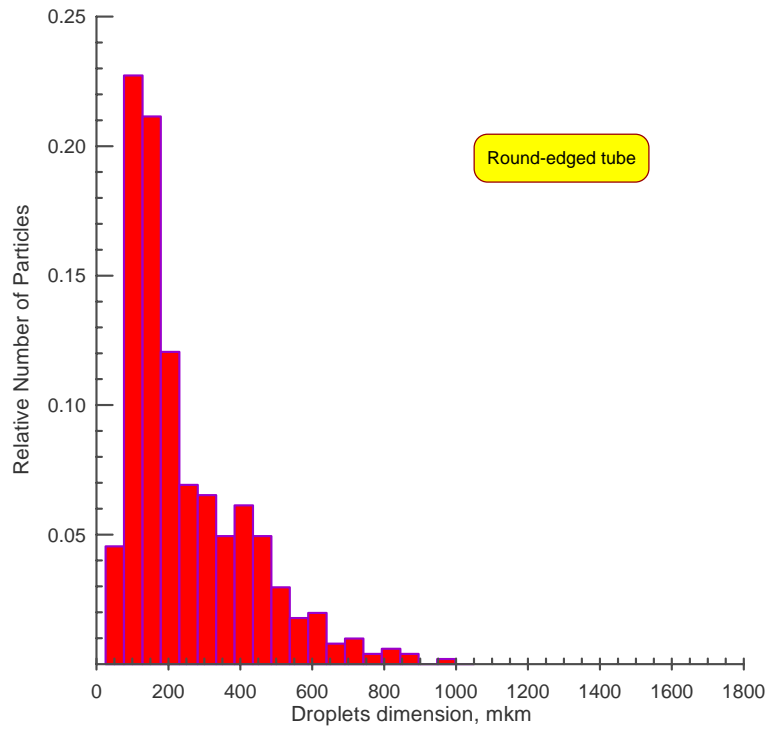


Fig. 2.39. Size distribution of drops for the tube with ethanol for $p_o = 7.6 \cdot 10^4$ Pa

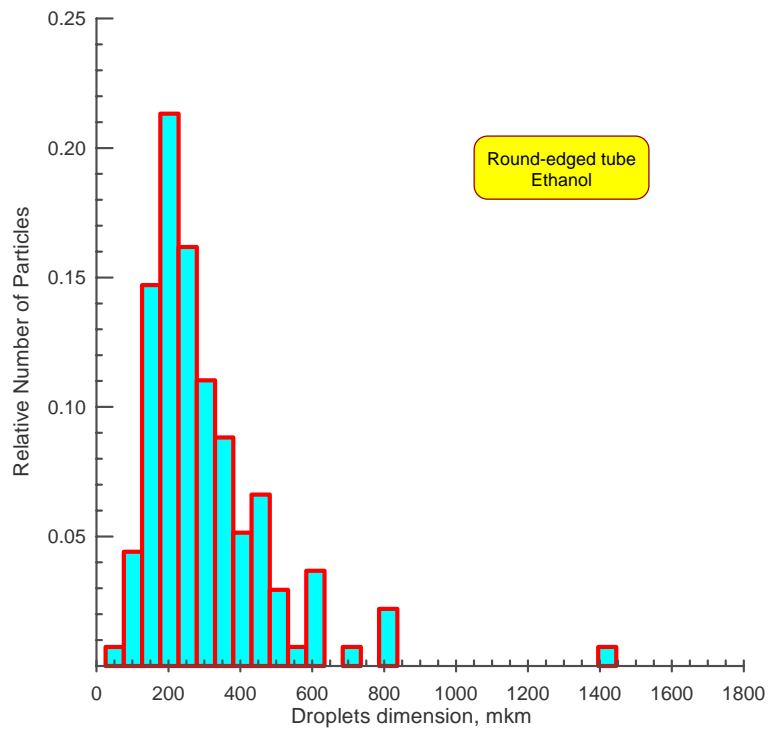


Fig. 2.40. Size distribution of drops for the tube with ethanol for $p_o = 1.3 \cdot 10^5$ Pa

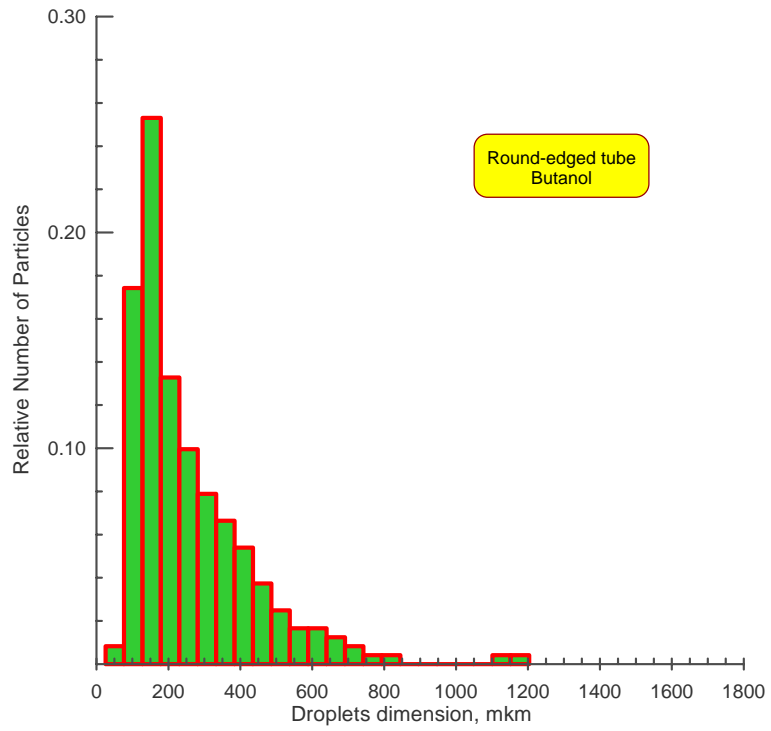


Fig. 2.41. Size distribution of drops for the tube with butanol

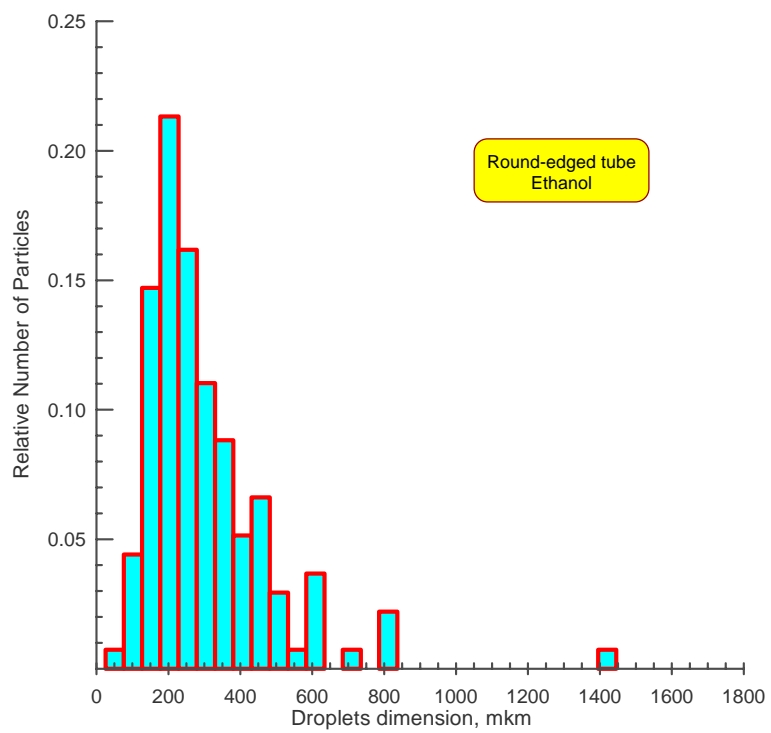


Fig. 2.42. Size distribution of drops for the tube with ethanol

General structure of the droplet phase flow

According to experimental researches performed at the Institute of Thermophysics SB RAS, the general structure of the droplet phase flow arising upon supersonic ejection of a gas from a supersonic nozzle into vacuum with a near-wall liquid film (Fig. 2.43) was found.

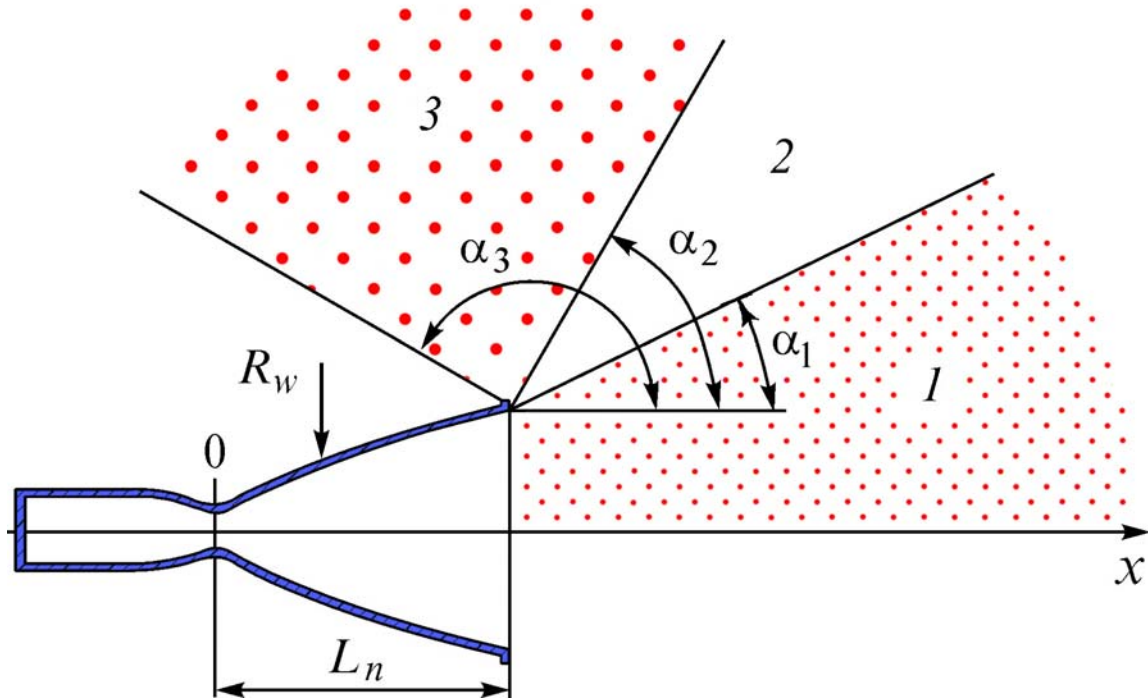


Fig. 2.43. General structure of the droplet phase flow

Two characteristic regions of the droplet phase flow (central 1 and peripheral 3) are observed. Region 1 is caused by droplet shedding from the film surface near the nozzle throat, and their subsequent fragmentation and acceleration in the gas flow inside the nozzle and in the jet behind it. Region 3 is formed by disintegration of the near-wall liquid film on the exit edge of the nozzle, where the pressure drastically increases and the liquid becomes overheated. The process of disintegration is complicated and is caused by interaction of inertial, viscous, surface, gas-dynamic, and other forces. It is obvious that a competition of these forces is caused by the influence of the basic physical properties of the liquid (saturated vapor pressure, evaporation heat, surface tension, and viscosity), parameters of the co-current gas flow (relative velocity, nozzle shape, pressure, and temperature), and the shape of the nozzle exit edge.

In region 2, either the gaseous or the gas-cluster structure of the flow is observed.

One of the features of the considered problem of the gas-droplet flow arising upon joint ejection of the liquid film and gas into vacuum is the transformation of the gas phase flow pattern from continual inside the nozzle and in its vicinity to transient in the near field of the jet and free-molecular in the far field of the jet. Inside the jet, therefore, one can expect the influence of nonequilibrium and rarefaction effects on interaction of drops with the supersonic rarefied flow.

Proceeding from the objectives of the Project, the main attention at this stage of research was paid to the near-wall film whose evolution results in formation of back flows of the droplet phase. Note that the central region of the droplet phase flow is also of great interest, as its occurrence is caused by interaction of the co-current gas flow with the near-wall liquid film inside the nozzle.

Parameters of the near-wall liquid film at the exit section of the nozzle

A significant effect on formation of the structure of the gas-droplet jet escaping into vacuum can be exerted by its history: motion of the near-wall liquid film with the co-current gas flow inside the nozzle. The film thickness δ_1 and its average velocity V_1 at the nozzle-exit section can be taken as the basic parameters of the near-wall liquid film. The values of δ_1 and V_1 can be calculated if the flow rate of the liquid per second m and the shear stress τ on the gas-liquid interface are known:

$$m = 2\pi R\delta_1\rho_1V_1, \quad (2.1)$$

$$\tau_w = \frac{C_f}{2}\rho V^2 = \mu_1 \frac{2V_1}{\delta_1}. \quad (2.2)$$

Therefore, we obtain

$$\delta_1 = \sqrt{\frac{m\mu_w}{\pi R\rho_1\tau_w}}, \quad (2.3)$$

$$V_1 = \sqrt{\frac{m\tau_w}{4\pi R\rho_1\mu_1}}. \quad (2.4)$$

Currently, there is no information in the literature for determining τ on the external boundary of the film in the presence of a high-velocity (including supersonic) co-current gas flow. However, owing to a small thickness of the near-wall liquid film, the magnitude of the shear stress τ on the external surface of the film can be taken as the first approximation equal to its value τ_w on the channel wall in the absence of the film.

Though the accepted flow model is rather simple, it allows one to estimate the thickness and velocity of the film moving inside the nozzle with a co-current gas flow. The estimations show that, under conditions of our experiments, the characteristic values of the film thicknesses and velocities at the nozzle exit section did not exceed 0.1 mm and 1 m/s, respectively.

Effect of film lifting on the external surface of the nozzle against gravity

It was noticed in the experiments that, being ejected into vacuum with a co-current gas flow, the near-wall liquid film flowing on the internal surface of the nozzle not only decomposes into drops at the nozzle-exit edge but also goes out onto the external surface of the nozzle, moving in the opposite direction, even against gravity. The phenomenon observed depends, other parameters being equal, mainly on the value of pressure in the ambient space. As an example, Figs. 2.44 and 2.45 show the photographs for a nozzle shaped as a cylindrical tube, which demonstrate how the flow structure varies with decreasing pressure in the vacuum chamber. Figure 2.44 corresponds to ejection into space with atmospheric pressure, and Fig. 2.45 refers to ejection into space with a low pressure ($p_\infty \leq 10$ Pa). One can see that ejection into vacuum leads to appearance of a liquid film (approximately 1 mm thick) on the external surface of the nozzle. The same picture is observed with a supersonic nozzle.

Figures 2.46 and 2.47 show the measured results on the height of film lifting at different pressures in the vacuum chamber for the tube (Fig. 2.46) and supersonic nozzle (Fig. 2.47). The stagnation pressure p_0 was approximately $1.3 \cdot 10^5$ Pa in the first case and 10^5 Pa in the second case. The stagnation temperature in both cases was identical and equal to 300 K. The mass flow rate of the liquid was about 10 % of the gas flow rate.



Fig. 2.44. Ejection of the liquid with a co-current gas flow into the atmosphere

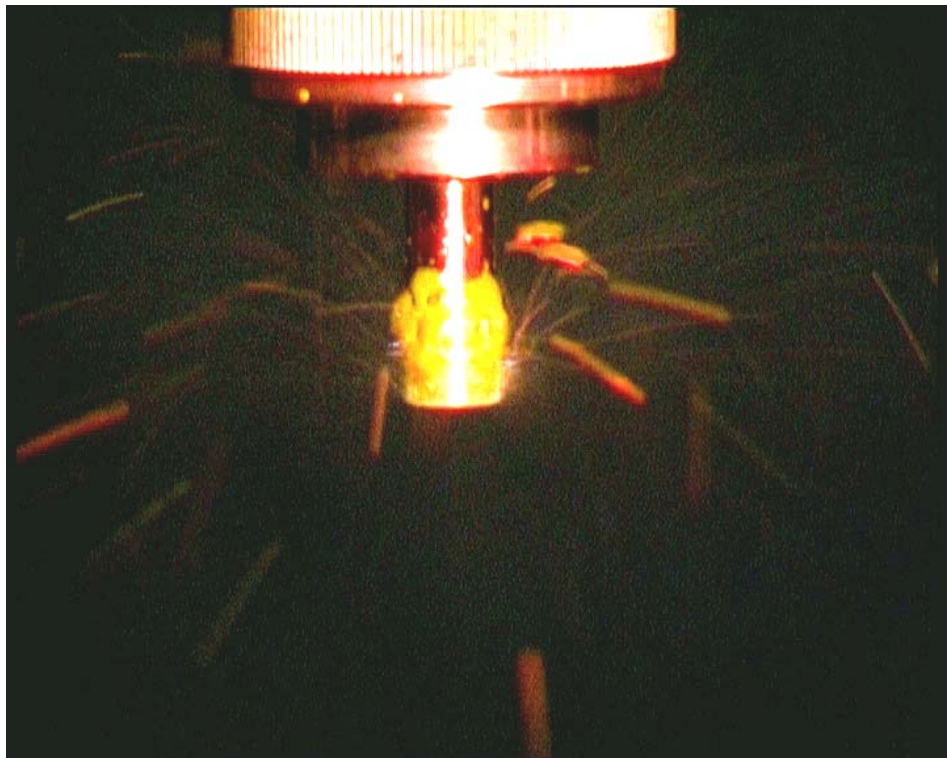


Fig. 2.45. Ejection of the liquid with a co-current gas flow into vacuum

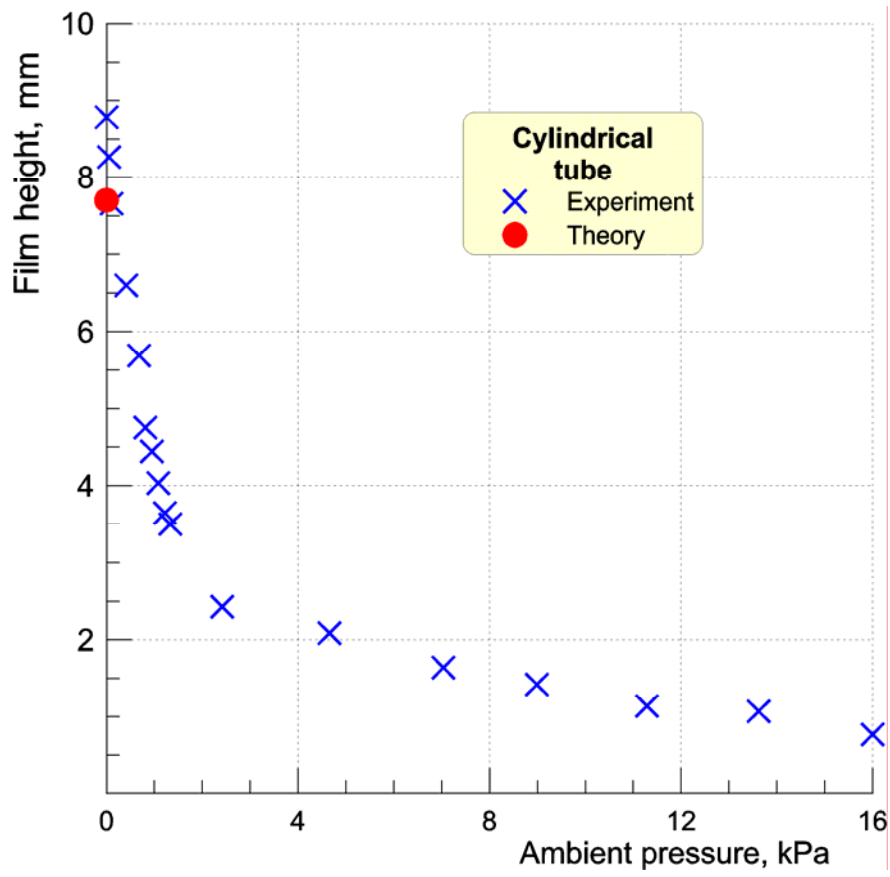


Fig. 2.46. Film height on the external surface of the tube

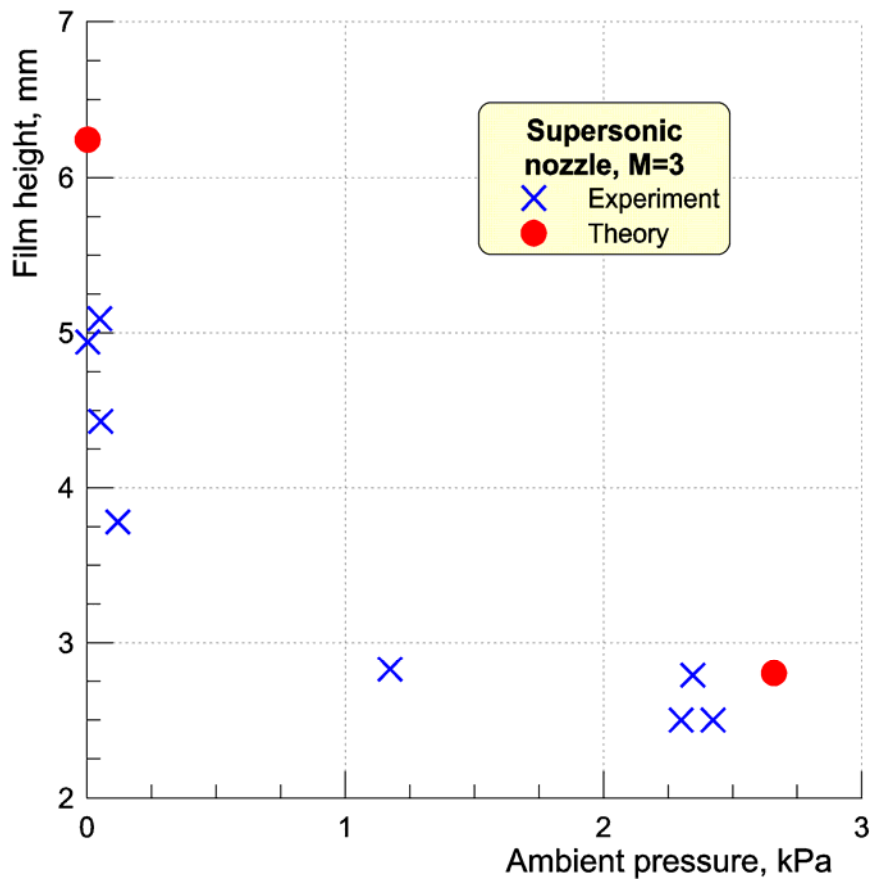


Fig. 2.47. Film height on the external surface of the nozzle

The analysis of experimental results leads to the following scheme of the stationary regime of flow formation. When the gas and liquid are injected, a liquid film is formed on the internal wall of the nozzle; under the influence of the gas stream and gravity, mainly owing to the first factor, the film moves to the nozzle edge. At the nozzle edge, the film turns and goes out onto the external surface of the nozzle. Film turning is stipulated by forces of adhesion and, probably, the Coanda effect, and film lifting is caused by interaction with the gas stream. Thus, there exists a maximum height h_m of film lifting, which depends on the gas-stream and liquid parameters. Accordingly, there is a certain, critical amount of liquid that can be contained in the film. Therefore, as soon as this amount of liquid in the film is accumulated, the stationary condition of the flow is formed: there is a film of height h_m on the external surface of the nozzle, and all new incoming liquid is carried away by the jet from the lower edge of the nozzle in the form of drops. Disintegration of the film into drops occurs owing to the Rayleigh-Taylor instability of the film under the influence of both the gas stream and gravity.

Certainly, the real process is much more complicated. Disturbances can be formed on the surface of the film inside the nozzle, resulting in shedding of drops and/or disintegration of the film, and also stimulating the Rayleigh-Taylor instability of the film on the bottom edge. At the exit edge and external surface of the nozzle, the liquid can be subjected to explosive boiling and/or intensive evaporation. The effects of viscosity can be essential for some liquids, and adhesion forces can be important for some combinations of the liquid and nozzle material.

Nevertheless, the offered scheme allows one to construct a model that yields estimates in satisfactory agreement with the experimental results.

Under conditions of the experiments (the nozzle is mounted vertically with the exit cross section directed downward), the height of film lifting h_m can be estimated from the balance of forces on the film

$$\rho_l g h_m = p_{g1} - p_{g2} + p_L \quad (2.5)$$

where ρ_l is the density of the liquid, g is the acceleration of gravity, p_{g1} and p_{g2} are the pressures in the gas at the bottom and top edges of the film, and p_L is the Laplace pressure at the bottom edge of the film, which in this case equals σ/r , where σ is the surface tension of the liquid and r is the radius of curvature of the film. For ethanol, $\rho_l = 0.79 \text{ g/cm}^3$ and $\sigma = 0.022 \text{ N/m}$.

Taking into account that the characteristic thickness of the film inside the nozzle ($\approx 0.1 \text{ mm}$) is much smaller than the edge thickness l , and the thickness of the film on the external surface is commensurable with l , it can be assumed that $r = l$ for calculation of the Laplace pressure; in both cases (for cylindrical and conical nozzles), we have $p_L = 22 \text{ Pa}$.

It is possible to use the pressure reached at turning by 90° in the Prandtl-Meyer wave of the gas flow with a Mach number at the nozzle-exit cross section $M_C = 1$ and a ratio of specific heats $\gamma = 1.4$ as p_{g1} for a cylindrical nozzle. Then, $p_{g1}/p_0 \approx 2.9 \cdot 10^{-4}$, and we obtain $p_{g1} \approx 39 \text{ Pa}$ for conditions of the experiments in Fig. 2.46. The same value of p_{g1}/p_0 can also be accepted for a conical nozzle, taking into account that there is a boundary layer inside the nozzle; therefore, close to the nozzle edge, the value $M = 1$ is more typical rather than the "geometrical" value $M_C = 3$. In this case, we have $p_{g1} \approx 29 \text{ Pa}$.

As to pressure on the top border of the film, it depends on a number of factors (jet pressure ratio, its rarefaction, etc.) and generally requires numerical calculation of the flow field. However, there are two cases, when the estimations can be carried out without numerical modeling. In the first case, the expansion occurs practically into vacuum ($p_\infty \approx 0$), and the value of p_{g2} can be neglected. As a result, using expression (2.5), we obtain $h_m \approx 7.7 \text{ mm}$ for a cylindrical nozzle and $h_m \approx 6.6 \text{ mm}$ for a conical nozzle. The second case corresponds to

conditions of an isobaric jet $p_c = p_\infty$, which occurs in experiments with a conical nozzle. Here, $p_{g1} = p_{g2}$, and formula (2.5) predicts $h_m \approx 2.8$ mm. As is visible in Figs. 2.46 and 2.47, which show the values of h_m by filled circles, the theoretical estimations correspond to the experimental data fairly well. It gives grounds to hope that the simple model proposed takes into account the major factors determining film formation on the external surface the nozzle.

Task 2.6.1. Verification of the technique of a quartz microbalance for measuring spatial distributions of droplet-phase flows of the liquid evaporating into vacuum. Assembling and testing of the system for registration of small droplets

The measurement of spatial distributions of droplet phase flows in supersonic gas-droplet streams is an important and, simultaneously, a difficult task. The basic difficulty consists in fast evaporation of the drops hitting the sensor or substrate. Certainly, it is possible to speak about cryogenic freezing of drops; however, this way is technically complicated and little promising since we are speaking about measurements not at a separate point but within the entire flow field, including back flows. In the present work, the difficulty in measurements associated with liquid evaporation in vacuum was avoided by adding a specially chosen dye that is not sublimating in vacuum into the modeling liquid. In such an approach, the quantity of the liquid phase is determined by the quantity of the dye remaining on the sensor after liquid evaporation. Rhodamine 6gKDM (xanthene dye) was used as a dye. The weight concentration of the dye was 0.065 % and, in our opinion, could not significantly affect the physical properties of liquids that were used in experiments (ethanol and butanol).

In performing this stage of the Project, three above-mentioned independent techniques of measuring spatial distributions of droplet-phase flows were developed. A description of the techniques and their comparison by an example of measurements of spatial distributions of the droplet phase in the gas-droplet flow formed upon supersonic expansion of the gas from the nozzle into vacuum with a near-wall liquid film is given below. A conical nozzle with a Mach number $M = 3$, nozzle-throat diameter of 5 mm, and nozzle-exit diameter of 10 mm was used in these experiments. The test gas was air, and the test liquid was butanol. The stagnation pressure P_0 was $1.2 \cdot 10^5$ Pa, and the flow rate of the liquid was 0.5 g/s.

Scheme of measurements

The measurement scheme shown in Fig. 2.48 was used to obtain spatial distributions of the droplet phase. It includes a source of the gas-droplet flow 1 with a replaceable nozzle 2, a measuring ring (hoop) 3 with sensors 4 mounted on it, and a rotary mechanism 5. The rotary mechanism provided a required residence time of the measuring ring in the gas-droplet flow. The center of the measuring ring coincided with the center of the exit cross section of the nozzle. The ring radius R was equal to 75 mm and was chosen proceeding from minimization of the influence of gravity forces on measurement results and maintenance of necessary accuracy of measurements. The measurements were performed in the range of angles from the jet axis θ from -30° to $+150^\circ$.

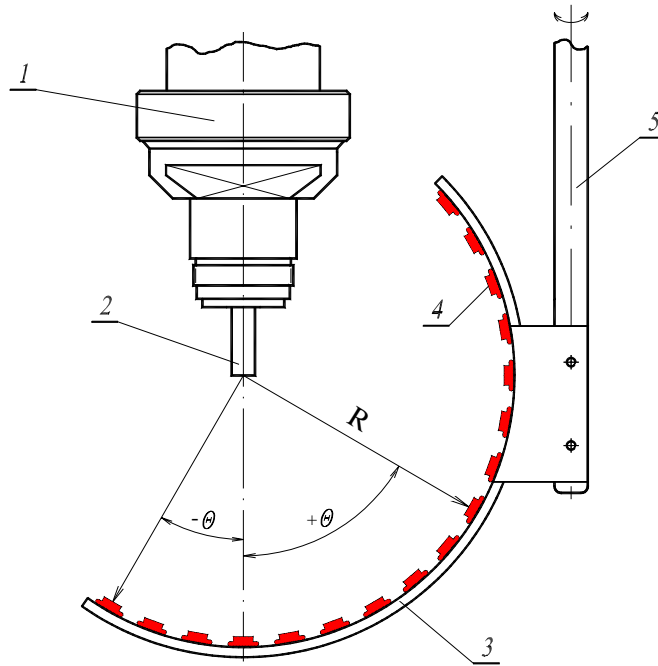


Fig. 2.48. Scheme of measurements

Technique of a quartz microbalance

At the first stage of mastering the measurement technique, a quartz microbalance (QMB) was used as a sensor. A similar method is widely applied to control the thickness of sprayed films in microelectronics, for example, during manufacturing microchips. The method has high sensitivity and can be used for measurements in vacuum in any space position. The sensor is a quartz disk 5-15 mm in diameter with current supplies. The working part of the sensor (sprayed Ag film) is in the centre of the quartz disk. The diameter of the working part is approximately 1/3 of the disk diameter. The principle of measurement is based on the change in frequency of superficial fluctuations of a quartz plate included into the oscillator circuit depending on the sprayed film thickness or, which is the same, on its weight:

$$\Delta \nu = C \cdot m,$$

where C is the sensitivity coefficient and m is the film weight. The frequency of such fluctuations for specially cut plates weakly depends on temperature and other external conditions. The QMB sensitivity can reach 10^{-9} g.

For implementation of the QMB method, a driving oscillator was developed and assembled.

Since the dependence of the change in QMB frequency versus the film weight is unknown a priori, is necessary to calibrate each sensor, which is a rather difficult procedure, as we are speaking about very small quantities of substance.

Calibration was reduced to deposition of a known quantity of the liquid with a given weight concentration of the dye on the QMB working surface and measurement of quartz fluctuation frequency after liquid evaporation.

An example of calibration for one of the sensors is given in Fig. 2.49.

The sensors were calibrated every time before their installation into the vacuum chamber for conducting measurements of spatial distributions of the droplet phase.

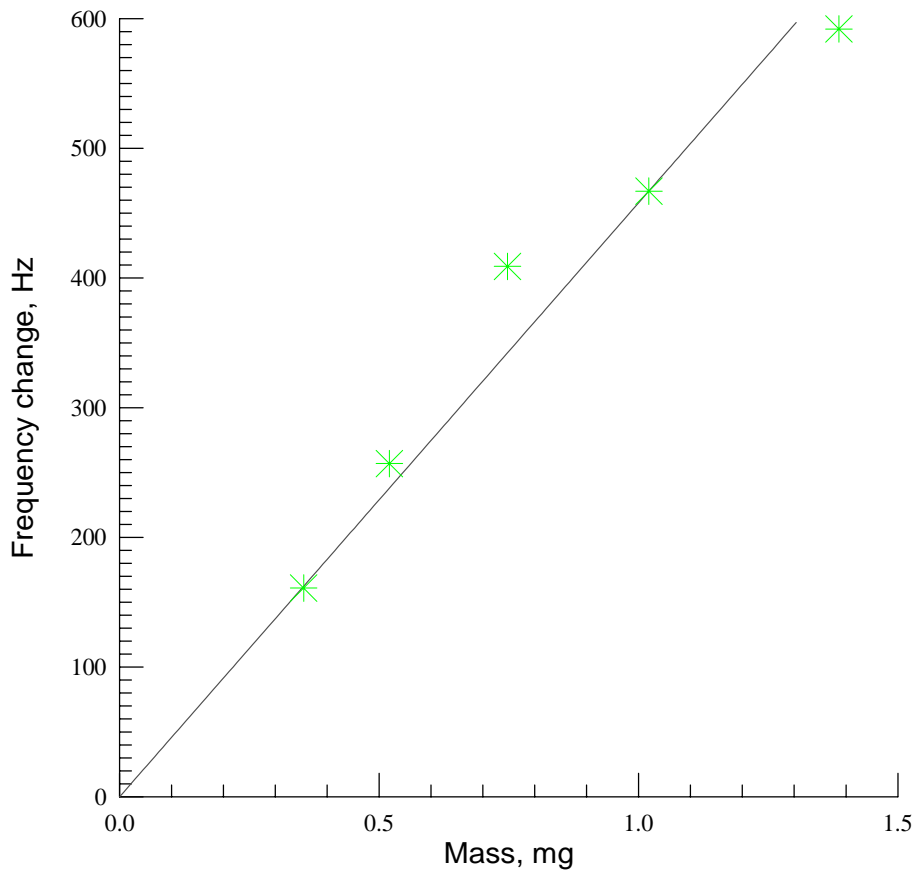


Fig. 2.49. Example of QMB sensor calibration

The capabilities and restrictions of the QMB method for diagnostics of supersonic gas-droplet flows were found out in methodical measurements. In particular, it was established that, in our conditions, this method has a restriction from above on the quantity of the droplet phase flow incoming onto the sensor. As this value exceeded, the drops formed a film flowing down the sensor before they evaporated. The effect depends on the spatial orientation of the sensor and is maximal if the working plane of the sensor is located vertically.

In addition, it was found that the QMB method is inapplicable for measurements in the central (axial) region of the gas-droplet flow. This region (see Fig. 2.43) is characterized by the presence of finely dispersed high-speed drops. Apparently, these drops have a rather high erosive ability, because destruction of the working part (sprayed Ag film) on the sensors in the axial region was observed.

Despite of the specified restrictions, the QMB method allows receiving quantitative information on the spatial distribution of the droplet phase in gas-droplet flows in vacuum. The results of measurements for the above-mentioned test conditions are shown in Fig. 2.50. One can see that there is a preferential direction (maximum at $\theta \approx 60^\circ$ relative to the jet axis) and also back flows of the droplet phase (at $\theta > 90^\circ$). The data on the central part (for angles θ approximately equal to $\pm 30^\circ$) are not given for the reasons stated above.

The rather severe restrictions of the QMB method under our conditions made us seek other principles and develop, on their basis, other techniques of droplet-phase diagnostics in supersonic gas-droplet flows. Two of these techniques described below proved to be rather successful.

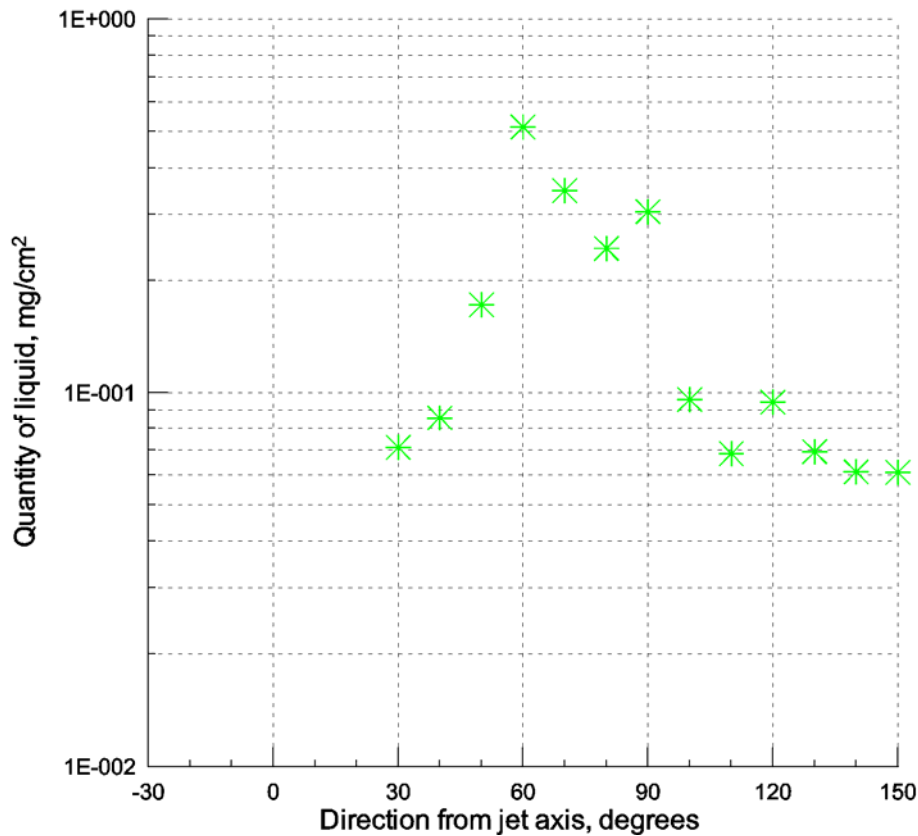


Fig. 2.50. Spatial distribution of the droplet phase measured by the QMB technique

Technique of spectrophotometry

The basic idea of this technique consists in using methods of spectral photometry for determining the amount of the dye (solid residue) remaining on the sensor after evaporation of drops incoming onto the sensor. The water solutions of rhodamine 6gKDM chosen as a dye have a maximum of absorption at $\lambda = 5260 \text{ \AA}$. Thus, for obtaining the spatial distribution of the droplet phase in the gas-droplet flow, it is necessary to experimentally obtain an appropriate spatial distribution of the solid residue, to prepare a necessary amount of vats with a water solution of the solid residue, and obtain the spatial distribution of the dye with the help of a spectrophotometer and results of previous calibrations. Further, with a known initial concentration of the dye, this distribution is recalculated to the true distribution of the droplet phase.

A photograph of the ring with the sensors located on it for measuring the spatial distribution of the droplet phase by this technique is shown in Fig. 2.51.

Sampling of drops from the gas-droplet flow was performed with the help of thin-walled tubes about 6 mm in diameter and about 15 mm long. Inside each tube, there was a volumetric absorber of drops. Surgical cotton wool was used as an absorber. The use of a volumetric absorber eliminated the effect of liquid trickling and provided capturing of all the incoming drops. In vacuum, the working liquid rapidly evaporated, and the dye remained in the absorber.

When the experiment was finished and the vacuum chamber was filled up to atmospheric pressure, the tubes with the absorber were taken out from the vacuum chamber and were located for approximately 2 hours into separate vats with a 40% solution of ethanol in water to wash out the dye from the absorber and internal surface of the tube. To increase the measurement accuracy, the outside surface of the tube was wiped to remove the traces of the dye before placing into the vat.

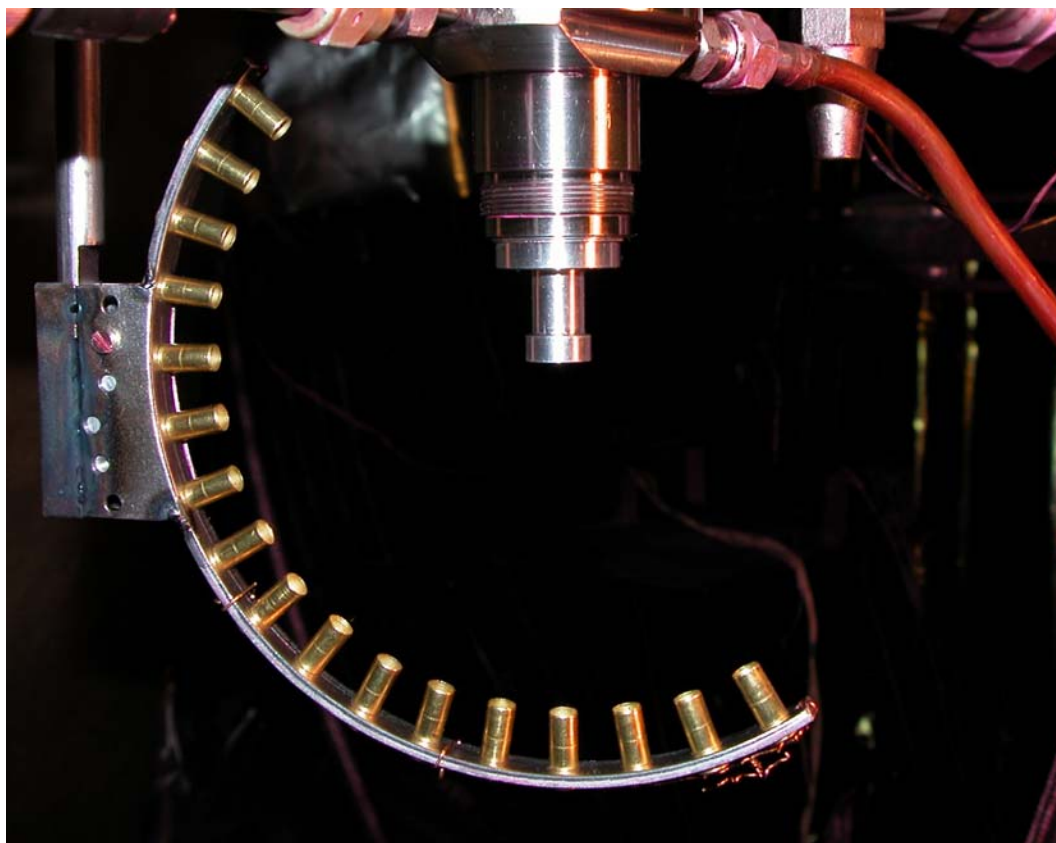


Fig. 2.51. Photo of the measuring ring with tubes-sensors

The concentration of the dye in the resultant solution was determined by the value of light absorption by the solution at the wavelength $\lambda = 5260 \text{ \AA}$. An SF-26 single-beam spectrophotometer designed for measuring the spectral transmittance of liquid and solid substances was used in these measurements. The spectral range of measurements of this device is 1900-11,000 \AA .

An example of calibration and the measurement results are shown in Figs. 2.52 and 2.53, respectively. Though this technique is rather labor-consuming (approximately 5 hours after extraction of tubes-sensors from the vacuum chamber are required before the final results are obtained), it allows obtaining quantitative information on the spatial distribution of the droplet phase in the entire flow field, including the central part of the gas-droplet flow. An analysis of the data obtained will be given below.

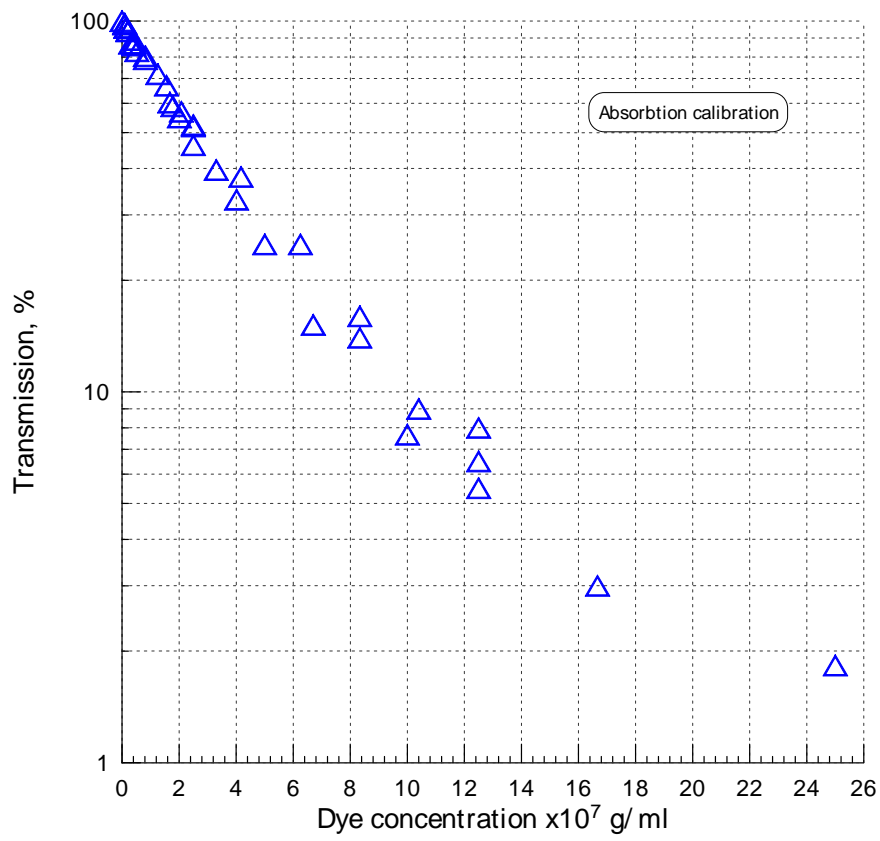


Fig. 2.52. Example of calibration by the spectrophotometry technique

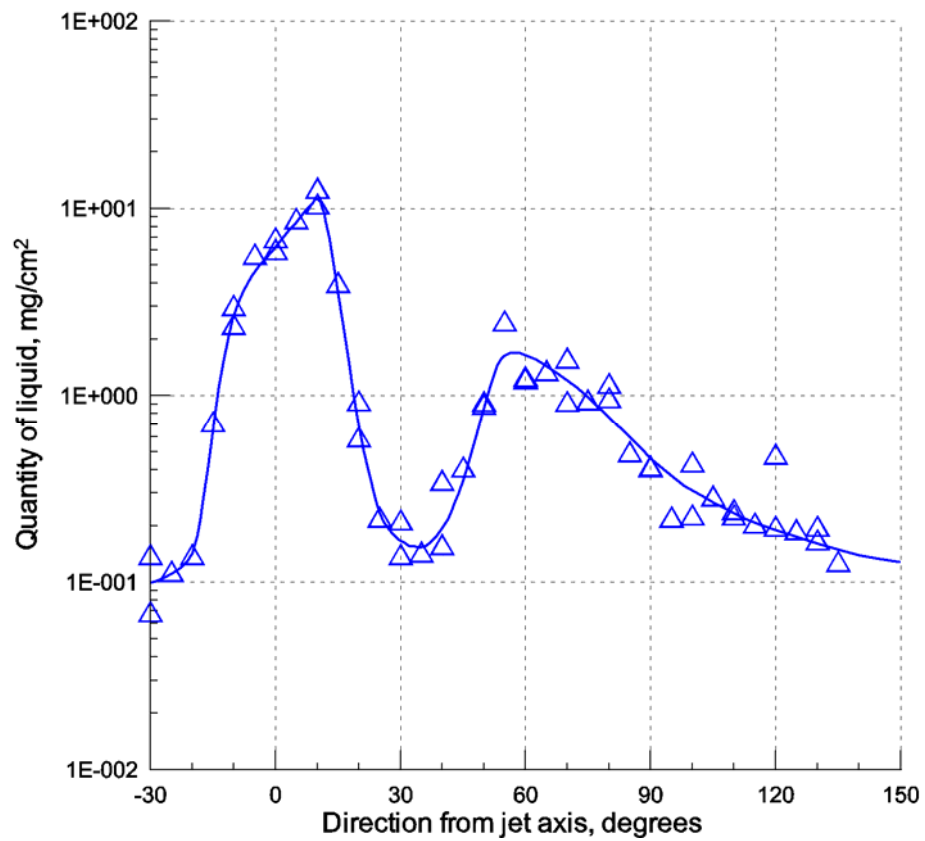


Fig. 2.53. Spatial distribution of the droplet phase measured by the spectrophotometry technique

Technique of deposition on a paper strip

The techniques described above, especially the technique of spectrophotometry, allow measuring flows of the droplet phase in chosen directions. These measurements have a discrete character and are rather labor-consuming. It is often necessary to obtain real-time information of the preliminary character on the spatial distribution of the droplet phase in range of variation of regime parameters of interest. This can be done by placing a paper or film strip on the measuring ring. We chose narrow (6 mm wide) strips of paper for jet printers. As the experiments have shown, this paper can absorb a rather large amount of the liquid without trickling, whereas the trickling effect was rather frequently observed if a film was used.

After the experiment, the paper strip was taken out from the vacuum chamber and was scanned on a scanner. The resultant full-color image was converted into an 8-bit gray image and then the angular dependence of dyeing intensity with simultaneous averaging over the strip width was observed from the digitized image with the help of a specially developed program.

The general view of the paper strip is shown in Fig. 2.54; the result of processing are plotted in Fig. 2.55 and compared to the corresponding data obtained by the QMB and spectrophotometry techniques. As the measurement results on paper strips give only the relative spatial distribution of the droplet phase, they were “attached” to the corresponding results obtained by the QMB and spectrophotometry techniques.

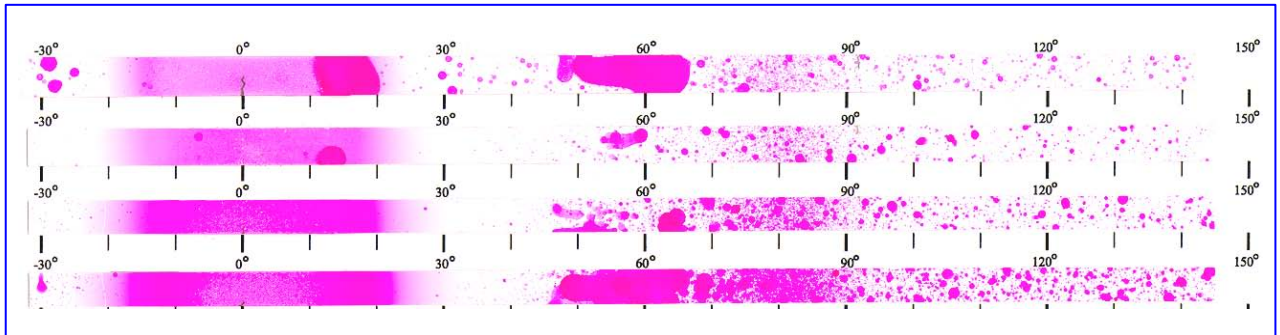


Fig. 2.54. View of the paper strips with deposited droplets

Let us give some comments on the measurement results shown in Fig. 2.55. The most comprehensive information on the distribution of the droplet phase in the gas-droplet flow is provided by the techniques of spectrophotometry and paper strips. The results measured by these techniques rather accurately specify the existence of two characteristic regions of the flow: central (at $\theta \approx \pm 30^\circ$) and peripheral (at $\theta > 40-45^\circ$). The occurrence of these quite different regions of the droplet phase flow is related to specific features of interaction of the cocurrent gas flow with the near-wall liquid film inside the nozzle and on its lip. From Fig. 2.55, one can see that the measurement results near the jet axis are qualitatively different: the technique of spectrophotometry shows the presence of a maximum, and the technique of droplet deposition on a strip predicts a horizontal curve, which, in our opinion, is associated with the effect of saturation of the substrate by the dye.

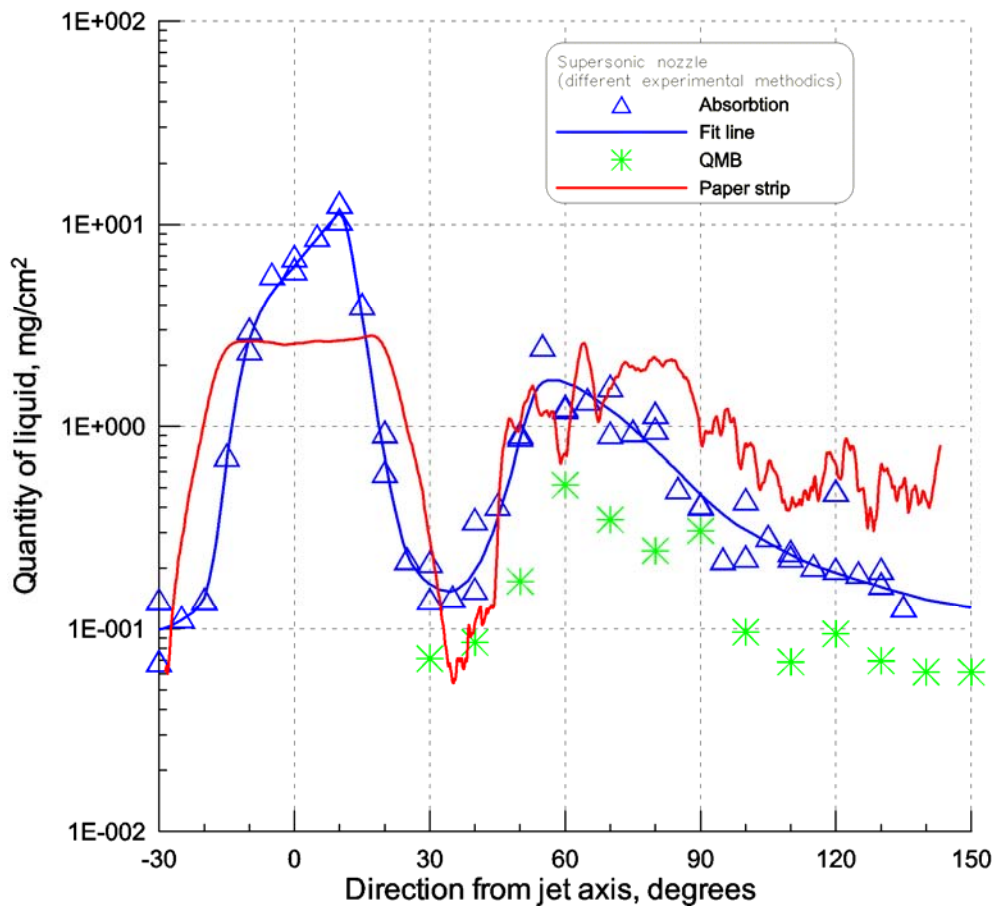


Fig. 2.55. Comparison of the measurement results obtained by different techniques

As a whole, as is seen from Fig. 2.55, the results of measurements by different techniques are rather close. Certainly, the most reliable results are provided by the technique of spectrophotometry. At the same time, rather interesting and useful information is given by the technique of droplet deposition onto a substrate. It is seen, e.g., the curve obtained by processing the paper strip is smooth in the central part of the flow and there are located peaks in the peripheral part of this curve, which is related to the presence of sufficiently large drops in the flow in this region. It is also well seen from Fig. 2.54 that the character of dyeing paper strips in the central and peripheral regions of the flow is different.

The main result of this task of the Project was the creation of three independent techniques for measuring spatial distributions of the droplet phase in supersonic gas-droplet flows. This improves accuracy and reliability of measurements and expands the possibilities of quantitative investigations of gas-droplet flows.

Task 2.6.2. Experiments on studying the droplet phase in a supersonic flow, including the backflow measurements

The measurements of spatial distributions of the droplet phase in a supersonic flow were performed in a range of corners of 0-150° from the jet axis. The corners < 90° correspond to direct flows of the droplet phase, and the corners > 90° correspond to backflows.

In the program of experimental researches, the influence of the following parameters was determined:

- properties and parameters of the gas flow;
- nozzle geometry;
- properties of the liquid;
- shape of the nozzle lip.

The distributions of drops in terms of sizes, velocities, and directions were also measured; a model of near-wall liquid film disintegration into drops at the nozzle lip was suggested.

Influence of gas flow properties and parameters

The basic composition used in experiments on studying the influence of properties and parameters of the co-current flow was air. The stagnation pressure p_0 varied in the range of $(0.4-1.2) \cdot 10^5$ Pa. In part of experiments, which had a research character, Ar and CO₂ were used instead of air.

Typical results of measurements for a supersonic conical nozzle and for a tube nozzle are plotted in Figs. 2.56 and 2.57, respectively. Butanol was used as a modeling liquid. The results were obtained with the use of the spectrophotometry technique.

In Figs. 2.56 and 2.57, the existence of two characteristic regions of the droplet-phase flow in the supersonic gas-droplet flow (central and peripheral) is clearly visible. The reasons for the occurrence of these regions were discussed in detail earlier. Here, we shall dwell only on the experimentally observed fact of the influence of co-current flow properties. In Figs. 2.56 and 2.57, one can see that this influence becomes apparent mainly in the region of backflows. Thus, the values of backflows of the droplet phase with the use of CO₂ as a co-current flow are appreciably lower than those for air. This occurs both in the supersonic nozzle and in the tube nozzle. At the same time, the difference between Ar and air is not so obvious. It is necessary to emphasize here that these data are not results of single experiments and are well reproduced, i.e. reflect some statistics. For the present time, unfortunately, it is not possible to give a clear physical explanation for the fact obtained. Reasoning from the point of view of the change in parameters of the carrier-gas flow, the main difference between Ar, CO₂, and air under the conditions considered consists in possible appearance of effects of homogeneous condensation in Ar and CO₂ flows. Estimations on the magnitude of the parameter $p_0 d_*$ (p_0 is the stagnation pressure and d_* is the diameter of the nozzle throat) show that condensation can affect the gas-dynamics of Ar and CO₂ jets. For data shown in Figs. 2.56 and 2.57, we have $p_0 d_* \approx 6 \cdot 10^5$ Pa·mm. It is known from the literature that, for stagnation temperatures close to room temperature, the influence of condensation in nozzles and in Ar and CO₂ jets is possible for $p_0 d_* \geq 4 \cdot 10^5$ Pa·mm. For $p_0 d_* \leq 4 \cdot 10^5$ Pa·mm, the nonequilibrium processes are frozen. Condensation can essentially affect the distribution of parameters of the gas flow inside the nozzle and in the plume behind it. Another possible reason for the effect observed refers to specific features of interaction of Ar, CO₂, and air with the near-wall liquid film inside the nozzle and in the plume behind it.

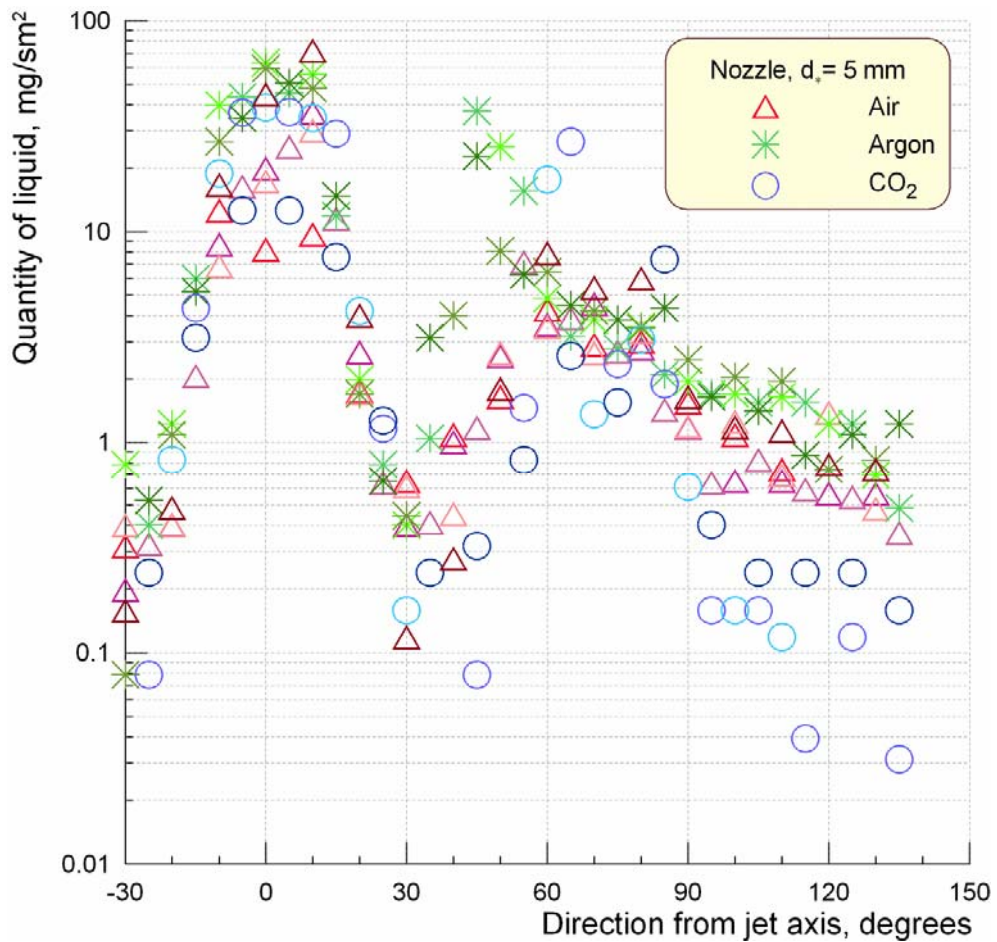


Fig. 2.56. Spatial distribution of the droplet phase.
Conical nozzle. Working liquid – butanol.

Let us now address the results of experiments on the influence of p_0 (parameters of the co-current flow). As was mentioned above, the value of stagnation pressure p_0 varied in experiments in the range of $(0.4-1.2) \cdot 10^5$ Pa. At the same time, all other parameters, first of all, liquid discharge, remained constant. Air was used as a co-current gas flow. The results of experiments for the supersonic conical nozzle and tube nozzle are shown in Figs. 2.58 and 2.59, respectively. Within the experimental error, there is no any appreciable change in the peripheral region of the flow, including backflows of the droplet phase. At the same time, reduction of p_0 by decreasing the dynamic pressure of the gas leads to reduction of the amount of the liquid detached by the co-current flow from the film surface inside the nozzle and entrained into the central part of the jet. Accordingly, the amount of the liquid in the film at the nozzle exit increases. Probably, this compensates for the reduction of the dynamic influence of the gas on drops at the nozzle exit with decreasing p_0 .

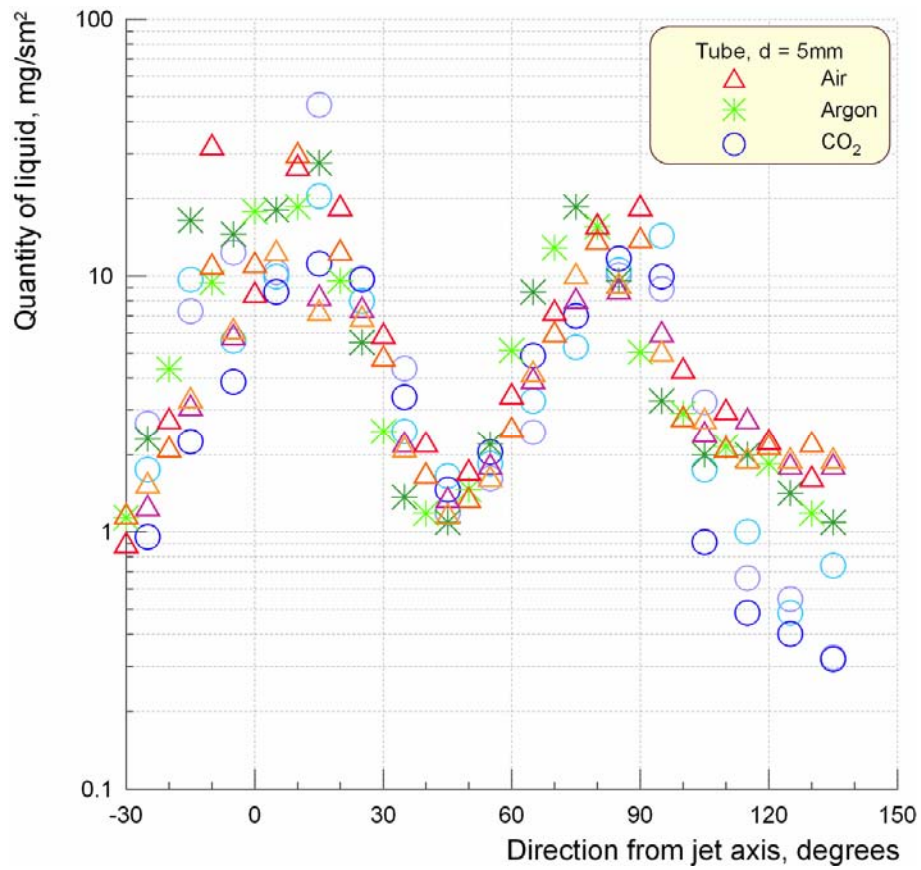


Fig. 2.57. Spatial distribution of the droplet phase.
Tube nozzle 5 mm in diameter. Working liquid - butanol

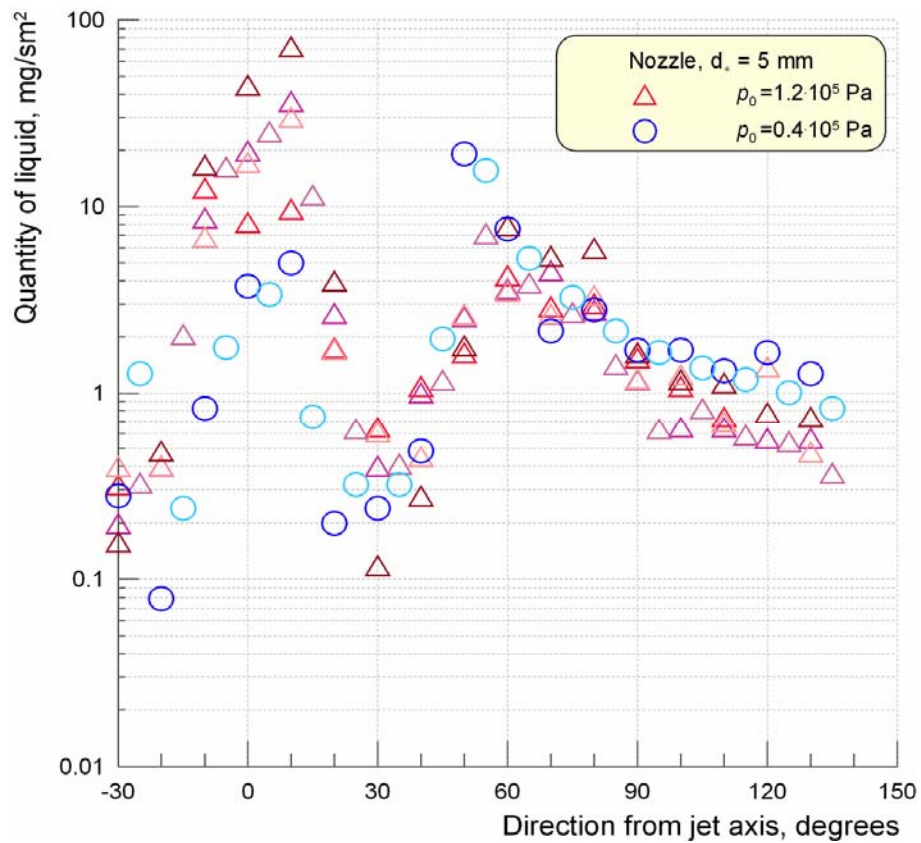


Fig. 2.58. Spatial distribution of the droplet phase.
Conical nozzle. Working liquid - butanol

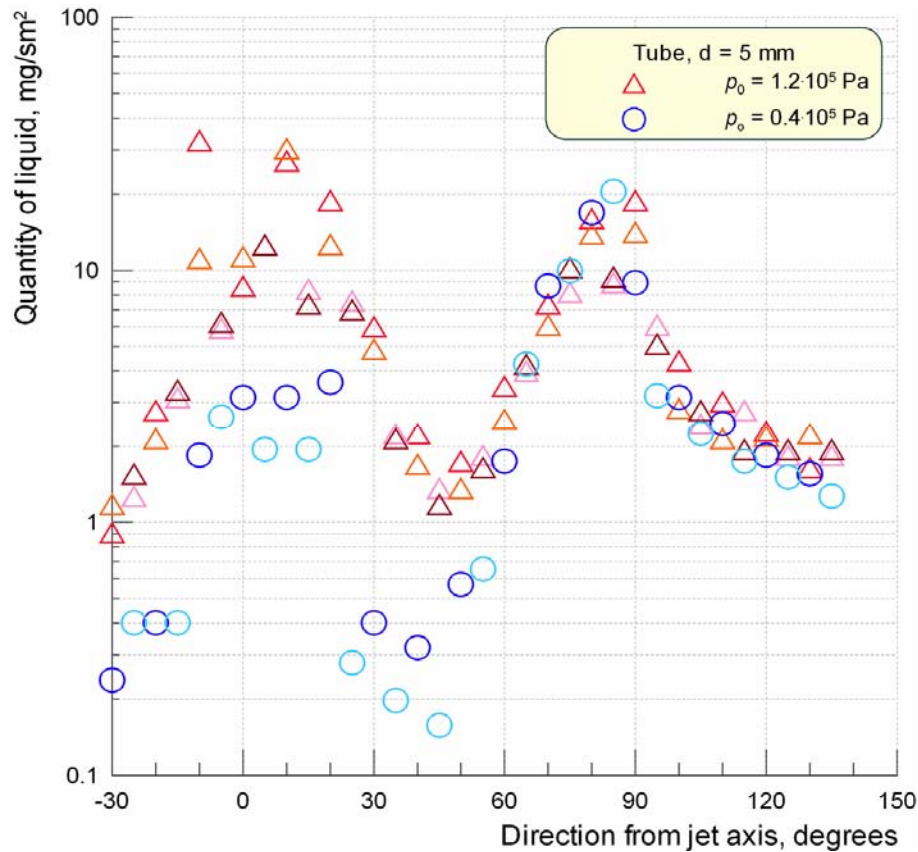


Fig. 2.59. Spatial distribution of the droplet phase.
Tube nozzle 5 mm in diameter. Working liquid - butanol

Influence of the nozzle geometry

In experiments on studying the influence of the nozzle geometry, nozzles having the shape of cylindrical channels and supersonic conical nozzles were investigated. A large volume of experimental data was obtained and analyzed. As was expected, the results obtained showed a significant effect of the nozzle geometry on the droplet-phase distribution in the supersonic flow. It can be seen, for example, in Figs. 2.56-2.59 shown above. With an increase in the nozzle Mach number (transition from a tube with $M = 1$ to a supersonic nozzle with $M = 3$), the peripheral region of the droplet-phase flow is considerably transformed, namely, for the tube, the preferable direction of dispersion of the droplet phase (the maximum in the angular distribution) corresponds to corners of approximately 80° from the jet axis (Figs. 2.57 and 2.59); for the supersonic nozzle, this corner is appreciably lower, about 60° (Figs. 2.56 and 2.58). The reason, apparently, is the increase in the effect of the jet direction with the increase in the nozzle Mach number. This effect is also responsible for reduction of backflows of the droplet phase.

Influence of properties of the liquid

In experiments on studying the influence of liquid properties, ethanol and butanol were considered. Their choice as modeling liquids was proved earlier, proceeding from the purposes of the Project and the program of experimental researches. Though these liquids differ significantly (approximately tenfold) in pressure of saturated vapor and approximately threefold in the value of dynamic viscosity, the research performed both on the angular distributions of the droplet phase and on distribution functions of drops in terms of sizes and velocities showed fairly close results.

Influence of the nozzle-lip shape

In experiments on studying the influence of the nozzle-lip shape, three variants of the lip (round, right-angled, and sharp) were investigated. The corresponding results of experiments obtained with the use of spectrophotometry are shown in Fig. 2.60. It follows from Fig. 2.60 that the highest magnitude of backflows of the droplet phase is observed for the round lip, and the lowest values are obtained for the right-angled lip. This conclusion is confirmed more evidently by experimental results obtained with the use of the technique of droplet-phase deposition on paper strips (Fig. 2.61). The results of experiments for the round lip produced results that could be expected (the greatest flows of the droplet phase), the results of experiments for right-angled and sharp lips forced us to change our preliminary concept about the influence of the nozzle-lip shape on the angular distributions of the droplet phase. It was expected that, owing to better dispersion, the least backflows of the droplet phase should be produced by the sharp lip. According to measurement results, however, the least back flows of the droplet phase were produced by the right-angled lip. In our opinion, the reason is the effect of shielding, which is created by the face part of the right-angled lip.

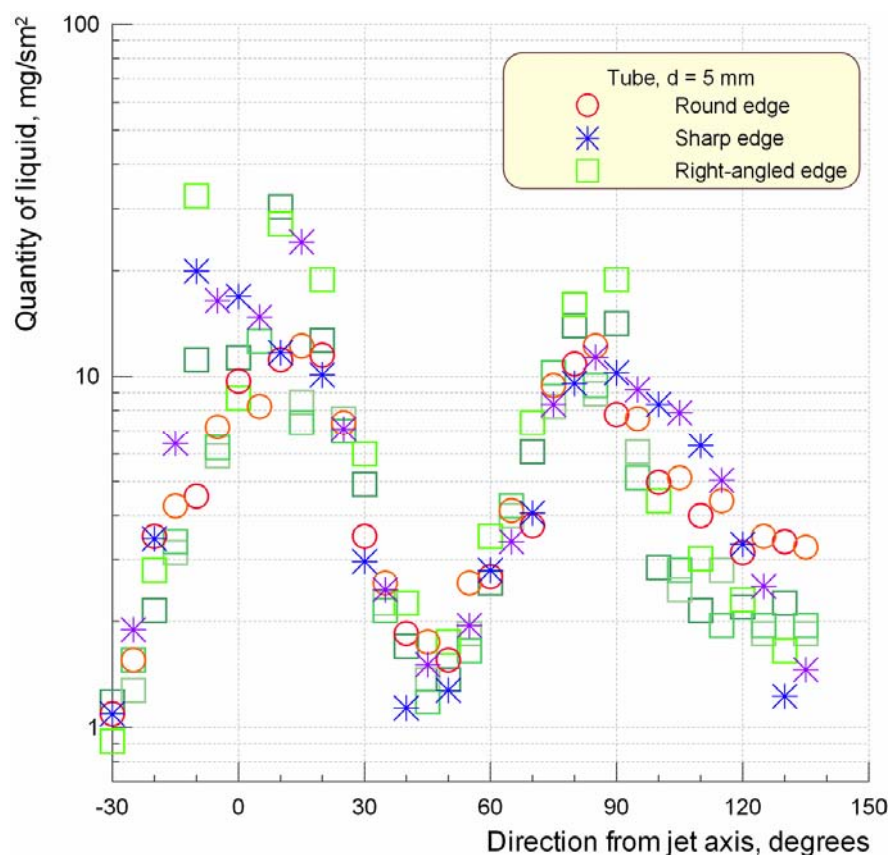


Fig. 2.60. Spatial distribution of the droplet phase. Results of spectrophotometry. Tube nozzle 5 mm in diameter. Working liquid – butanol, working gas - air

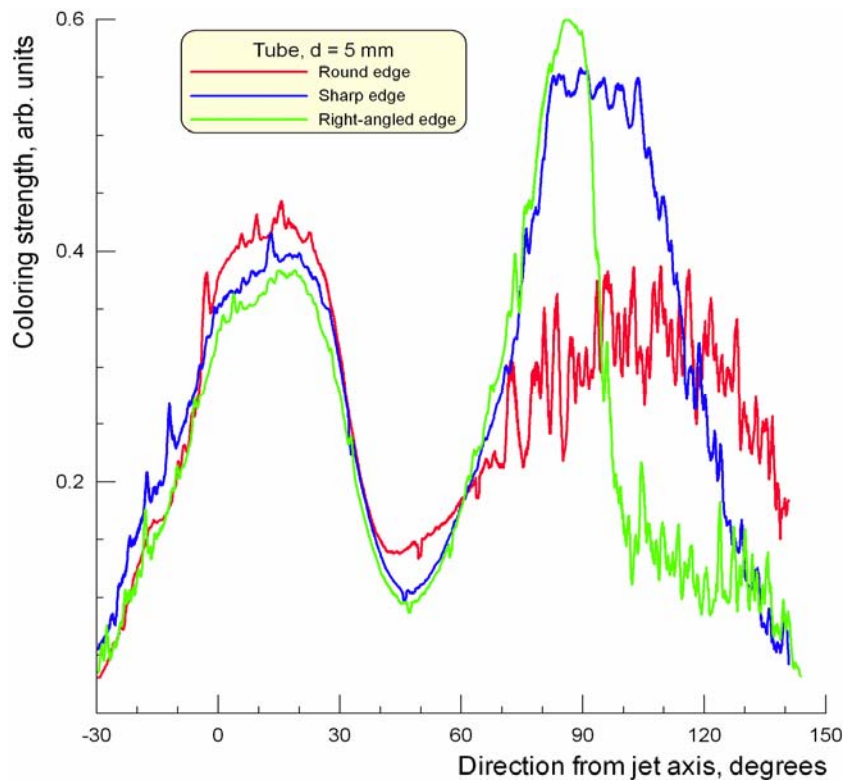


Fig. 2.61. Spatial distribution of the droplet phase. Results of deposition on paper strips. Tube nozzle 5 mm in diameter. Working liquid – butanol, working gas – air

Distribution of droplets in terms of sizes, directions, and velocities

For the period under report, new experimental data on the distribution functions of drops in a supersonic flow in terms of their sizes, directions, and velocities were obtained with the use of the «laser sheet» technique. The corresponding results are shown in Figs. 2.62-2.64 for the tube nozzle. Three configurations of the nozzle lip (sharp, round, and right-angled) were investigated. The stagnation temperature of the gas and the temperature of the liquid had room values (300 K) in these experiments, the stagnation pressure of the gas was $p_0 = 1.2 \cdot 10^5$ Pa, and the liquid flow rate was $G_l = 0.5$ g/s.

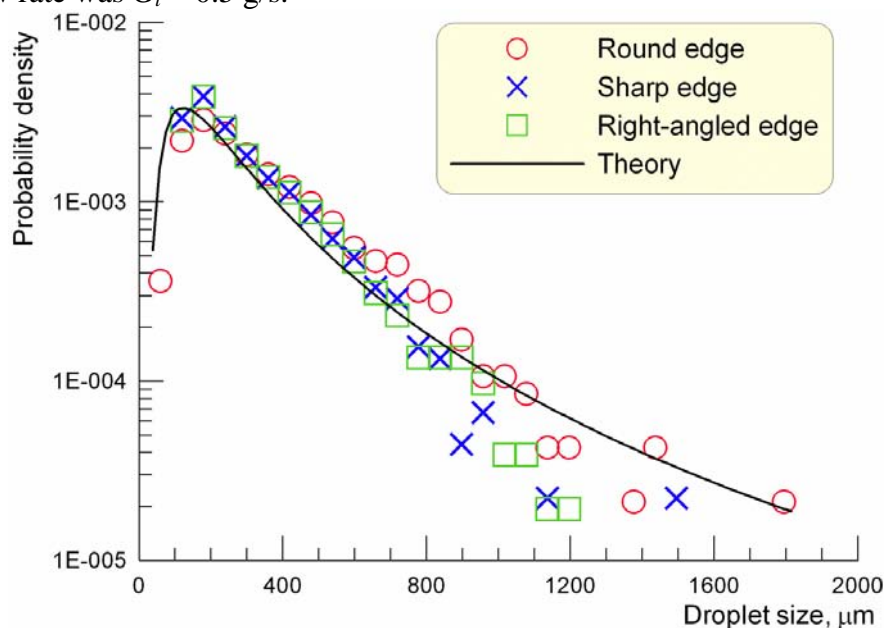


Fig. 2.62. Size distribution of droplets. Tube nozzle 5 mm in diameter. Working liquid – butanol, working gas – air

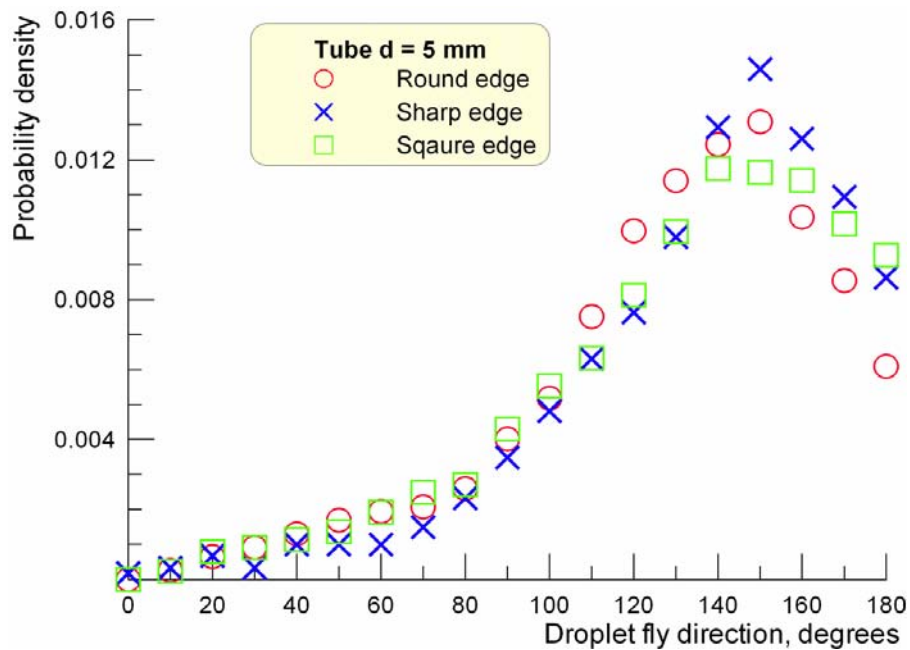


Fig. 2.63. Directional distribution of droplets. Tube nozzle 5 mm in diameter. Working liquid – butanol, working gas – air

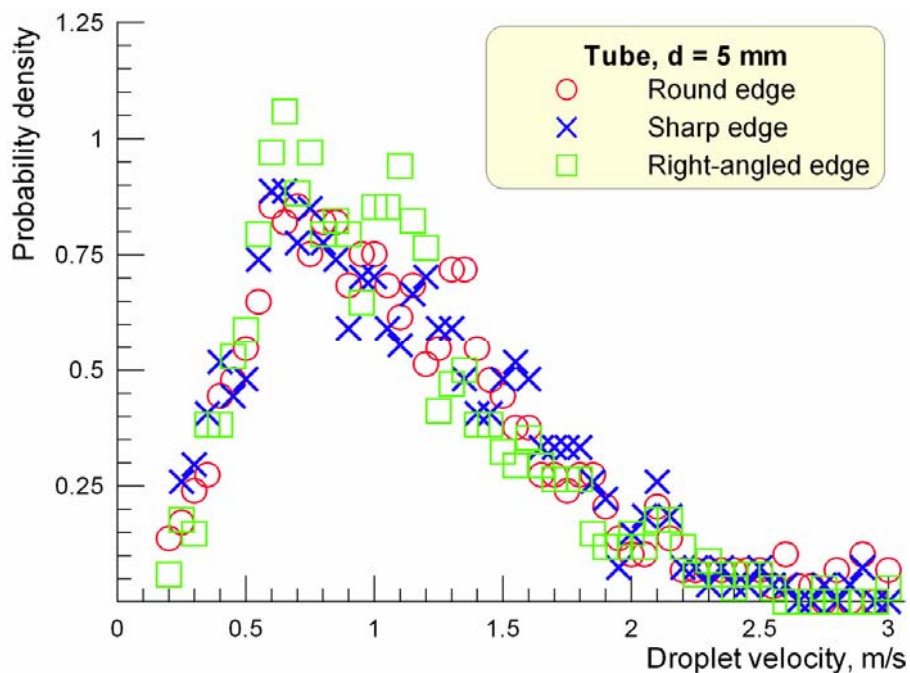


Fig. 2.64. Velocity distribution of droplets. Tube nozzle 5 mm in diameter. Working liquid – butanol, working gas – air

From these data, it is possible to see that, under the present test conditions, the droplets have characteristic values of velocity and size of about 1 m/s and 200 microns, respectively, and starting mainly at an angle of 150° relative to the jet axis, creating the backflow. It can also be noted that the distribution functions only weakly depend on the nozzle-lip shape.

For the period under report, the model of disintegration on droplets of the near-wall liquid film at the nozzle exit was further developed. The experimental results suggest that the steady flow formation obeys the following scheme [1]. As the gas and liquid are fed, a liquid film is formed on the inner wall of the nozzle. Under the action of the gas flow and gravity (predominantly, due to the first factor), the liquid film moves towards the edge of the nozzle. At this edge, the film turns around and emerges onto the external surface of the nozzle. At the same

time, there is a maximum height of film lifting, depending on the parameters of the gas flow and the liquid. Correspondingly, there is a certain critical amount of the liquid that can be contained in the film. As this amount of the liquid is accumulated in the film, a steady flow is formed: the film of a certain height is formed on the external surface of the nozzle, and the newly fed liquid is completely carried away from the bottom edge of the nozzle by the flow in the form of droplets. The film is broken into droplets due to the Rayleigh-Taylor instability of the film under the action of both the gas flow and gravity.

Although the real process is certainly much more complicated (e.g., the liquid can be subject to boiling), the above-described scheme turns out to be quite reasonable and yields satisfactory agreement with the experimental results, in particular, for the height of film lifting [1].

According to this scheme, the time variation of the droplet-size distribution at the nozzle edge can be described by the kinetic equation

$$\frac{\partial n_g}{\partial t} = \beta_{g-1} n_{g-1} - \beta_g n_g - \gamma_g n_g, \quad (2.6)$$

where n_g is the number of droplets containing g molecules; β_g and γ_g are the rates of the droplet growth and shedding, respectively. Measuring the drop size by the drop volume $v = g v_1$, where v_1 is the liquid volume per one molecule, and assuming the drops to be large enough, so that $\beta_{g-1} n_{g-1} \approx \beta_g n_g - \partial(\beta_g n_g) / \partial g$, we can rewrite Eq. (1.7) as

$$\frac{\partial n_v}{\partial t} + \frac{\partial(\beta_v n_v)}{\partial v} = -\gamma_v n_v.$$

The steady solution of this equation is

$$n_v = \frac{C}{\beta_v} \exp\left(-\int_0^v \omega_v dv\right),$$

where

$$\omega_v = \gamma_v / \beta_v \quad (2.7)$$

and C is the normalizing factor. Correspondingly, the distribution function of the shed droplets is written as

$$p_v = \gamma_v n_v = C \omega_v \exp\left(-\int_0^v \omega_v dv\right). \quad (2.8)$$

Assume that the growth of droplets is determined by liquid inflow from the film, with the rate of the influx into the v -th droplet being proportional to the droplet cross-section S_v . Then the droplet growth rate β_v is

$$\beta_v = \frac{S_v G_l}{\rho_l A}, \quad (2.9)$$

where G_l is the total discharge of the liquid, ρ_l is the liquid density, and A is a constant, having the meaning of the total cross-section of the droplets $S_{\text{tot}} = \int S_v n_v dv$.

To estimate the rate of droplet shedding, γ_g , we used the following model. Let the droplet of v -th size be shed, under the gas flow forcing, with the probability

$$P_{\text{tear}} = \exp(-\alpha / We_v), \quad (2.10)$$

where

$$We_v = 2\rho_g u_g^2 r_v / \sigma \quad (2.11)$$

is the Weber number, ρ_g and u_g are the density and velocity of the gas flow, r_v is the drop radius, and σ is the surface tension of the liquid. After shedding, the droplet is transported by the gas flow turning around the nozzle edge, which affects the droplet with a force equal to $\rho_g u_g^2 S_v$. Thus, the droplet performs a uniformly accelerated motion, with the acceleration equal to

$$a_v = \frac{\rho_g u_g^2 S_v}{\rho_l v}, \quad (2.12)$$

and passes a distance equal to its diameter, $2r_v$, i.e. is shed from the liquid film, during the time

$$t_v = \left(\frac{4r_v \rho_l v}{\rho_g u_g^2 S_v} \right)^{1/2}. \quad (2.13)$$

Correspondingly, the droplet shedding rate $\gamma_v = P_{\text{tear}}(\text{We})/t_v$ is expressed as

$$\gamma_v = \left(\frac{\rho_g u_g^2 S_v}{4r_v \rho_l v} \right)^{1/2} \exp\left(-\frac{\alpha}{\text{We}_v}\right). \quad (2.14)$$

Substituting Eqs. (2.9) and (2.14) into Eqs. (2.7) - (2.8) and performing integration in Eq. (2.8), we obtain for the droplet distribution on radius $p_r = 4\pi r^2 p_v$

$$p_r = C \frac{K}{r} \exp\left\{-\left[KE_1\left(\frac{\alpha}{\text{We}_r}\right) + \frac{\alpha}{\text{We}_r}\right]\right\}. \quad (2.15)$$

Here

$$K = \frac{(3\rho_g u_g^2 \rho_l)^{1/2} A}{G_l} \quad (2.16)$$

is a dimensionless complex of parameters, $E_1(x) = \int_1^\infty \exp(-xt) dt/t$ is the integral exponential function, We_r is the local Weber number (2.11), and C is a constant defined by the condition

$$\int_0^\infty p_r dr = 1.$$

The distribution function given by Eq. (2.15) is shown in Fig. 2.62 by the solid curve. Here, according to the test conditions, $\rho_l = 0.8 \text{ g/cm}^3$, $\sigma = 0.022 \text{ N/m}$, $T_0 = 300 \text{ K}$, $p_0 = 1.2 \cdot 10^5 \text{ Pa}$, and $G_l = 0.5 \text{ g/s}$. The values of ρ_g and u_g were the gas density and velocity obtained in the Prandtl-Meyer flow turning at an angle of 90° around the nozzle lip, which gave $\rho_g = 3.4 \cdot 10^{-6} \text{ g/cm}^3$ and $u_g = 7 \cdot 10^2 \text{ m/s}$ ($M_g = 6.85$). The constants A and α , entering Eqs. (2.9) and (2.10), were fitted to reach the best agreement of the theoretical distribution (2.15) with the experimental data, and were obtained as $A = 5.7 \cdot 10^{-3}$ and $\alpha = 25$. It is seen that the theoretical relation (2.15) reproduces the size distribution of droplets quite well. In particular, Eq. (2.15), which is independent of the nozzle-lip shape, agrees with the experimental data in terms of the weak effect of the nozzle-lip shape on the behavior of droplets. Note also that the value of $S_{\text{tot}} = \int S_v n_v dv$ calculated with the help of Eq. (2.15) shows that the effective cross-section of the droplet for the liquid influx into the droplet is approximately equal to $0.67 \cdot S_v$.

This model can, in principle, be extended to describe the direction-of-flight and velocity distribution functions of droplets, which requires a consideration of droplet interaction with a gas flow expanding behind the nozzle exit. In this connection, note that, according to the model, the velocity of the droplet after its shedding from the liquid film is

$$V_v = a_v t_v = \left(4\rho_g u_g^2 r_v S_v / \rho_l v \right)^{1/2},$$

where a_v and t_v are defined by Eqs. (2.12) and (2.13), respectively. For the conditions of the present experiments, this equation yields $V_v = 2.5 \text{ m/s}$, which is in good agreement with the experimental data by the order of magnitude (see Fig. 2.64).

References used

1. V.G. Prikhodko, S.F. Chekmarev, V.N. Yarygin, I.V. Yarygin. Rise of a Near-Wall Liquid Film over the Outer Surface of a Nozzle Accompanying Supersonic Gas Flow into Vacuum // Doklady Physics (Doklady Akademii Nauk), 2004, Vol.49, No.2, pp. 119-121.

Numerical investigations during the second year of project fulfillment include development of software system for simulation of dynamics of droplet phase particles and the processes of interaction between droplets and carrier gas. The system is based on the use of a discrete Lagrangian model of particles and allows us to take into account various physical processes taking place in the high-speed two-phase. Further, this software system is used for detailed parametric simulations of gas-droplet flows in the nozzle in the exhausting plume. The results obtained are compared with the experimental data on spatial distribution of liquid droplets.

Numerical research of gas and gas-droplet flows

Task 2.7.1. Developing software module for simulating the dynamics of liquid droplets with discrete Lagrangian model of test particles

Lagrangian description of droplet motion. Within the framework of one of the most effective and flexible approaches to the analysis of evolution of heterogeneous mixtures, which is the Lagrangian-Eulerian approach, the dynamics of the carrier phase (in the general case, a mixture of an inert gas and vapor) at the Eulerian stage is described either by continuum models, such as the Euler, Navier-Stokes, Reynolds equations, etc., or by direct numerical simulation based on Monte Carlo algorithms. At the Lagrangian stage, disperse (droplet) phase dynamics is described by the model of probe particles, each representing a certain number of real drops. The equations of the Lagrangian stage for motion and heat and mass transfer of the probe particles can be written as

$$\frac{d\vec{X}_p}{dt} = \vec{R}_p, \quad (2.17)$$

where

$$\vec{X}_p = \begin{pmatrix} \vec{r}_p \\ m_p \\ m_p \vec{V}_p \\ m_p c_p^0 T_p \end{pmatrix}, \quad \vec{R}_p = \begin{pmatrix} \vec{V}_p \\ J_{gp} \\ \vec{F}_{gp} \\ Q_{gp} \end{pmatrix},$$

$\vec{r}_p, \vec{V}_p, m_p, c_p^0, T_p$ are the radius vector, velocity, mass, heat capacity, and temperature of disperse inclusions and $J_{gp}, \vec{F}_{gp}, Q_{gp}$ are terms that describe interphase transfer of mass, momentum, and energy.

Under the assumption of spherical symmetry of evaporation/condensation of droplets, equations (2.17) can be rewritten in the form

$$A_g \frac{d\bar{X}_p}{dt} = \bar{R}_{gp}, \quad (2.18)$$

where

$$A_g = \begin{pmatrix} 1 & 0 & 0 & 0 \\ 0 & 1 & 0 & 0 \\ 0 & 0 & m_p & 0 \\ 0 & 0 & 0 & c_p^0 m_p \end{pmatrix}, \quad \bar{X}_p = \begin{pmatrix} \bar{r}_p \\ m_p \\ \bar{V}_p \\ T_p \end{pmatrix}, \quad \bar{R}_p = \begin{pmatrix} \bar{V}_p \\ J_{gp} \\ \bar{F}_{gp} \\ Q_{gp} + J_{gp} h_v \end{pmatrix},$$

h_v is the latent heat of evaporation of the material of disperse inclusions. The terms that describe interphase transfer of mass, momentum, and energy, J_{gp} , \bar{F}_{gp} , Q_{gp} , can be obtained with the help of the phenomenological description based on experimental data on the drag coefficient and Nusselt and Sherwood numbers. Taking into account a significant difference in phase densities, $\rho_p/\rho_g \sim 10^3$, and the fact that the nozzle flow under rarefied conditions is characterized by developed boundary layers with large gradients of gas-dynamic functions, we can assume that the main contribution to interphase transfer of momentum is made by interphase friction, Stokes force, and ‘‘transverse’’ Saffman force caused by the shear character of the flow near the disperse inclusion:

$$\bar{F}_{gp} = \bar{F}_{gp}^{st} + \bar{F}_{gp}^{saf}. \quad (2.19)$$

Here

$$\bar{F}_{gp}^{st} = \frac{c_D \pi d_p^2 \rho_g}{8} |\bar{V}_g - \bar{V}_p| (\bar{V}_g - \bar{V}_p) \quad \text{is the Stokes force,} \quad (2.20)$$

$$\bar{F}_{gp}^{saf} = 1.61 d_p \left(\frac{\mu_g \rho_g}{|\bar{\omega}_g|} \right)^{0.5} [(\bar{V}_g - \bar{V}_p) \times \bar{\omega}_g] \quad \text{is the Saffman force,} \quad (2.21)$$

c_D is the drag coefficient for the disperse inclusion and ρ_g, \bar{V}_g, μ_g are density, velocity and dynamic viscosity of the carrier phase, $\bar{\omega}_g = \nabla \times \bar{V}_g$. It should be noted that the latter expression is valid under the condition $\text{Re}_{gp} \ll \sqrt{\text{Re}_G}$, where $\text{Re}_{gp} = d_p \rho_g |\bar{V}_g - \bar{V}_p| / \mu_g$ is the Reynolds number of the relative motion of the phases and $\text{Re}_G = (d_p^2 \rho_g / \mu_g) dV_i/dx_j$, the subscripts i and j refer to the longitudinal and transverse coordinates. There exists an approximation for the ‘‘transverse’’ force, F_L , which allows one to extend the range of Reynolds numbers:

$$F_L / F_{gp}^{saf} = \begin{cases} (1 - 0.3314\beta^{0.5}) \exp\left(-\frac{\text{Re}_{gp}}{10}\right) + 0.3314\beta^{0.5} & \text{Re}_{gp} \leq 40 \\ 0.0524(\beta \text{Re}_{gp})^{0.5} & \text{Re}_{gp} > 40 \end{cases} \quad (2.22)$$

Here

$$\beta = \frac{d_p}{2|\vec{V}_g - \vec{V}_p|} |\vec{\omega}_g|$$

and $0.005 < \beta < 0.4$

Within the framework of the phenomenological description of interphase transfer, the contact heat transfer can be represented as

$$Q_{gp} = \pi \lambda_g d_p Nu (T_g - T_p), \quad (2.23)$$

and diffuse mass transfer as

$$J_{gp} = \pi D d_p Sh (\rho_v - \rho_s(T_p)), \quad (2.24)$$

where λ_g is the thermal conductivity of the carrier phase, D is the diffusivity of vapor of the disperse phase in the carrier medium, ρ_v , $\rho_s(T_p)$ are the densities of vapor and saturating vapor at the temperature of the disperse phase, Nu is the Nusselt number, and Sh is the Sherwood number.

Close to the boiling point, the mass-transfer intensity is determined by heat addition to the disperse phase:

$$J_{gp} = -\frac{Q_{gp}}{h_v}. \quad (2.25)$$

In the code developed, we use the generalization of these limiting cases:

$$J_{gp} = \pi D d_p Sh (\rho_v - \rho_s(T_p)) (1 - \delta) - \frac{Q_{gp}}{h_v} \delta \quad (2.26)$$

(here $\delta = p_{ps}/p_g$).

Thus, to close the model considered, we have to determine the dependences of the drag coefficient c_D and also the Nusselt Nu and Sherwood Sh numbers on flow parameters. For a gas-droplet medium, these dependences can be written in the form

$$\begin{aligned} c_D &= c_D(\text{Re}_{gp}, M_{gp}, Kn, We_{gp}, \dots) \\ Nu &= Nu(\text{Re}_{gp}, M_{gp}, Kn, We_{gp}, \dots) \\ Sh &= Sh(\text{Re}_{gp}, M_{gp}, Kn, We_{gp}, \dots), \end{aligned} \quad (2.27)$$

where $M_{gp} = |\vec{V}_g - \vec{V}_p| / \sqrt{\gamma p_g / \rho_g}$, $Kn = \Lambda / d_p$, $We_{gp} = \rho_g d_p |\vec{V}_g - \vec{V}_p|^2 / \sigma_p$ are the Mach, Knudsen, and Weber numbers for the disperse inclusions, Λ is the mean free path in the carrier phase, and σ_p is the surface tension coefficient.

Approximations for c_D , Nu , and Sh . As was already mentioned, droplet deformation and internal circulation can be neglected under conditions considered; therefore, in what follows, we consider approximations obtained for non-deformable solid particles.

Figure 2.65 shows a typical qualitative dependence of the friction coefficient on the Mach number for high and low Reynolds numbers. For Mach numbers lower than unity, the

behavior of the curves corresponding to low and high Reynolds numbers is qualitatively different; but for high Mach numbers, both curves tend to 2.0.

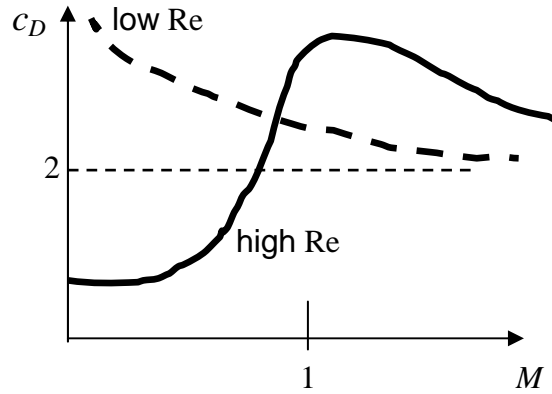


Fig. 2.65. Drag coefficient versus the Mach number.

The literature offers many approximations valid in a wide range of flow parameters. One of the most widespread approximations, which is rather convenient in computations, is

$$c_D = 2 + (c_{D0} - 2) \exp\left(-3.07\sqrt{k}g(\text{Re}_{gp})\frac{M_{gp}}{\text{Re}_{gp}}\right) + \frac{h(M_{gp})}{\sqrt{k}M_{gp}} \exp\left(-\frac{\text{Re}_{gp}}{2M_{gp}}\right). \quad (2.28)$$

Here

$$g(\text{Re}_{gp}) = \frac{1 + \text{Re}_{gp}(12.278 + 0.548\text{Re}_{gp})}{1 + 11.278\text{Re}_{gp}}, \quad h(M_{gp}) = \frac{5.6}{1 + M_{gp}} + 1.7\sqrt{\frac{T_p}{T_g}},$$

k is the ratio of specific heats of the carrier phase, and c_{D0} is the drag coefficient at $M_{gp} = 0$ (standard curve). Note, for high Knudsen numbers (ratio of Mach and Reynolds numbers), the drag coefficient in this approximation tends to 2.

For the Nusselt and Sherwood numbers, one can find approximations taking into account the effects of compressibility (Reynolds number) and rarefaction (Knudsen number) up to the free-molecular regime:

$$Nu = \frac{2 + 0.552\text{Re}_{gp}^{0.5}\text{Pr}^{0.33}}{1 + 3.42\frac{M_{gp}}{\text{Re}_{gp}\text{Pr}}}, \quad (2.29)$$

$$Sh = \frac{2 + 0.552\text{Re}_{gp}^{0.5}Sc^{0.33}}{1 + 3.42\frac{M_{gp}}{\text{Re}_{gp}Sc}}. \quad (2.30)$$

Here $\text{Pr} = \frac{\mu_g c_g}{\lambda_g}$ is the Prandtl number, $Sc = \frac{\mu_g}{D\rho_g}$ is the Schmidt number, and D is the diffusivity.

Thus, the formulated model is closed; it takes into account the special features of rarefied flows of gas-droplet media in nozzles.

Droplet deformation and break-up. In the case of a droplet disperse phase, the processes of interphase transfer are affected by both possible deformation of droplets in the carrier phase flow and internal circulation flow in the droplets. In the detailed review [1] a diagram of droplet deformation and break-up modes in flows with a velocity lag is presented (see Fig. 2.66a). The Roman numerals denote (see Fig. 2.66b):

I – droplet deformation and break-up in the vibrational, “parachute”, and “parachute + stamen” modes;

II – droplet deformation and break-up in the “stripping” mode.

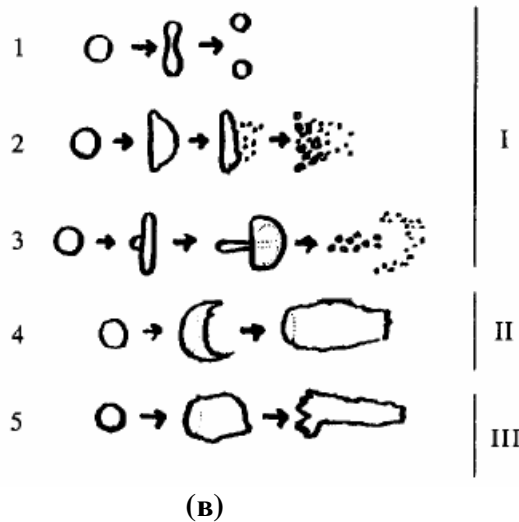
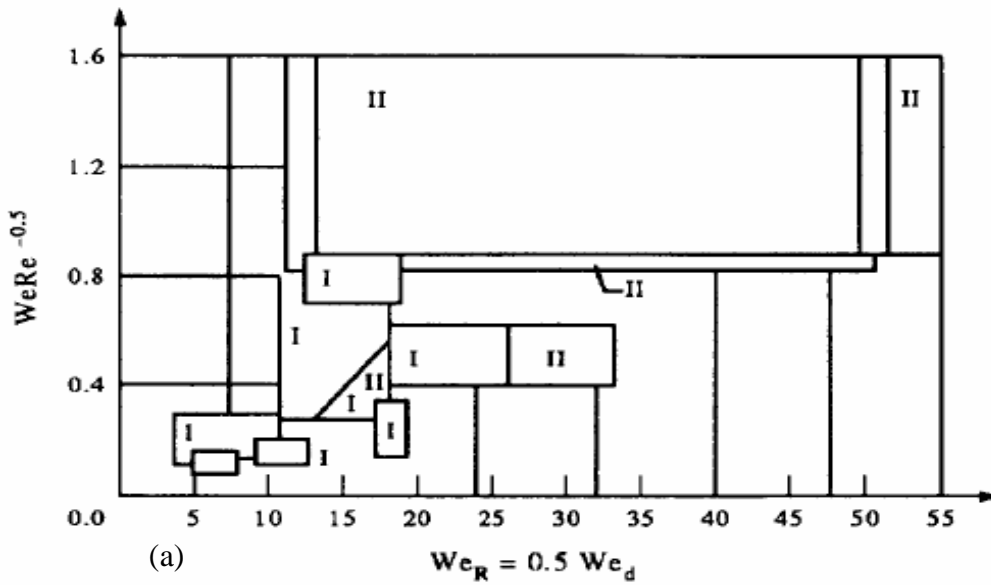


Fig. 2.66. Diagram of droplet deformation and break-up modes in flows with a velocity lag.

There is one more regime, which is not shown in Fig. 2.66a), regime III, droplet deformation and “explosive” break-up (see Fig. 2.66b). This regime is a result of the Rayleigh-Lamb-Taylor interface instability development. Numerous investigations have shown that such a mode of droplet deformation and break-up is characterized by high values of the Reynolds and the Weber numbers.

Under conditions considered (the carrier phase is nitrogen and vapor of ethyl alcohol, the disperse phase is liquid ethyl alcohol), the following inequalities are valid:

$$\frac{\mu_p}{\mu_g} \gg 1, \quad We_{gp} = \frac{\rho_g d_p |\vec{V}_g - \vec{V}_p|^2}{\sigma_p} \ll 1.$$

The Reynolds number, $Re_{gp} = \frac{\rho_g d_p |\vec{V}_g - \vec{V}_p|}{\mu_g}$, can reach 10, approximately, depending

on the velocity lag and disperse phase parameters. Thus, the domain of parameters under study is a vertical strip located in the vicinity of the ordinate axis, to the left of the I-st break-up mode domain. It enables one to ignore both possible droplet deformation and break-up and droplet inner flows and, therefore, to ignore their effect on interphase transport.

Droplet condensation/evaporation. Evaporation and condensation of droplets, can substantially affect interphase transfer of mass, momentum, and energy. Corrections taking into account the influence of evaporation/condensation on the drag coefficient and Nusselt and Sherwood numbers can be introduced with the help of the Spaulding number $Br = c_{pg}(T_g - T_p)/h_v$:

$$\begin{aligned} c_D(1 + Br)^{0.2} &= c_{D0}, \\ Nu(1 + Br) &= Nu_0, \\ Sh(1 + Br) &= Sh_0. \end{aligned} \quad (2.31)$$

Here c_{pg} is the heat capacity of the carrier phase at constant pressure; the subscript 0 indicates the drag coefficient and the Nusselt and Sherwood numbers corresponding to the case where evaporation/condensation are ignored.

Thus, to close the problem, one needs to choose approximations of c_{D0} , Nu_0 , and Sh_0 corresponding to the flow regime around the droplets under the conditions considered. In the problem under study, the source of droplets can be condensation in the carrier phase flow expanding toward the low-pressure region and also entrainment of droplets from the film flowing along the nozzle walls and formation of droplets resulting from film destruction after leaving the nozzle.

Condensation and evaporation of droplets in an expanding flow can be described by the following model. The equation for the mass fraction of vapor is written as

$$\frac{d\gamma}{dt} = F(\gamma, p, T), \quad (2.32)$$

where γ is the mass fraction of vapor. The right-hand part of this equation determining the rate of interphase mass transfer has the form

$$F(\gamma, p, T) = \frac{4}{3} \pi \rho_p r_*^3 \frac{I}{\rho_v} + 4 \pi \rho_p \int_{r_*}^{\infty} r^2 f(r) \dot{r} dr, \quad (2.33)$$

where

$$I = 2 \left(\frac{N_A}{M} \right)^{2/3} \frac{\rho_g + \rho_p}{\rho_p} \frac{p}{RT} \sqrt{\frac{\sigma_p}{2\pi}} \exp \left[-\gamma_c \frac{16\pi N_A \sigma_p^3}{3MRT(\rho_p h_v)^2 \left(\ln \frac{T_s}{T} \right)^2} \right]$$

is the nucleation rate, γ_c is a coefficient taking into account the heterogeneous character of nucleation, M is the molecular weight of vapor, N_A is the Avogadro constant, and the radius of the critical “nucleus” is

$$r_* = \frac{2M\sigma_p}{\rho_p RT \ln T/T_s},$$

Assuming that the droplet growth rate is independent of its size, we can use the Hertz-Knudsen formula

$$\dot{r} = \frac{\alpha_c p}{\rho_p \sqrt{2\pi RT}} \left[1 - \frac{p_s(T_p)}{p} \sqrt{\frac{T}{T_p}} \right], \quad (2.34)$$

where α_c is the condensation coefficient; unfortunately, this coefficient is unknown for ethyl alcohol vapors and varies from 0.04 to 1.0 for water vapors in various references.

The model of condensation should be supplemented by the equation for the distribution function of the droplet size, $f(r)$, which has the form

$$\frac{\partial f(r)}{\partial t} + \bar{V} \frac{\partial f(r)}{\partial \bar{x}} + \frac{\partial \dot{r} f(r)}{\partial r} = \frac{I}{\rho_g + \rho_p} \delta(r - r_*), \quad (2.35)$$

where $\delta(r - r_*)$ is the delta function.

To simplify solving the equations of the model of droplet condensation/evaporation, we introduce the moments of the distribution function of the droplet size:

$$\Omega_n = \int_{r_*}^{\infty} r^n f(r) dr, \quad (2.36)$$

thus, for instance, $1 - \gamma = \frac{4}{3} \pi \rho_p \Omega_3$. Then, Eq. (2.32) can be transformed to

$$\frac{d \Omega_n}{d t} = n \dot{r} \Omega_{n-1} + \frac{I}{\rho_g + \rho_p} r_*^n. \quad (2.37)$$

Thus, the kinetic equation for the distribution function is reduced to three ($n = 0, 1, 2$) ordinary differential equations. In the general case, the Lagrangian-Eulerian algorithm should be supplemented by equations (2.32) – (2.37).

Taking into account that the main objective at this stage of research is the development of a general algorithm and determination of the characteristic parameters of the gas-droplet nozzle flow under conditions considered, it is assumed in this report that the droplets emerge in the nozzle throat with given initial parameters.

Numerical method

In some cases, e.g., as a result of evaporation, equations (2.17) become stiff, and the procedure of their numerical solution should allow consideration of this type of equations. Two algorithms (Adams and Gear) are used in the present work.

Adams method. The system of ordinary differential equations that describe the dynamics of droplets was solved by the implicit Adams method for stiff equations. For system (2.17), the implicit Adams method can be written in the following form (the subscript p is omitted):

$$X^{n+1} = X^n + \frac{\Delta t}{2} [R(X^{n+1}) + R(X^n)].$$

Using the Newton iterations, we obtain

$$X^{m+1} = X^m - N t(X^m) \cdot J^{-1}(X^m),$$

where $N t = X^n + \frac{\Delta t}{2} R(X^n) - X^{n+1} + \frac{\Delta t}{2} R(X^{n+1})$, $J^{-1}(X^m)$ is a matrix of the form

$$\left\{ \frac{\Delta t}{2} \frac{\partial R}{\partial X} (X^{n+1(m)}) - I \right\}^{-1}, \text{ } I \text{ is a unit matrix, and } m \text{ is the iteration number.}$$

Thus, the computations are performed by the following scheme:

$$X^{n+1(m+1)} = X^{n+1(m)} - \left\{ \frac{\Delta t}{2} \frac{\partial R}{\partial X} (X^{n+1(m)}) - I \right\}^{-1} \left\{ X^n + \frac{\Delta t}{2} R(X^n) + \frac{\Delta t}{2} R(X^{n+1(m)}) - X^{n+1(m)} \right\}$$

This method has the second order of accuracy.

Gear method. Another effective algorithm is the Gear method. In this case, the computational procedure is as follows:

$$X^{n+2} = \frac{2\Delta t}{3} R(X^{n+2}) - \frac{1}{3} X^n + \frac{4}{3} X^{n+1}.$$

To determine $R(X^{n+2})$, we use the Newton iterations

$$X^{m+1} = X^m - N t(X^m) \cdot J^{-1}(X^m),$$

where m is the iteration number, $N t = \frac{2\Delta t}{3} R(X^m) - \frac{1}{3} X^n + \frac{4}{3} X^{n+1} - X^m$, and $J^{-1}(X^m)$ is a matrix of the form $\left\{ \frac{2\Delta t}{3} \frac{\partial R}{\partial X} (X^{n+1(m)}) - I \right\}^{-1}$.

Thus, the computations are performed by the following scheme:

$$X^{n+2(m+1)} = X^{n+2(m)} - \left\{ \frac{2\Delta t}{3} \frac{\partial R}{\partial X} (X^{n+2(m)}) - I \right\}^{-1} \times \left\{ \frac{2\Delta t}{3} R(X^{n+2(m)}) - \frac{1}{3} X^n + \frac{4}{3} X^{n+1} - X^{n+2(m)} \right\}$$

This method also has the second order of accuracy.

Code verification and validation

Comparison of model predictions with experimental data for drag coefficient

Despite the authors' testing of the c_D approximation, it seems of interest to compare the drag coefficient calculated by formula (1.7) with independent experimental data. For this purpose, we used the results of Bailey and Hiatt [2] who measured the drag of a spherical particle in a wide range of Mach and Reynolds numbers and also the results of drag measurements in rarefied flows [3].

The dependence of the drag coefficient on the Reynolds number for two Mach numbers ($M=1.25$ and $M=0.5$) is compared with the above-mentioned experimental data in Fig. 2.67. It is seen that the approximation used yields a higher error for a higher Mach number.

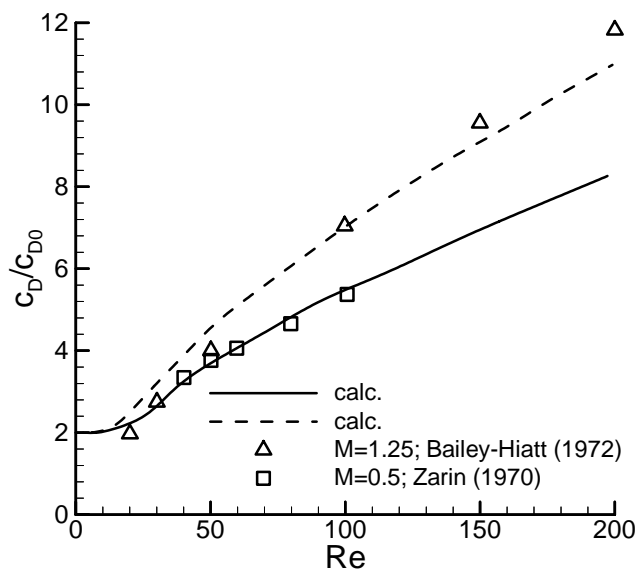


Fig.2.67. Drag coefficient vs. the Reynolds number.

The solid and dashed curves show the computation results by formula (1.6) for $M=0.5$ and 1.25 , respectively; the squares and triangles are the experimental data of [15, 16], respectively.

Droplet heating and evaporation. The objective of this paragraph is to validate the evaporation model proposed above. A comparison of model predictions with experimental results for the quiescent droplet surface area and temperature evolutions is presented below.

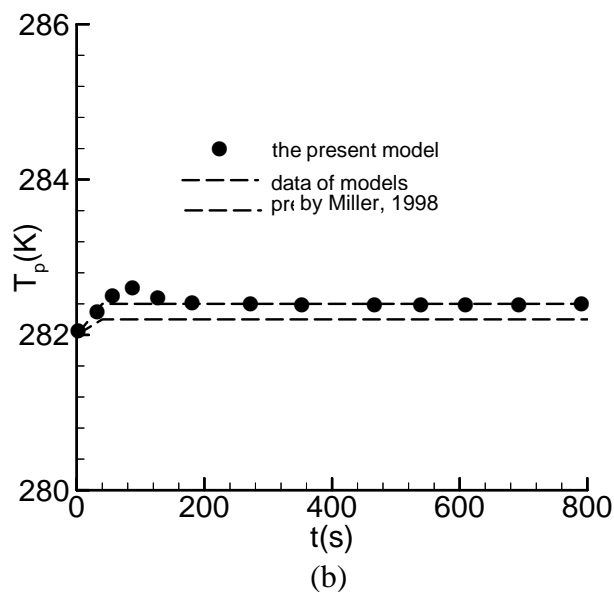
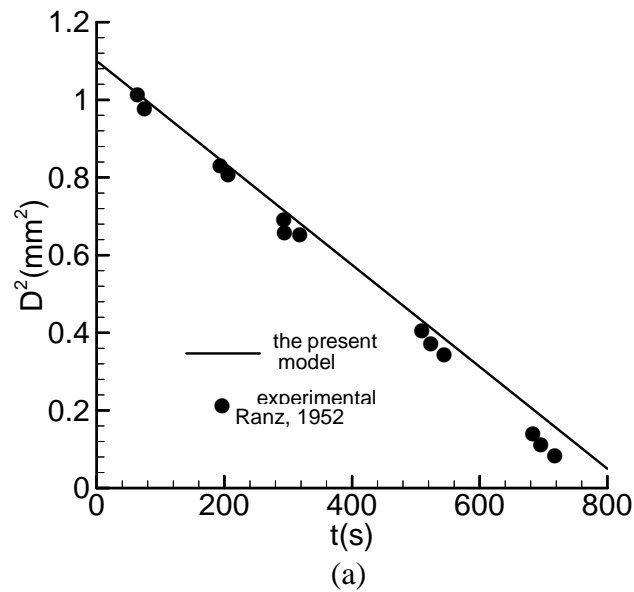


Fig. 2.68. Temporal evolution of the quiescent droplet diameter squared, (a), and the droplet temperature, (b), for water. The conditions are: $T_g=298$ K, $T_{p0}=282$ K, $D_0=1.1$ mm, ambient air pressure is equal to one standard atmosphere, and $Re_p=0$.

Figure 2.68 depicts the temporal evolutions of the relative surface area and temperature for a single isolated water droplet evaporating in a quiescent air environment. The model prediction for D^2 is compared to the experimental results [4] obtained under the same conditions. Note that here the droplet Reynolds number is zero and the empirical convective contributions to both the Nusselt and Sherwood numbers are irrelevant. For this relatively low evaporation rate, Fig. 2.68a shows that the model predicts nearly identical evaporation history which is in satisfactory agreement with the experimental data. The temperature evolution prediction is also in good agreement with results provided by eight models considered in [5] (see Fig. 2.68b). The results obtained with all models of Miller and with the proposed model are close. These results

show that, for large initial droplet diameters and low evaporation rates, the difference between various models is minor.

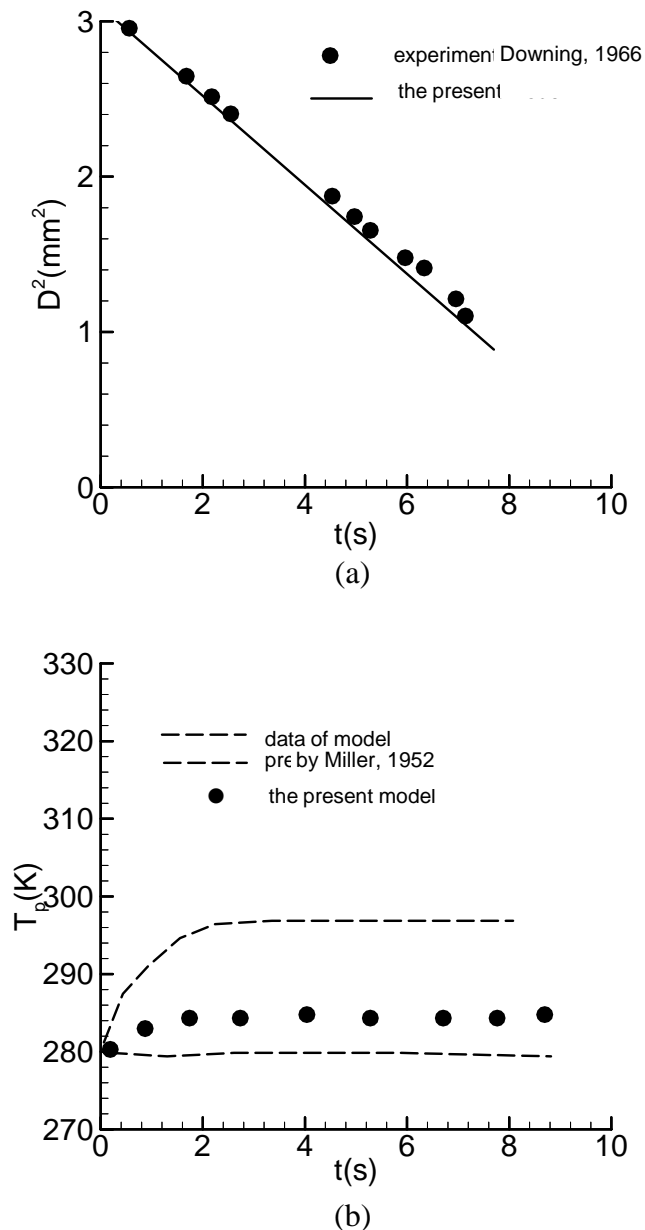


Fig. 2.69. Temporal evolution of the droplet diameter squared, (a), and the droplet temperature, (b), for hexane. $T_g=437$ K, $T_{p,0}=281$ K, $D_0=1.76$ mm, , ambient air pressure is equal to one standard atmosphere, and $Re_{p,0}=110$.

To validate the proposal model for droplet evaporation in a convective air flow, the temporal evolution of the diameter squared and the temperature for hexane droplets are compared to the experiments [6] at a moderate evaporation rate (see Figs. 2.69a and 2.69b). The simulation corresponds to hexane with an initial droplet size and temperature of $D_0=1.76$ mm and $T_{p,0}=281$ K, suspended in a convective flow with a relatively large initial droplet Reynolds number $Re_{p,0}=110$, for which the gas temperature, $T_g=437$ K, is almost one hundred degrees above the liquid boiling point. The observed linear surface area reduction is also supported by the experimental results.

Simulations of water vapor condensation in the nozzle flow. The proposed description of spontaneous condensation in the nozzle flow was validated by comparisons with the data presented in [7]. The water vapor flow in the Laval nozzle presented in Fig. 2.70 was simulated for two conditions: superheated vapor (non-condensable) low and vapor flow at $T_0=380\text{K}$. In the latter case, the energy release due to condensation results in an abrupt increase in pressure downstream of the nozzle throat, $x=40\text{mm}$. The filled circles show the results of simulation in the framework of the proposed algorithm. The data are seen to be in qualitative agreement. Nevertheless, in computations, the shock wave caused by condensation is located closer to the nozzle throat, which is probably due to the quasi-one-dimensional approach to nozzle-flow simulation used in this study. The rate of gas expansion in this case is somewhat lower and, thus, the shock is shifted upstream.

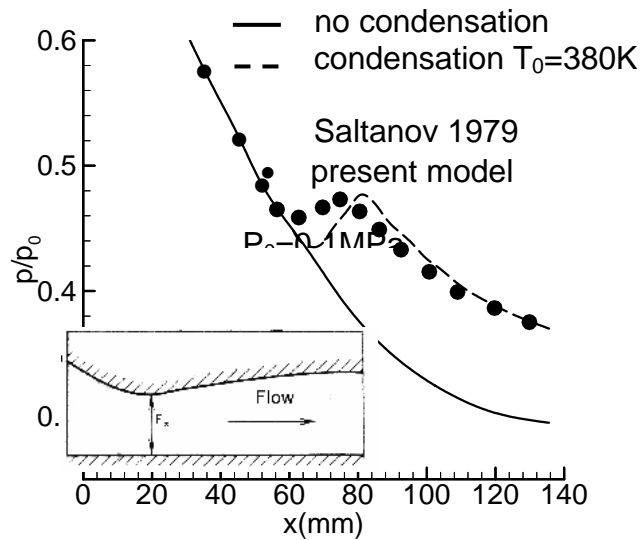


Fig. 2.70 “Condensation shock” in the Laval nozzle. $P_0=0.1\text{MPa}$, $T_0=380\text{K}$. Nozzle throat, $x=40\text{mm}$

2.7.2. Procedure of simulating gas-liquid droplet interaction

The mutual influence of the phases is taken into account as follows: the trajectory parameters of probe particles are averaged in space and time in each cell, and the data obtained are used to compute the sources of mass, momentum, and energy, associated with the disperse phase. These sources are used in computing the gas-dynamic field of the carrier phase at the next iteration. The flow chart of the Lagrangian-Eulerian algorithm is shown in Fig. 2.71.

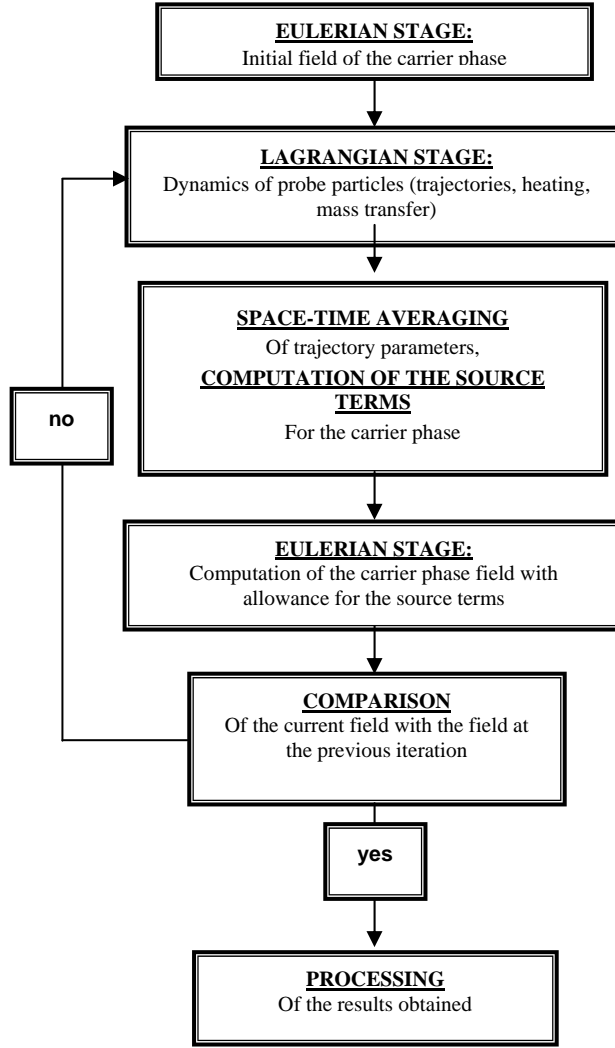


Fig. 2.71. Flow chart of the Lagrangian-Eulerian description of the disperse mixture.

Eulerian stage

In the simplest case of an axisymmetric flow of a perfect ideal carrier gas, the equations of the Eulerian stage have the form

$$\frac{\partial \bar{X}_g}{\partial t} + \frac{\partial \bar{P}_g}{\partial x} + \frac{\partial \bar{Q}_g}{\partial y} + \bar{R}_g + \langle \bar{R}_{gp} \rangle n_p = 0, \quad (2.38)$$

where

$$\bar{X}_g = \begin{pmatrix} \rho_g \\ \rho_g u_g \\ \rho_g v_g \\ E_g \end{pmatrix}, \quad \bar{P}_g = \begin{pmatrix} \rho_g u_g \\ \rho_g u_g^2 + p_g \\ \rho_g u_g v_g \\ (E_g + p_g) u_g \end{pmatrix}, \quad \bar{Q}_g = \begin{pmatrix} \rho_g v_g \\ \rho_g v_g u_g \\ \rho_g v_g^2 + p_g \\ (E_g + p_g) v_g \end{pmatrix},$$

$$\bar{R}_g = \frac{1}{y} \begin{pmatrix} \rho_g v_g \\ \rho_g v_g u_g \\ \rho_g v_g^2 \\ (E_g + p_g) v_g \end{pmatrix}, \quad \bar{R}_{gp} = \begin{pmatrix} J_{gp} \\ F_{gpy} \\ F_{gpy} \\ W_{gp} \end{pmatrix},$$

ρ_g, p_g, T_g are the density, pressure, and temperature of the carrier phase, u_g, v_g are the components of the velocity vector \vec{V}_g of the carrier phase, n_p is the number density of disperse inclusions, $E_g = c_V T_g + 0.5(u_g^2 + v_g^2)$, c_V is the heat capacity of the carrier phase at constant volume, the subscripts g , and p refer to the carrier (gas) and disperse (particle) phases, x, y indicate projections to the corresponding Cartesian coordinates, $J_{gp}, \bar{F}_{gp}, W_{gp}$ are terms that describe interphase transfer of mass, momentum, and energy. The terms obtained by space-time averaging of the trajectory parameters of the probe particles are written in broken brackets. Note, the field of the carrier phase at the first iteration is computed under the assumption that $\bar{R}_{gp} = 0$.

Space-time averaging

To obtain the spatial distribution of gas-dynamic functions of the disperse phase and calculate terms that describe the interphase transfer processes $J_{gp}, \bar{F}_{gp}, W_{gp}$, the trajectory parameters of the probe particles are averaged in space and time within each cell. Figure 2.72 shows schematically how the probe particles pass a fragment of the computational domain. For a certain function φ in the computational cell $\{ij\}$, this procedure has the following form:

$$\langle \varphi \rangle_{ij} = \frac{\sum_{l \in \{ij\}} \int_0^{\tau_{lij}} \varphi_l dt}{\sum_{l \in \{ij\}} \tau_{lij}}, \quad n_{pij} = \frac{\sum_{l \in \{ij\}} \tau_{lij}}{V_{ij}}. \quad (2.39)$$

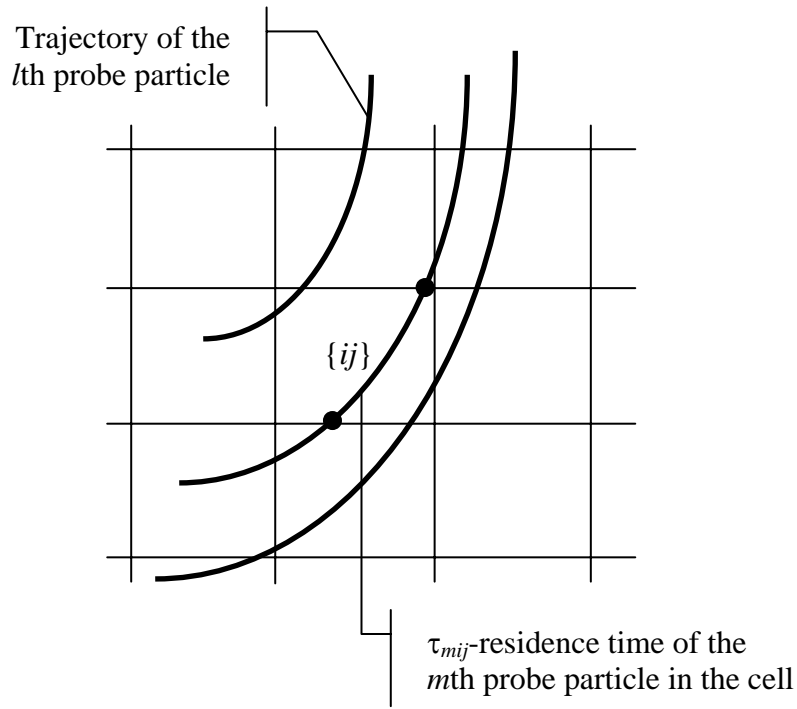


Fig. 2.72. Schematic of passage of the probe particles over a fragment of the computational domain

Here τ_{ij} is the residence time of the l th probe particle in the cell $\{ij\}$, $\dot{r}_l = n_{p0}V_{p0}S/N_p$ is the numerical flux of disperse inclusions, associated with the l th probe particle, n_{pij} is the numerical concentration of disperse inclusions in the cell $\{ij\}$, V_{ij} is the volume of the computational cell $\{ij\}$, S is the cross-sectional area through which the disperse particles enter the computational domain, and N_p is the number of probe particles; the subscript 0 indicates parameters at the entrance of the computational domain. Summation is performed over all probe particles that enter the cell $\{ij\}$.

Validation: shock-wave interaction with a cloud of disperse particles

The algorithm was used to simulate the interaction of a cloud of disperse particles with a shock wave. The main goal of this study was to analyze the reverse influence of disperse inclusions on the carrier phase flow. The computed results were compared with the experimental data reported in [8].

The effect of disperse particles on the carrier gas flow is taken into account in the following iteration procedure:

- at the first (Eulerian) step, equations of the carrier gas are solved;
- at the second (Lagrangian) step, trajectories of the probe particles are calculated using the carrier-phase flowfield obtained at the previous stage;
- at the third (phase coupling) step, the space-time averaging procedure (Eqs. (5)) is carried out within each computational cell in order to calculate distributions of the disperse phase parameters;
- the data obtained at the previous step are used to calculate the source terms due to the disperse phase. These terms are incorporated in computation of the carrier phase flowfield at the next Eulerian step. In the first iteration, when the sources caused by the influence of the disperse phase are unknown, they are assumed to be equal to zero.

The computations were performed for a shock wave propagating in air, the shock-wave Mach number was $M=2.8$, and the initial test-gas pressure was $P=0.1$ MPa; bronze and acrylic

monodisperse spherical particles were considered, and their volume content was assumed to be $m=0.001$ and $m=0.03$.

Figure 2.73 (a, b) shows the trajectories of disperse particles. The dashed and solid curves show the computation results without and with allowance for the influence of disperse inclusions on the carrier phase, respectively. If the initial volume content of particles is low (Fig. 2.73a), their influence on the carrier gas is insignificant, and the computation that ignores this influence ensures good agreement with experimental data. As the initial volume content of particles increases (Fig. 2.73b), their influence on the carrier gas increases, and it becomes necessary to include the above-described iterative procedure for this reverse influence of the disperse phase in the carrier gas into computations. In the case of a high initial volume content of particles, the absence of the reverse influence of the disperse phase in the computational algorithm leads to some overrating of the particle velocity.

The computations show that, for a rather high volume content of the disperse phase, the developed algorithm requires up to five global iterations to account for the effect of particles on the carrier-phase flow. However, a significant increase in the required number of iterations with increasing initial volume content of the disperse phase was observed.

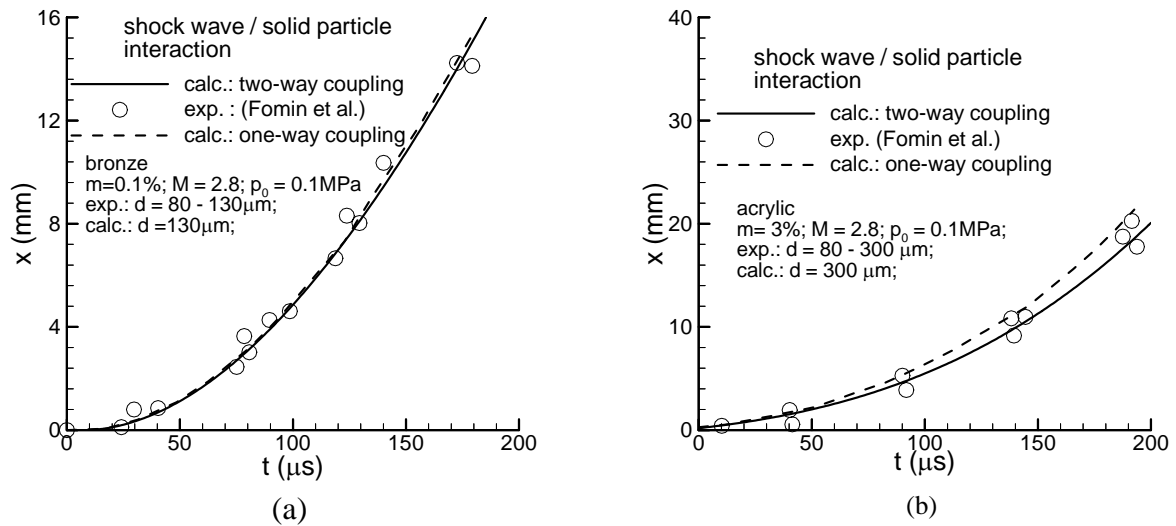


Fig. 2.73. Disperse particle trajectories resulting from interaction with the shock wave.

Task 2.8. Validation of theoretical models of gas-droplet plume flow via comparison with the experimental results on the angular distribution of the droplet phase.

Task 2.8.1. Developing a software module for simulation of condensation of carrier gas in plume flows

In the experiments performed within the present project, either a conical nozzle with the design Mach number at the nozzle exit $M=2.84$ or a constricted tube (sonic nozzle) is used. The stagnation temperature has the room value. Under these conditions, there is no condensation of the carrier gas inside the nozzle.

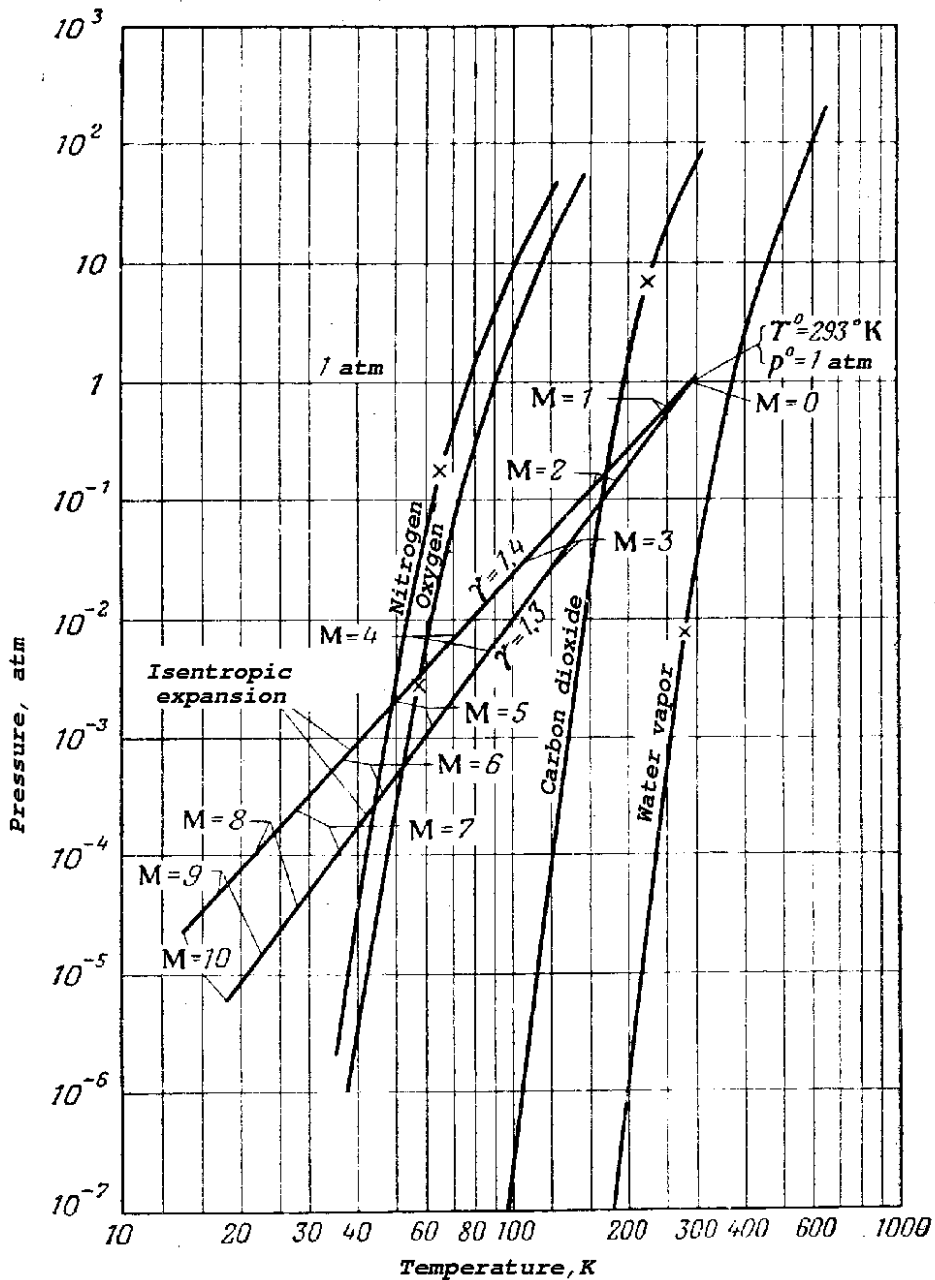


Fig. 2.74. Saturation curves for water vapor, carbon dioxide, oxygen, and nitrogen.

Figure 2.74 borrowed from [9] shows the saturation curves for several gases in the pressure-temperature coordinates. The figure also shows the behavior of pressure and temperature of the gas isentropically expanding from the state at room temperature and normal atmospheric pressure. It is seen from the figure that condensation both for nitrogen and for oxygen starts when the Mach number reaches approximately $M=5$. Thus, the above-made conclusion on the absence of carrier-gas condensation inside the nozzle under test conditions of the present project is validated.

Let us now consider the possibility of gas condensation outside the nozzle, in the exhausting plume. To determine the role of this process, we used the pressure field $P(x,y)$ obtained in numerical simulations of the flow on the basis of Navier-Stokes equations. We constructed isolines of $P/P_s(N_2)$, where P_s is the saturation pressure. The data on nitrogen saturation were taken from a reference book for the range of pressures $1 \div 3.396 \cdot 10^6$ Pa, which corresponds to the range of temperatures $37 \div 126$ K. Data processing in the coordinates

$\ln p_s, x=1/T$ yielded an approximation in the form $\ln p_s = 19.8317 - 557.728x - 6635.94x^2$, which is in excellent agreement with the tabular data.

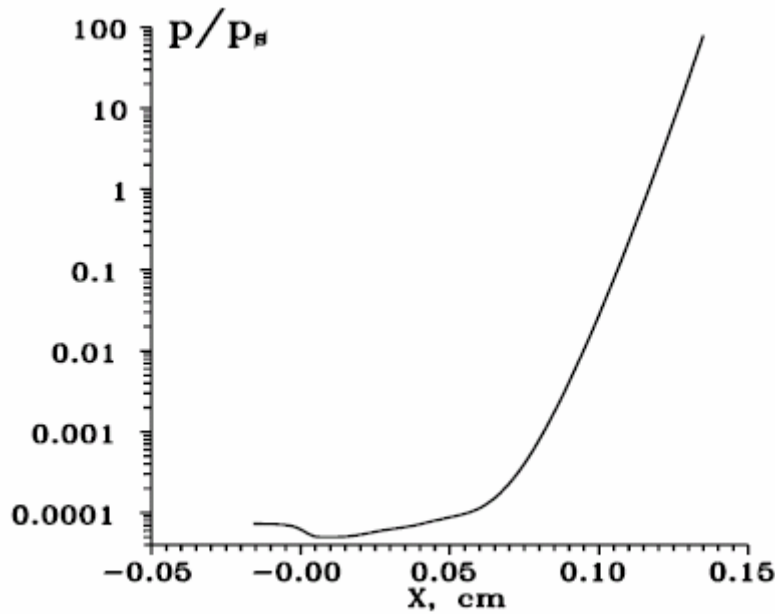


Fig. 2.75. Variation of p/p_s along the nozzle centerline.

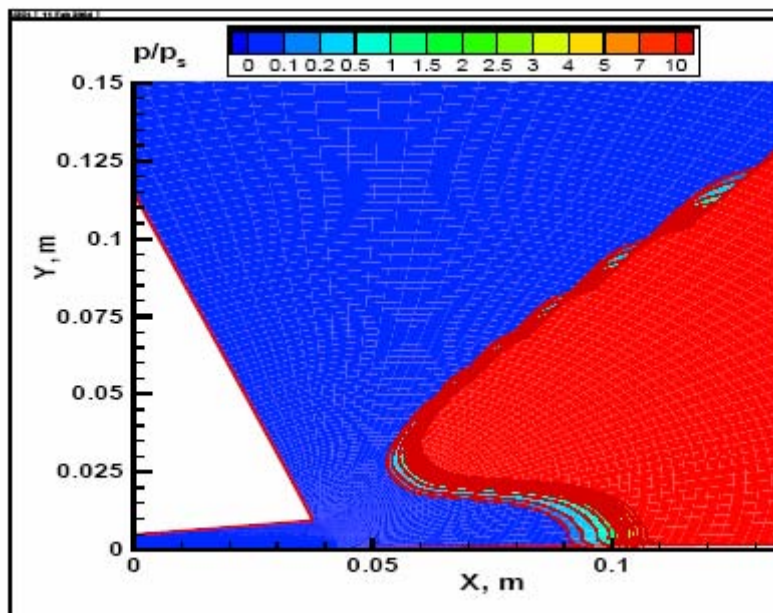


Fig. 2.76. Field of p/p_s , which shows the boundary of the region of carrier-gas condensation

The field of the quantity P/P_s is shown for the centerline $y=0$ (Fig. 2.75) and for the entire working area (Fig. 2.76). Figure 2.75 shows that, except for the subsonic part of the nozzle, the saturation pressure decreases more rapidly than the gas pressure when approaching the nozzle exit. The function $p/p_s(x,0)$ drastically increases, and the pressure ratio becomes

higher than unity at a distance of ≥ 10 cm, which corresponds to the necessary condition of condensation. The boundary of the condensation region $p(x, y)/p_s(x, y) > 1$ has a rather complicated curved shape with a typical ridge at a certain distance from the nozzle centerline and a valley near the flow centerline. It follows from Figs. 2.75 and 2.76 that there is no condensation inside the nozzle. Outside the nozzle, condensation occurs at a rather large distance from the nozzle exit. A significant difference in the positions of the carrier-gas condensation region and backflow region allows us to conclude that the liquid phase formed by the carrier gas does not enter the backflows. The fields of gas-dynamic quantities calculated without allowance for condensation should be corrected inside the indicated region.

Thus, under test conditions performed within the framework of the present project, condensation of the carrier phase occurs at a rather large distance from the nozzle exit, in the region without gas backflows. Hence, condensation cannot affect on formation of backflows on the disperse phase. Taking this fact into account, it was decided to ignore carrier-gas condensation in further works of the present ISTC project.

2.8.2. Numerical simulation of the gas-droplet plume flow

This task includes numerical computations on exhaustion of a two-phase gas-droplet plume from a supersonic nozzle under conditions of experiments performed at the Institute of Thermophysics of the Siberian Branch of the Russian Academy of Sciences.

Figure 2.77 shows the geometry of the supersonic conical axisymmetric nozzle used in the experiments. The nozzle has the following geometric characteristics: nozzle-throat radius $R^* = 5$ mm, radius of the generatrix in the nozzle throat $r_{\alpha\beta} = 5$ mm, radius of the exit cross section $R_e = 9.55$ mm, and apex half-angle of the cone in the divergent part of the nozzle $\alpha = 7^\circ$. The design Mach number of this nozzle is 2.84.

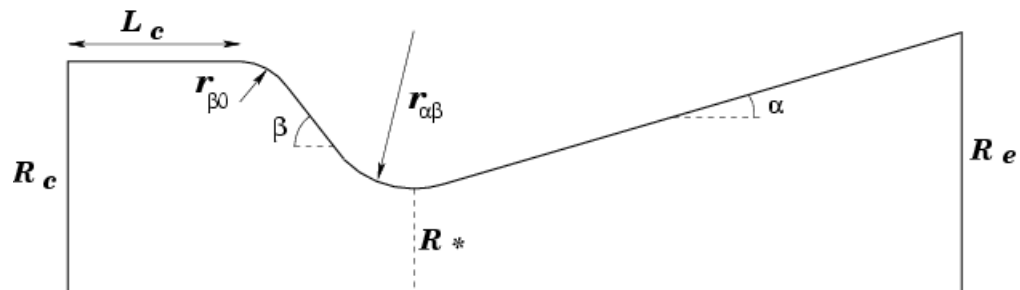


Fig.2.77. Geometry of the supersonic conical nozzle.

In the first experimental test case considered, the flow parameters correspond to a stagnation pressure $P_0 = 3390$ Pa and stagnation temperature of 293.15 K. The carrier-gas phase is N_2 , and the disperse droplet phase is ethanol.

Based on the hybrid Lagrangian-Eulerian algorithm developed, the exhaustion of the gas-droplet flow from the nozzle was numerically simulated. The carrier-gas flow was simulated by solving the full unsteady Navier-Stokes equations, and the dynamics of the disperse phase was modeled on the basis of the Lagrangian approach. The flow was assumed to be axisymmetric.

The trajectories and distributions of the Reynolds, Mach, Knudsen, and Weber numbers in the region occupied by the disperse phase were calculated with the help of the numerical algorithm developed. Figure 2.78 shows the data for droplets $0.5 \mu\text{m}$ in diameter. The flow is appreciably stratified, and $Re_{gp}, M_{gp}, We_{gp} \ll 1$, and $Kn \gg 1$ in the entire region occupied by the disperse phase. This result confirms the above-made assumptions that it is possible to neglect deformation of droplets and indicates that the flow around the droplets is free-molecular. Similar distributions for droplets $1 \mu\text{m}$ in diameter are plotted in Fig. 2.79.

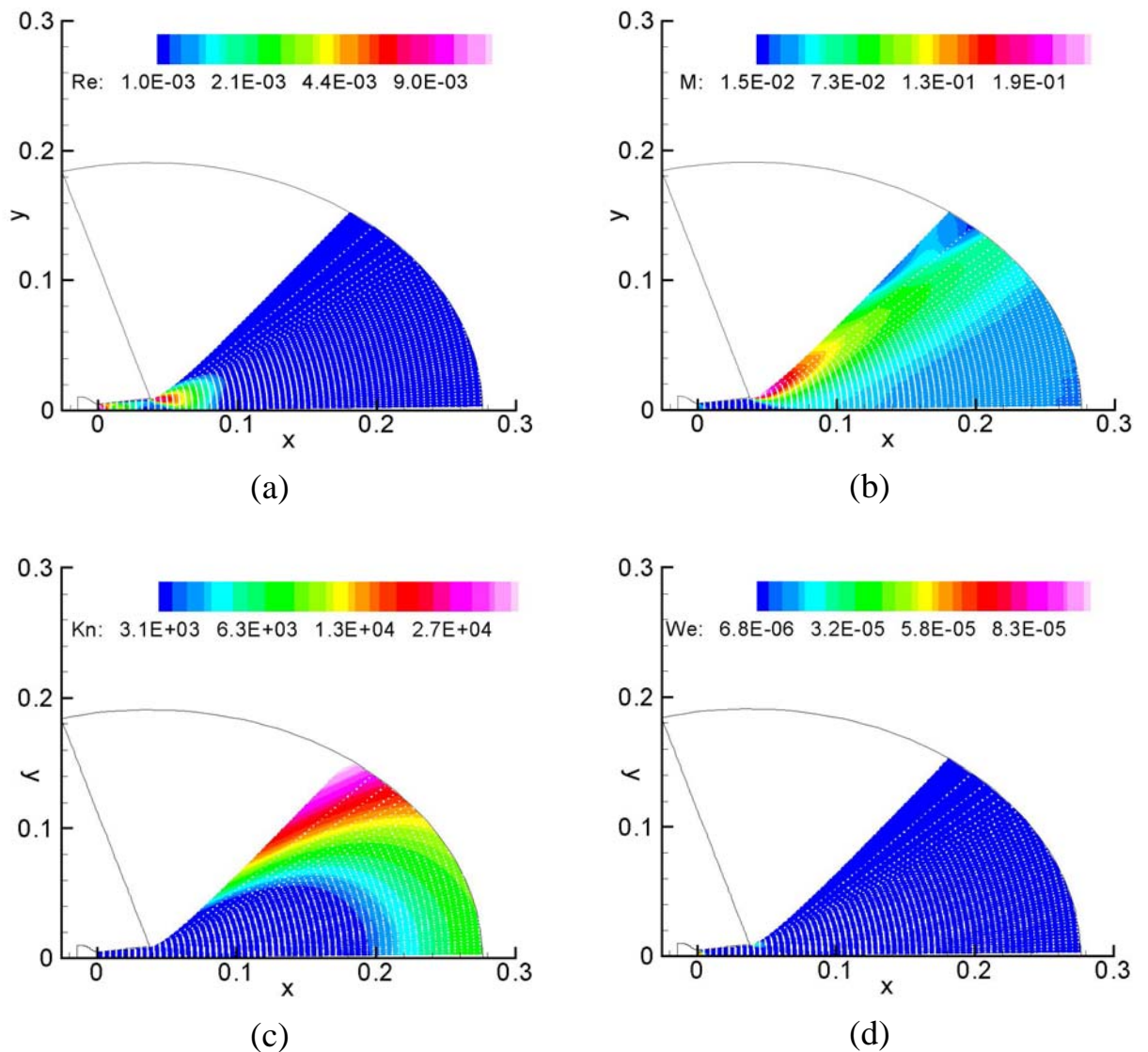


Fig. 2.78. Trajectories of probe particles (white traces) and distributions of the Reynolds (a), Mach (b), Knudsen (c), and Weber (d) numbers. The probe-particle diameter is $d_p=0.5 \mu\text{m}$.

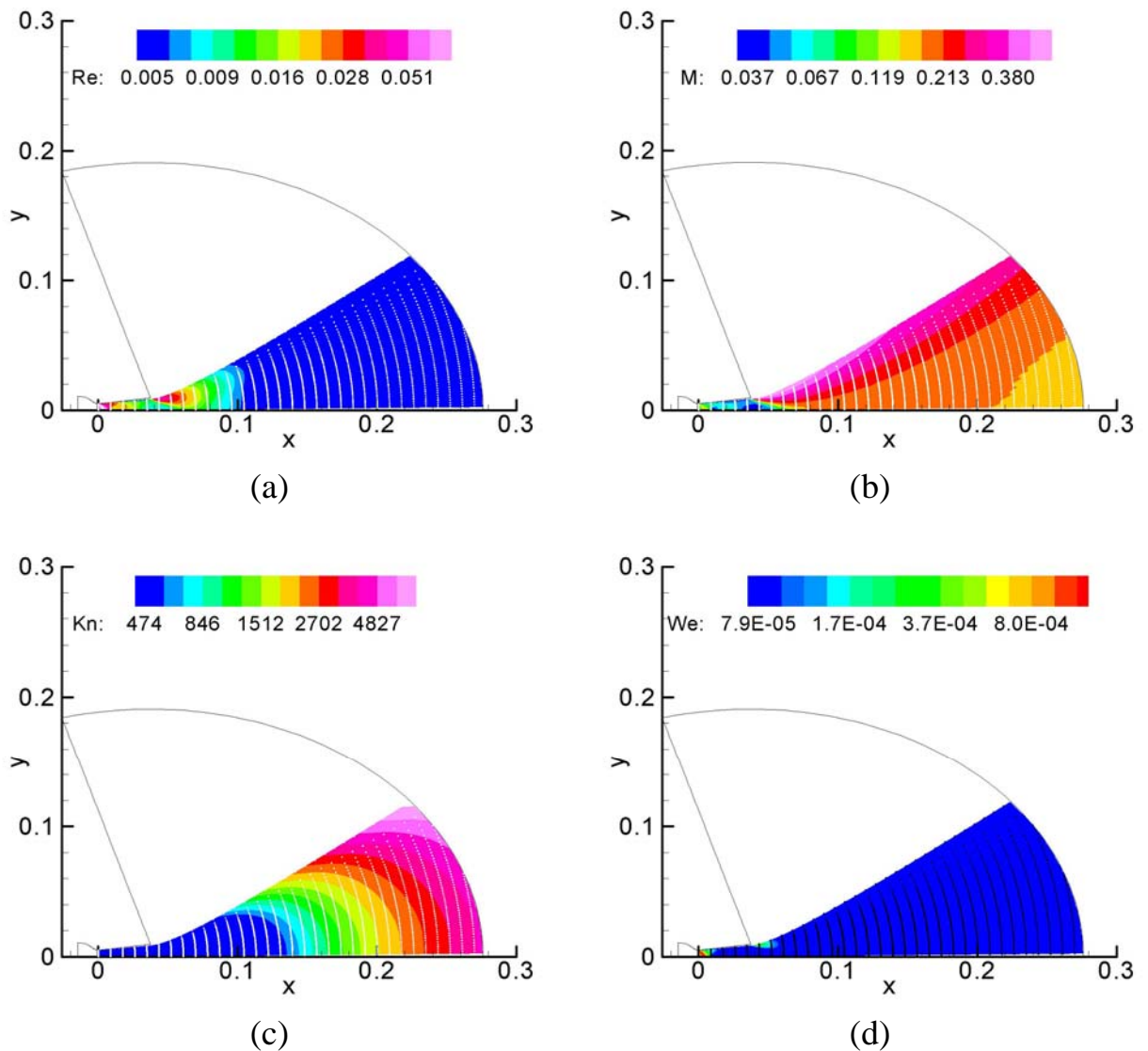


Fig. 2.79. Trajectories of probe particles (white traces) and distributions of the Reynolds (a), Mach (b), Knudsen (c), and Weber (d) numbers. The probe-particle diameter is $d_p=1.0 \mu\text{m}$.

Figure 2.79 also indicates that $Re_{gp}, We_{gp} \ll 1$, and $Kn \gg 1$ in the entire region occupied by the disperse phase; however, at the periphery of the disperse flow, after the flow leaves the nozzle, the Mach number reaches ≈ 0.5 , i.e., the effects of compressibility of the carrier phase near the droplet are manifested. It should be noted that the disperse flow region in this case is smaller than that in Fig. 2.78 for smaller droplets.

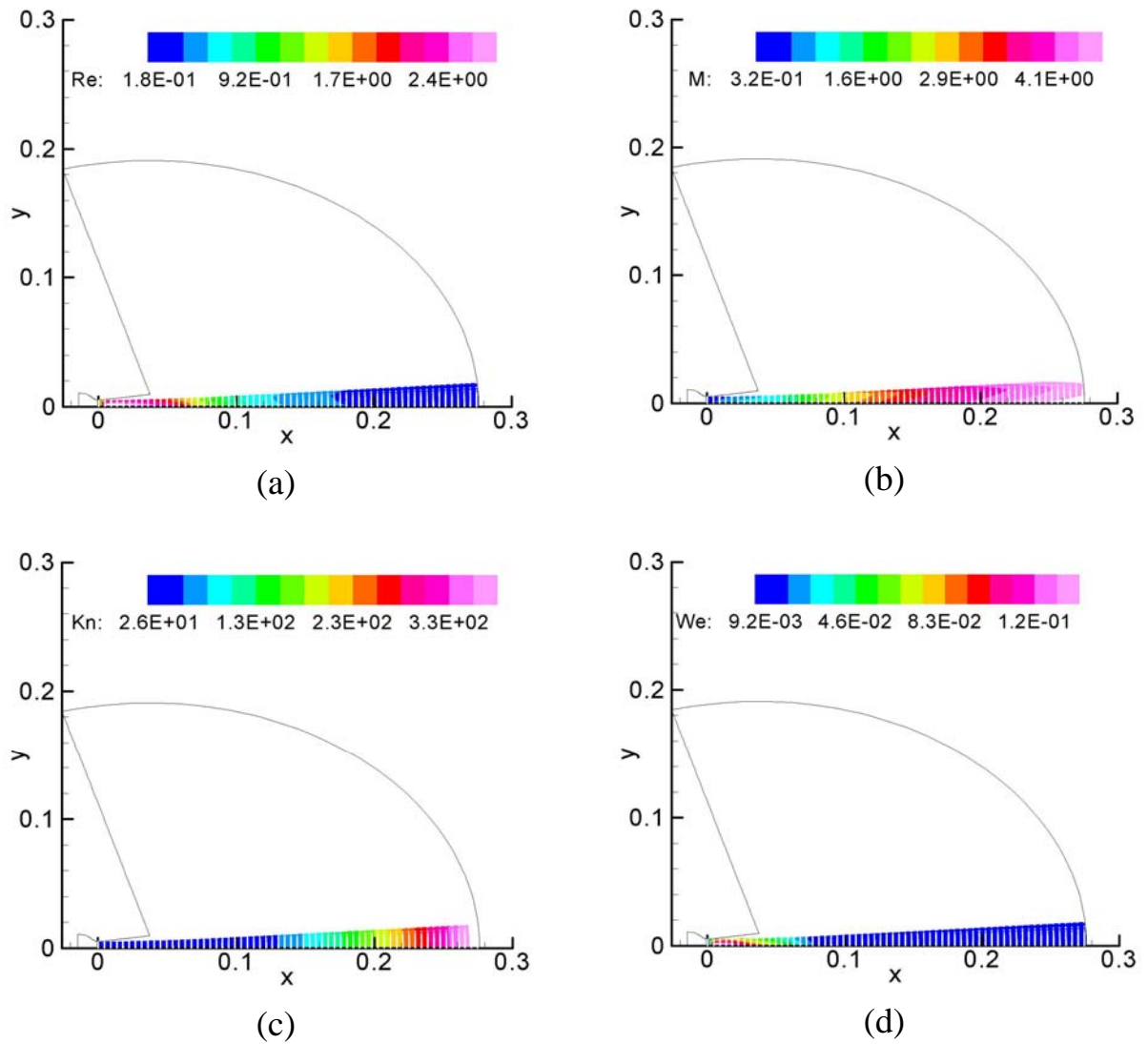


Fig. 2.80. Trajectories of probe particles (white traces) and distributions of the Reynolds (a), Mach (b), Knudsen (c), and Weber (d) numbers. The probe-particle diameter is $d_p=10.0 \mu\text{m}$.

Figure 2.80 shows similar data for drops $10 \mu\text{m}$ in diameter. The disperse flow region becomes even narrower, the Mach number reaches ≈ 5.0 , the Reynolds number is 5.0 , but we still have $We_{gp} \ll 1$, and $Kn \gg 1$.

It should be noted that the assumptions made in describing the processes of interphase exchange of mass, momentum, and energy, agree with the range of parameters observed in simulations.

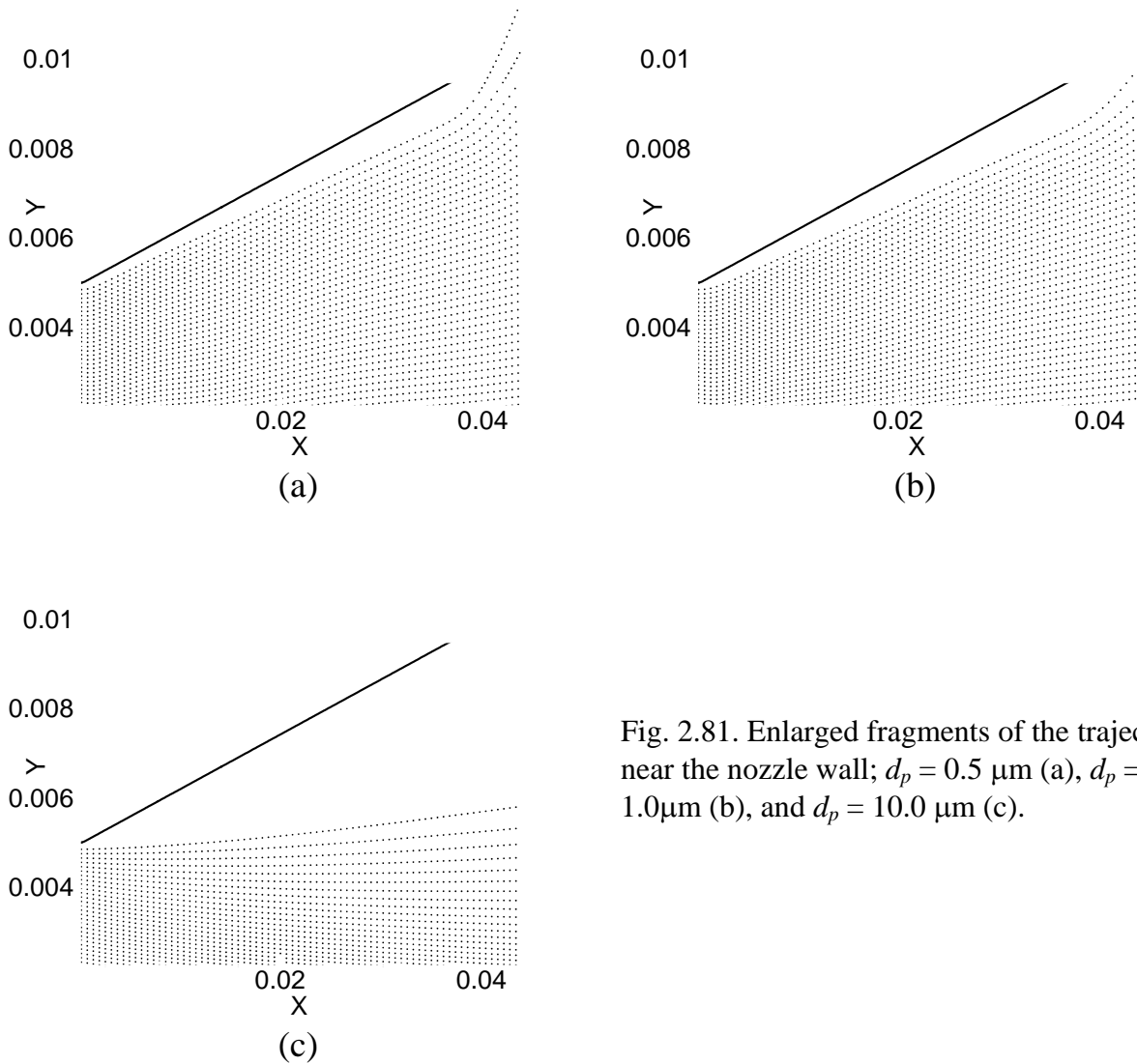


Fig. 2.81. Enlarged fragments of the trajectory near the nozzle wall; $d_p = 0.5 \mu\text{m}$ (a), $d_p = 1.0 \mu\text{m}$ (b), and $d_p = 10.0 \mu\text{m}$ (c).

Figure 2.81 shows the fragments of trajectories near the nozzle wall for droplets of different diameters. One can clearly see the “boundary” trajectories separating the regions of the gas-droplet flows and the “pure” gas near the wall. It should be noted that flow stratification can be additionally affected by the “transverse” Saffman force. The phenomenon of flow stratification is important because it plays a significant role in analyzing the interaction between the drops and the film flowing along the nozzle walls.

In the second case considered, exhaustion from the nozzle with a stagnation pressure $P_0=1 \times 10^5$ Pa was simulated. In this case, gas-flow simulation was performed within the framework of the viscous approach, which is fairly justified in the first approximation at high Reynolds numbers corresponding to the flow parameters used. The initial positions of particles were set from the condition of their uniform axisymmetric distribution in the nozzle throat. The trajectories of drops of different diameters are plotted in Fig. 2.82. Note that the results obtained in this case are in qualitative agreement with those shown above for a lower stagnation pressure. As in the case with $P_0=3390$ Pa, the region occupied by the disperse phase becomes significantly narrower for large drops.

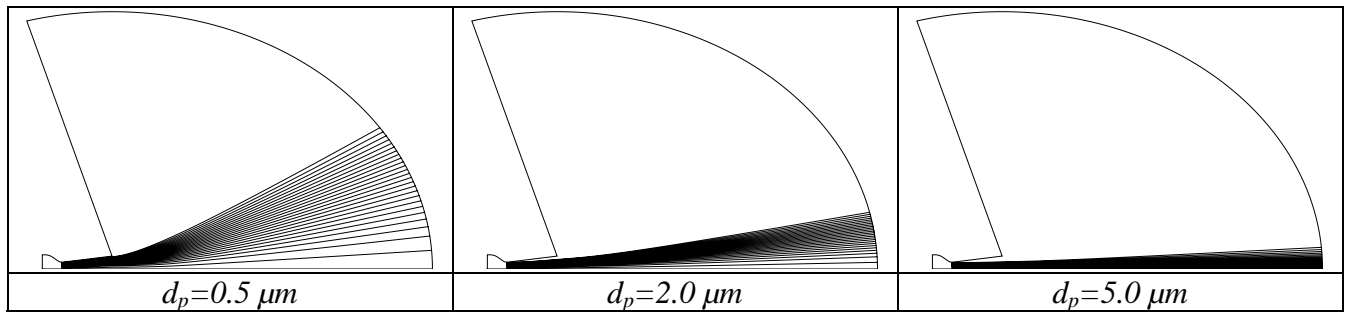


Fig.2.82. Trajectories of probe particles of different size.

Spatial distributions of droplets at the exit of the computational domain were plotted. Figure 2.83 shows the angular distributions of density of particles in the range of particle size of 0.5 – 5 μm. The number of Lagrangian probe particles in each case was $N_p=5000$.

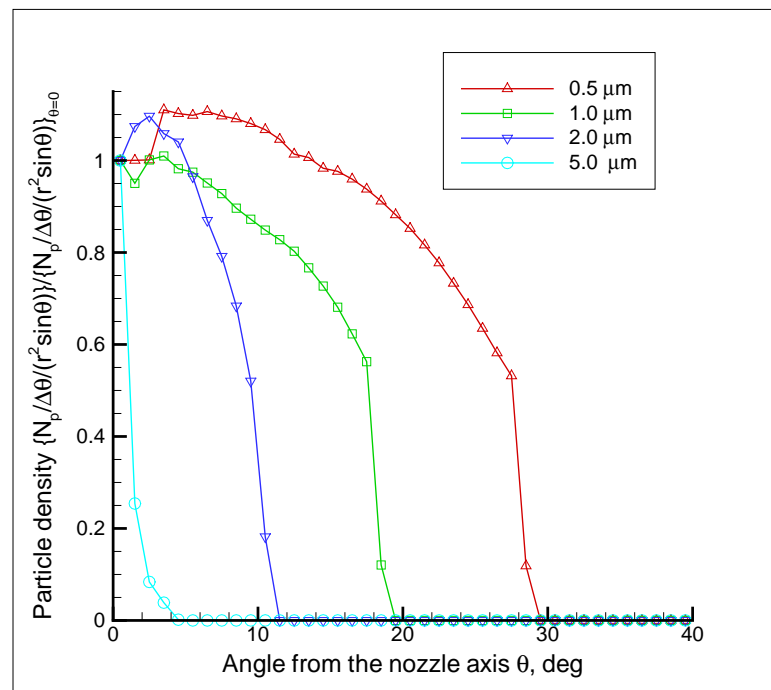


Fig.2.83. Angular distributions of droplets of different size at the exit of the computational domain

An analysis of the distributions obtained shows that the liquid droplets in the flow near the nozzle throat cannot serve as a source of a contaminating backflow because their spatial distribution in the case of plume exhaustion from the nozzle is limited to a narrow sector near the plume axis. Note, the angular distribution becomes even narrower for large drops, which make a significant contribution to the liquid-phase mass flux. Based on the results obtained, we can conclude that the main source of the disperse-phase backflow is, apparently, the liquid drops formed by liquid-film disintegration caused by abrupt expansion of the flow near the nozzle lip. Investigation of these processes is the main subject of the study at the subsequent stages of the project.

References used

1. Gelfand B.E. Droplet breakup phenomena in flows with velocity lag, Progr. Energy Comb. Sci., 1996, v. 22, pp. 201-265

2. Bailey AB; Hiatt J Sphere drag coefficients for a broad range of Mach and Reynolds numbers, AIAA J., 1972, v.10, pp. 1436–1440
3. Zarin N.A. Measurement of non-continuum and turbulence effects on subsonic sphere drag, 1970, NASA CR 1585.
4. Ranz W.E., Marshall, W.R. Evaporation from drops: II. Chem. Engng. Prog., 1952, v. 48, pp.173-180.
5. Miller R. S., Harstad K., Bellan J. Evaluation of equilibrium and non-equilibrium evaporation models for many-droplet gas-liquid .flow simulations, International Journal of Multiphase Flow, 1998, v. 24, pp.1025-1055.
6. Downing C.G. The evaporation of drops of pure liquids at elevated temperatures: rates of evaporation and wet-bulb temperatures, AIChE J., 1966, v. 12, No. 4, pp.760-766.
7. Saltanov G.A. Nonequilibrium and Unsteady Processes in Gas Dynamics [in Russian], Nauka, Moscow, 1979, 286 pp.
8. Boiko V.M., Kiselev V.P., Kiselev S.P., Papyrin A.N., Poplavsky S.V., Fomin V.M. Shock wave interaction with a cloud of particles, Int. J of Shock Waves, 1997, No. 7, pp.275-285.
9. Fundamentals of Gas dynamics. Ed. By H.W.Emmons. Princeton, NJ, Princeton University Press, 1958.

Thus, in the course of the 2nd year of the project

1. Two schemes of registration of videoimages of droplet-phase ejection into vacuum (with the use of conventional illumination and with the use of the laser («laser sheet» technique)) have been developed and assembled. The first scheme allows obtaining the general structure of the flow, and the second one provides the flow structure in an arbitrary plane parallel to the plume axis. The methodical aspects of obtaining and processing videoimages have been considered.
2. The influence of the governing parameters on formation and behaviour of droplets, starting from the nozzle exit, has been experimentally examined.
3. The general structure of the droplet-phase flow in the gas-droplet flow in vacuum has been established: in the case of ejection of the near-wall liquid film with the co-current gas flow into vacuum, there are two characteristic regions of the droplet-phase flow (central and peripheral). The central region is caused by drop shedding from the film surface near the nozzle throat and their further splitting and acceleration in the gas flow moving inside the nozzle and in the plume behind it; the peripheral region is formed by disintegration of the near-wall liquid film at the nozzle exit, where the pressure drastically decreases and the liquid becomes overheated.
4. A model of the previously found effect of liquid film lifting on the external surface of the nozzle against gravity has been constructed. Satisfactory correlation of the model with experimental results has been demonstrated.
5. A model of interaction of the co-current gas flow with the near-wall liquid film inside the nozzle has been proposed; the model allows one to estimate the film thickness and velocity near the nozzle lip.
6. Three independent techniques for measuring spatial distributions of droplet-phase flows have been developed and justified:
 - technique of the quartz microbalance;
 - technique of spectrophotometry;
 - technique of deposition on a paper substrate.

7. The influence of the nozzle geometry, properties of gas-flow parameters, and properties of the liquid on the spatial distribution of the droplet phase in the gas-droplet flow has been investigated.
8. The distributions functions of droplets in terms of sizes, directions, and velocities have been measured.
9. A model of disintegration of the near-wall liquid film into droplets at the nozzle exit has been proposed; the model is in satisfactory agreement with experimental results.
10. A software module has been developed for simulating the dynamics of droplet–phase particles on the basis of the Lagrangian approach with allowance for evaporation and condensation.
11. A numerical algorithm has been developed for taking into account the reverse effect of the droplet phase on the carrier-gas flow by means of a special procedure of space-time averaging and iterative approach.
12. Verification and validation of the software codes have been performed by comparing the results with experimental data available in the literature.
13. Effects of the possible influence of carrier-gas condensation have been examined. It has been shown that carrier-gas condensation can occur only outside the nozzle, at a sufficient distance from the nozzle exit; hence, condensation cannot affect the formation of backflows of the droplet phase.
14. Parametric computations of gas-droplet flows inside the nozzle and in the exhausting plume have been performed. In contrast to experimental results, the computed angular distributions of disperse-phase droplets do not reveal the second maximum associated with the droplet backflow. This confirms the conclusion that backflow formation is related to disintegration of the liquid film on the nozzle lip rather than to turning of droplets leaving the nozzle.

Task 2. Investigation of gas-droplet flows. 3rd year

Task 2.9. Numerical study of the physical mechanisms for the entrainment of the liquid droplets into the backflow motion.

Task 2.9.1. Consideration of the interaction of the liquid wall cooling film flow with the carrier gas.

The work in the third year involved the study of physical mechanisms of entrainment of liquid-phase drops into the backflow. Namely, the interaction between the cooling liquid film flow along the nozzle wall and the high-velocity gas flow was considered. A mathematical model was constructed, which describes the liquid-film flow in a supersonic nozzle in the case of heat and mass transfer between the phases. The liquid flow is described by boundary-layer equations with constant values of density and thermal conductivity and a temperature-dependent coefficient of viscosity. Evaporation of the liquid, entrainment of drops by the gas flow, and deposition of drops are taken into account at the interface. The resultant system of equations is solved by an integral method.

The computations were performed for different values of the flow rate of the coolant and gas pressures in the plenum chamber. The film thickness, mean velocity of the film, and temperature of the liquid at the interface were obtained as functions of the streamwise coordinate (see Figs. 2.84, 2.85). It is shown that liquid evaporation from the interface prevails for low flow rates of the coolant and low pressures. It is found that the mean velocity and thickness of the liquid film outside a small vicinity of the liquid-injection point become independent of their initial values. The thickness of the relaxation region is proportional to the liquid flow rate.

The film temperature decreases along the nozzle because of liquid evaporation (Fig. 2.86). The most drastic decrease in temperature at the interface is observed near the injection point in the region of the maximum temperatures. In the supersonic part of the nozzle, the temperature is stabilized near a value determined by the balance between the heat flux from the wall and heat consumption for evaporation. The pressure gradient near the nozzle-exit section is low, and the film flow occurs under the action of the friction force, which is approximately constant across the film.

The liquid remaining in the film flows down to the exit section, where it decomposes into individual fragments and forms droplets under conditions of drastic changes in gas parameters and forces acting on the film. This mechanism is consistent with the experiments, where trajectories of coarse droplets emanating from the neighborhood of the trailing edge of the nozzle were observed.

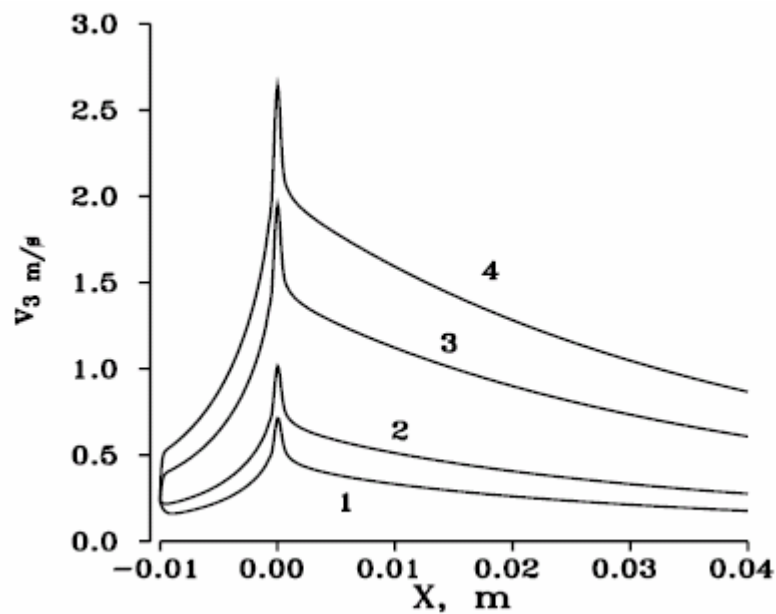


Fig.2.84. Mean velocity of the liquid film along the nozzle $v_3(x)$ for different pressures in the plenum chamber, Pa: 1) $4 \cdot 10^3$, 2) 10^4 , 3) $5 \cdot 10^4$, 4) 10^5 .

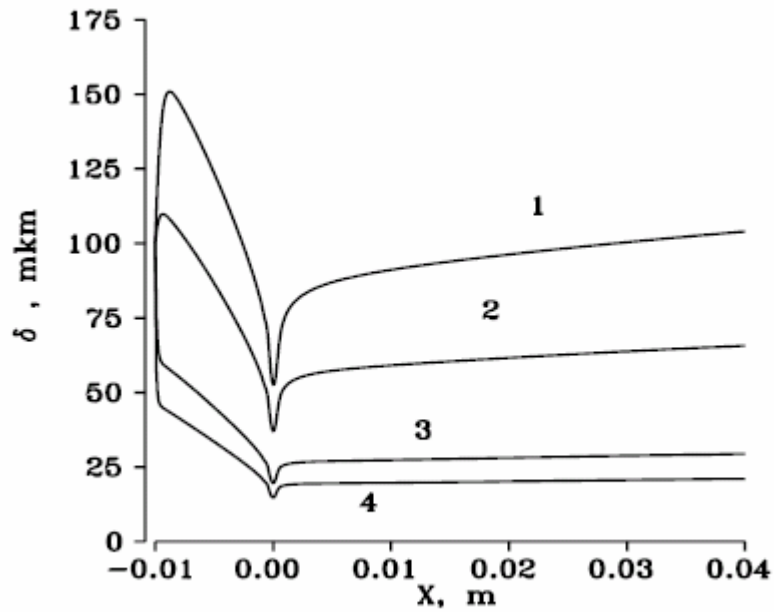


Fig.2.85. Cooling liquid film thickness along the nozzle $\delta(x)$ for different pressures in the plenum chamber, Pa: 1) $4 \cdot 10^3$, 2) 10^4 , 3) $5 \cdot 10^4$, 4) 10^5 .

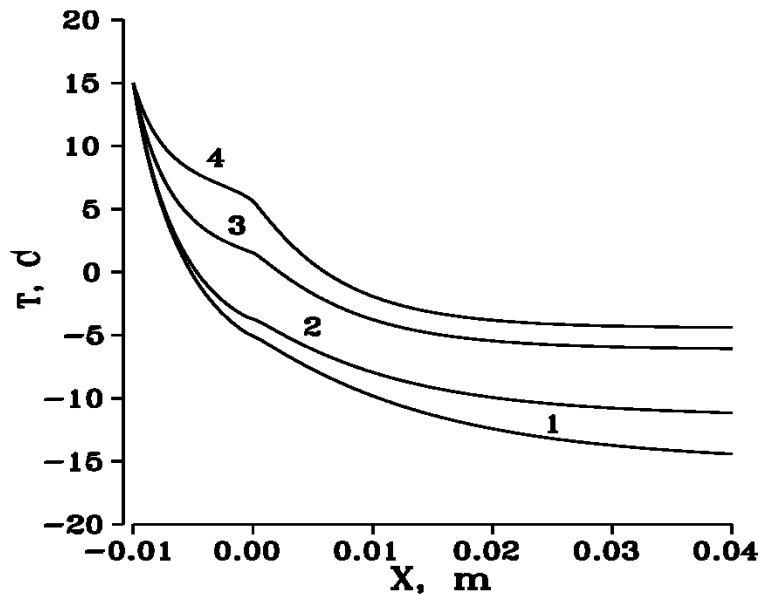


Fig.2.86. Temperature at the interface along the nozzle $T_i(x)$ for different pressures in the plenum chamber, Pa: 1) $4 \cdot 10^3$, 2) 10^4 , 3) $5 \cdot 10^4$, 4) 10^5 .

Task 2.9.2. Droplet formation in the vicinity of the nozzle lip.

Disintegration of the cooling film and formation of droplet, which further enter the backflow, was considered. To understand physical mechanisms controlling these processes, the possibility of boiling up of the liquid film inside the nozzle, the behavior of the liquid outside the nozzle in the vicinity of the exit section, and condensation of the carrier gas due to rapid cooling of the gas stream outside the nozzle were analyzed. It was found that the maximum possible size of the vapor bubble remains smaller than the critical value despite a significant decrease in pressure along the nozzle; hence, no boiling of the liquid inside the film occurs. Disintegration of

the film on the nozzle lip can occur because of the loss of stability of the liquid-layer flow. This occurs under the action of surface-tension forces, which pull the liquid jet separated from the wall into individual droplets. Significant nonuniformity of gas parameters in the vicinity of the nozzle lip make this process substantially more complicated. The characteristic times of film disintegration into individual fragments and coalescence of these fragments into droplets were estimated on the basis of the theory of stability of the liquid layer. The most probable size of the droplets being formed was also evaluated. It was predicted to be approximately 100 μm . The results obtained show that disperse-phase formation occurs in a very small region near the nozzle lip, and the direction of the vector of initial velocity of droplets coincides with the velocity vector of the carrier gas in this region.

It also seems possible that the liquid film can reach the outer surface of the nozzle, where its destruction can be induced by explosive boiling. The reason is a drastic increase in film thickness at the nozzle lip to a size greater than the critical value.

At the same time, consideration of the process of condensation of the carrier phase makes us conclude that it occurs at a significant distance from the nozzle exit; therefore, we can believe that the droplets of the liquid carrier phase do not enter the backflow.

The analysis described was used to study the dynamics of droplets in the vicinity of the nozzle lip. The trajectories of droplets originating near the nozzle lip were calculated. For this purpose, we used the flow fields outside the nozzle (including backflow regions), which were obtained in computations performed by the DSMC method. The computation results showed that the droplets originating near the nozzle lip are entrained by the gas backflow, which is responsible for the disperse phase flow in a considerable range of angles higher than 90° .

The disperse-phase dynamics in the backflow region was calculated for droplets of different sizes (1 μm – 1 mm) with varied initial positions and velocities. In these computations, the carrier gas flow was modeled by a hybrid approach including the Navier-Stokes equations and the DSMC method, which allows one to obtain results in the region of strongly rarefied backflows. The flow inside the nozzle was computed by the Navier-Stokes equations. The resultant numerical solution was used as the initial conditions for the DSMC computations. The input boundary of the DSMC computations was located inside the nozzle close to the exit. In simulating droplets originating near the nozzle lip, the droplets at the initial time were uniformly distributed over the surface of a torus “wrapped” around the nozzle lip. Figures 2.87-2.89 show the trajectories of probe particles (black lines) constructed for droplets with radii of 1, 10, and 100 μm . Figure 2.89 also shows the Mach number flow field of the carrier gas flow near the nozzle lip and in the backflow region (white lines with arrows indicate the streamlines of the carrier phase). In these computations, the distance from the nozzle lip to the torus surface was $r=0.5$ mm, and the nozzle lip was rounded with a radius $r=0.167$ mm. The initial particle velocity varied from zero to the local velocity of the carrier phase flow, and the direction of the particle-momentum vector coincided with the carrier-phase flow direction. It was also assumed that the temperature of droplets at the initial time equaled the local temperature of the gas.

It is quite clear that the droplets acquire a large enough cross-streamwise velocity component to get into the far field of the plume. As a result, the droplets can penetrate deeply into the backflow region. Despite extremely low densities of the gas in the backflow region (about 1×10^{-5} kg/m³ and lower), liquid particles are entrained by the carrier-gas backflow and propagate in directions at angles of 90 to 140° to the nozzle plume direction. The results of numerical computations showed that the trajectories of disperse particles in the backflow region depend little on the particle size and on the absolute value of the initial momentum of particles. These results convincingly show that formation of liquid droplets near the nozzle lip indeed leads to formation of the backflow of the liquid phase. The limiting trajectories make angles up to 140° to the nozzle plume direction. This value agrees surprisingly well with the liquid phase distributions observed in the experiments.

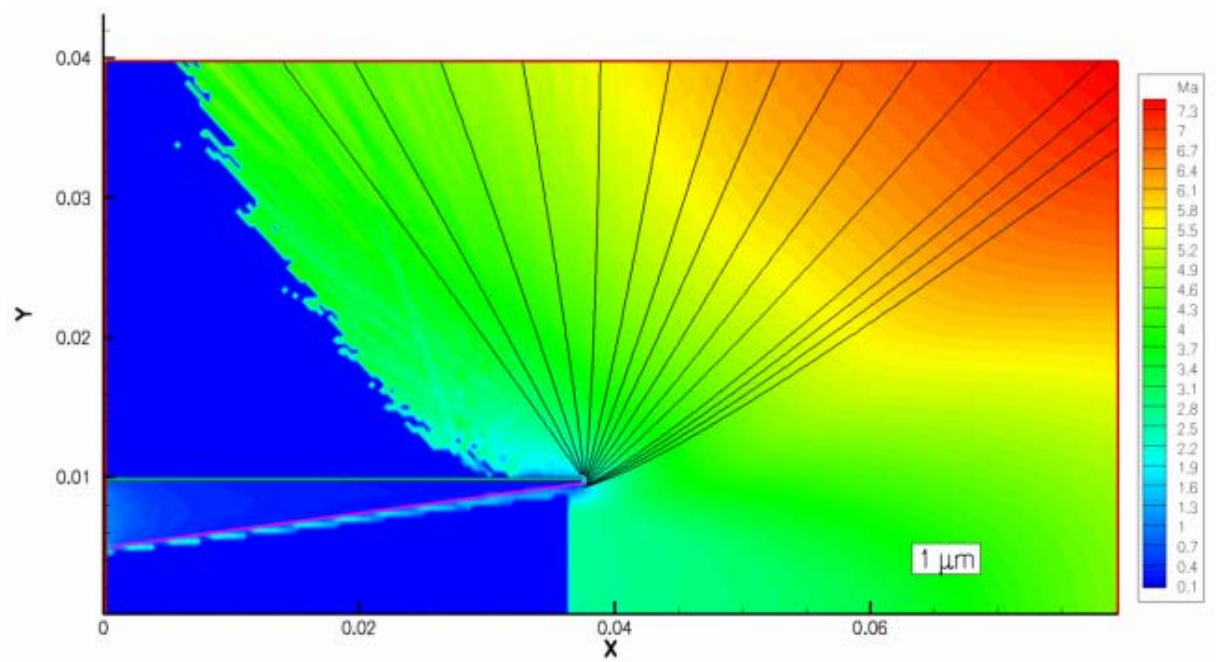


Fig.2.87. Trajectories of the droplets emerging near the nozzle lip. Droplet radius 1 μm .

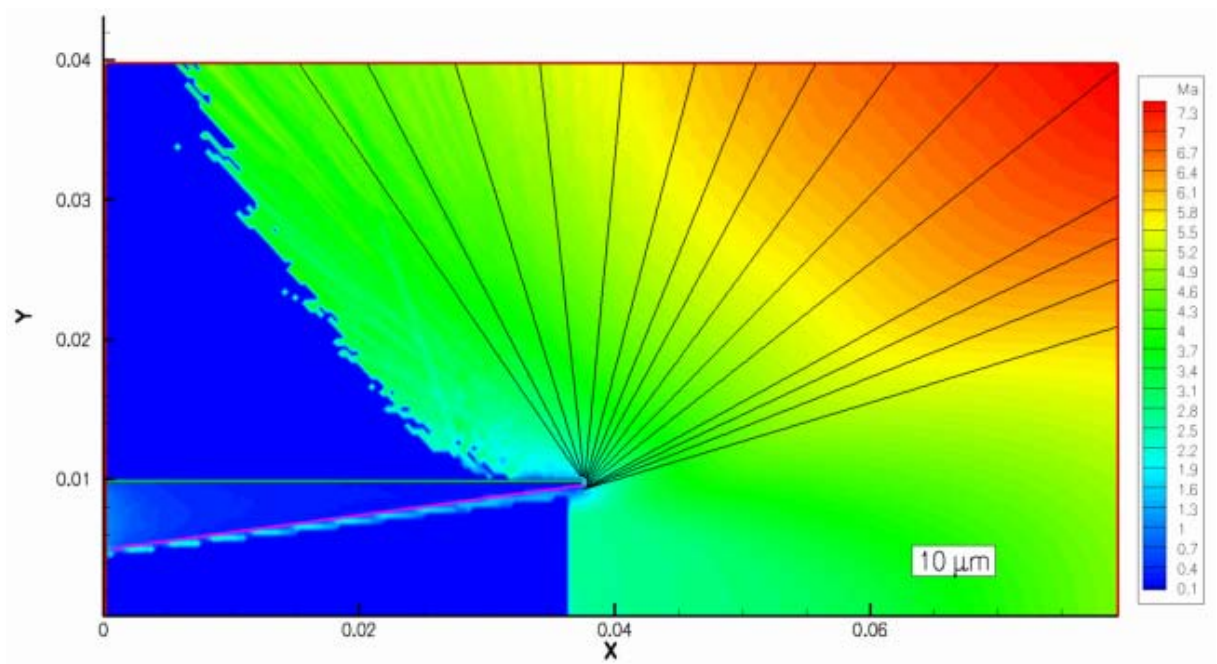


Fig.2.88. Trajectories of the droplets emerging near the nozzle lip. Droplet radius 10 μm .

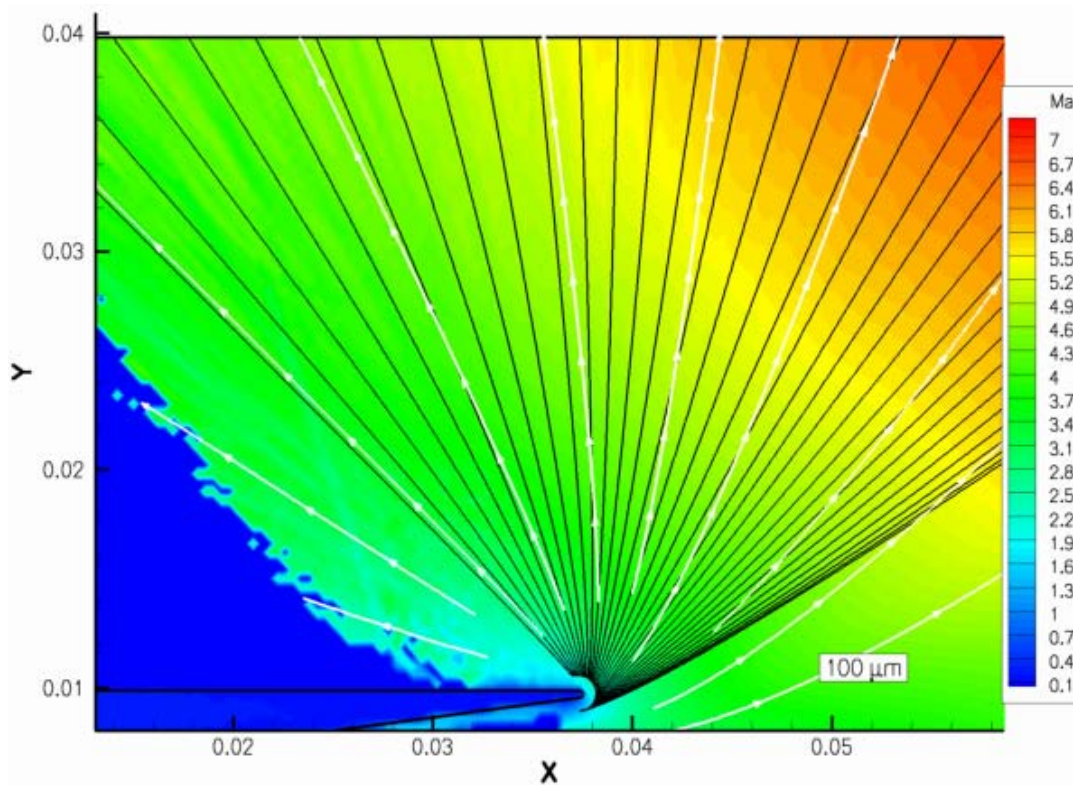


Fig. 2.89. Trajectories of liquid droplets formed near the nozzle lip.

Task 2.10.1. Analysis of factors of possible action on the angular distribution of the droplet phase

On the basis of experimental research performed at the previous stages within the framework of the present ISTC Project, it was established that the angular distribution of the droplet phase in the gas-droplet flow depends on initial parameters and properties of the gas flow, geometry of the nozzle and its exit edge, and parameters and properties of the near-wall liquid film. It was also revealed that the angles of the droplet phase significantly exceed 90° from the plume axis, i.e., a backflow of drops occurs. It is an adverse factor and explains the nature of contamination of spacecraft surfaces by plumes of control thrusters, in which the fuel film is used for cooling the nozzle walls.

The main objective of the given stage of the Project consists in consideration of opportunities of reducing the droplet-phase backflows.

It was shown that, among all possible factors of influence on the angular distribution of the droplet phase, the major factor is the dynamic influence (dynamic pressure $q = \frac{\rho \cdot V^2}{2}$) of the gas flow on the drops. Thus, for reducing droplet-phase backflows, it is necessary to decrease the dynamic influence of the gas flow on drops at the flow periphery. Here it is also possible to notice that the basic criterion determining the aerodynamic influence of the gas on the droplets is the Weber number

$$We = \frac{\rho \cdot (V - U)^2 \cdot d}{2\sigma},$$

where ρ is the gas density, V and U are the gas and droplet velocities, respectively, d is the droplet diameter, and σ is the coefficient of surface tension.

For better understanding of the situation we show the estimated values of q and We for typical test conditions ($p_0 = 1.3 \cdot 10^5$ Pa, $T_0 = 293$ K, working gas - air, working liquid - ethanol,

butanol). Such estimations were made for a supersonic nozzle ($M_a = 3$) and a cylindrical tube ($M_a = 1$). The values of q and We at the exit cross-section of the nozzles and in the plumes behind them were estimated.

The distributions of Mach numbers in the plumes behind sonic and supersonic nozzles, which are necessary for such estimations, were taken from appropriate calculations of exhaustion of an inviscid gas into vacuum.

In calculating the Weber numbers, the droplet size was assumed to be 200 μm as the most probable size in accordance with the results of measurements of the distribution function of the droplet size (eighth quarter report, task 2.6.2).

The estimates yielded the following results:

- **supersonic nozzle**
 - a) nozzle exit cross-section
 $q_a = 2.3 \cdot 10^4 \text{ Pa}$, $We_a = 200$;
 - b) plume behind the nozzle

| | |
|----------------|--|
| $x/r_a = 12.5$ | $q = 5.8 \cdot 10^2 \text{ Pa}$, $We = 5.2$, |
| $x/r_a = 25$ | $q = 1.4 \cdot 10^2 \text{ Pa}$, $We = 1.3$, |
| $x/r_a = 60$ | $q = 2.2 \cdot 10^1 \text{ Pa}$, $We = 0.2$; |
- **cylindrical tube**
 - a) nozzle exit cross-section
 $q_a = 4.8 \cdot 10^4 \text{ Pa}$, $We_a = 400$;
 - b) plume behind the nozzle

| | |
|----------------|--|
| $x/r_a = 12.5$ | $q = 1.1 \cdot 10^3 \text{ Pa}$, $We = 9.6$, |
| $x/r_a = 27.4$ | $q = 2.2 \cdot 10^2 \text{ Pa}$, $We = 2$, |
| $x/r_a = 60.8$ | $q = 4.4 \cdot 10^1 \text{ Pa}$, $We = 0.4$. |

We can state that the maximum values of q and We are reached at the nozzle exit. With distance from the nozzle exit cross-section, the values of q and We in the plume change proportionally to the change in the gas density ρ (the gas velocity in the plume is close to its limit, about 750 m/s in our case). As we have $\rho \sim \frac{1}{r^2}$ in the case of exhaustion into vacuum, the dynamic influence of the gas flow on the droplets decreases very rapidly with distance from the nozzle exit.

From the given data, we can conclude that the basic dynamic influence of the gas flow on the droplets occurs near the nozzle lip. It should be mentioned here that the pressure in the gas flow drastically decreases near the nozzle lip, and the liquid becomes overheated. It should result in explosive disintegration of the liquid.

As the basic events in the considered problem on exhaustion of the near-wall liquid film with a co-current gas flow from the nozzle into vacuum occur near the nozzle lip, it is reasonable to give the analysis of the influence of the nozzle-lip shape (round, right-angled, or sharp) on the angular distribution of the droplet phase mainly in the area of backflows. Direct measurements (see eighth quarter report, task 2.6.2) showed that such an effect is really observed. In particular, it was experimentally established that the right-angled edge produces the smallest back flows of the droplet phase and the round edge produces the greatest flows. Thus, from the viewpoint of reduction of backflows of the droplet phase, the right-angled edge of the nozzle is more preferable.

Now let us come back to the idea of reduction of dynamic influence (dynamic pressure) on the droplets with the purpose to decrease backflows of the droplet phase. It can be realized with the help of special devices – screens installed on the exit part of the nozzle. Within the

framework of the Project, four schemes of screens shown in Fig. 2.90 were considered. These schemes of screens differ:

- by the operation principle
 - non-absorbing (Fig. 2.90, *a, b, c*),
 - absorbing (Fig. 2.90, *d*);
- by design of the bottom part
 - closed (Fig. 2.90, *a, b, d*),
 - open (Fig. 2.90, *c*);
- by quantity of screens
 - single (Fig. 2.90, *a, c, d*),
 - double (Fig. 2.90, *b*).

The absorbing screens (Fig. 2.90, *d*) contain special absorbing material on the internal surface of the screen for catching droplets from the nozzle lip. This variant of the screen can be considered only for orientation thrusters of space vehicles with a rather small time of residence in space and with sufficiently large periods of time between thruster launches. Otherwise, it is preferable to use non-absorbing (smooth) screens.

A comparative analysis of screens with closed (Fig. 2.90, *a*) and open (Fig. 2.90, *c*) bottom parts shows that the scheme with the closed bottom part is obviously preferable. Confirmation of such a conclusion is the effect revealed in our experimental researches: the existence of back motion of the near-wall liquid film on the external surface of the nozzle (sixth quarter report, task 2.5.2). Therefore, it is necessary to avoid any sort of slits and holes in the bottom part of the screen. Moreover, the presence of the screen with an open-ended bottom part can, in our opinion, even strengthen the backflows of the droplet phase because of some increase in gas pressure in the space between the screens. Therefore, in a situation where the thruster structure does not allow mounting of the screen with a closed bottom part, it is better, in general, not to use the screen at all.

Based on the analysis performed, we can conclude that the screens of the schemes of Fig. 2.90, *a, b* are the best ones for solving the problem of reducing droplet-phase backflows. Decreasing the dynamic pressure of the gas flow at the nozzle lip by single (Fig. 2.90, *a*), double (Fig. 2.90, *b*) or multiple (if necessary) screens should result in reduction of droplet-phase ejection into the peripheral area of the flow. We chose these schemes as a basis for design and experimental researches for the subsequent stages under the Project.

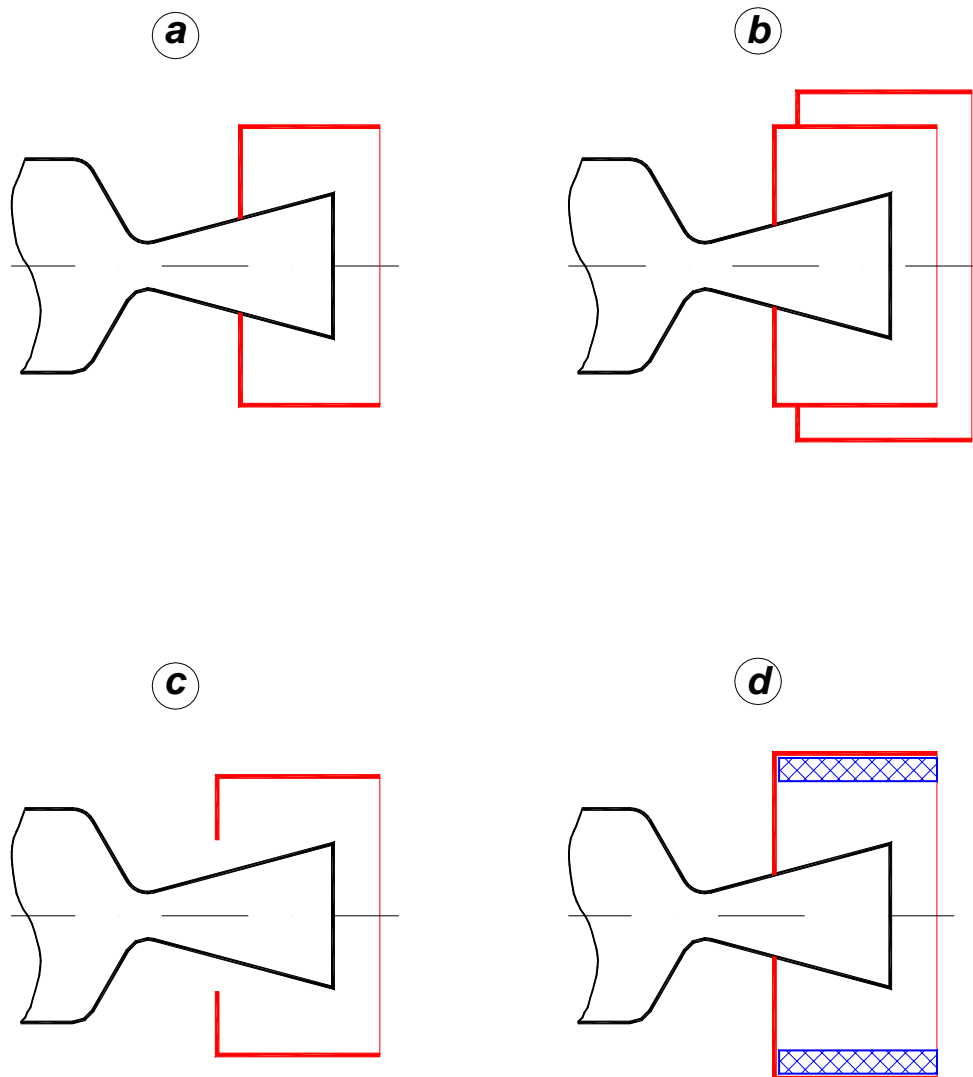


Fig. 2.90. Schemes of the screens

2.10.2. Justification, development, and manufacturing of a screen

On the basis of the analysis performed at the previous stage under the Project, a single screen with a closed bottom part (Fig. 2.90a) was chosen as the basic variant for experimental investigations.

The main reason for such a choice consists in simplicity of the screen scheme (canonical scheme) and in the opportunity to establish experimentally the influence of relative parameters of the screen on the angular distribution of the droplet phase and, first of all, magnitude of backflows.

The structural scheme of screen installation to the gas-dynamic source is shown in Fig. 2.91. The developed design provides an opportunity to measure the pressure in space between the screen and the nozzle through the tube 7. The space between the screen and the nozzle is hermetically sealed from the ambient space (vacuum chamber) with the help of the

pads 6. In order to investigate the influence of the angle φ (Fig. 2.91) on the value of pressure in space between the screen and the nozzle, and also on the angular distribution of the droplet phase, changeable screens of different length were manufactured. The chosen lengths of the screens provide an opportunity to change the angle φ in the range $\varphi = 30-90^\circ$. Thus, the ratio of the internal diameter of the screen to the exit diameter of the nozzle at the given stage of investigations was chosen constant and equal to 1.75. A total of five screens were manufactured.

The drawing of the screens is given in Fig. 2.92, the general view of the manufactured screens in Fig. 2.93, and the general view of the gas-dynamic source with the mounted screen in Fig. 2.94.

In the period under report, the expected values of pressure in space between the screen and the nozzle were estimated. Taking in account these estimations, the pressure gauges TDM2-D and IKD-6TDa were chosen. These gauges were calibrated, and the dynamic characteristics of the gauges, important for measurements in pulse modes, were investigated. The results of the calibrations are given in the protocols and in Figs. 2.95 and 2.96. Figure 2.97 shows the dynamic characteristics of the chosen gauges. It can be seen that the gauge TDM2-D has a significantly smaller time lag.

The program of experimental researches on the influence of the screen on the structure of the supersonic gas-droplet flow was justified and worked out.

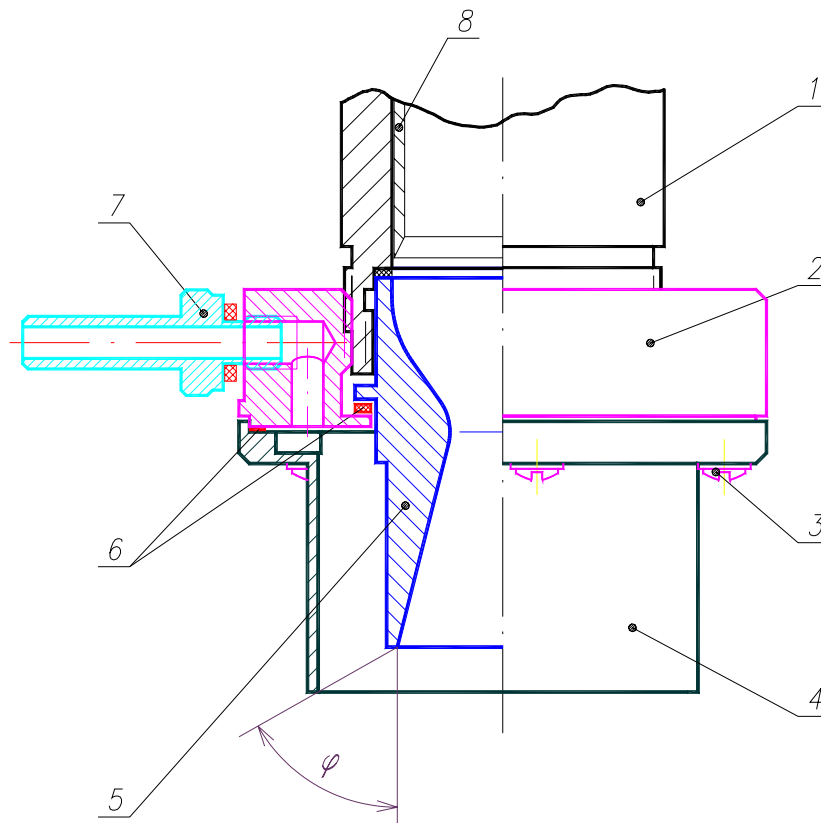


Fig. 2.91. Scheme of the screen installation to the gas-dynamic source.

1 – body of the gas-dynamic source, 2 – screw, 3 – screw M3,
4 – screen, 5 – nozzle, 6 – pads, 7 – tube for pressure gauge connection,
8 – bush for near-wall liquid film formation

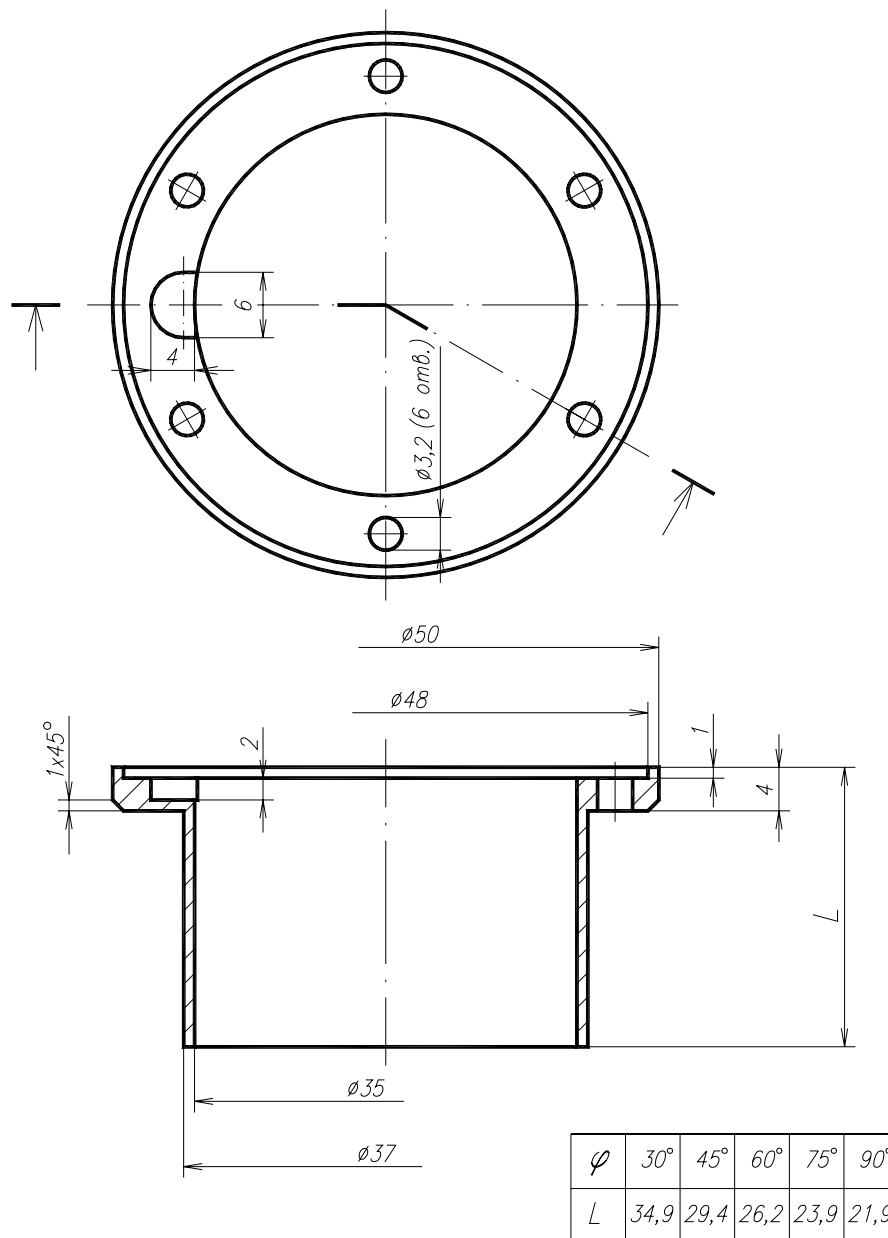


Fig. 2.92. Drawing of the screens



Fig. 2.93. General view of changeable screens

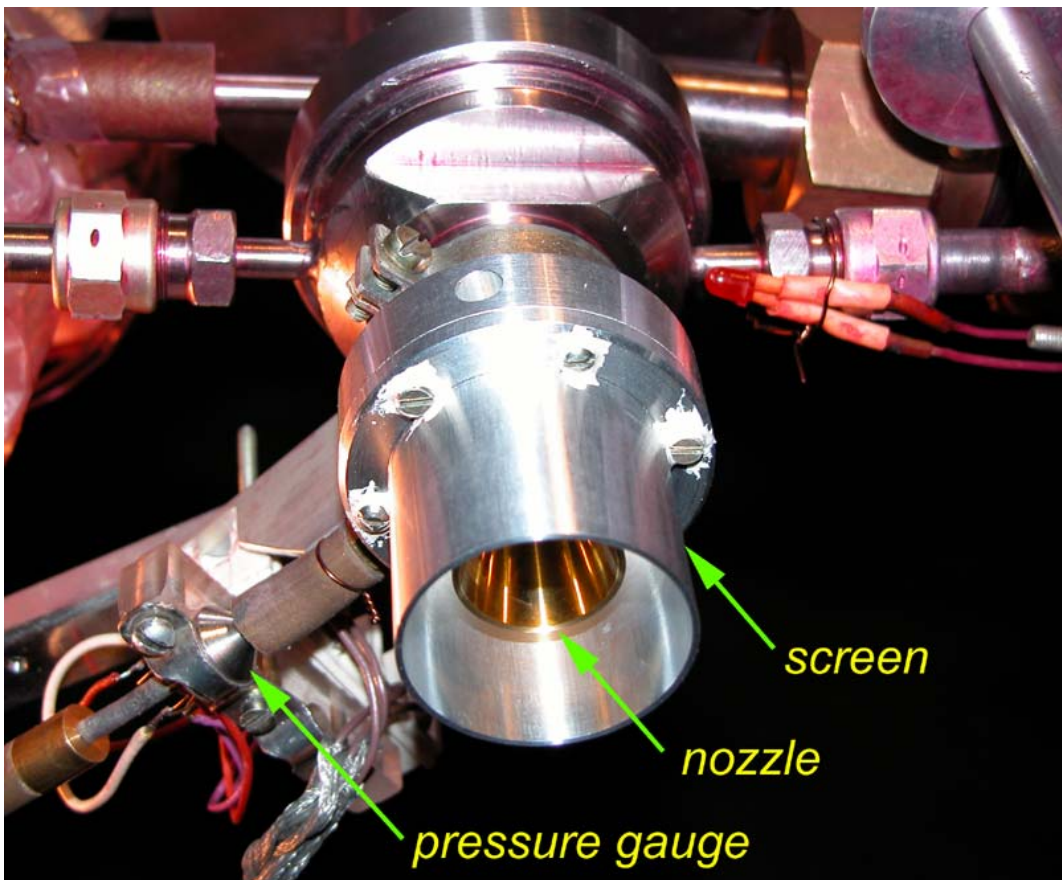


Fig. 2.94. General view of the gas-dynamic source with a mounted screen

Test protocol of the system for pressure measurement
in space between the nozzle and the screen

| Pressure gauge TDM2-D | | Pressure gauge IKD-6TDa | |
|-------------------------------|---------------------|--------------------------------|---------------------|
| Pressure in the chamber, torr | Gauge signal, volts | Pressure in the chamber, torr | Gauge signal, volts |
| 0.007 | 2.58 | 1.11 | 0.2439 |
| 0.09 | 2.61 | 1.27 | 0.2499 |
| 0.15 | 2.64 | 1.41 | 0.3405 |
| 0.25 | 2.69 | 1.55 | 0.3609 |
| 0.29 | 2.73 | 1.92 | 0.492 |
| 0.3 | 2.79 | 2.37 | 0.7215 |
| 0.5 | 2.85 | 2.81 | 0.984 |
| 0.6 | 2.9 | 3.39 | 1.35 |
| 0.7 | 2.95 | 3.99 | 1.722 |
| 0.9 | 3.01 | 4.63 | 2.1135 |
| 1 | 3.06 | 5.33 | 2.535 |
| 1.1 | 3.12 | 5.96 | 2.8905 |
| 1.2 | 3.18 | 6.54 | 3.2205 |
| 1.4 | 3.24 | 7.07 | 3.6525 |
| 1.5 | 3.29 | 7.07 | 3.4875 |
| 1.6 | 3.35 | 7.93 | 4.047 |
| 1.8 | 3.4 | 8.7 | 4.4085 |
| 1.9 | 3.46 | 9.73 | 4.842 |
| 2 | 3.52 | 10.84 | 5.289 |
| 2.3 | 3.62 | | |
| 2.5 | 3.76 | | |
| 2.8 | 3.86 | | |
| 3 | 3.95 | | |
| 3.3 | 4.08 | | |
| 3.6 | 4.18 | | |
| 3.8 | 4.31 | | |
| 4.1 | 4.43 | | |
| 4.5 | 4.58 | | |
| 4.7 | 4.69 | | |
| 5 | 4.81 | | |
| 5.4 | 4.97 | | |
| 5.7 | 5.15 | | |
| 6 | 5.25 | | |
| 6.3 | 5.36 | | |
| 6.5 | 5.49 | | |
| 6.9 | 5.65 | | |
| 7.4 | 5.87 | | |
| 8 | 5.94 | | |
| 9 | 6.38 | | |
| 10 | 6.83 | | |
| 11 | 7.22 | | |
| 12 | 7.66 | | |

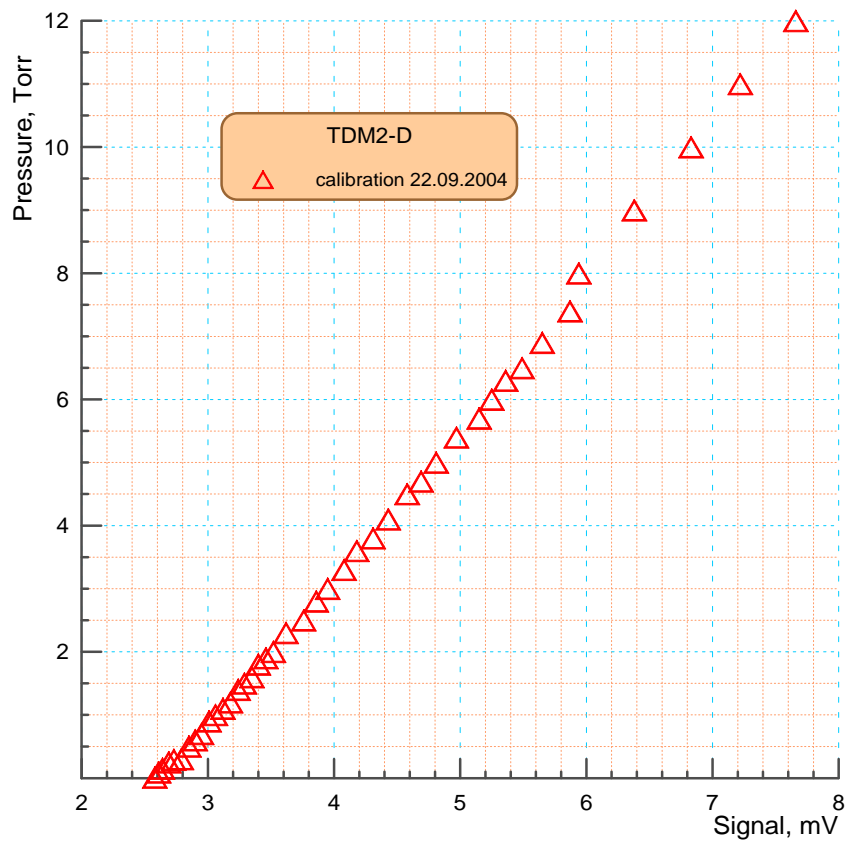


Fig. 2.95. Calibration of the TDM2-D gauge

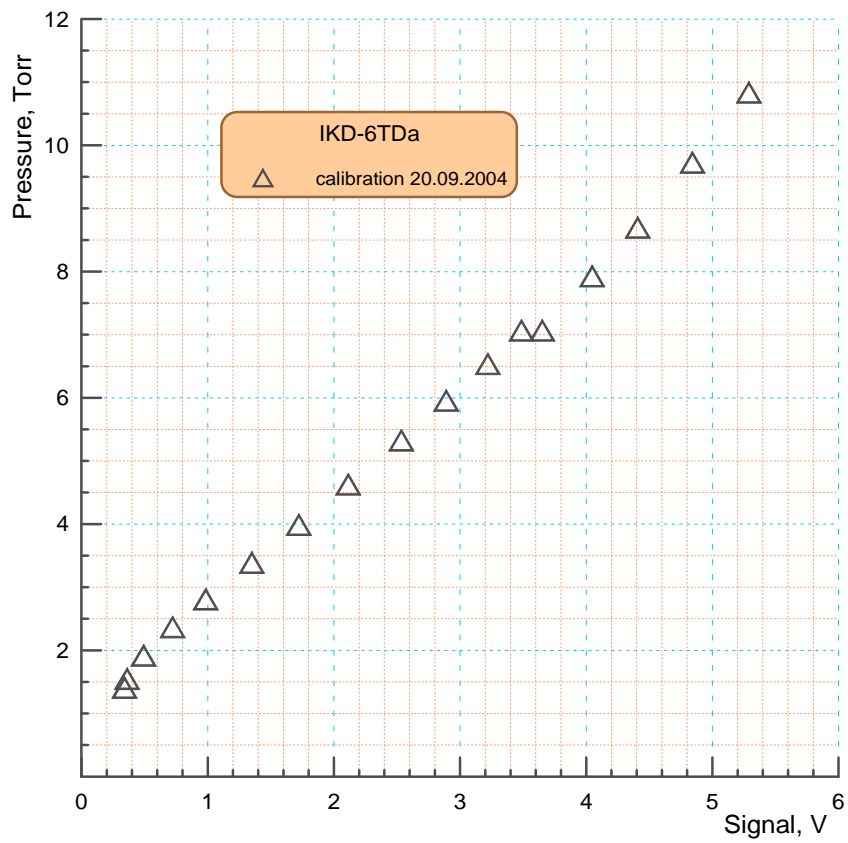


Fig. 2.96. Calibration of the IKD-6TDA gauge

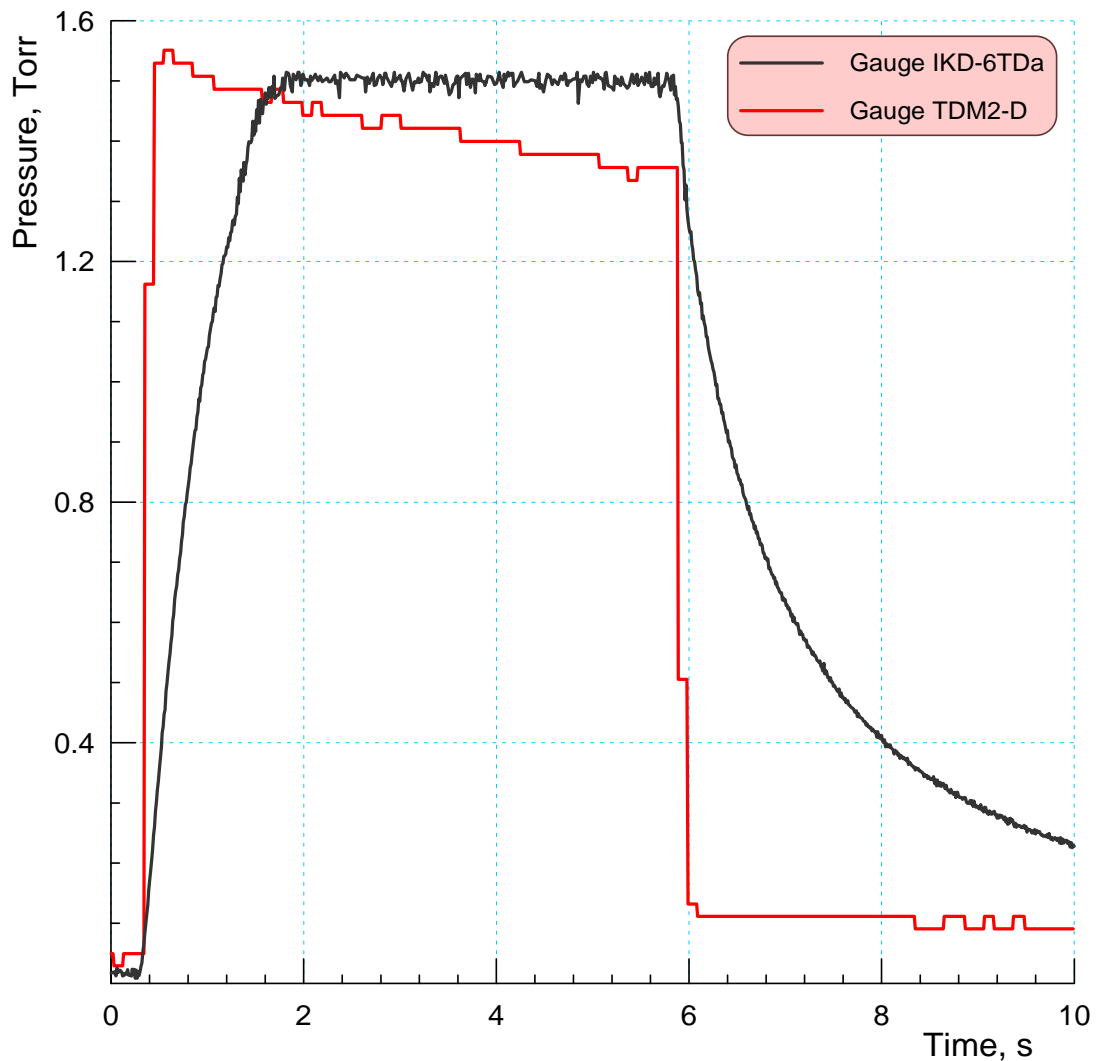


Fig. 2.97. Dynamic characteristics of the pressure gauges

Task 2.10.3. Measurement of the pressure distribution in the region between the nozzle and the shield, density fields behind the nozzle with the shield with and without liquid injection, measurement of the spatial distribution of the droplet phase and analysis of the shield effect on this distribution

In the period under report, a comprehensive experimental research of the influence of the screen on the supersonic gas-droplet flow structure was performed.

The program of experimental researches included measurement of pressure between the nozzle and the screen, and also determination of the influence of the screen on the structure of the gas- and droplet-phase flow. Researches were carried out for five fixed positions of the screen with respect to the nozzle, which ensured variation of the angle φ in the range of interest from 30° up to 90° (the angle φ determines the screen position with respect to the nozzle, see Fig. 2.91).

A supersonic conic nozzle with the Mach number $M = 3$ was used in all experiments for the period under report. Air was used as a working gas, and ethanol was used as a working liquid. The weight concentration of ethanol did not exceed 10%. The initial temperatures of the gas and the liquid were identical and equal to room temperature.

Measurement of pressure in the region between the nozzle and the screen

Typical oscillograms of pressure between the nozzle and the screen obtained in experiments for variants without liquid supply and with liquid supply for screens with angles $\varphi = 30^\circ$ and $\varphi = 90^\circ$ are shown in Figs. 2.98. and 2.99, respectively. Oscillograms of pressure p_0 in the stagnation chamber and the pressure p_∞ in the vacuum chamber of the VIKING setup are plotted in Figs. 2.100 and 2.101, respectively.

For the screen with $\varphi = 30^\circ$ (Fig. 2.98), the flow in the region between the nozzle and the screen is closed (does not depend on the change in pressure in the vacuum chamber p_∞) for both variants (without liquid supply and with liquid supply). For the screen with $\varphi = 90^\circ$ (Fig. 2.99), the flow in the region between the nozzle and the screen for the variant without liquid supply remains closed only up to the time equal to 4 seconds. For the variant with liquid supply, the flow is closed for the entire duration of the pulse (5 seconds). For intermediate values of the angle $\varphi = 45^\circ, 60^\circ,$ and 75° , the flow in the region between the nozzle and the screen is closed.

It is seen in Figs. 2.98 and 2.99 that the liquid supply in the nozzle (for generation of the near-wall liquid film) leads to a pressure increase in the region between the nozzle and the screen. This effect becomes more significant for the screen with $\varphi = 90^\circ$. The increase in pressure between the nozzle and the screen is obviously related to evaporation of the liquid that entered the cavity. The process of evaporation has an irregular character, which results in pressure fluctuations. For intermediate values of the angle $\varphi = 30^\circ, 60^\circ,$ and 75° , the pattern is qualitatively the same.

The results of pressure measurements in the cavity between the nozzle and the screen are plotted in Fig. 2.102 as a function of the angle φ . It is seen that the influence of the angle φ on the value of pressure between the nozzle and the screen is rather strong.

Measurement of density fields behind the source with the screen and without the screen, with and without liquid supply

These measurements were performed with the use of the electron-beam method. The idea of the method and its hardware implementation were described earlier (see 3 and 4 quarter reports). The measurements were carried out in an electron-beam measuring module connected to the vacuum chamber of the VIKING facility through a gate 400 mm in diameter.

The main objective of the experiments was to study the influence of the screen on the gas-dynamic flow structure (fields of density) of supersonic underexpanded jets. Two series of experiments were conducted. In the first series, the influence of the screen on the longitudinal and transverse distributions of density in the jet without liquid supply was investigated; in the second series, the same parameters were measured in the case with liquid supply.

All measurements were taken in pulse modes with a characteristic time of the pulse $\tau = 5$ s.

For better understanding of test conditions, let us consider Figs. 2.93-2.105, which show the typical oscillograms of stagnation pressure (pressure of air in the stagnation chamber of the nozzle), pressure in the vacuum chamber (in the measuring module) and in the receiver (in the vacuum chamber VIKING), and the current of the electron beam, respectively. We briefly comment on these figures.

It is possible to see that the parameters change most significantly (almost stepwise) at the initial moment of time, immediately after the electromagnetic valve of air supply into the stagnation chamber is switched on.

The pressure in the settling chamber (Fig. 2.103) reaches approximately 500 torr and decreases approximately to 420 torr during the pulse (by the fifth second). Such a change in stagnation pressure with time has not any physical meaning and is caused only by features of the system for air supply into the settling chamber after its installation into the electron-beam measuring module.

The pressure in the measuring module (Fig. 2.104) during the initial moment of time grows stepwise by one or two orders approximately up to 0.1 torr, remains roughly constant up to $\tau = 3$ s, and further (by the end of the pulse) smoothly grows up to 0.14 torr. The stepwise increase in pressure at the moment the electromagnetic valve is switched off (at $\tau = 5$ s) is caused by the difference in gas pressure in the measuring module and in the receiver at the end of the pulse. As was mentioned earlier (see 4 quarter report), this difference in pressure is associated with the fact that the vacuum gate between the measuring module and the receiver plays the role of an ejector.

The current of the electron beam (Fig. 2.105) decreases stepwise from 10 mA down to 4.5 mA during the initial period of time and further (by the end of the pulse) smoothly decreases to 3.5 mA.

As a whole, the results plotted in Figs. 2.103 – 2.105 are qualitatively clear and hardly demand any additional comments. At the same time, these results give clear understanding of conditions of the experiments performed and allow us "to attach" density measurements to a chosen time instant.

Let us consider now the results of experiments on the influence of the screen on the density fields in the plume for the cases with and without liquid supply. In both cases, the screen position corresponded to $\varphi = 30^\circ$.

The measurement results for the case without liquid supply (without the near-wall liquid film) are shown in Figs. 2.106 and 2.107. The streamwise distributions of normalized density in the plume behind the nozzle with the screen and without the screen for the time $\tau = 5$ s are compared in Fig. 2.100; the transverse distributions of normalized density at a distance of 300 mm from the nozzle-exit section for the times $\tau = 1, 2, 3, 4,$ and 5 s are shown in Fig. 2.107. The main conclusion that can be drawn from the results shown in Figs. 2.106 and 2.107 is that the screen under the present test conditions does not exert any significant influence on the density fields in the plume. At the same time, it is seen that the plume is insignificantly shortened in the case with the screen (see Fig. 2.106). The same effect can be seen on transverse profiles (see Fig. 2.107).

The following series of experiments involved investigations of the influence of the screen on the density fields in the plume in the case with liquid supply. Within the measurement error, these data coincide with those in Figs. 2.106 and 2.107. The result obtained was not unexpected and only confirmed the conclusion made earlier (see 4 quarter report) that, if the initial mass concentration of the liquid is rather low (less than 10%), it does not produce any appreciable influence on the gas-dynamic structure of the flow. Therefore, the "gas-dynamic" and "droplet" parts of the problem can be separated.

Small differences in the characteristic sizes of the jet without the screen and with the screen verify that the use of screens under actual conditions will not exert any substantial influence on gas dynamics of the plume and on the thrust of the control thruster.

Certainly, this statement is not absolute and only reflects the situation for the chosen and examined normalized sizes and arrangements of the screen and the nozzle, and also for the chosen test conditions (Mach number of the nozzle, normalized mass concentration of the liquid, etc.). However, these chosen normalized sizes and conditions approximately model the plumes of control thrusters of space vehicles and, consequently, are of practical significance.

In conclusion of this part of the report, we estimate the position of the central shock wave by the known approaches (e.g., [1]) and compare these estimates with the results of experiments.

According to [1], we have

$$\frac{x_m}{d_a} \approx 0.7 \cdot M_a \sqrt{\kappa \frac{p_a}{p_\infty}},$$

where x_m is the distance from the nozzle lip to the central shock, d_a is the diameter of the nozzle-exit section, M_a is the Mach number of the nozzle, and p_a and p_∞ are the pressures at the nozzle and in the ambient medium, respectively.

For the conditions of experiments whose results are given in Fig. 2.107 ($\tau = 5$ s, $p_0 = 420$ torr, $p_a = \pi \cdot p_0 = 0.0298 \cdot 420 = 12.5$ torr, $p_\infty = 0.14$ torr, $\kappa = 1.4$, $M_a = 3$, and $d_a = 20$ mm), we have $x_m \approx 470$ mm.

The result obtained $x_m = 470$ mm is rather close to the experiment (see Fig. 2.106), which can testify to the correctness of the measurements performed.

Measurement of the spatial distribution of the droplet phase and analysis of the influence of the screen on this distribution

The spatial distributions of the droplet phase were measured over the radius $R = 70$ mm with respect to the center of the nozzle-exit cross section with the help of the method of spectrophotometry, which was developed within the framework of the Project. The measurements were performed for five variants of the screen arrangement with respect to the nozzle, corresponding to the angles $\varphi = 30, 45, 60, 75,$ and 90° . The resultant distributions were compared to the corresponding distribution without the screen. The results obtained for all variants are shown in Fig. 2.108; the results for the nozzle without the screen are compared with the results for the nozzle with the screen with the angles $\varphi = 30, 45, 60, 75,$ and 90° in Figs. 2.109-2.113.

Let us analyze the distributions of the droplet phase in more detail by the example of Fig. 1.113 for $\varphi = 30$, which ensured the maximum effect under the test conditions used. It is possible to clearly distinguish the central and peripheral areas of the droplet-phase flow. The reasons for their occurrence in a supersonic gas flow and the parameters of droplets in these areas (sizes and velocities) were considered previously (see 6 quarter report).

The central area of the droplet-phase flow ($\theta \approx \pm 30^\circ$ relative to the plume axis) remains approximately identical both for the nozzle without the screen and for the nozzle with the screen. A small valley is observed at the plume axis, which is caused by specific features of interaction of the co-current gas flow with the near-wall liquid film in the area of the nozzle throat. It was established experimentally that formation of the central area of the droplet-phase flow strongly depends on the angle of inclination of the subsonic part of the nozzle relative to its centerline. This angle actually determines the initial trajectory of the droplet after shedding from the near-wall liquid film surface by the gas flow. The greater this angle, the greater the probability for the droplet to reach the axis. Certainly, it also depends on the droplet size and on the nozzle and co-current gas-flow parameters. The experiments showed that the valley at the plume axis is observed for an inclination angle of the subsonic part of the nozzle equal to 35° (Fig. 2.113), but it does not exist for an inclination angle equal to 60° ; instead, a general maximum (see, e.g., Fig. 2.56 of the 2 year annual report) is observed. It is worth noting here that the considered feature of formation of the central area of the droplet-phase flow is only a small part of the problem. Certainly, of much interest are the issues of fragmentation and acceleration of droplets during their motion inside the supersonic part of the nozzle, determination of the droplet sizes and velocities, etc.

Let us now address the analysis of the peripheral area of the droplet-phase flow (Fig. 2.113). The reason of occurrence of this area of the droplet-phase flow is associated with dispersion of the near-wall liquid film at the nozzle lip. It is possible to see that the flow from the nozzle without the screen displays a certain direction in scattering of the droplet phase from the nozzle exit, approximately equal to 65° relative to the jet axis.

Mounting of the screen with $\varphi = 30^\circ$ substantially (approximately by two orders of magnitude) reduces the maximum value of the droplet-phase flow (see Fig. 2.113). Backflows of the droplet phase also become considerably smaller.

The angular distributions of the droplet phase were also measured by the technique of droplet-phase deposition on paper substrates, and the influence of screens on these distributions was analyzed. Though this technique, as was mentioned earlier, yields only qualitative results, it is fairly demonstrative. The general view of the substrates is shown in Figs. 2.114 and 2.115. It is

seen that the central and peripheral areas on the pictures are appreciably different. The central area ($\theta \approx \pm 30^\circ$ relative to the plume axis) for all the modes investigated (nozzle without the screen and nozzle with the screens at $\varphi = 30, 45, 60, 75,$ and 90°) is well reproduced in all modes and is characterized by fairly homogeneous coloring. As was mentioned earlier, the presence of small high-speed droplets is typical for this area of the flow. In the peripheral part of the plume (angles more than 30° relative to the jet axis), one can see the presence of drops of various sizes, sometimes rather large. The results of data processing confirm this fact. As an example, Figs. 2.116 and 2.117 show the angular distributions of the droplet phase for the screens with $\varphi = 45$ and 75° . It is seen that the distributions of the droplet phase in the central area of the jet practically coincide with each other, and these distributions have no irregular features. The distributions of the droplet phase in the peripheral area shows irregular features related to the presence of droplets of different sizes, including large sizes, in this area of the plume. It can be seen that the distribution of the droplet phase in this area has a statistical nature, i.e., it varies from launch to launch. It should be noted here that the presented results of measurements of the angular distributions of the droplet phase obtained with the help of the spectrophotometry technique were averaged over 30 launches.

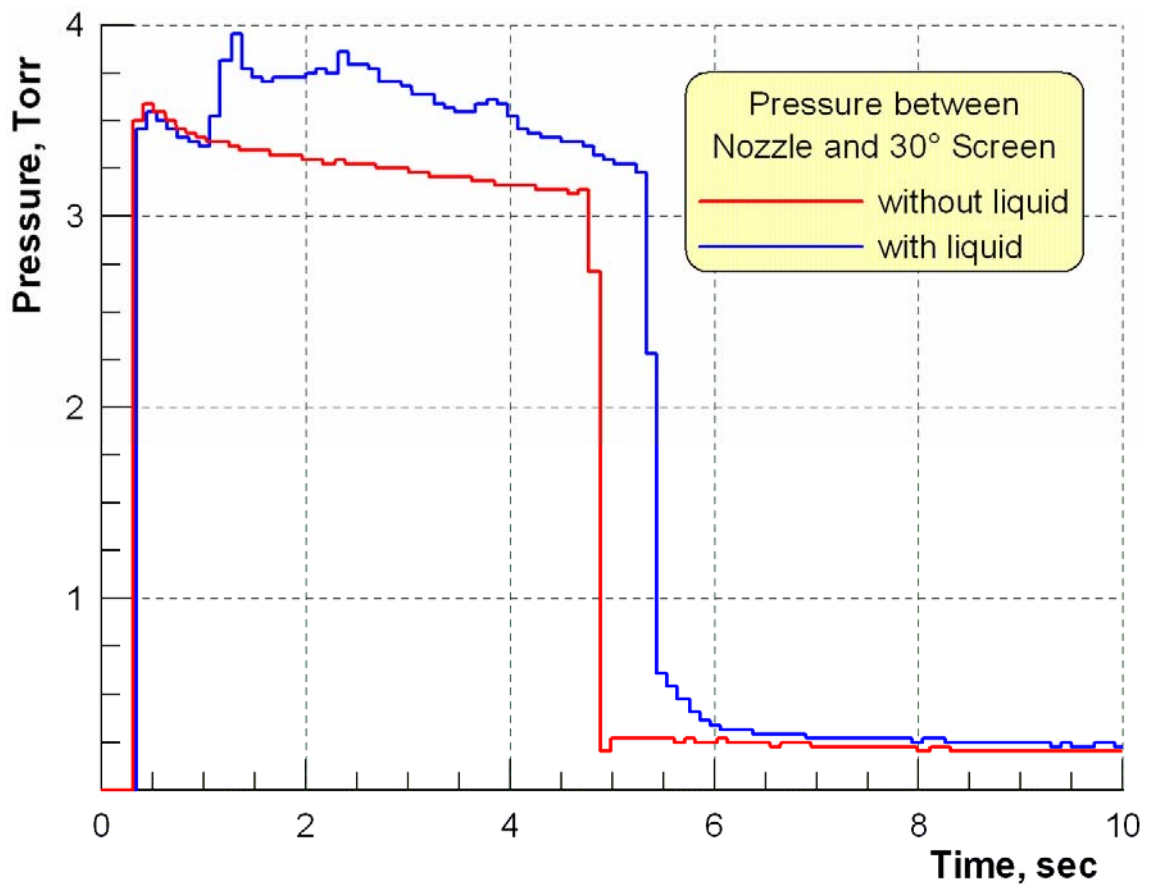


Fig. 2.98. Pressure between the nozzle and the 30° screen

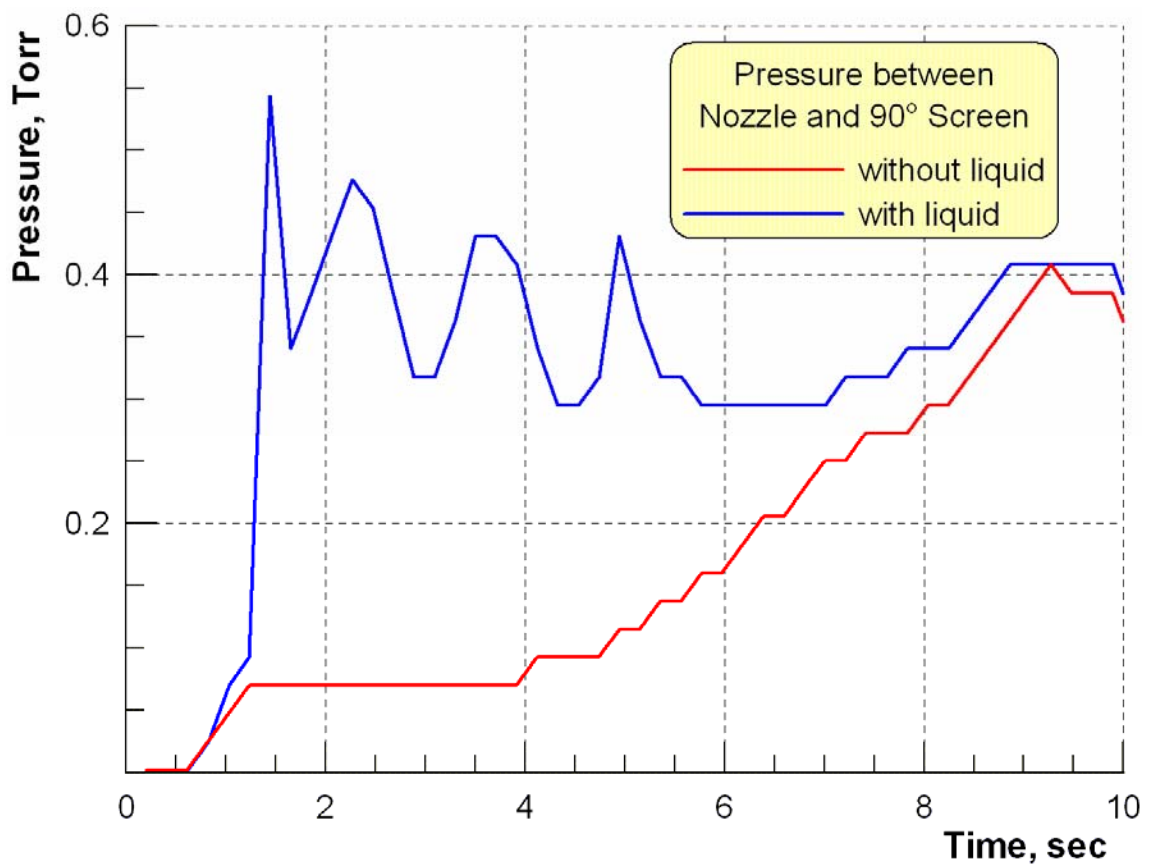


Fig. 2.99. Pressure between the nozzle and the 90° screen

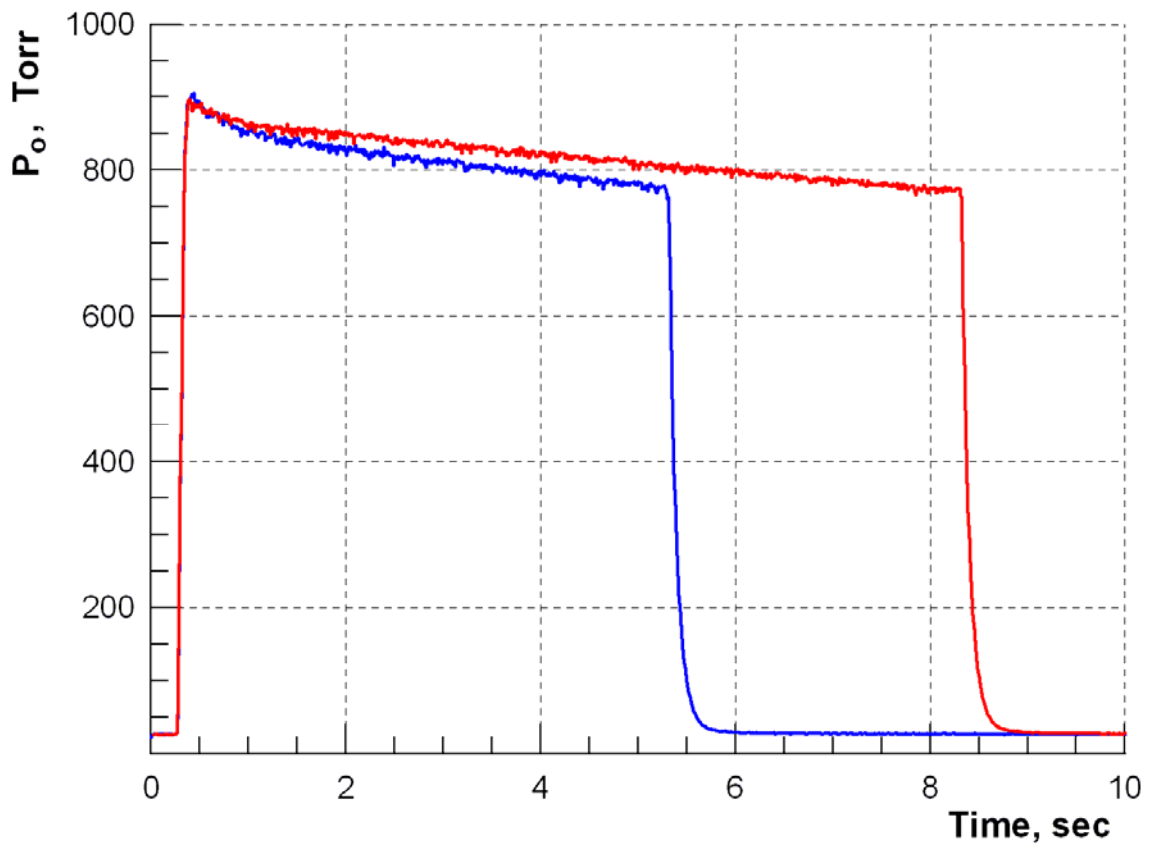


Fig. 2.100. Pressure in the stagnation chamber of the nozzle for 5 s and 8 s launches

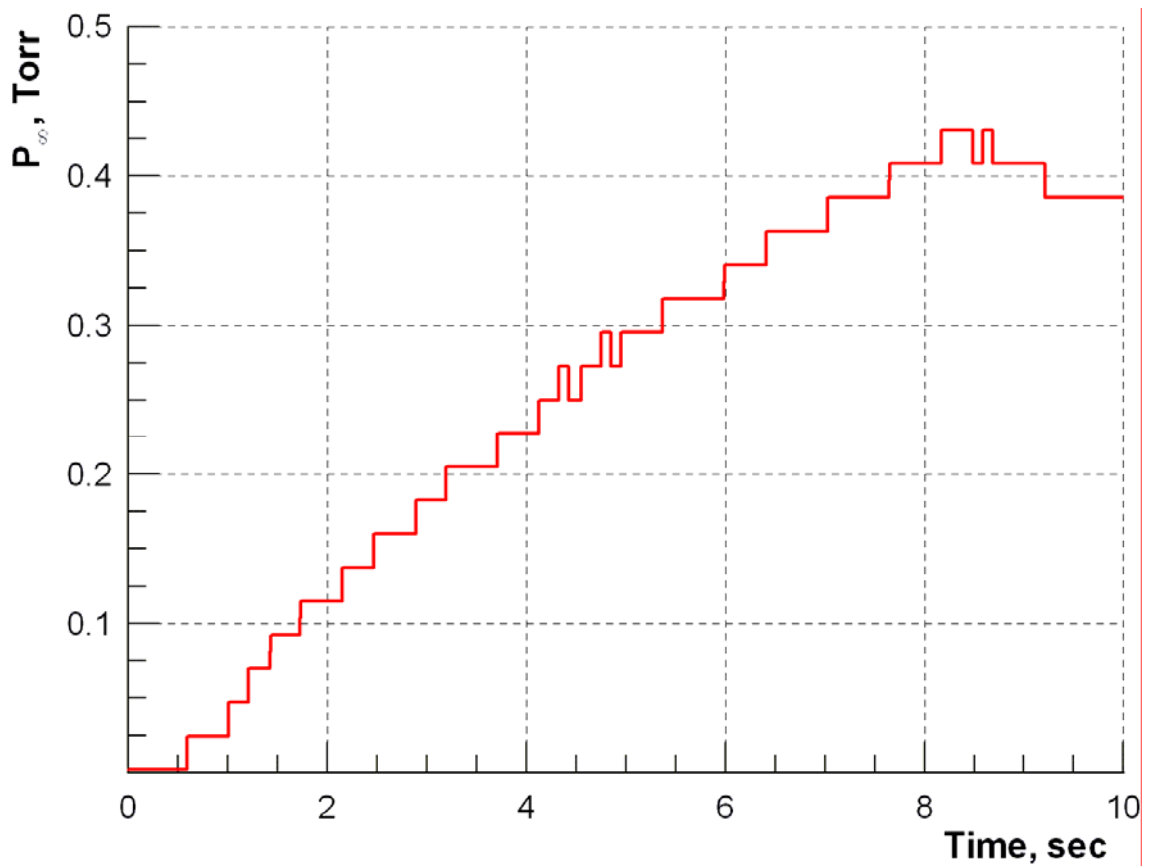


Fig. 2.101. Pressure in the VIKING vacuum chamber

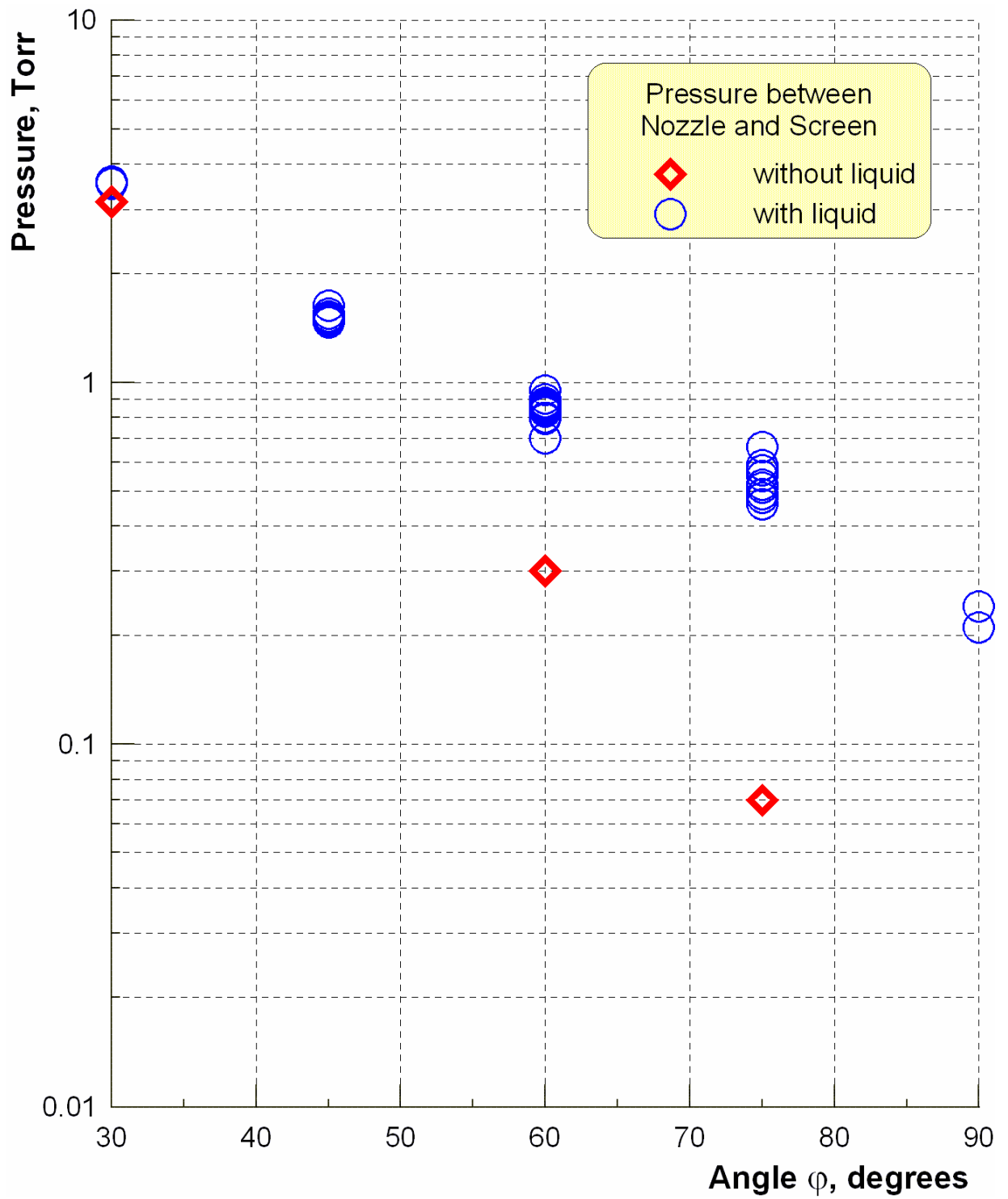


Fig. 2.102. Pressure between the nozzle and the screen versus the angle ϕ of the screen

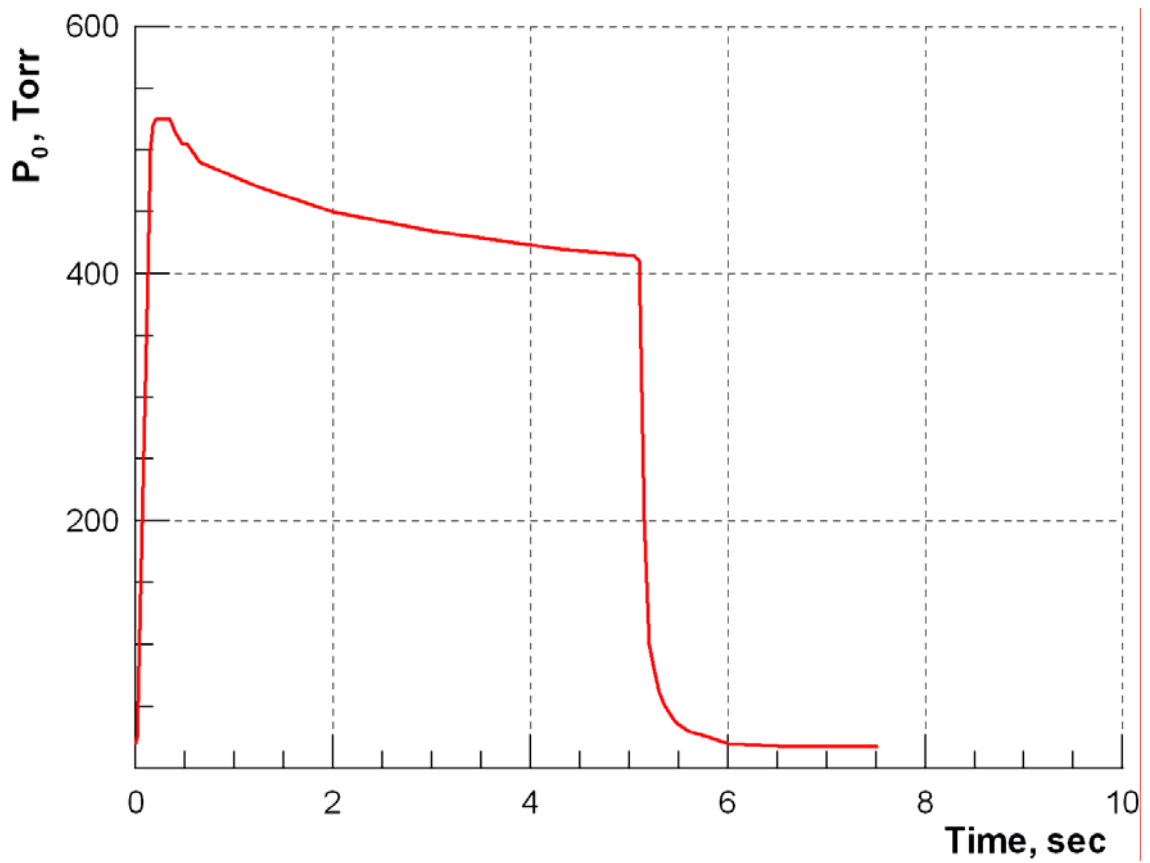


Fig. 2.103. Pressure in the stagnation chamber of the nozzle

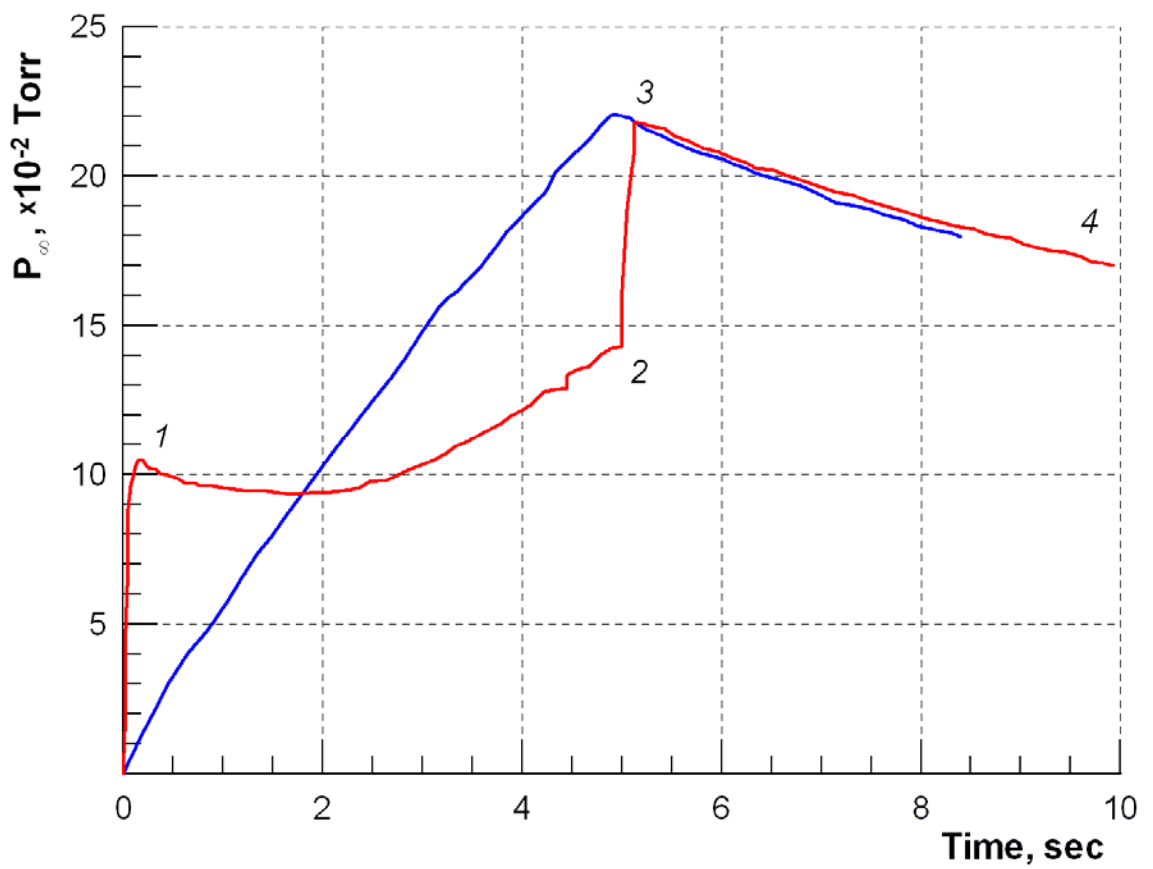


Fig. 2.104. Pressure in the measuring module and in the receiver of the VIKING setup

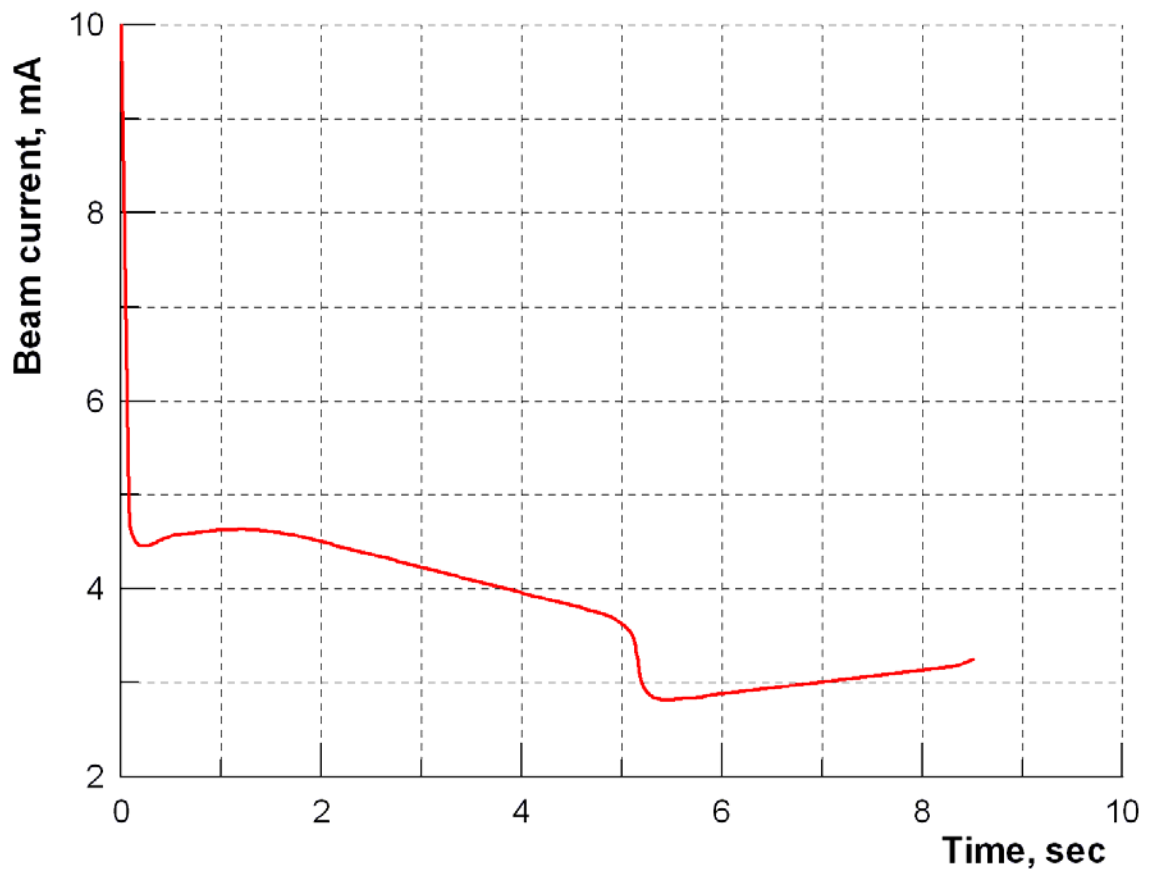


Fig. 2.105. Current of the electron beam

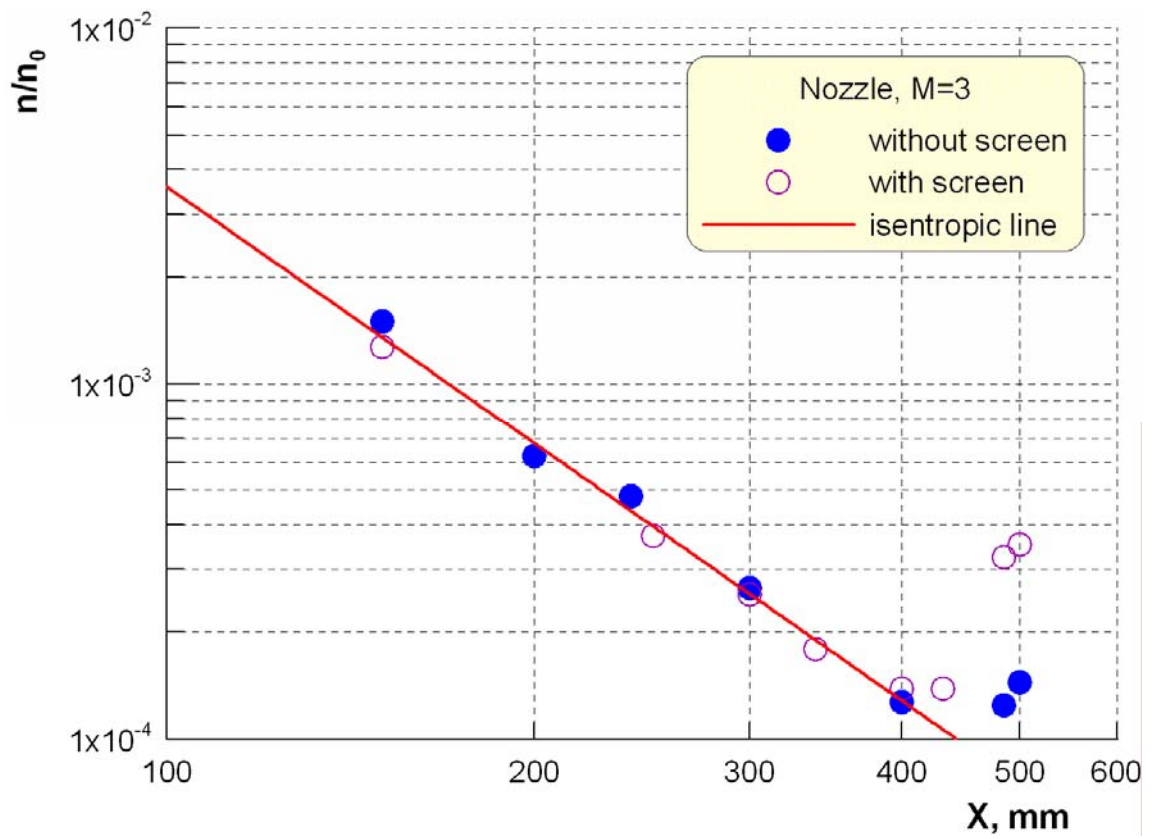


Fig. 2.106. Streamwise distribution of density in the plume behind the nozzle

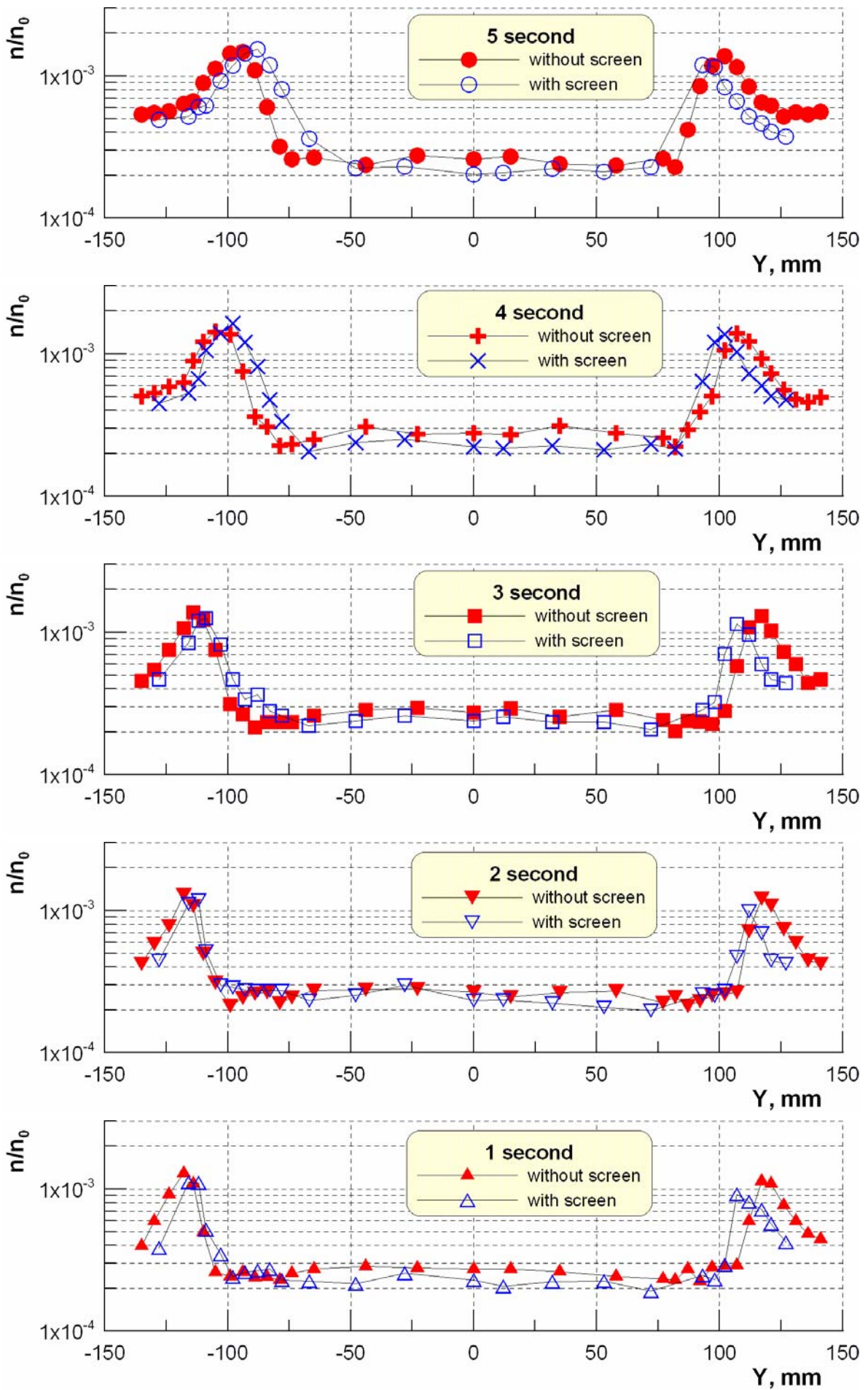


Fig. 2.107. Transverse distribution of density at a distance of 300 mm from the nozzle

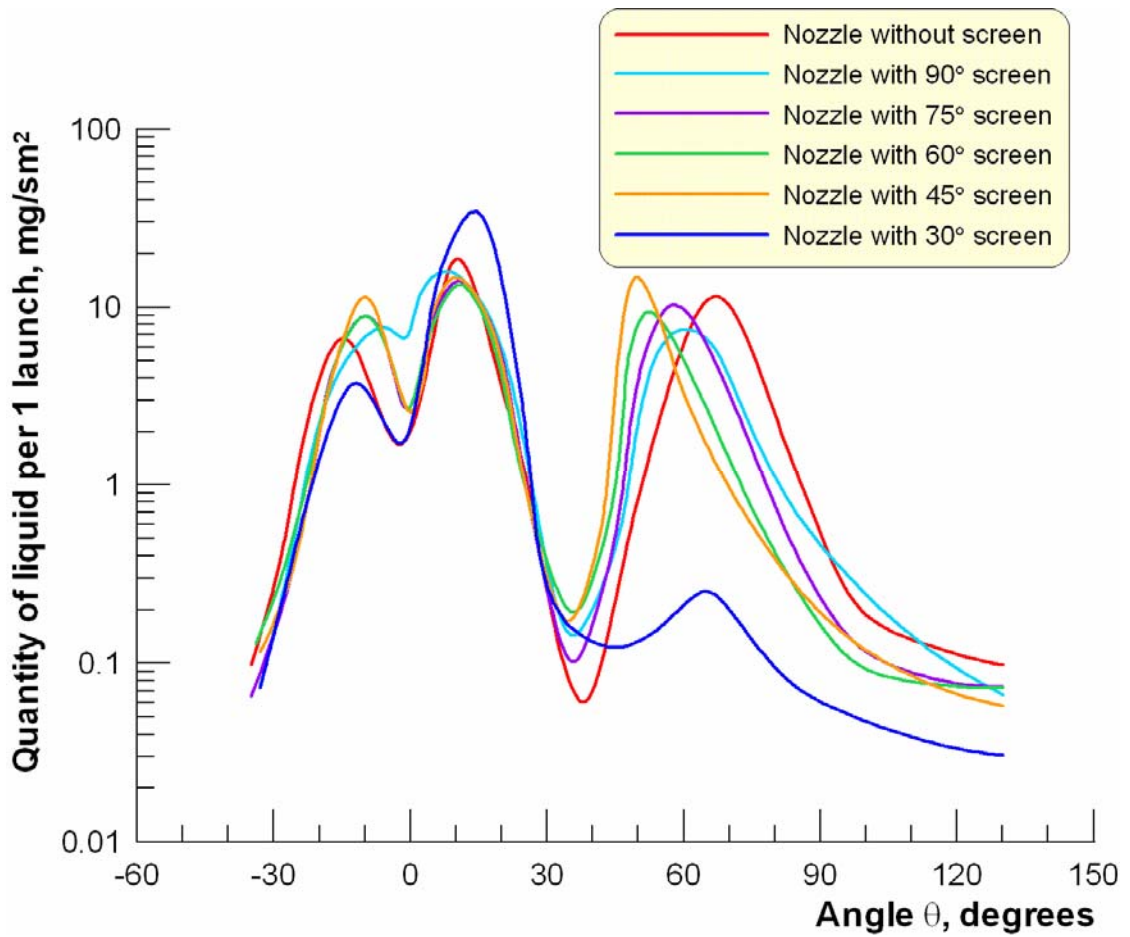


Fig. 2.108. Angular distribution of the droplet phase

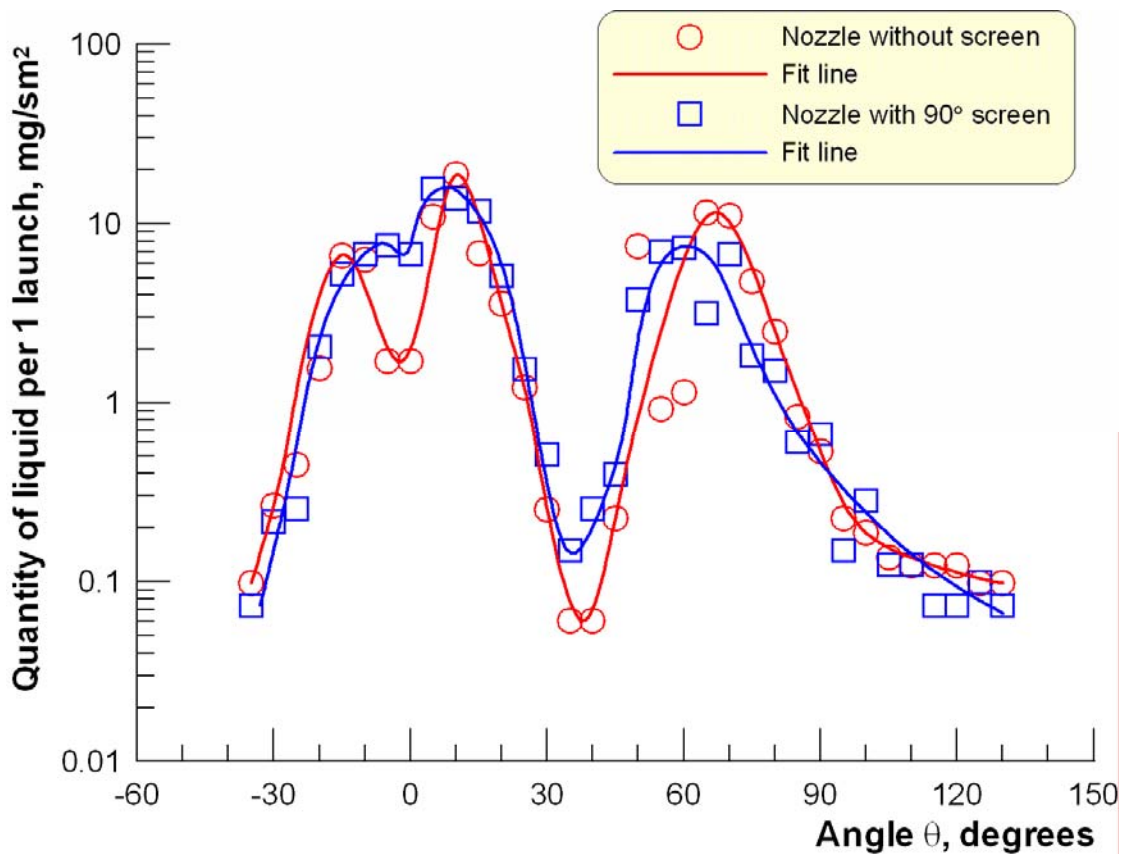


Fig. 2.109. Angular distribution of the droplet phase

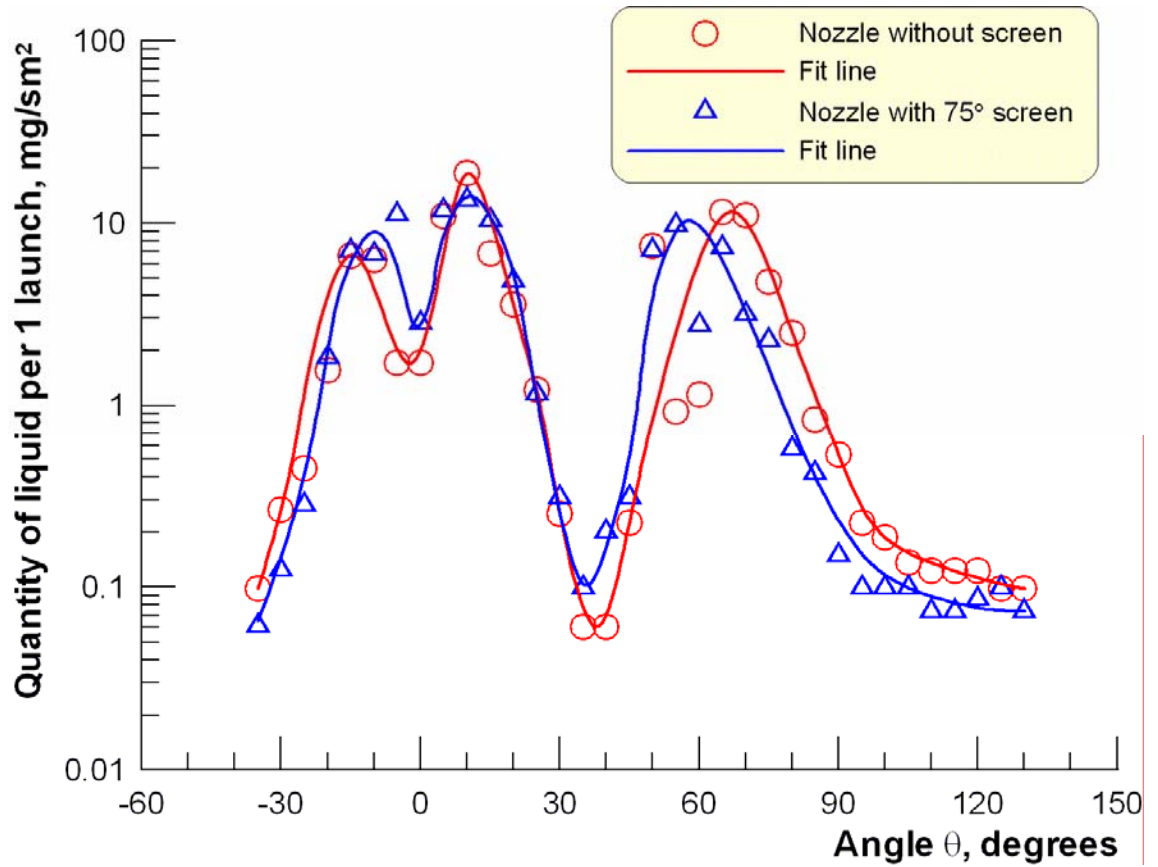


Fig. 2.110. Angular distribution of the droplet phase

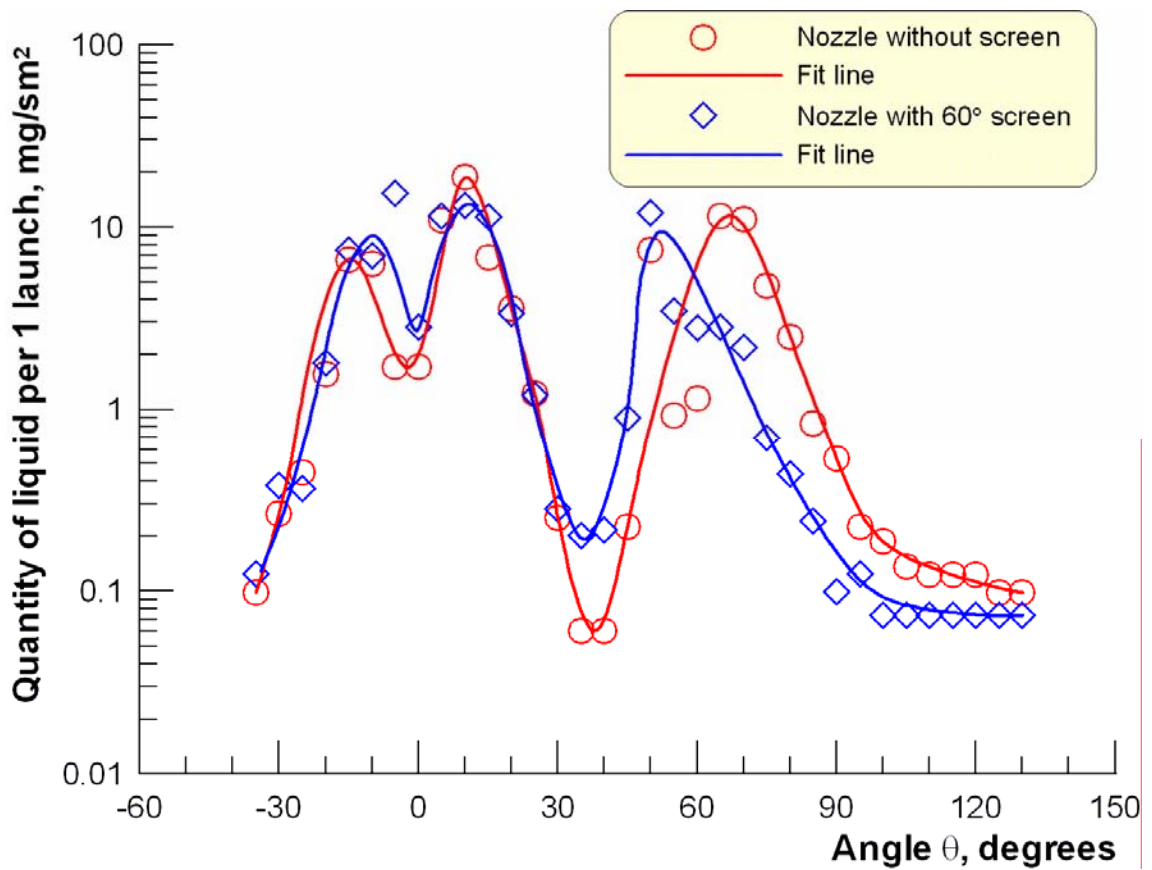


Fig. 2.111. Angular distribution of the droplet phase

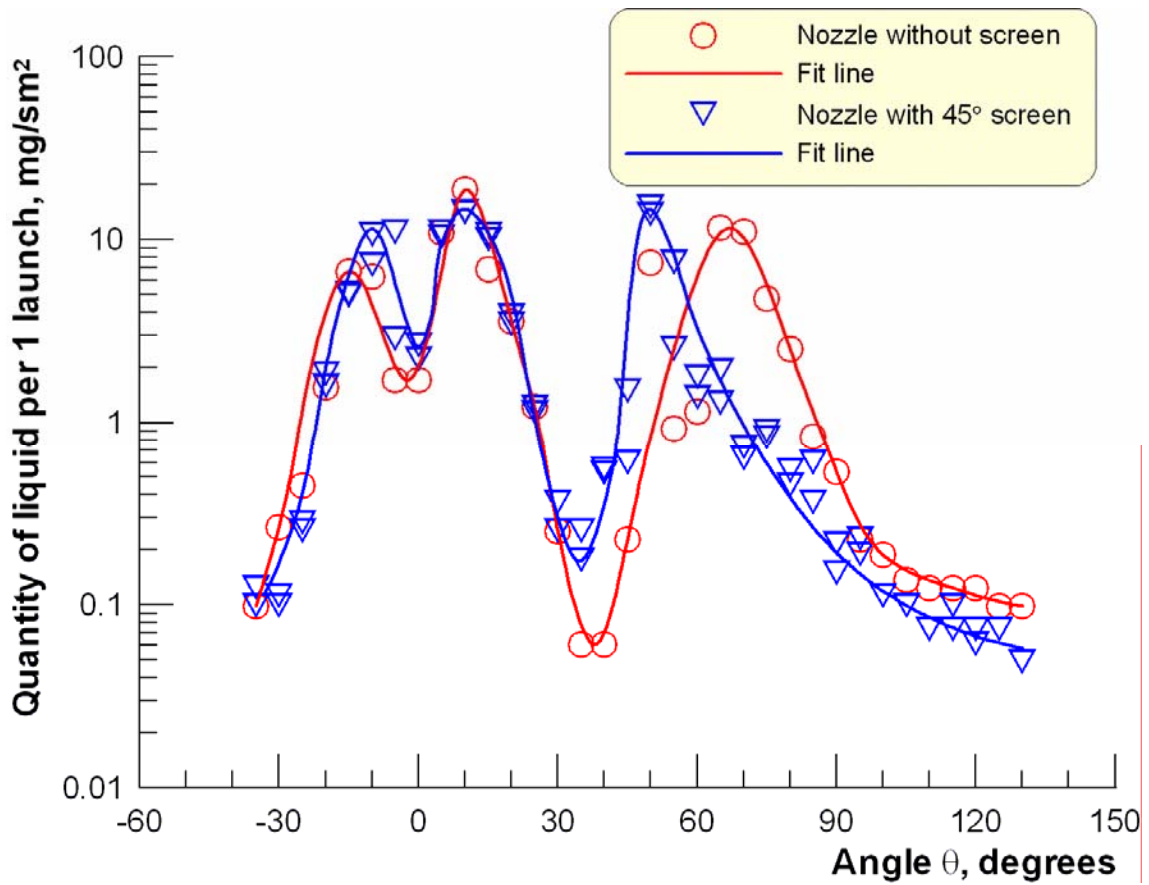


Fig. 2.112. Angular distribution of the droplet phase

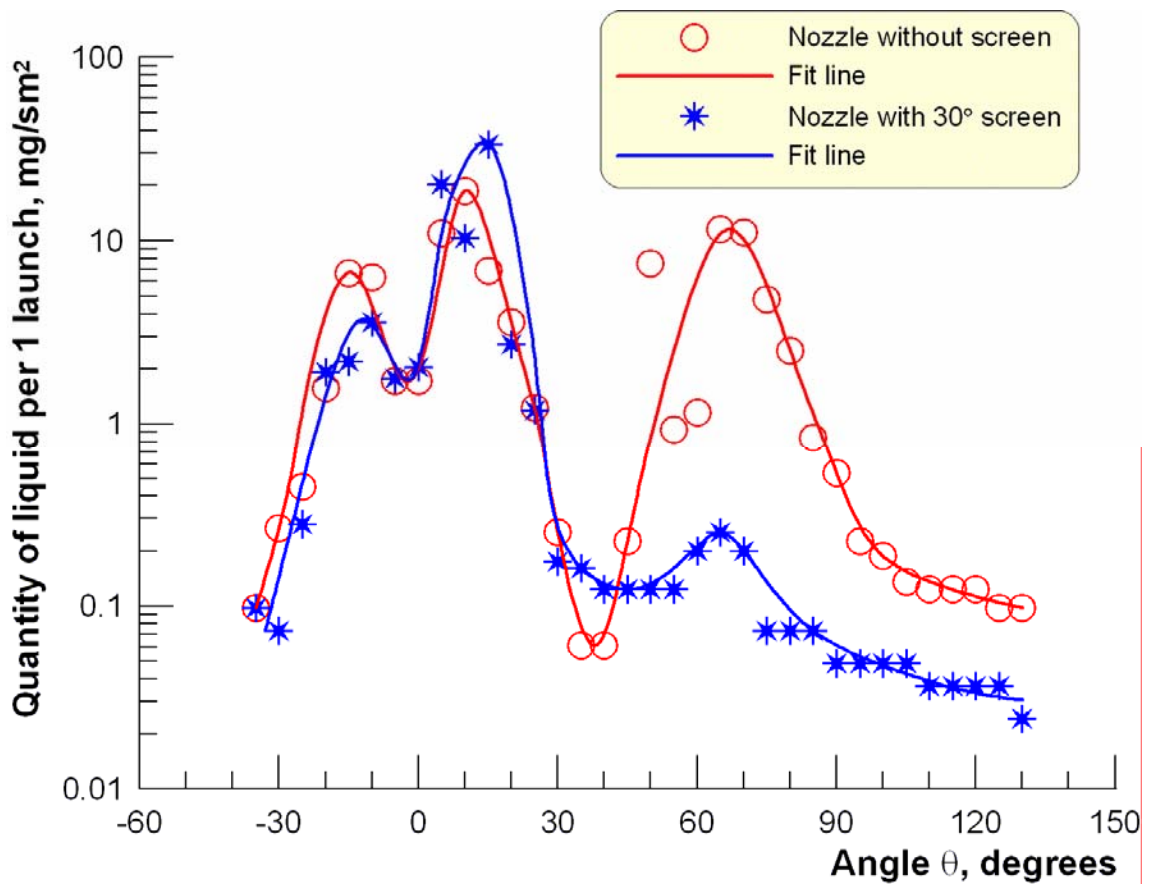


Fig. 2.113. Angular distribution of the droplet phase

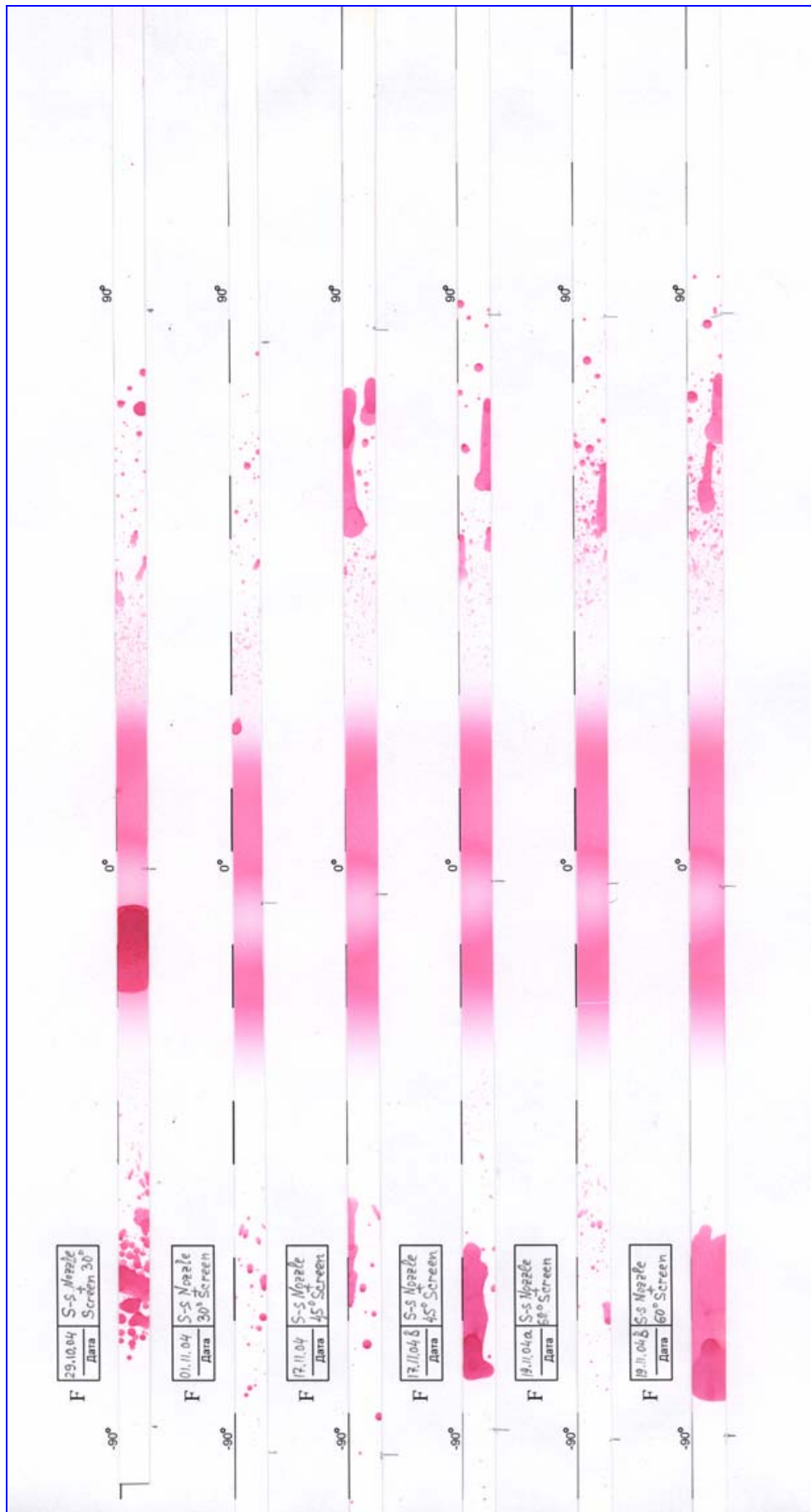


Fig. 2.114. General view of paper substrates

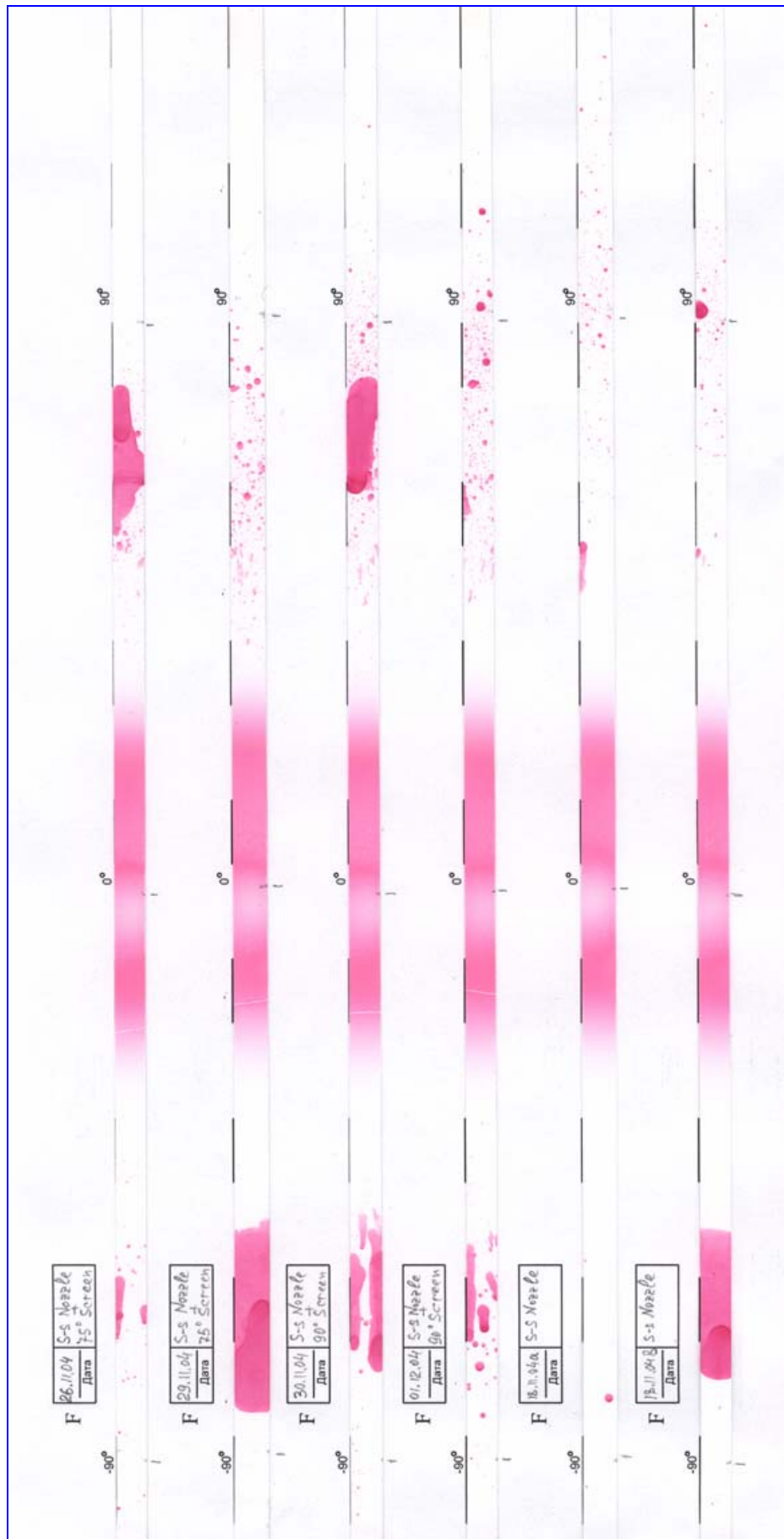


Fig. 2.115. General view of paper substrates

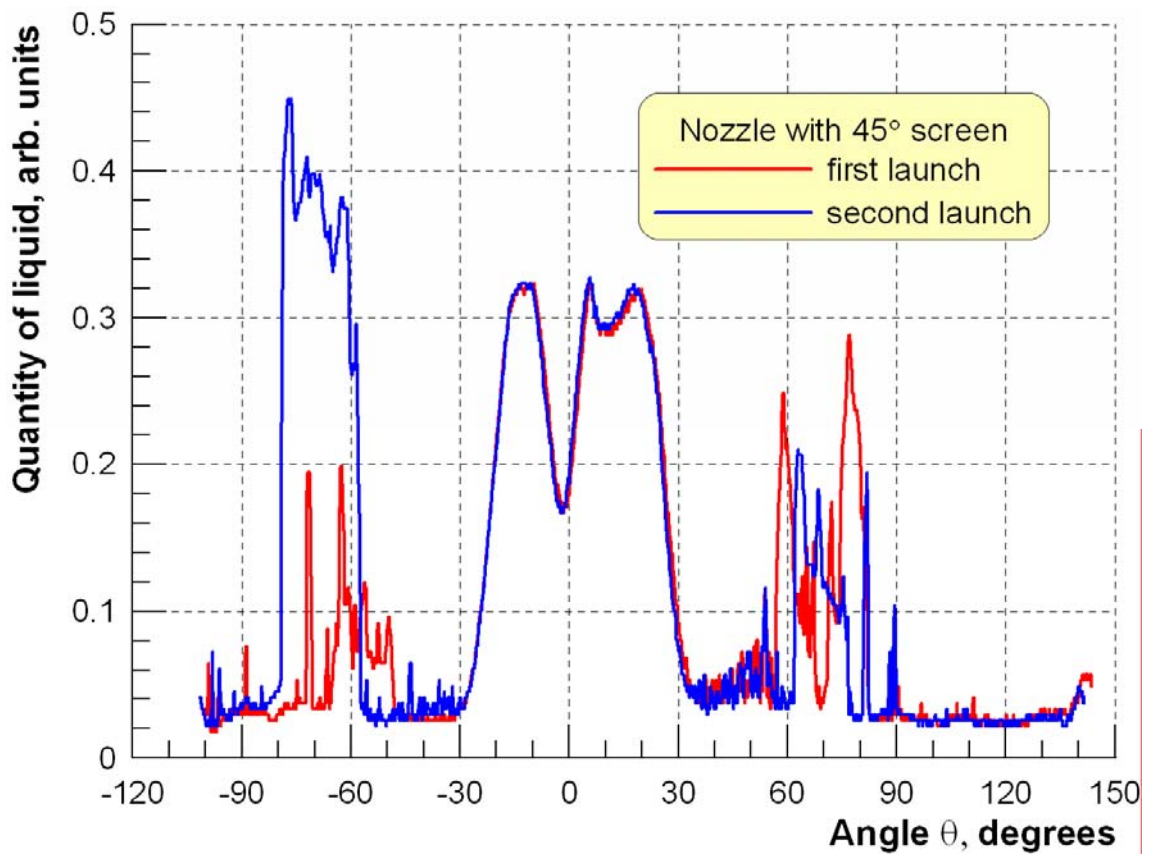


Fig. 2.116. Angular distribution of the droplet phase

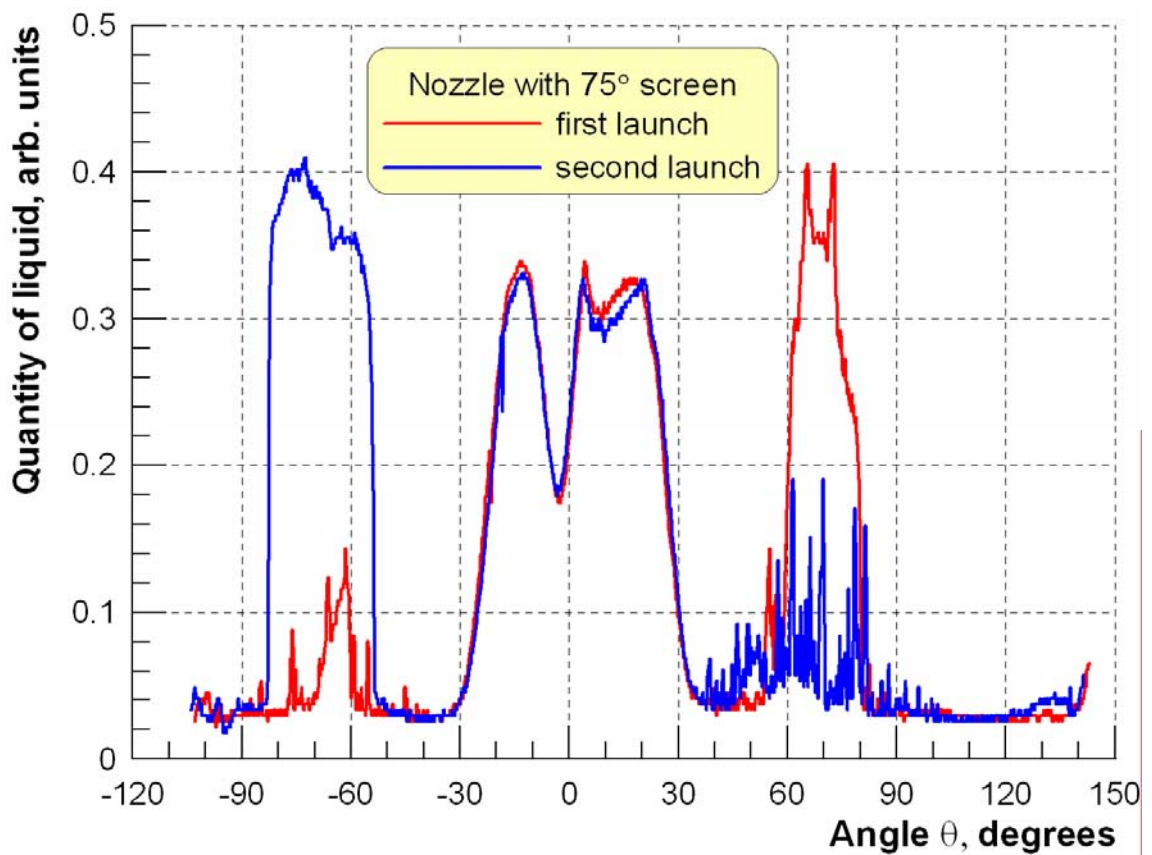


Fig. 2.117. Angular distribution of the droplet phase

Task 2.10.4. Analysis of experimental results

The experimental data on the influence of the screen on the flow structure downstream of a supersonic nozzle were analyzed. The main attention was given to expansion of capabilities of the electron-beam method for visualization of the flow structure behind the nozzle without the screen and with the screen.

There are two approaches to visualization of the flow structure by the electron-beam method.

The first approach employs the effect of afterglow of the gas; in this case, "swinging" of the beam in the chosen plane is organized with the help of a magnetic deflecting system and photographing of the illuminated area. The snapshots obtained offer a qualitative picture of the flow structure, mainly its shock-wave structure. The transition to local density distributions is complicated by the absence of data on the magnitude of the beam current at the point of measurement.

In the second approach, luminescence of a motionless beam is registered. In this case, for obtaining the flow structure in the chosen plane, simultaneous motion of the gas-dynamic source and the film in the photo camera with the same speeds relative to the motionless beam is organized. The film shows the plume image, which can be converted to local density distributions with the use of calibration dependences for the film.

Appearance of digital video cameras with opportunities of computer processing of videomages for their matching offers new opportunities for electron-beam visualization of gas flows. Such an approach was developed in the present work. The gas-dynamic source was mounted on a traversing gear in experiments and could be moved with a chosen speed relative to the motionless electron beam. The video camera, which was mounted outside of the vacuum chamber, and the traversing gear were switched on simultaneously. The beam current was also registered simultaneously.

Figure 2.118a, b shows the videomages of the electron beam in the vicinity of the nozzle lip and at some distance from it. These results do not demand special comments, we shall only note that the position of the shock wave (two luminous points) is well visible in Fig. 2.118b.



Fig. 2.118. Pictures of the electron beam in the plume behind the nozzle with the screen

The developed approach to electron-beam visualization of flows at the given stage was used basically to study the influence of the screen on the transverse size of the plume (position of the shock waves).

Figure 2.119 shows the transverse distributions of density in the plume at different distances from the nozzle exit. These distributions are obtained by processing videoimages of the beam. The asymmetry observed is related to attenuation of the electron beam passing through the plume. The analysis shows that the streamwise distributions of density are close enough to the corresponding isentropic values for the given nozzle.

The transverse sizes of the plume behind the nozzle without the screen and with the screen with the angle $\varphi = 30^\circ$ are compared in Fig. 2.120. One can see that the screen does not have any essential influence on the flow in the plume under test conditions used in the present experiments.

A small difference in the characteristic sizes of the plume without the screen and with the screen gives reasons to affirm that the use of screens in real conditions will not render any essential influence on gas-dynamics of the plume and on the thrust of control thrusters.

Certainly, this statement is not absolute and only reflects the situation for the chosen and investigated relative sizes and arrangements of the screen and the nozzle, and test conditions (Mach number of the nozzle, normalized mass concentration of the liquid, etc.). However, these chosen and investigated relative sizes and conditions approximately model plumes of control thrusters of space vehicles and, in this meaning, are of practical significance.

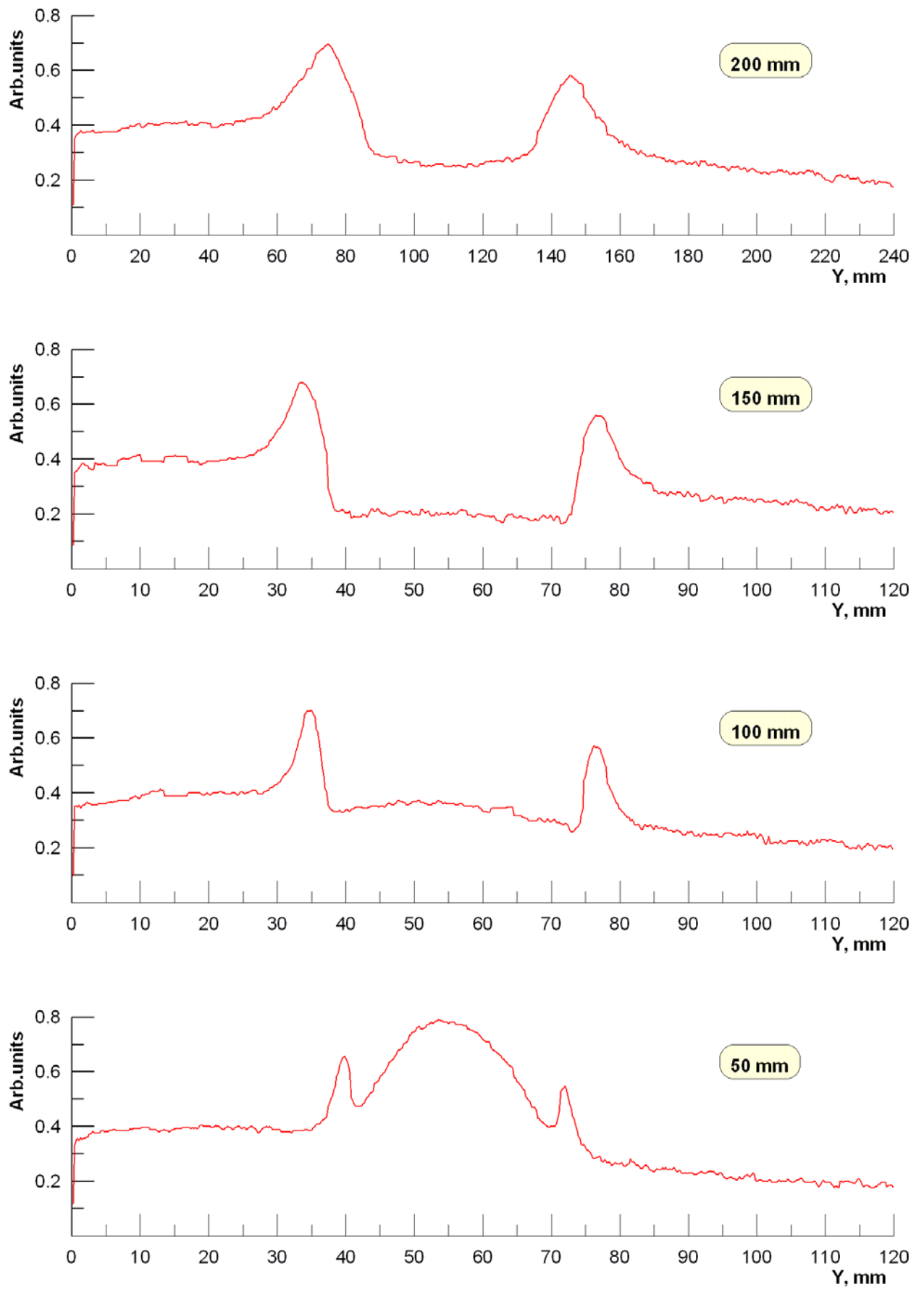


Fig. 2.119. Transverse distributions of density in the plume behind the nozzle with the screen

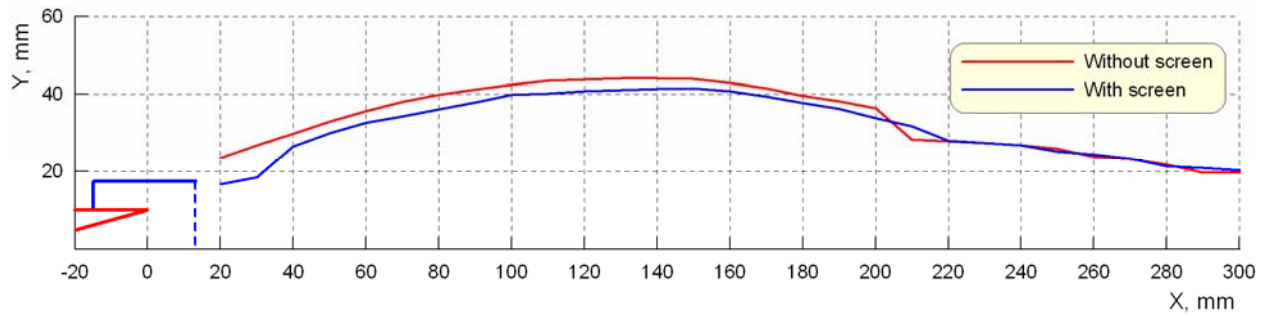


Fig. 2.120. Transverse sizes of plumes (location of shock waves) behind the nozzle without the screen and with the $\varphi = 30^\circ$ screen

References used:

1. **C. Lewis, D. Carlson.** Normal Shock Location in Underexpanded Gas and Gas-Particle Jets, AIAA Journal, Vol.2, No. 4, 1964. pp. 776-777

Task 2.11. Multiparametric numerical studies of the side and back portions of the plume flow with droplets and analysis of possibilities of reducing contamination

2.11.1. Parametric numerical studies of the entire plume flow

2.11.2. Numerical analysis of possibilities of reducing contamination

The plume flow, with the peripheral region and the backflow region included into the computational domain, was numerically simulated. The flow inside the nozzle was computed by the Navier-Stokes equations. The resultant distributions of quantities in the vicinity of the nozzle exit were further used as the boundary conditions for computing the external plume flow by the DSMC method. The motion of liquid-phase droplets was determined by the Lagrangian algorithm on the basis of the computed fields of gas-dynamic parameters.

The computations were performed for the case where the pressure in the settling chamber was $p_0=4000$ Pa. The droplets were injected in the vicinity of the nozzle lip, where the previous researches revealed liquid-film disintegration and formation of liquid droplets, which enter the backflow afterwards. The varied parameters were the point of injection, direction and magnitude of the velocity vector, and droplet size.

The specific features of the two-phase flow in the case of mounting protective screens were numerically examined. The computations were performed for several variants of screen positions; the angle φ characterizing this position was varied from 30° to 90° . In addition, both solid screens and screens with an orifice in the bottom region were considered. The computations show that a stagnant zone is formed between the outer surface of the nozzle and the screen; the pressure in this stagnant zone is several percent of the pressure at the center of the nozzle-exit section. The plume exits the nozzle, hits the screen, and becomes decelerated. After that, the flow turns at the screen edge, which acts as a new nozzle lip in the case under consideration. The flow field of the carrier phase for $\varphi=30^\circ$ is shown in Fig. 2.121.

The results of computation of the droplet motion support the possibility of a noticeable reduction of the droplet backflow owing to the use of a protective screen (Fig. 2.122). Based on the computation results, recommendations on the point where the screen operates most efficiently are given.

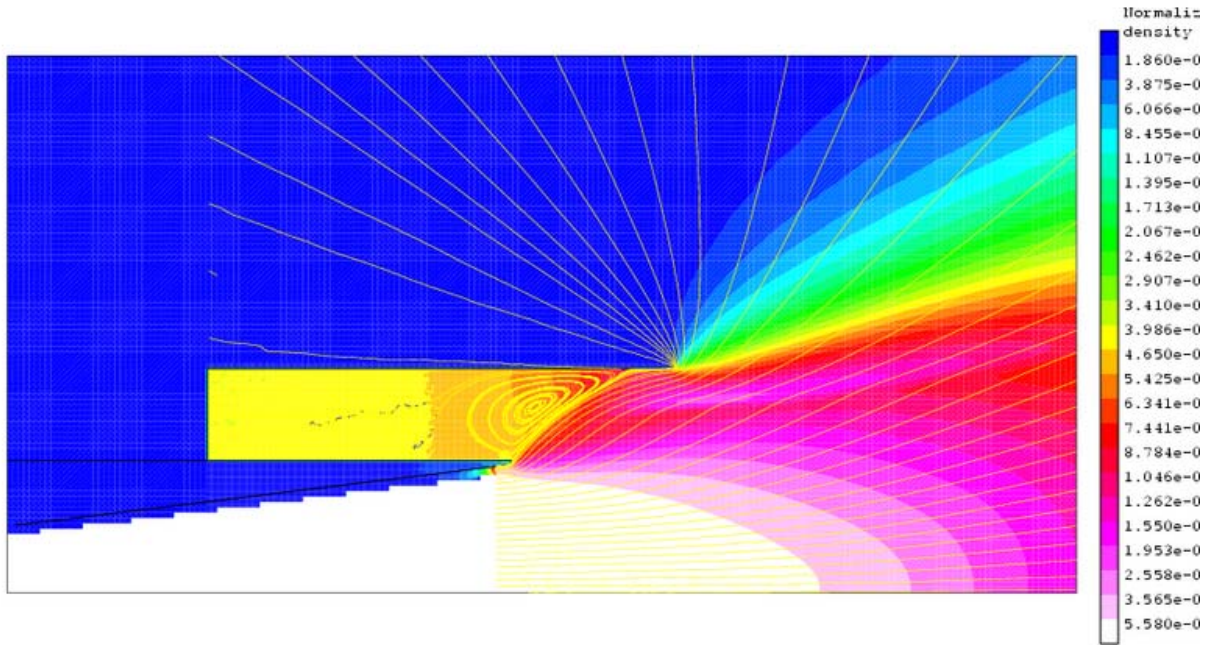


Fig.2.121. Computed density field and streamlines for the carrier gas plume exhausted from the nozzle with a screen.

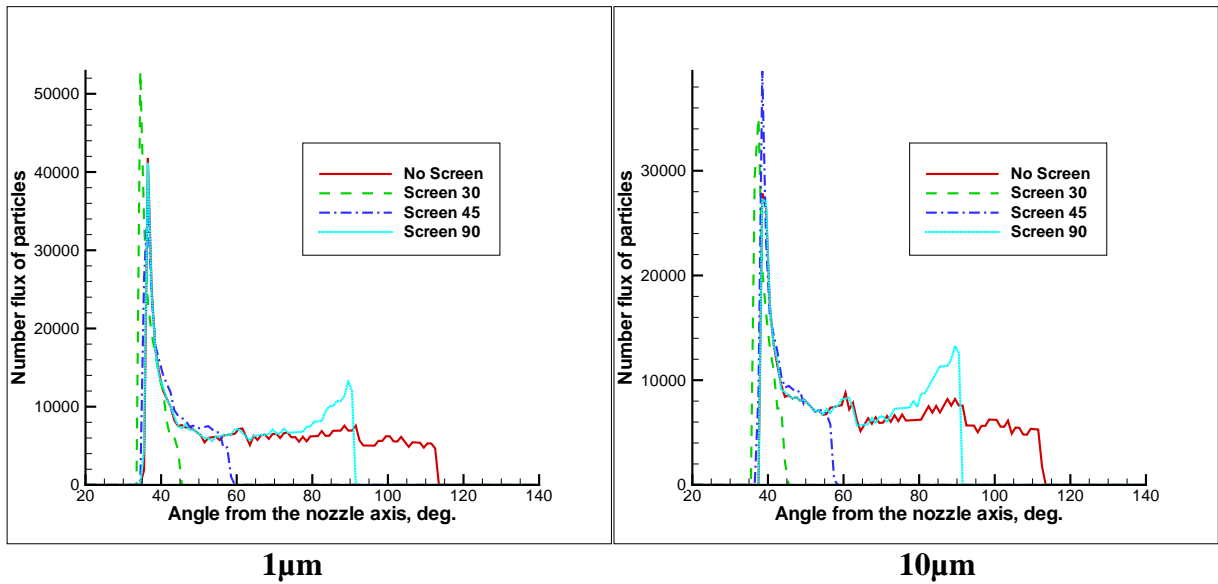


Fig.2.122. Angular distribution of droplets of two different sizes with different configurations of the protective screen.

Thus, during the 3rd year of the project

1. The liquid-film flow on the wall of a supersonic nozzle under the action of a pressure gradient and friction from the side of the gas flow and nozzle wall was theoretically studied. Dependences of the film thickness, its mean velocity, and temperature of the liquid at the gas-liquid interface were obtained.

2. Mechanisms of liquid-film disintegration and formation of liquid droplets, which subsequently enter the backflow, were analyzed. The characteristic times of film disintegration into separate fragments and their subsequent coalescence into droplets and the most probably sizes of the droplets formed were estimated. The motion of droplets formed in the vicinity of the nozzle lip in the gas-phase backflow field was modeled. It was shown that the droplets are entrained into the backflow and move in directions that make angles up to 140° to the nozzle centerline.

3. The gas-droplet plume flow in the peripheral region and in the backflow was numerically examined by a hybrid approach. The influence of various parameters, such as the place of liquid-film disintegration, the magnitude and direction of droplet velocities, and the droplet size, on motion of droplets was considered. The possibility of reducing contamination of spacecraft surfaces with the use of screens was numerically analyzed. This analysis confirmed the experimental results, namely, a substantial decrease in droplet backflows due to mounting of screening surfaces.

4. It was shown that exhaustion of the near-wall film with the gas flow into vacuum leads to formation of droplet-phase backflows caused by film disintegration on the nozzle lip and outer surface of the nozzle under the action of a cocurrent gas flow and phase explosion.

5. Methods of controlling droplet-phase backflows, aimed at backflow reduction, were analyzed. It was shown that the most effective method of decreasing the backflows is to reduce the dynamic action of the gas flow on the droplets (to reduce the Weber number).

6. The dynamic impact of the cocurrent flow on the droplets at different distances from the nozzle exit was evaluated. The greatest dynamic impact of the flow on the droplets was observed in the region of the nozzle lip.

7. Several variants of the special screens to be installed on the exit part of the nozzle were considered and proposed. Five different screens were proved, developed, and manufactured.

8. The pressure between the nozzle and the screen with and without liquid injection was measured. It was shown that the flow inside the screen is closed and independent of the pressure in the vacuum chamber. A vortex flow arises inside the screen.

9. New approaches to electron-beam visualization of the flow structure were developed. The influence of the screen on gas dynamics of the underexpanded jet downstream of a supersonic nozzle was considered.

10. A series of experiments was performed to study the influence of the screens on the flow structure of the gas and droplet phases in vacuum behind a supersonic nozzle. It was shown that the screen does not affect the flow in the central part of the plume. At the same time, the use of the screens allows a substantial decrease in droplet-phase backflows (by two orders of magnitude).

Task 2. Investigation of gas-droplet flows. Months 37-41.

The project duration was increased on 5 month, in the course of those additional investigations were conducted.

Task 2. Development of numerical models of multiphase flows on the basis of a Lagrangian description of liquid droplets with allowance for evaporation and possible agglomeration of solid particles during their collisions in accordance with phenomenological models. Testing and validation of numerical codes implementing these models by comparisons with available experimental data.

In accordance with the work plan, a numerical algorithm is developed for modeling multiphase flows with a Lagrangian description of liquid and solid particles with allowance for evaporation. This algorithm is based on a hybrid Eulerian/Lagrangian description of the gas/vapor carrier flow and disperse liquid droplets. The carrier-gas dynamics is described by a continuum approach (Navier-Stokes equations), and the dynamics of disperse liquid particles has a Lagrangian description. Evaporation of droplets is taken into account through available phenomenological/kinetic models for kinetic and continuum regimes, which were developed previously and are described in available publications. The system of equations that describe the dynamics of the liquid particles,

$$\frac{d\bar{X}_p}{dt} = \bar{R}_p, \text{ где } \bar{X}_p = \begin{pmatrix} \bar{r}_p \\ m_p \\ m_p \bar{V}_p \\ m_p c_p^0 T_p \end{pmatrix}, \quad \bar{R}_p = \begin{pmatrix} \bar{V}_p \\ J_{gp} \\ \bar{F}_{gp} \\ Q_{gp} \end{pmatrix},$$

includes the terms J_{gp} and Q_{gp} , which are responsible for mass and heat transfer between the carrier gas and the liquid particle. The process of contact heat transfer at the interface between the two phases is described by the expression $Q_{gp} = \pi \lambda_g d_p Nu (T_g - T_p)$, where λ_g is the thermal conductivity of the carrier phase, d_p is the diameter of the liquid particle, Nu is the Nusselt number, and T_g and T_p are the temperatures of the carrier phase and the liquid droplet, respectively. The diffusion mass transfer is described by the relation $J_{gp} = \pi D d_p Sh (\rho_v - \rho_s(T_p))$, where D is the diffusivity of vapor of the disperse phase in the carrier gas, ρ_v , $\rho_s(T_p)$ are the densities of vapor of the disperse phase and saturated vapor at the temperature of the disperse phase, respectively, and Sh is the Sherwood number. Under conditions close to the boiling point, the mass-transfer intensity is determined by heat supply to the disperse phase: $J_{gp} = -\frac{Q_{gp}}{h_v}$,

where h_v is the latent heat of evaporation of the disperse phase. Our algorithm employs a combination of these two cases:

$$J_{gp} = \pi D d_p Sh (\rho_v - \rho_s(T_p)) (1 - \delta) - \frac{Q_{gp}}{h_v} \delta.$$

Here $\delta = p_{ps}/p_g$ is the ratio of the pressure of saturated vapor of the disperse phase to the pressure of the carrier gas. The model of heat and mass transfer is closed by empirical correlations

$$Nu = \frac{2 + 0.552 Re_{gp}^{0.5} Pr^{0.33}}{1 + 3.42 \frac{M_{gp}}{Re_{gp} Pr}}, \quad Sh = \frac{2 + 0.552 Re_{gp}^{0.5} Sc^{0.33}}{1 + 3.42 \frac{M_{gp}}{Re_{gp} Sc}}.$$

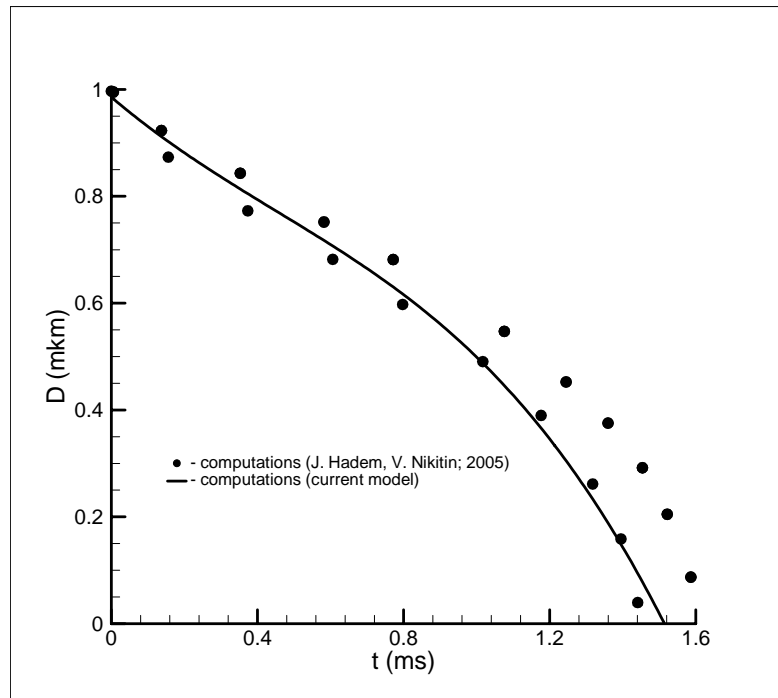
Here $Pr = \frac{\mu_g c_g}{\lambda_g}$, $Sc = \frac{\mu_g}{D \rho_g}$, $M_{gp} = |\bar{V}_g - \bar{V}_p| / \sqrt{\kappa p_g / \rho_g}$, and $Re_{gp} = d_p \rho_g |\bar{V}_g - \bar{V}_p| / \mu_g$ are the

Prandtl, Schmidt, Mach, and Reynolds numbers, respectively. The results of test computations with the use of this model are described below.

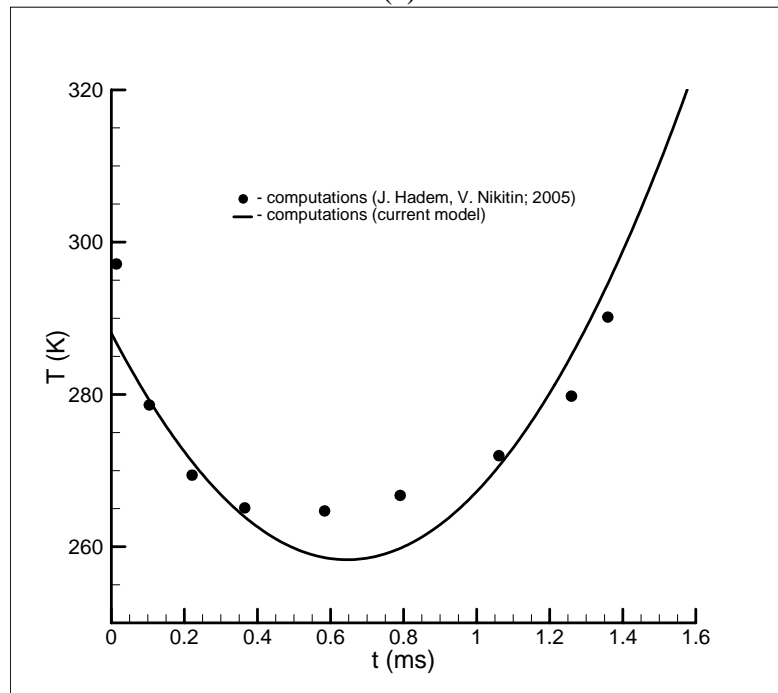
To validate the implemented model of heat and mass transfer, we considered a model problem where a droplet of a prescribed size penetrates with a given velocity into a quiescent gas. The thermophysical properties of the droplet and the ambient gas substances were fixed in all computations, the gas temperature was substantially higher than the boiling point, and the concentration of the evaporating substance far from the droplet was equal to zero, which was assumed to always lead finally to complete evaporation of the droplet. This test case was chosen deliberately to test the developed numerical model under conditions of intense heat and mass transfer.

The computations were performed under conditions corresponding to those in [1]: the quiescent ambient gas is air with a pressure $p=1.013\times 10^5$ Pa and a temperature $T=1000$ K, the droplet substance is a hydrocarbon from the class of kerosene (*n*-decane), and the initial temperature of the droplet is $T_d=300$ K. The computations were performed for a droplet with a diameter $d_d=1$ μ m at the initial time. The initial velocity of the droplet was varied in different computations from 10 to 100 m/s. The results computed for this problem are compared with the results of [1] in Fig. 2.123. Droplet deceleration in the quiescent gas occurs very rapidly, as compared to the characteristic time of evaporation. Heat transfer in the course of relaxation of the droplet velocity affects only the temperature acquired by the droplet at the initial time. After droplet deceleration, the process of evaporation reaches a quasi-steady regime during which the droplet temperature decreases approximately to 260 K owing to intense evaporation. Further on, as the droplet size decreases, heat transfer with the hot ambient gas starts to play the governing role; as a result, the droplet at the final stage of its existence is heated to a temperature of 320 K. Note that the results computed by our model are in reasonable agreement with the results of [1].

To validate the developed numerical algorithm under more realistic conditions, exhaustion of a gas-droplet flow from a supersonic nozzle possessing a thrust of 10 N was numerically simulated. The shape and size of the nozzle and the flow parameters corresponded to conditions in [2]: the nozzle-throat radius was $R_t=1.425$ mm, the nozzle-exit radius was $R_e=17.5$ mm, the nozzle length was $L_n=49$ mm, and the angle of the conical part of the nozzle was 7° . The pressure in the high-pressure chamber was $P^c=7\times 10^5$ Pa, and the temperature was 3040 K. Exhaustion of the gas-droplet flow from the nozzle was computed for droplets with a diameter $d_d=2.5$ μ m, which make the most significant contribution to the mass flux of the liquid phase, according to the data of [2] and Trinks' experimental measurements [3]. The droplets were assumed to be uniformly distributed in the nozzle throat at the initial time. Figure 2.124 shows the angular distribution of the liquid-phase flow, which is compared with the experimental data of [3] cited in [2]. It is seen from Fig. 2.124 that the angular distribution of the liquid phase is in good agreement with the experimental data, which proves the adequacy of the model used to describe the dynamics of the gas-droplet flow with intense heat and mass transfer.



(a)



(b)

Fig. 2.123 (a, b). Droplet diameter and temperature versus time. Quiescent air ($T=1000$ K, $p=1$ atm), kerosene droplet ($T_d=300$ K, $d_d=1$ μm , $V_d=10 - 100$ m/s).

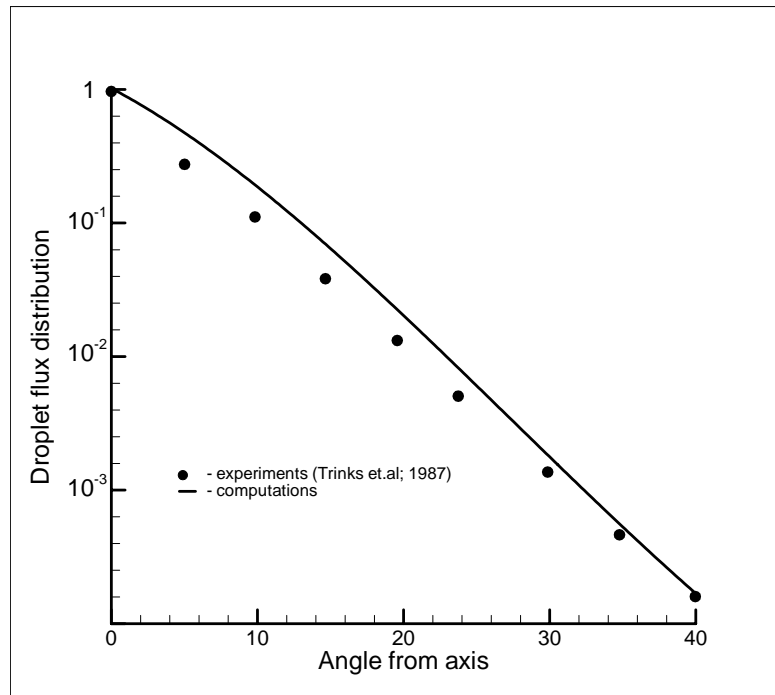


Fig. 2.124. Comparison of the angular distribution of the droplet mass flux in the plume. Droplets 2.5 μm in diameter, which ensure the main contribution to the mass flux, are considered.

Based on the algorithm developed, which employs the above-described model of mass and energy transfer between the phases, exhaustion of a two-phase gas-droplet flow from a supersonic nozzle was numerically simulated for conditions of experiments performed at the Institute of Thermophysics SB RAS. The nozzle geometry and the flow parameters were identical to those used in our earlier computations performed at the previous stages of the project. The nozzle-throat radius was $R_* = 5$ mm, the radius of the generatrix in the nozzle throat was $r_{\alpha\beta} = 5$ mm, the nozzle-exit radius was $R_e = 9.55$ mm, and the apex half-angle in the diverging part of the nozzle was $\alpha = 7^\circ$. The design Mach number of the nozzle was 2.84. The computations were performed for a stagnation pressure $P_0 = 4000$ Pa and a stagnation temperature of 293.15 K. The corresponding Reynolds number was 10,460. The carrier-gas phase was N_2 , and the disperse droplet phase was water.

Exhaustion of the gas-droplet flow from the nozzle was numerically simulated on the basis of the developed hybrid Lagrangian-Eulerian algorithm. The carrier-gas flow was modeled by solving full unsteady Navier-Stokes equations, and the dynamics of the disperse phase was obtained within the Lagrangian approach. The flow was assumed to be axisymmetric. The liquid droplets at the initial time were uniformly distributed in the nozzle throat. The initial diameter of the droplets was varied from 1 to 10 μm . Figure 2.125 shows several selected trajectories of the droplets and the carrier-gas pressure field for droplets with an initial diameter of 1 μm . The liquid droplets are entrained by the carrier-gas flow and deflect from the nozzle centerline at angles of the order of 10-30°. The changes in the droplet diameter, temperature, and velocity along the trajectory for three typical initial positions of the droplet are illustrated in Figs. 2.126, 2.127, and 2.128, respectively. Acceleration of droplets in an expanding gas flow results in rapid evaporation of the liquid, which is accompanied by a decrease in temperature. At distances of the order of 0.15 m along the trajectory, the droplet parameters reach quasi-equilibrium values. Note that the liquid-solid phase transitions are not considered here. Figures 2.127 and 2.128 clearly display an interesting feature of liquid droplets moving along trajectory No. 3: the temperature for these droplets at the initial part of the trajectory (upstream of the nozzle) is significantly higher and the velocity is lower than these parameters for droplets moving in the vicinity of the nozzle. This can be attributed to the influence of the boundary layer on the nozzle wall.

Downstream of the nozzle exit, the temperature and velocity of such droplets jump to values corresponding to local parameters of the carrier gas. Results of similar computations for droplets with initial diameters of 5 and 10 μm are plotted in Figs. 2.129-2.132 and Figs. 2.133-2.136, respectively.

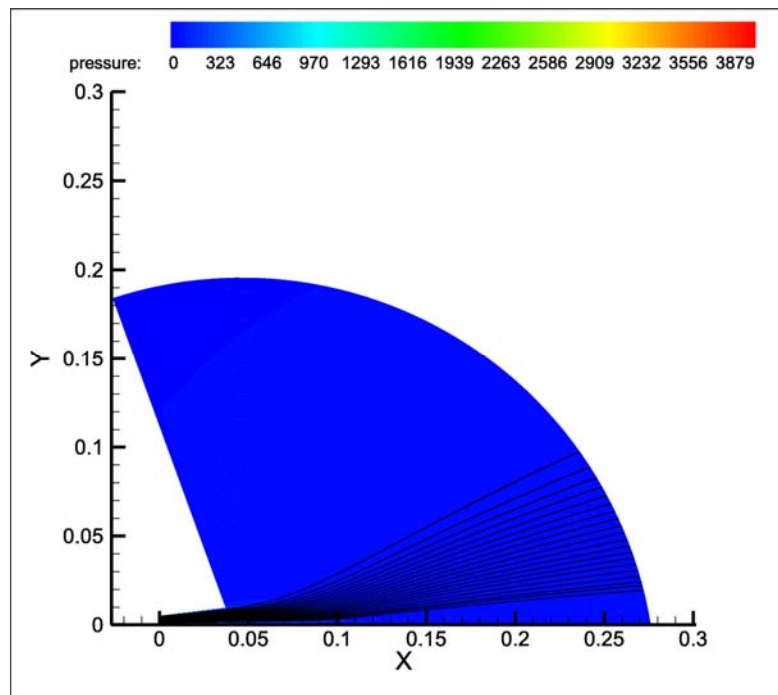


Fig. 2.125. Trajectories of droplets with an initial diameter of 1 μm . The carrier phase is N_2 , and the droplet substance is water.

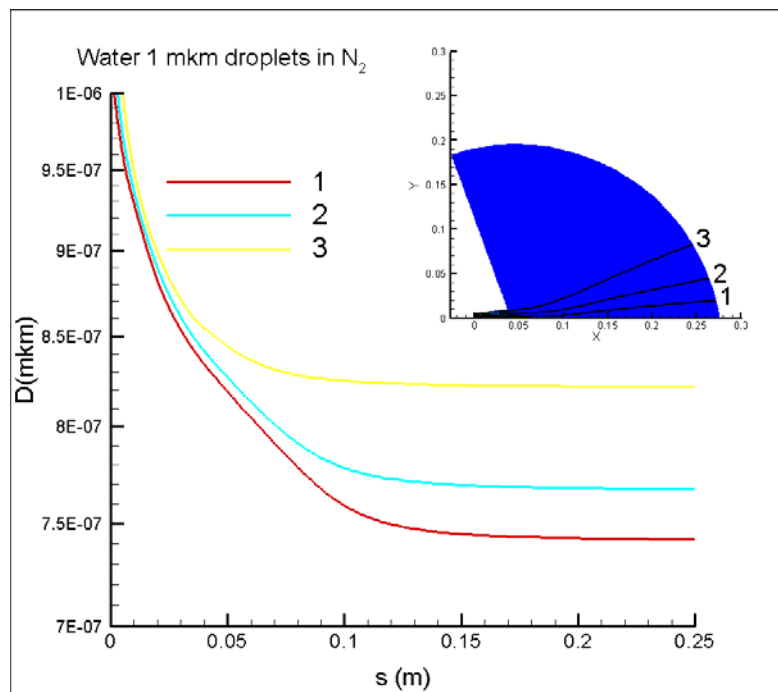


Fig. 2.126. Variation of the droplet size along the trajectory. The initial diameter is 1 μm . The carrier phase is N_2 , and the droplet substance is water.

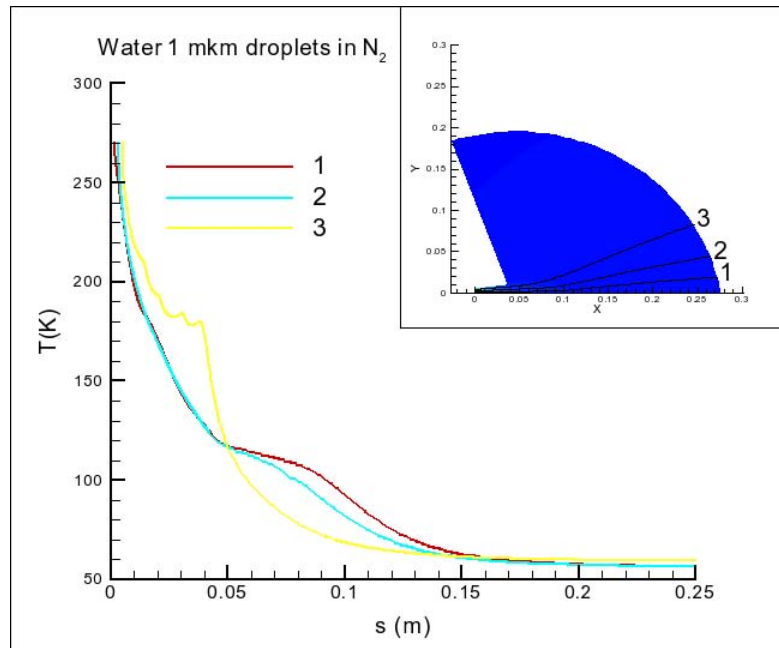


Fig. 2.127. Variation of the droplet temperature along the trajectory. The initial diameter is 1 μm. The carrier phase is N₂, and the droplet substance is water.

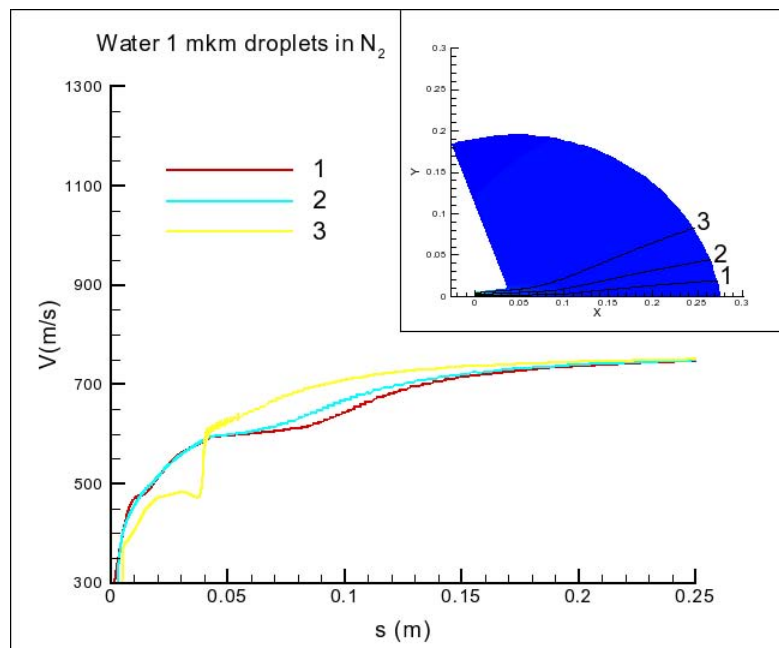


Fig. 2.128. Variation of the absolute value of droplet velocity along the trajectory. The initial diameter is 1 μm. The carrier phase is N₂, and the droplet substance is water.

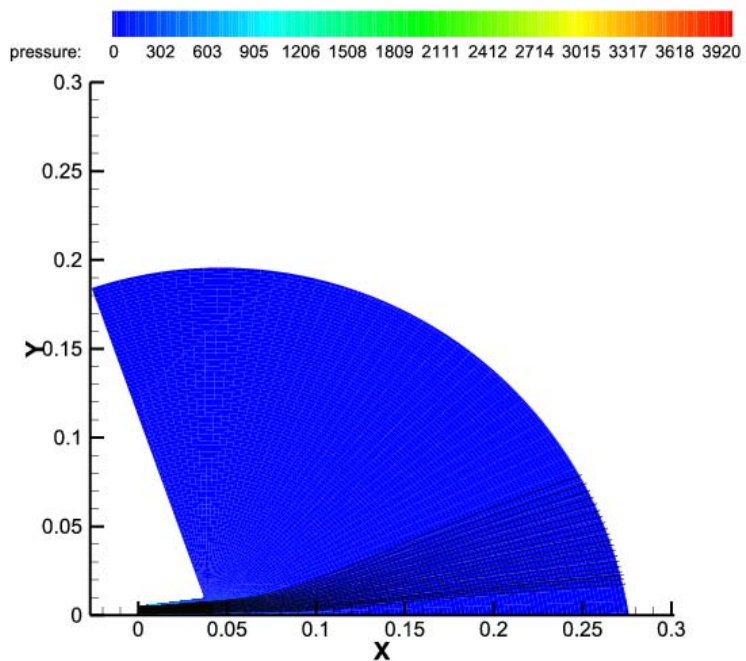


Fig. 2.129. Trajectories of droplets with an initial diameter of 5 μm . The carrier phase is N_2 , and the droplet substance is water.

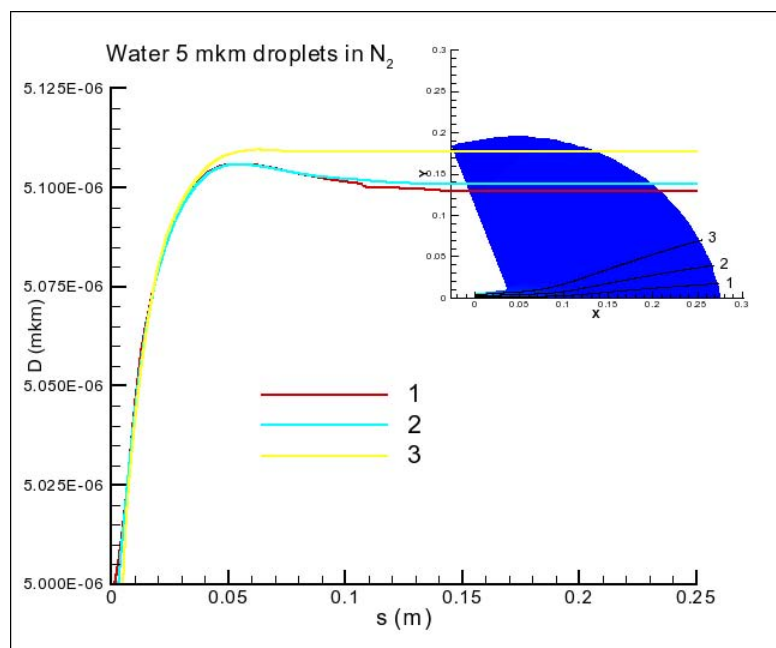


Fig. 2.130. Variation of the droplet size along the trajectory. The initial diameter is 5 μm . The carrier phase is N_2 , and the droplet substance is water.

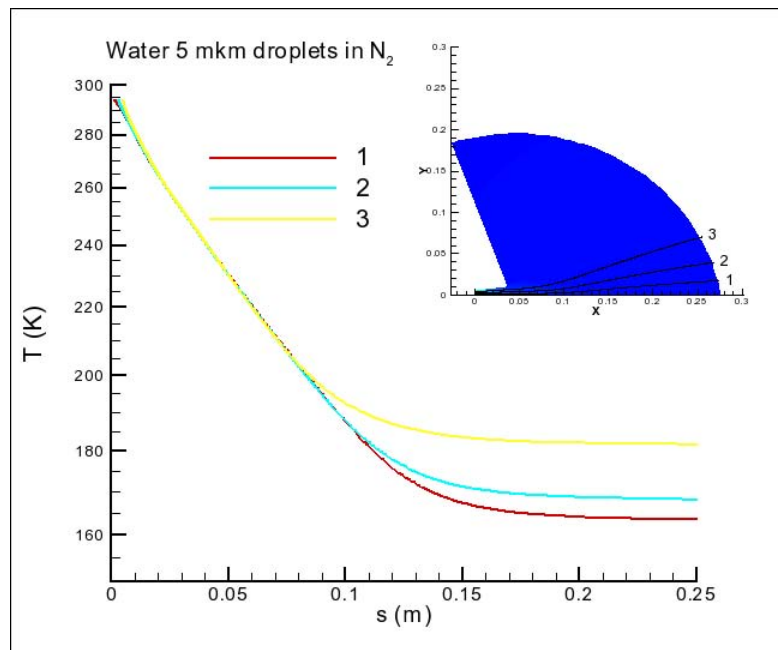


Fig. 2.131. Variation of the droplet temperature along the trajectory. The initial diameter is 5 μm . The carrier phase is N₂, and the droplet substance is water.

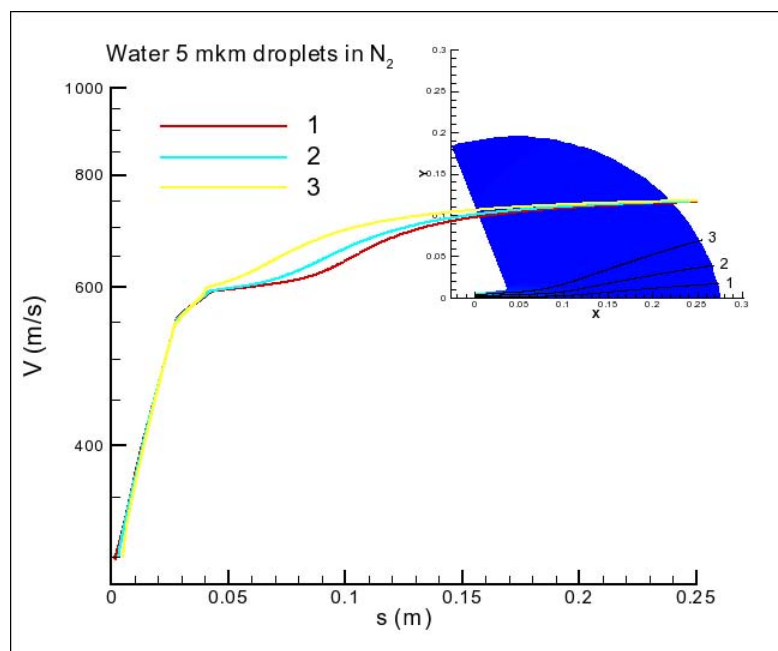


Fig. 2.132. Variation of the absolute value of droplet velocity along the trajectory. The initial diameter is 5 μm . The carrier phase is N₂, and the droplet substance is water.

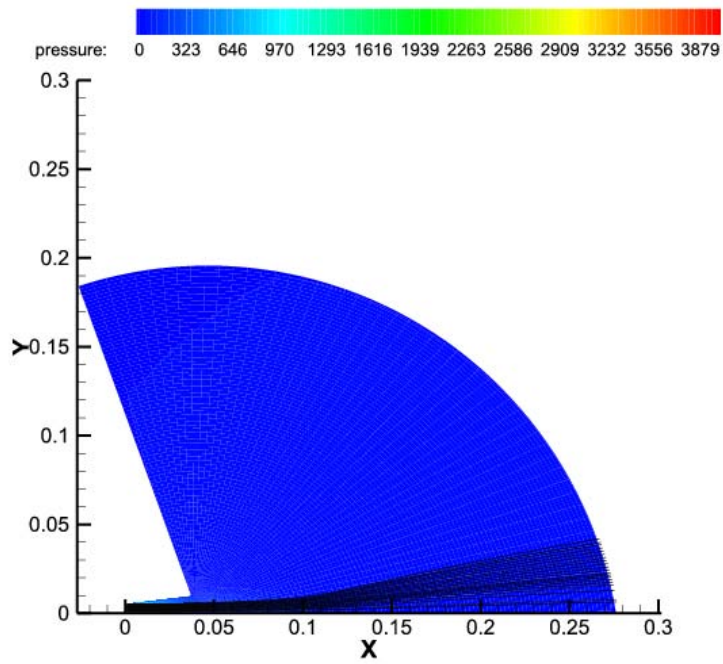


Fig. 2.133. Trajectories of droplets with an initial diameter of 10 μm . The carrier phase is N_2 , and the droplet substance is water.

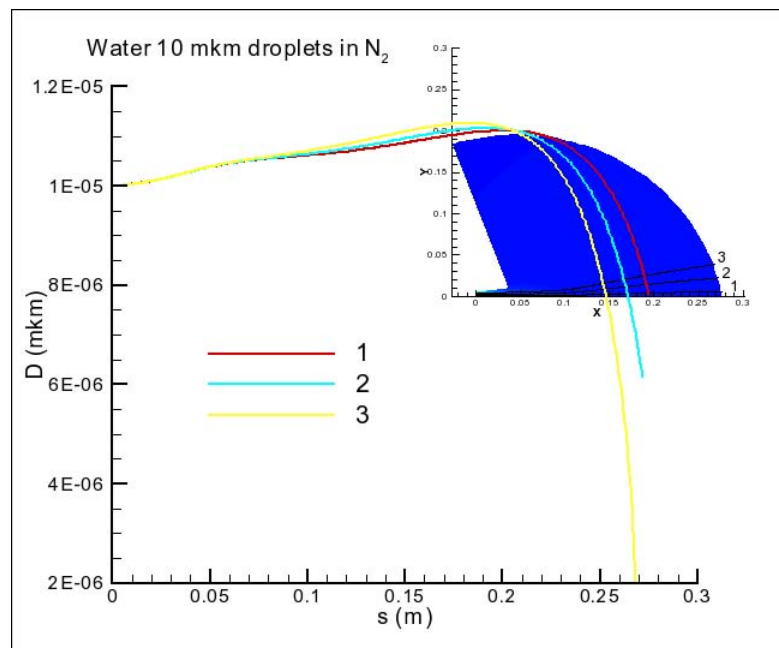


Fig. 2.134. Variation of the droplet size along the trajectory. The initial diameter is 10 μm . The carrier phase is N_2 , and the droplet substance is water.

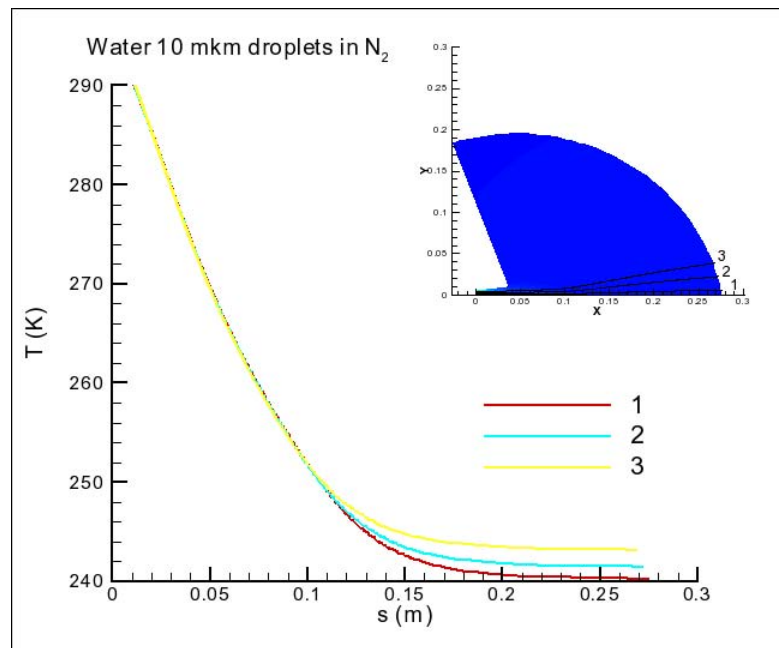


Fig. 2.135. Variation of the droplet temperature along the trajectory. The initial diameter is 10 μm . The carrier phase is N₂, and the droplet substance is water.

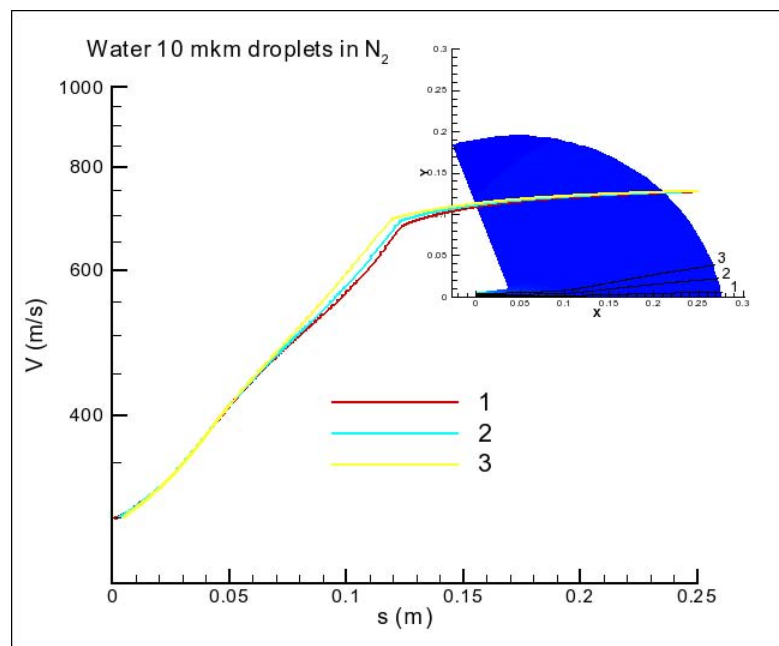


Fig. 2.136. Variation of the absolute value of droplet velocity along the trajectory. The initial diameter is 10 μm . The carrier phase is N₂, and the droplet substance is water.

Thus, a numerical algorithm for modeling gas-droplet flows with allowance for mass and energy transfer between the phases was developed and tested during the last stage of the project. The algorithm was validated on the basis of model problems by comparisons with available experimental and numerical results. Exhaustion of a gas-droplet flow from a supersonic nozzle was numerically simulated with the use of the developed numerical algorithm.

References used

1. J. Hadem and V.F.Nikitin. Modeling of heat and mass transfer during interaction of a liquid droplet with a gas flow. Vestnik MGU, Ser. 1, Matematika, Mekhanika. 2005, No. 3, pp. 33 – 40.
2. L.Genkin, V.Baer, and J.Falcovitz. A random simulation of droplet distribution in nozzle and plume flows. Shock waves. 1997, No. 7, pp. 211 – 218.
3. H. Trinks, et. al. Experimental investigation on plume contamination and surface effects. FTR Univ. Hamburg TRI-ESA-1987.

4. SUMMARY

All research engineering and technical work fulfilled completely corresponds to the tasks and milestones of the work plan.

Task 1. A number of models for real gas effects (internal degrees of freedom of molecules and chemical reactions) for the DSMC method were developed. These models are numerically efficient, accurately describe complicated physical and chemical processes in a real gas, and can be applied to polyatomic molecules. Applicability of these models to studying near-continuum nonequilibrium flows is analyzed. A comparison of numerical data with experimental results proved high accuracy of these models.

The models developed were used to create a highly efficient system for statistical modeling of flows with real gas effects (SMILE), which is based on the object-oriented approach. The SMILE software system contains databases with properties of various molecules, collision processes, and models that describe real gas effects. The system has a powerful graphical interface, which ensures easy definition of the initial data for computations, monitoring of the computation, and processing and visualization of results. The SMILE software system allows accurate prediction of force and heat loads and contamination due to interaction of thruster plumes with the spacecraft surface.

The ADDENDUM was aimed at the development of a model for the DSMC method for the description of high-temperature nonequilibrium dissociation, which allows accurate modeling of chemically reacting flows under conditions of strong translational-vibrational nonequilibrium.

Task 2. A comprehensive numerical and experimental study of exhaustion of supersonic gas-droplet plumes into vacuum was performed within the project. The objective of the study was to find the principal mechanisms responsible for the formation of backflows of the droplet phase leading to contamination of the spacecraft surface by exhaustion products of thruster plumes. For this purpose, an experimental technique for testing gas-droplet flows exhausting into a rarefied gas medium was developed, and detailed experiments in a vacuum chamber were performed.

The experimental aspect of the project included finding new concepts for generating supersonic gas-droplet flows in vacuum and development of novel methods for diagnosing the droplet phase in the gas-droplet flow. These methods include visualization of the flow structure, measurement of distribution functions for the particle size, direction, and velocity, and the following independent techniques of measuring the spatial distribution of the droplet phase:

- technique of the quartz microbalance;
- technique of spectrophotometry;
- technique of deposition on a paper substrate.

The use of the methods mentioned above allowed establishing the general structure of the droplet-phase flow in vacuum: it was demonstrated that exhaustion of the near-wall liquid film with a cocurrent gas flow into vacuum leads to formation of two typical regions of the droplet-

phase flow – the central region and the peripheral region. The central region is formed owing to shedding of droplets from the film surface in the vicinity of the nozzle throat and their subsequent fragmentation and acceleration in the gas flow during their motion inside the nozzle and in the plume downstream of the nozzle. The peripheral region is formed owing to decomposition of the near-wall liquid film at the nozzle lip, where the pressure drastically decreases and the liquid becomes overheated.

The influence of the nozzle geometry, properties of gas-flow parameters, and properties of the liquid on the spatial distribution of the droplet phase in the gas-droplet flow was investigated.

The distributions functions of droplets in terms of sizes, directions, and velocities were measured. It was shown that exhaustion of the near-wall liquid film with the gas flow from the nozzle into vacuum leads to the formation of droplet-phase backflows caused by film disintegration at the nozzle lip and on the outer surface of the nozzle under the action of the cocurrent gas flow and phase explosion.

Methods of controlling droplet-phase backflows, aimed at reducing the latter, were analyzed. It was shown that the most effective method of backflow reduction is to decrease the dynamic action of the gas flow onto droplets (to decrease the Weber number).

Several variants of special screens mounted at the nozzle exit were proposed and examined. The effect of the screens on the flow structure in the gas and droplet phases downstream of a supersonic nozzle in vacuum was studied experimentally. It was shown that the screen does not affect the flow in the central part of the plume. At the same time, the use of screens allows a significant (by two orders) reduction of droplet-phase backflows.

A number of codes for numerical simulation of gas-droplet flows were developed. A hybrid approach is used to compute the carrier-gas flow, with the finite-difference solution of Navier-Stokes equations and the DSMC method for solving the Boltzmann equation being used in different zones of the computational domain. The motion of liquid droplets is modeled on the basis of the Lagrangian approach. The mutual influence of two phases is taken into account by including mass, momentum, and energy transfer between the phases. The software developed is used to compute flows in a supersonic nozzle and in the exhausting plume, including the backflow region.

The investigations performed revealed that entrainment of the liquid phase into the gas flow is particularly intense at two points: first, in the vicinity of the nozzle throat and, second, on the nozzle lip. The computations showed that droplets formed in the vicinity of the nozzle throat continue their straightforward motion when they leave the nozzle and do not enter the backflow. The aerodynamic forces acting on the droplets are too weak to turn the latter into the opposite direction: the angles of deflection of even the finest droplets are much smaller than 90° . Thus, the main mechanism leading to emergence of the liquid phase in the backflow is disintegration of the coolant film flowing over the nozzle walls, which occurs at the nozzle lip. The estimates showed that another possible source of the liquid phase (condensation of the carrier gas) cannot be important under the present conditions, because such condensation is expected to occur in the plume at a certain distance from the nozzle exit and the droplets formed thereby cannot enter the backflow.

An effort was made to study the disintegration of the liquid film on the nozzle lip, which leads to the emergence of the disperse phase in the backflow, in more detail. The experiments revealed that the liquid film from the nozzle lip passes to the outer surface of the nozzle and moves upstream to a certain distance over the outer wall of the nozzle against the force of gravity acting in the experiment. At that position, the film experiences an extremely low ambient pressure. Based on integral boundary-layer equations, the liquid-film flow over the nozzle wall under the action of an external supersonic flow was numerically simulated. The computations showed that the film flow becomes decelerated in the vicinity of the nozzle lip, and the film thickness increases fairly rapidly. In the main part of the nozzle, the film thickness is smaller than the critical vapor-bubble size that has to be reached for boiling to begin. At the same time, the rapid growth of the film thickness in the vicinity of the nozzle lip generates appropriate

conditions, and the possibility of explosive boiling of the liquid cannot be waived off. The photographs of the experiments clearly display liquid droplets following the radial directions from the nozzle lip and, obviously, formed as a result of film disintegration at this point.

It was suggested that protective screens should be used to prevent contamination of spacecraft surfaces. Several configurations of such protective screens were developed. The experiments performed showed that the use of such screens really allows a drastic attenuation of disperse-phase backflows. This conclusion was confirmed by numerical computations of the gas-droplet flow, which were performed for a configuration with protective screens.

The most important result obtained within the project is identifying how the disperse phase enters the backflow. This phenomenon is associated with disintegration of the cooling liquid film on the nozzle lip. An effective method of decreasing contamination of spacecraft surfaces by the products of film decomposition can be mounting protective screens.

5. PAPERS AND REPORTS PUBLISHED

1. Gimelshein, S.F., Gimelshein, N.E., Levin, D.A., Ivanov, M.S., and Wysong, I.J. "On the use of chemical reaction rates with discrete internal energies in the direct simulation Monte-Carlo method," *Physics of Fluids*, July 2004, Vol. 16, Issue 7, pp. 2442-2451

The conventional chemical reaction models of the direct simulation Monte Carlo method developed with the assumption of continuous rotational or vibrational modes that are shown to exhibit systematic errors when used with discrete energy modes. A reaction model is proposed that is consistent with the use of discrete energy distributions of rotational and vibrational modes, and is equally applicable to diatomic and polyatomic systems. The sensitivity of the model to variations of different reaction rate parameters is examined. The revised chemical reaction model is then applied to the modeling of hypersonic flows over spacecraft in the Martian and Earth atmospheres.

2. Bondar Ye.A., Markelov G.N., Gimelshein S.F., Ivanov M.S. "Numerical Modeling of Near-Continuum Flow over a Wedge with Real Gas Effects," *Journal of Thermophysics and Heat Transfer* (accepted for publication in No.2, 2006).

Effects of vibrational relaxation and dissociation on the stand-off distance of the bow shock wave on a wedge are numerically examined with the use of the kinetic (DSMC method) and continuum (Navier--Stokes equations) approaches. A hypersonic flow around the wedge is computed for Knudsen numbers about 0.0005 in a wide range of wedge angles both for a monatomic gas (argon) and a diatomic reacting and nonreacting gas (nitrogen). DSMC computations are based on three different real gas effect models. The kinetic and continuum results for the stand-off distance are in good agreement for argon and nonreacting nitrogen. The influence of vibration-dissociation coupling on the results of numerical simulations was analyzed. Sensitivity of simulation results to chemical reaction rate constants was also estimated. Numerical simulations show that dissociation is responsible for the nonlinear form of the dependence of the stand-off distance on the wedge angle, which qualitatively agrees with available experimental data.

3. Bondar Ye.A., Markelov G.N., Gimelshein S.F., Ivanov M.S. "DSMC Study of Shock Detachment Process in Hypersonic Chemically Reacting Flow," *Rarefied Gas Dynamics: 24th Int. Symp., Porto Giardino, Italy, July 10-16, 2004*, (Ed. M.Capitelly), AIP Conference proceedings, Vol. 762, 2005, pp.523-528.

Hypersonic chemically reacting flow around a wedge in the near-continuum regime was numerically studied by the DSMC method with the main goal of validation of real gas effect models. The influence of vibration-dissociation coupling on the results of numerical simulations was analyzed. To this end, two models of chemical reactions were used in the computations, the total collisional energy model and a vibrationally favored model. The numerical results were compared with the experimental data of Hornung and Smith on the shock-wave stand-off distance in a hypersonic flow around the wedge. Sensitivity of simulation results to chemical reaction rate constants was also estimated.

4. Ye. Bondar, N. Gimelshein, S. Gimelshein, M. Ivanov, I. Wysong "On the Accuracy of DSMC Modeling of Rarefied Flows with Real Gas Effects," Rarefied Gas Dynamics: 24th Int. Symp., Porto Giardino, Italy, July 10-16, 2004, (Ed. M.Capitelly), AIP Conference proceedings, Vol. 762, 2005, pp.607-611.

The applicability analysis of DSMC models of real gas effects, namely, translational-internal energy transfer and chemical reactions, is performed. Three models are considered: conventional Larsen--Borgnakke/Total Collision Energy model for continuous internal energies, modified Larsen--Borgnakke/Total Collision Energy model for discrete internal energies, and new vibrationally favored model for discrete internal energies, which is proposed in the present paper. The detailed comparison of the DSMC results, obtained using all the three models, with the Jeans, Landau--Teller and Arrhenius rates is given for diatomic and polyatomic molecules.

5. Kashkovsky A., Bondar Ye., Zhukova G., Ivanov M., Gimelshein S. "Object-Oriented Software Design of Real Gas Effects for the DSMC Method," Rarefied Gas Dynamics: 24th Int. Symp., Porto Giardino, Italy, July 10-16, 2004, (Ed. M.Capitelly), AIP Conference proceedings, Vol. 762, 2005, pp.583-588.

The main goal of the present work is to develop the structure of objects of an object-oriented DSMC code that takes into account real gas effects. The paper also describes the developed pre- and post-processing systems, including a database of physico-chemical properties of gases, a GUI for preparing all initial data and processing results, and a system for visualization of results.

6. Bondar Ye.A., Gimelshein S.F., Markelov G.N., Ivanov M.S. "Study of internal structure of shock wave in CO₂ / N₂ mixture." Proceedings of the 24th International Symposium on Shock Waves (Beijing, China, July 11-16, 2004). Ed. by Z.L.Jiang, Tsinghua Univ. Press, Paper No. 1382, 6 p.

The main goal of the present paper is to apply the DSMC method to study the strong shock wave structure for free stream conditions corresponding to the spacecraft entry in the rarefied CO₂/N₂ Martian atmosphere. Modeling was performed both for 1D (a planar shock wave in non-reacting mixture) and 2D (non-reacting and reacting flow about a cylinder) formulations at a free stream velocity typical for aerocapture maneuvers and Knudsen numbers of the order of 0.001-0.01. The results are presented both for macroparameters, velocity distribution functions, and populations of rotational and vibrational levels.

7. Ye.A. Bondar, G.N Markelov, S.F. Gimelshein, and M.S. Ivanov, "DSMC Modeling of Near-Continuum Flow Over a Wedge with Real Gas Effects", AIAA Paper 2004-1183 (2004).

Validation of the models of real gas effects (internal degrees of freedom and chemical reactions) implemented in the SMILE++ system was presented. DSMC simulations of a hypersonic near-continuum inert gas (Ar) flow around a wedge were performed and the results were compared

with the experimental data of Hornung (1979) on the stand-off distance of the shock wave on the wedge. An additional set of computations of this flow was performed within the framework of the continuum approach (Navier-Stokes equations). The resultant dependence of the stand-off distance on the wedge angle is in excellent agreement with the DSMC results. Then, a hypersonic near-continuum flow of dissociating nitrogen around the wedge was simulated. The numerical simulation results are in good qualitative agreement with experimental data for dissociating nitrogen.

8. Bondar Ye.A., Gimelshein S.F., Markelov G.N., Ivanov M.S. "DSMC Study of the Internal Shock-Wave Structure in a Dissociating Gas", AIAA Paper 2004-2588 (2004).

A recently developed DSMC model of real gas effects was verified and applied to study the internal structure of the shock wave and the relaxation zone behind it for conditions corresponding to spacecraft entry into the CO₂/N₂ Martian atmosphere. The impact of free stream conditions on relaxation of different energy modes inside and behind the shock was examined, and the effect of chemical reactions was also studied. Flow nonequilibrium was analyzed in detail on the basis of computed velocity distribution functions and internal energy populations.

9. V.N. Yarygin, V.G. Prikhodko, I.V. Yarygin, Yu.I. Gerasimov, A.N. Krylov. Gas-Dynamic Aspects of the Contamination Problem at the International Space Station. 1. Model Experiments // Thermophysics and Aeromechanics, 2003, Vol.10, No.2, pp. 269-286.

The results of experimental vacuum-chamber modeling of processes of International Space Station surface contamination by plumes of attitude-control thrusters are reported. Problems of modeling of attitude-control thruster plumes are considered; descriptions of the experimental setup, methods, and results of measurements of the angular distribution of the droplet phase with a co-current supersonic gas flow are given. It is shown that mounting of gas-dynamic protectors on the attitude-control thruster allows ensures a significant decrease in the droplet (contaminating) phase backflow.

10. Yu.P.Golovachev, M.S.Ivanov, D.V.Khotyanovsky, A.N.Kudryavtsev, V.A.Mazurkevich, B.I.Reznikov, and A.A.Schmidt. Numerical Simulation of a Multiphase Three-component Flow in a Supersonic Nozzle. AIAA Paper 2003-3494.

This study is focused on the development of a mathematical model of multiphase three-component flow in the nozzles of spacecraft control thrusters. The model incorporates the Eulerian-Lagrangian description of the medium, which implies utilization of continuous models (Euler, Navier-Stokes, etc.) for the carrier phase and the probe particle model for the dispersed phase (droplets). The model is completed by a description of a liquid film flow on the nozzle wall. Two-way coupling between all the components (the carrier phase, the drops, and the liquid film) is taken into account in the course of iterations, a special time-space averaging procedure is used to obtain distributions of droplet-phase parameters. At this stage of the study, to get an initial idea about the flow structure, simplified models of the components are considered within the framework of the one-way coupling approach.

11. V.G. Prikhodko, S.F. Chekmarev, V.N. Yarygin, I.V. Yarygin. Rise of a Near-Wall Liquid Film over the Outer Surface of a Nozzle Accompanying Supersonic Gas Flow into Vacuum // Doklady Physics (Doklady Akademii Nauk), 2004, Vol.49, No.2, pp. 119-121.

The results of investigation of a new, previously unknown, effect of film lifting on the external surface of the nozzle against gravity, caused by ejection of a near-wall liquid film with a co-

current flow from the nozzle into vacuum are described. The observed effect occurs only in the case of exhaustion into a low-pressure medium and has a hydro-gas-dynamical nature.

12. M.S. Ivanov, A.N.Kudryavtsev, G.N.Markelov, and P.V.Vashchenkov. Numerical Study of Backflow for Nozzle Plumes Expanding into Vacuum. AIAA Paper 2004-2687.

The goal of the paper is a detailed numerical investigation of the backflow phenomenon by a hybrid approach combining the continuum (Navier-Stokes) and kinetic (DSMC) computations. A Navier-Stokes solver is used to simulate a dense flow inside a supersonic convergent/divergent nozzle, while the flow around the nozzle lip and in the backflow region is computed with a DSMC code. The computations are performed for two different axisymmetric conical nozzles. First, the low-Reynolds-number nozzle flow investigated experimentally by Rothe is simulated. Three different nozzle lips are considered: one with an absolutely sharp edge and two others rounded with different radii. Further, numerical simulations are also carried out for the nozzle used in the recent experiments performed at the Institute of Thermophysics (Novosibirsk) for a nozzle operating under much higher Reynolds numbers.

13. V.G. Prikhodko, S.F. Chekmarev, I.V. Yarygin, and V.N. Yarygin, “Droplet size, direction-of-flight and velocity distributions in a supersonic gas-droplet flow expanding into vacuum,” Proc. XII International Conference on Methods of Aerophysical Research ICMAR’2004, Novosibirsk, 2004, Part 1, pp.183-188.

Methods and results of measurements of the size, direction-of-flight, and velocity distribution functions of the droplets in a supersonic flow expanding into vacuum from a nozzle with a near-wall liquid film are described. A model of disintegration of the liquid film at the nozzle exit is suggested, which shows reasonable agreement with the experimental data.

14. V.N. Yarygin, Yu.I. Gerasimov, V.G. Prikhodko, and I.V. Yarygin, “Research of gas-droplet flows with reference to contamination problem of the International Space Station by jets of its orientation thrusters,” Proc. XX Anniversary International seminar on jet, separated and non-stationary flows, Saint-Petersburg, 2004, pp.260-261.

Problems of vacuum-chamber modeling of full-scale jets of orientation thrusters of space vehicles and space stations are considered. Results of experimental investigations of gas-droplet flows expanding into vacuum are presented.

15. V.G. Prikhodko, N.I. Timoshenko, and I.V. Yarygin, “Some issues of diagnostics of supersonic gas-droplet flows in vacuum,” Proc. XX Anniversary International seminar on jet, separated, and non-stationary flows, Saint-Petersburg, 2004, pp.214-215.

Various approaches to diagnostics of droplet-phase flows are considered by an example of ejection of the near-wall liquid film (ethanol, butanol) with a co-current air flow from axisymmetric channels (tube, supersonic nozzle) into vacuum.

16. V.G. Prikhodko, S.F. Chekmarev, I.V. Yarygin, and V.N. Yarygin, “Exhaustion of a gas from a nozzle into vacuum with a near-wall liquid film,” Proc. XXVII Siberian Thermophysical Workshop, Novosibirsk, 2004. CD, ISBN-5-89017-027-9, No. 120.

Ejection of the near-wall liquid film (ethanol, butanol) with a co-current gas flow (air) from axisymmetric channels (cylindrical tube, supersonic conical nozzle) into vacuum is studied experimentally and theoretically.

17. I.V. Yarygin, “Gas-droplet flows from axis-symmetrical channels into vacuum,” Proc. VIII All-Russia conference of young scientists «Actual problems of thermophysics and physical hydro-gas-dynamics», Novosibirsk, 2004, pp.58-59.

Physical and applied problems associated with gas-droplet flows in vacuum are considered. Ways of organization and methods of diagnostics of such flows are examined. Results of studying the spatial structure of the gas and droplet phases in the case of co-current exhaustion of the near-wall liquid film with the gas flow into vacuum are presented.

18. I.V. Yarygin and A.A. Obuhov, “Measurement of spatial distributions of the droplet phase in a supersonic gas-droplet stream in vacuum,” Proc. VIII All-Russia conference of young scientists «Actual problems of thermophysics and physical hydro-gas-dynamics», Novosibirsk, 2004, pp. 177-178.

Various techniques of diagnostics of angular distributions of the droplet phase are considered by an example of exhaustion of the near-wall film of ethanol with a co-current flow of air from a supersonic nozzle into vacuum.

19. Yu.P.Golovachov, M.S.Ivanov, D.V.Khotyanovsky, A.N.Kudryavtsev, B.I.Reznikov, A.A.Smirnovsky, and A.A.Schmidt, “Multiphase three-component nozzle flow (model validation),” Proc. European Congress on Computational Methods in Applied Sciences and Engineering (ECCOMAS 2004), Jyvaskyla, Finland, July 24-28, 2004. Proceedings, Vol. II, ISBN 951-39-1869-6. Paper No. 750, 20 p.

The paper deals with development and validation of the Eulerian-Lagrangian algorithm of numerical simulation of a three-phase (carrier gas, liquid droplets, and liquid film) nozzle flow. The model takes into account a number of effects of interphase interaction and exchange. Particular attention is paid to model verification and comparison of results with available experimental data.

20. Yu.P.Golovachov, B.I.Reznikov, A.A.Smirnovsky, A.A.Schmidt, M.S.Ivanov, and A.N.Kudryavtsev, “Disintegration of cooling film at the nozzle lip as an origin of spacecraft external atmosphere,” Proc. of International Conference on Fundamental Problems of High-Speed Flows (Zhukovsky, Russia, September 21-24), 5 p.

The flow of a thin liquid film on the wall of a supersonic nozzle under the action of a pressure gradient and friction on the side of the gas flow is theoretically examined. Liquid evaporation and mass exchange between the liquid and disperse phases at the interface are taken into account. The boundary-layer equations are solved by an integral method, and dependences of the film thickness, flow rate of the coolant, mean velocity of the liquid, and film temperature at the interface on the streamwise coordinate are obtained. Possible mechanisms of film disintegration at the nozzle lip are considered.

21. P.V. Vashchenkov, A.N. Kudryavtsev, G.N. Markelov, and M.S.Ivanov, “DSMC study of backflow for nozzle plumes expanding into vacuum,” Proc. of 24th International Symposium on Rarefied Gas Dynamics (June 10-16, 2004, Bari, Italy), Ed. by M.Capitelli, AIP, 2005.

A detailed numerical study of the plume flow exhausting from the nozzle into vacuum is performed by the DSMC method. Special attention is paid to investigations of gas backflows resulting from flow turning at the nozzle lip to an angle greater than 90°.

22. B.I. Reznikov, A.A. Schmidt, Yu.P. Golovachev, A.N.Kudryavtsev, and M.S. Ivanov, "Flow of a coolant film along the nozzle lip under the action of a rarefied gas flow. Journal of Technical Physics (Zhurnal Tekhnicheskoi Fiziki). 2006. Vol.76. No.3. pp.30-37.

The flow of a thin liquid film along the nozzle contour under the action of shear friction and pressure gradient is considered. The process of film issuing to the nozzle lip in the case of gas exhaustion into vacuum is considered. It is shown that the film thickness drastically increases in the vicinity of the nozzle lip, which leads to possible dynamic and thermal disintegration of the film.

6. List of presentations at conferences and meetings with abstracts

1. Ye.A. Bondar, G.N Markelov, S.F. Gimelshein, and M.S. Ivanov, "DSMC Modeling of Near-Continuum Flow Over a Wedge with Real Gas Effects", 42nd AIAA Aerospace Sciences Meeting and Exhibit, 5-8 Jan 2004 / Reno, Nevada

Validation of the models of real gas effects (internal degrees of freedom and chemical reactions) implemented in the SMILE++ system was presented. DSMC simulations of a hypersonic near-continuum inert gas (Ar) flow around a wedge were performed and the results were compared with the experimental data of Hornung (1979) on the stand-off distance of the shock wave on the wedge. An additional set of computations of this flow was performed within the framework of the continuum approach (Navier-Stokes equations). The resultant dependence of the stand-off distance on the wedge angle is in excellent agreement with the DSMC results. Then, a hypersonic near-continuum flow of dissociating nitrogen around the wedge was simulated. The numerical simulation results are in good qualitative agreement with experimental data for dissociating nitrogen.

2. Bondar Ye.A., Gimelshein S.F., Markelov G.N., Ivanov M.S. "DSMC Study of the Internal Shock-Wave Structure in a Dissociating Gas", 37th AIAA Thermophysics Conference, 28 Jun - 1 Jul 2004, Portland, Oregon

A recently developed DSMC model of real gas effects was verified and applied to study the internal structure of the shock wave and the relaxation zone behind it for conditions corresponding to spacecraft entry into the CO₂/N₂ Martian atmosphere. The impact of free stream conditions on relaxation of different energy modes inside and behind the shock was examined, and the effect of chemical reactions was also studied. Flow nonequilibrium was analyzed in detail on the basis of computed velocity distribution functions and internal energy populations.

3. Bondar Ye.A., Markelov G.N., Gimelshein S.F., Ivanov M.S. "DSMC Study of Shock Detachment Process in Hypersonic Chemically Reacting Flow," 24th Int. Symp. on Rarefied Gas Dynamics, Porto Giardino, Italy, July 10-16, 2004

Hypersonic chemically reacting flow around a wedge in the near-continuum regime was numerically studied by the DSMC method with the main goal of validation of real gas effect models. The influence of vibration-dissociation coupling on the results of numerical simulations was analyzed. To this end, two models of chemical reactions were used in the computations, the total collisional energy model and a vibrationally favored model. The numerical results were compared with the experimental data of Hornung and Smith on the shock-wave stand-off

distance in a hypersonic flow around the wedge. Sensitivity of simulation results to chemical reaction rate constants was also estimated.

4. Ye. Bondar, N. Gimelshein, S. Gimelshein, M. Ivanov, I. Wysong "On the Accuracy of DSMC Modeling of Rarefied Flows with Real Gas Effects," 24th Int. Symp. on Rarefied Gas Dynamics, Porto Giardino, Italy, July 10-16, 2004

The applicability analysis of DSMC models of real gas effects, namely, translational-internal energy transfer and chemical reactions, is performed. Three models are considered: conventional Larsen--Borgnakke/Total Collision Energy model for continuous internal energies, modified Larsen--Borgnakke/Total Collision Energy model for discrete internal energies, and new vibrationally favored model for discrete internal energies, which is proposed in the present paper. The detailed comparison of the DSMC results, obtained using all the three models, with the Jeans, Landau--Teller and Arrhenius rates is given for diatomic and polyatomic molecules.

5. Kashkovsky A., Bondar Ye., Zhukova G., Ivanov M., Gimelshein S. "Object-Oriented Software Design of Real Gas Effects for the DSMC Method," 24th Int. Symp. on Rarefied Gas Dynamics, Porto Giardino, Italy, July 10-16, 2004

The main goal of the present work is to develop the structure of objects of an object-oriented DSMC code that takes into account real gas effects. The paper also describes the developed pre- and post-processing systems, including a database of physico-chemical properties of gases, a GUI for preparing all initial data and processing results, and a system for visualization of results.

6. P.V. Vashchenkov, A.N. Kudryavtsev, G.N. Markelov, and M.S.Ivanov, "Numerical study of backflow for nozzle plumes by a hybrid approach," Proc. 4th International Conference on Spacecraft Propulsion, 2-4 June 2004, Sardinia, Italy.

A hybrid approach is used for simulating exhaustion of a gas plume into vacuum and formation of backflows. The flow inside the nozzle is computed by the Navier-Stokes equations, and the flow outside the nozzle is computed by the DSMC method. Formation of gas backflows is considered for different shapes of the nozzle lip.

7. V.N. Yarygin. Electron-beam diagnostics in gas flows. Invited Lecture. XI Int. Conf. On Methods of Aerophysical Research, 1-7 July 2002, Novosibirsk-Biysk, Russia (ICMAR'2002).

A review of the electron beam method for diagnostics of a supersonic gas and gas-droplet plume flows is given.

8. V.G. Prihodko, N.I. Timoshenko, I.V. Yarygin. Some Questions of Diagnostics of Supersonic Gas-Droplet Flows in Vacuum // XX Conf. on Jets. 1-3 July 2004, Saint-Petersburg, Russia.

Various approaches to droplet-phase flow diagnostics by an example of ejection of a near-wall liquid film (ethanol, butanol) with a co-current air flow from axisymmetrical channels (tube, supersonic nozzle) into vacuum are considered.

9. V.G. Prihodko, S.F. Chekmarev, I.V. Yarygin, V.N. Yarygin. Droplet Size, Direction-of-flight and Velocity Distributions in a Supersonic Gas-droplet Flow expanding into

Vacuum // XII Int Conf. On Methods of Aerophysical Research, 29 June – 5 July 2004, Novosibirsk, Russia (ICMAR'2004).

Methods and results of measurement of the size, direction-of-flight, and velocity distribution functions of droplets in a supersonic flow expanding into vacuum from a nozzle with a near-wall liquid film are given. A model of disintegration of the liquid film at the nozzle exit is suggested, which shows reasonable agreement with experimental data.

10. V.G. Prikhodko, S.F. Chekmarev, I.V. Yarygin, V.N. Yarygin. Ejection of Gas with Near-Wall Liquid Film From a Nozzle into Vacuum. XXVII Siberian Thermophysical Seminar, 5-7 October 2004, Novosibirsk, Russia.

Ejection of a near-wall liquid film (ethanol, butanol) with a co-current gas flow (air) from axisymmetric channels (cylindrical tube, supersonic conical nozzle) into vacuum is studied experimentally and theoretically.

Signatures

Director of ITAM
Corr. Member of RAS
Prof. V.M.Fomin

Project Manager
Doctor in Physics and Mathematics
Prof. M.S.Ivanov